

Institut de Chimie Physique
de l'Université de Fribourg (Suisse)

**DEVELOPMENTS AND APPLICATIONS
OF FOUR WAVE MIXING SPECTROSCOPIES
IN THE PICOSECOND AND FEMTOSECOND TIME REGIMES**

THESE

Présentée à la Faculté des sciences de l'Université de Fribourg (Suisse)
pour l'obtention du grade de *Doctor rerum naturalium*

par

GUMY Jean-Claude

de

Ecuvillens (FR)

Thèse N° 1302

Imprimerie St-Paul, Fribourg

2000

Acceptée par la Faculté des Sciences de l'Université de Fribourg (Suisse) sur proposition du jury composé de Messieurs

Prof. Dr. F. Emmenegger, Université de Fribourg, président du Jury

Dr. E. Vauthey, Université de Fribourg, directeur de thèse

Prof. Dr. E. Haselbach, Université de Fribourg, rapporteur

Prof. Dr. M. Chergui, Université de Lausanne, rapporteur

Fribourg, le 29 juin 2000

Le directeur de thèse:

Le doyen:

Dr. E. Vauthey

Prof. Dr. B. Hirsbrunner

Ce travail a été réalisé sous la direction de M. le Dr. E. Vauthey, à l'institut de chimie physique de l'Université de Fribourg (Suisse).

Je tiens à le remercier tout particulièrement pour sa passion et son enthousiasme si communicatif. Nos nombreuses discussions et ses précieux conseils ont permis l'élaboration de ce travail dans les meilleures conditions. Je tiens aussi à le remercier pour sa disponibilité et sa patience lors de la correction de ce mémoire.

Toute ma gratitude va à M. le Prof. Dr. E. Haselbach pour son chaleureux accueil au sein de son institut. Je lui suis aussi reconnaissant de m'avoir permis d'exercer la tâche d'assistant durant toute l'élaboration de ce travail.

Je remercie également M. le Prof. Dr. M. Chergui, pour avoir accepté de s'engager comme expert lors de l'examen de soutenance, et à ce titre d'avoir accepté de lire ce mémoire.

A Nadine

Summary

This thesis describes the development and the applications of four wave mixing techniques (Transient Grating (TG), Coherent Anti-Stokes Raman Scattering (CARS) and Transient Dichroism (TD)), to investigate processes taking place in the pico- and femtosecond time scales.

In the first part of the work, the TG technique is described using both the holography and the nonlinear optics formalisms. The latter formalism is also used to describe CARS spectroscopy and TD.

The excited-state lifetime of perylene radical cation in boric acid glass, in concentrated sulfuric acid and in acetonitrile, has been investigated with the ps time resolved TG technique. A variation of this technique, based on a calorimetric detection, has been developed to study the lifetime of the anthraquinone radical anion.

CARS experiment was performed in the ps time scale, in order to investigate structural changes, involved in photoinduced Electron Transfer (ET) reactions. Resonant CARS could not be achieved, due to the low repetition rate of our laser, and only high concentration compounds could be accurately characterized.

In the second part of this work, the complete setting up of a TG experiment with fs pulses (with nJ energy) is described in detail, from the experimental arrangement to the interfacing and acquisition programs.

Investigation of the solvation dynamics of an organic dye (IR140) in series of nitriles and alcohols was carried out, with a 60 fs resolution. Wavelength dependent measurements have also been performed. A new model for both inertial contributions of solvation is presented.

The last chapter is devoted to the development of an experiment with amplified fs pulses (μJ). TD experiment was achieved with the second harmonic of the fs amplifier output. Such an experiment was performed on perylene in order to demonstrate the nonlinear behavior of the Stokes-Einstein-Debye relationship in low viscosity solvents, and on cyano and methyl substituted perylene to investigate the influence of the solute-solvent interaction.

Résumé

Cette thèse décrit le développement et l'utilisation de techniques de "mélange de quatre ondes" (réseaux transitoires, CARS, et dichroïsme transitoire), pour l'étude de processus se déroulant dans le domaine de la pico- et femtoseconde. Dans la première partie de ce travail, la technique des réseaux transitoires est décrite à l'aide des formalismes de l'holographie et de l'optique non linéaire. Ce dernier est aussi utilisé pour expliquer la spectroscopie CARS et le dichroïsme transitoire.

La durée de vie de l'état excité du perylène radical cation a été étudiée en ps par la technique des réseaux transitoires résolus dans le temps, aussi bien dans un verre d'acide borique que dans l'acide sulfurique concentré, et dans l'acétonitrile. Une variante de cette technique, basée sur une détection

calorimétrique, a été développée pour étudier la durée de vie de l'état excité du radical anion de l'antraquinone.

Une expérience CARS a été réalisée dans l'échelle des ps, dans le but d'étudier les changements structuraux impliqués dans des réactions de transfert d'électron photoinduit. La forme résonante de la spectroscopie CARS n'a pas donné de résultats reproductibles, en raison de la faible cadence de notre laser. Seul des espèces fortement concentrées ont pu être caractérisées de façon fiable.

Dans la deuxième partie de ce travail, le développement complet d'une expérience de réseau transitoire avec des impulsions fs de faible énergie (nJ) est décrit en détails, de l'arrangement expérimental à l'interfaçage et la réalisation d'un programme d'acquisition.

L'étude de la dynamique de solvation d'un colorant organique (IR140) a été réalisée dans une série de nitriles et d'alcools linéaires, avec une résolution de 60 fs. La dépendance à la longueur d'onde d'analyse a aussi été étudiée. Un nouveau modèle expliquant les deux contributions inertielles est présenté.

Le dernier chapitre est consacré au développement d'une expérience avec des impulsions fs amplifiées (μJ). La technique du dichroïsme transitoire a été utilisée avec la seconde harmonique des impulsions fs amplifiées. Cette technique a été appliquée à la dynamique de rotation du perylène dans une série de solvants de faible viscosité, afin de démontrer le comportement anormal de la relation de Stokes-Einstein-Debye dans ces domaines de viscosité. Une telle étude a aussi été réalisée sur les dérivés 3-cyano et 3-méthyl du perylène, afin d'observer l'influence des interactions solvant-soluté sur le temps de rotation.

Table of Contents

Preface - Historical

Abbreviations and Symbols

1. Theory of Four-Wave Interactions	1
1.1. Introduction	1
1.2. Transient Grating Techniques	2
1.2.1. Introduction	2
1.2.2. Principle of Holography	2
Light Intensity Grating	4
Approximations	8
Real Time Holography	9
1.2.3. Photophysical Grating	10
1.2.4. Thermal Grating	14
1.2.5. Grating Detection	18
1.2.6. Thin and Thick Gratings	23
1.2.7. Beams Polarization	25
Intensity Grating	25
Polarization Grating	27
1.2.8. Advantages of TG over TA	31
1.3. Nonlinear Optics	33
1.3.1. Basic Principles	33
Second Order Susceptibility	35
1.3.2. TG in the Framework of NLO	37
Time Dependence	39

Symmetry Properties	40
Electronic Contribution $\chi_{ijkl}^{(3)}(e)$	42
Nuclear Contribution $\chi_{ijkl}^{(3)}(n)$	42
Density Contribution $\chi_{ijkl}^{(3)}(d)$	43
Population Contribution $\chi_{ijkl}^{(3)}(p)$	44
1.4. CARS	48
1.4.1. CARS in the NLO Formalism	48
1.4.2. CARS In the Grating Formalism: Moving Gratings	54
Moving Grating	55
Coherent Vibrations	56
1.5. Transient Dichroism (TD)	57
1.5.1. TD in the NLO Formalism	60
1.5.2. Homodyne and Heterodyne	61
Homodyne TD	61
Heterodyne TD	61
2. Experiment with ps Pulses	65
2.1. Introduction	65
2.2. Investigation of the Excited-State Dynamics of Radical Ions in the Condensed Phase Using the Picosecond Transient Grating Technique	66
2.2.1. Introduction	66
2.2.2. Picosecond Time Resolved TG	68
2.2.3. Experimental Conditions	70
Laser Pulses	70
Optical Delays	71

Discriminator	71
2.2.4. TG with Calorimetric Detection	72
2.2.5. Paper	73
2.3. Picosecond Resonance CARS Investigation of	
Intermolecular ET Reactions in Solution	80
2.3.1. Introduction	80
2.3.2. Experimental Conditions	81
Laser Pulses	81
Samples	85
Detection	88
Experimental Setup	89
2.3.3. Nonresonant CARS Spectroscopy	90
2.3.4. Time Resolved CARS Spectroscopy of PE ^{•+}	97
2.3.5. Conclusion	104
3. Experiment with Unamplified fs Pulses	106
3.1. Introduction	106
3.2. The fs Ti:sapphire Laser	106
3.2.1. Production of fs Pulses	107
Amplified Modes in a Cavity	108
Cavity Mode-locking	109
3.2.2. Characteristics	111
3.3. Pulse Duration Measurements	112
3.3.1. Fourier-Transform-Limited Pulses	112
3.3.2. Autocorrelation	114
Setup	115
Results	117

3.4. Interfacing of the fs Experiment	118
3.4.1. Real Time Measurements	119
3.4.2. Computer Controlled Delay Line	119
Explanations of the Fs_kin3 Program	120
Linearity of the Translation Stage	123
Turn Zero Detector	125
3.4.3. Data Acquisition	127
Acquisition Board	127
Program	128
3.5. Investigation of the Solvation Dynamics of an Organic Dye in Polar Solvents Using the Femtosecond Transient Grating Technique	134
3.5.1. Transient Spectral Hole Burning Spectroscopy	135
3.5.2. Experimental Conditions	137
Circulation Cell	138
Sample: IR140	140
3.5.3. Paper	142
4. Experiment with Amplified fs Pulses	150
4.1. Introduction	150
4.2. Amplification of fs Pulses	150
4.2.1. Characteristics	153
4.3. Modifications of the Experiment	154
4.3.1. Stepped Delay Line	154
4.3.2. Acquisition Program	157
4.3.3. Rotating Cell	162
4.3.4. Bi-directionally Adjustable Iris	164

4.4. Femtosecond Investigation of Excited-State Dynamics of Radical Ions in the Condensed Phase	165
4.4.1. Perylene Radical Cation in H ₂ SO ₄	165
4.4.2. Tetracene Radical Cation in H ₂ SO ₄ and D ₂ SO ₄	168
Time Resolved TG Spectroscopy with TRC in H ₂ SO ₄	169
Time Resolved TG of TRC ^{*+} in H ₂ SO ₄ at 840 nm	172
Time Resolved TG of TRC ^{*+} in D ₂ SO ₄	173
Conclusions	175
4.5. Investigation of the Rotational Dynamics of Perylene and Perylene Derivatives in Series of n-Alkanes and Nitriles using the Transient Dichroism Technique	176
4.5.1. Overview of Stokes-Einstein-Debye Theory	177
4.5.2. Experimental Conditions	181
Samples	181
Setup	182
4.5.3. Rotational Dynamics of Perylene in Low Viscosity Solvents	183
Rotational Dynamics of PE in a Series of Linear Nitriles	183
Rotational Dynamics of PE in a Series of Linear Alkanes	188
4.5.4. Effect of Substitution on the Rotational Dynamics of PE in Series of Polar and Nonpolar Solvents	191
3-cyanoPE and 3-methylPE in a Series of Linear Alkanes	192
3-cyanoPE and 3-methylPE in a Series of Linear Nitriles	194
Additional Results	196
5. Conclusion and Summary	199
Bibliography	201

Preface

In 1999, the Nobel Prize in Chemistry was given to Ahmed Zewail for his pioneering work in the field of ultrafast spectroscopy. The recognition of this field was mainly due to the fact that he was able to reach the time limit of the chemistry.

In organic chemistry most of the reactions take place in seconds or even hours but in photochemistry, one usually deals with nanosecond (ns) or picosecond (ps). What is the ultimate limit for a chemical reaction ?

This question is rather a problem of definition. If one assumes a reaction to be the path from one equilibrium state to another, then the cooling down of the system is part of the reaction. As it cannot be faster than vibrational frequency (typically tens of fs)¹ the time limit of chemical reactions is a few tens of femtoseconds.

However, one can also exclude the cooling from the reaction process, and a chemical reaction can thus be as fast as an electron transfer. Nevertheless, the ultimate limit to promote an electron, with light, to an excited state is an oscillatory period of light, which takes place in more than 1 fs in the visible. Femtochemistry is thus really the fastest limit of chemistry.

In this thesis we will show how to approach this border. However, before trying to deal with fs phenomena, it is better to understand the techniques used to study such processes. For this reason, the first part of this work is devoted to different techniques and different phenomena in the ps time scale.

In a second part, the basic principles of an experiment with fs pulses are shown and applied to investigations of solvation dynamics. Special care is also taken to explain the interfacing of such an experiment. Finally, an experiment

with amplified fs pulses is described, allowing the rotational time of small molecules to be determined.

An important part of the work described here has been invested in the technical development of new experiments. Furthermore, nonlinear techniques were applied to improve the resolution and the applicability of conventional techniques. For instance, a new technique based on the bleaching of thermal grating is described, which allows molecules of low absorption coefficient to be investigated. CARS experiment was also performed on a ps time scale, and femtosecond hole burning spectroscopy was used to investigate solvation dynamics of an organic dye in series of alcohols and nitriles. The second harmonic of amplified fs pulses extended the probe molecules to perylene derivatives, which were investigated through transient dichroism.

Historical

Chemistry induced by light is not a new phenomenon. The nature has been using it for ages in plants, in vitamin D synthesis, in vision processes, in almost all atmospherical reactions and many others^{2,3}. Chemists also used photochemistry for more than a century, for instance in photography since 1829⁴.

However, it is only in the 50's that people realized that light could be a very interesting tool to study the mechanisms of fast chemical reactions. This conclusion leads to the development of new spectroscopies such as flash photolysis in 1947 by G. Porter and R. G. W. Norrish⁵, this technique still being one of the most used in photochemistry.

Nevertheless, the use of conventional light sources, such as flashlamps, does not allow processes faster than the microsecond to be investigated.

A revolutionary step was made in April 1954 by Townes and Gordon⁶. The development of the MASER gave a wonderful acceleration to the field of optics, and the first LASER was built six years later by Maiman⁷.

This new light source allowed photochemistry to become one of the most studied topic of physical chemistry. In fact the laser does possess unique properties that are extensively used by scientists. For instance, its faculty to be pulsed, leads to the production of ultrafast light pulses as short as 4.8 femtoseconds⁸, allowing ultrafast chemical processes to be investigated⁹. Its high monochromaticity leads to high resolution spectroscopy in the kHz range¹⁰, and coherence of the laser wavefront allows the development of many interference based applications.

One of them was already described in 1948 by Gabor¹¹, and is called holography. This technique has the tremendous advantage to record not only

the intensity of the diffused light from an object, but also its phase. This property makes possible the production of 3D images by use of a reference beam (see chapter 1.2.2). This principle was first applied to photophysics in the seventies¹² in a technique called Transient Grating (TG). This technique has been widely used in this work and is described in detail (see chapter 1.2 and 1.3.2).

Several other new spectroscopies arise from the mixing of laser pulses, such as Transient Dichroism (TD) (chapter 1.5 and 4.4), Spectral Hole Burning (SHB) (chapter 3.5.1) or Coherent Anti-Stokes Raman Scattering (CARS) (chapter 1.4 and 2.3). These spectroscopies involve the interaction of four waves and can be theoretically described within the framework of NonLinear Optics (NLO).

Abbreviations and Symbols

Roman Letters

<i>a</i>	amplitude absorption constant
A	electric field amplitude vector
AQ	anthraquinone
ASE	amplification of spontaneous emission
B	solvent and nonresonant contributions to the optical susceptibility
BuCN	butyronitrile (C ₄)
BuOH	butanol (C ₄)
<i>c</i>	speed of light in vacuum
<i>C</i>	concentration or boundary constant (chapter 4)
<i>c.c.</i>	complex conjugated of the preceding expression
CCD	charge coupled device
CIP	contact ion pair
CS	charge separation
cw	continuous wave
cycloHx	cyclohexane
<i>d</i>	grating thickness
D	diffusion coefficient
DC	direct current
DCA	dicyanoanthracene
DCB	dicyanobenzene
DeCN	decanitrile (C ₁₀)
DiCl	dichloroethane
E	electric field vector

ET	electron transfer
EtOH	ethanol (C ₂)
<i>f</i>	Lorentz local field correction factor or shape factor (chapter 4)
F	Fourier transform or vibration driven force
f(D)	Onsager function
FI	free ion
FWHM	full width at half maximum
FWM	four wave mixing
ΔG	free energy
HTD	homodyne transient dichroism
I	intensity of a light beam or moment of inertia (chapter 4)
k	wave vector
<i>K</i>	attenuation coefficient
Δ <i>k</i>	phase mismatch
L	cavity length or interaction length
L _c	length of coherence
lcp	left circularly polarized grating
LED	light emitting diode
LIP	loose ion pair
LO	local oscillator
m	minus (-45°) linearly polarized grating
MeCN	acetonitrile (C ₂)
MeOH	methanol (C ₁)
n	refractive index
\tilde{n}	complex refractive index
NLO	nonlinear optics
OcCN	caprylonitrile (C ₈)
OKE	optical Kerr effect

p	plus (+45°) linearly polarized grating
P	polarization vector
PA	phthalic anhydride
PE	perylene
PentOH	pentanol (C ₅)
PM	photomultiplier tube
PrCN	propionitrile (C ₃)
q	grating vector
r	anisotropy
r	position vector
R6G	rhodamine 6 G
rcp	right circularly polarized grating
sech ²	squared hyperbolic secant
SED	Stokes-Einstein-Debye
SHG	second harmonic generation
S/N	signal to noise (ratio)
SPM	self phase modulation
t	time
TA	transient absorption
TCNE	tetracyanoethylene
TD	transient dichroism
TG	transient grating
THF	tetrahydrofurane
TRC	tetracene
TR ² -CARS	time resolved resonant coherent anti-Stokes Raman scattering
TZD	turn zero detector
V	molecular volume
VaCN	valeronitrile (C ₅)

Indices and exponents

~	changing
.	radical
+	cation
-	anion
*	complex conjugate or excited-state
^	unit vectors
	parallel
⊥	perpendicular
ac	acoustic
AS	anti-Stokes
d	density
dif	diffraction
e	electronic or excited-state
g	ground-state
mod	modulation of
p	population or pump
pop	due to population
pu	of the pump pulse
pr	of the probe pulse
rot	rotation
s	Stokes or sphere (chapter 4)
v	vibration
ρ	due to density
$\chi_i^{(j)}$	i^{th} element of the j^{th} order susceptibility tensor

Greek Symbols

α	molecular optical polarizability
δ	shift of central frequency or half width of Gaussian profile
Δ	changes in
ε	dielectric constant
γ	spectral bandwidth
Γ	attenuation (for acoustic) or frequency half width
η	efficiency or viscosity (chapter 4)
φ	angle of incidence
φ_B	Bragg angle
κ	coupling constant
λ	wavelength
Λ	fringe spacing
μ	transition dipole or permanent dipole moment
ρ	axial ratio
σ	molecular absorption cross section
τ	time or period
τ_p	pulse duration
v_{ac}	speed of an acoustic wave in a medium
ω	angular frequency
Ω	sweeping frequency

1. Theory of Four-Wave Interactions

1.1. Introduction

Conventional spectroscopies, such as Transient Absorption (TA), can easily be described with a simple formalism. But when the number of pulses interacting in the sample is increased, the corresponding theory becomes more complicated.

Fortunately, nonlinear optics allows all processes dealing with electromagnetic waves to be described in a comprehensive formalism. This is very useful to describe spectroscopies, where four different light beams are interacting.

During this work, we have been using different Four Wave Mixing (FWM) techniques, such as the transient grating, the CARS, the transient hole burning and the transient dichroism spectroscopies.

In this chapter an intuitive theory for the transient grating technique, based on the formalism of holography, is described. This technique will then be described within the formalism of NonLinear Optics (NLO).

This derivation will bring us to another FWM technique, the CARS spectroscopy, which can also be understood within the formalism of holography.

Finally, the transient dichroism, where only two pulses are used, will also be discussed as a FWM technique.

1.2. Transient Grating Techniques

1.2.1. Introduction

Transient absorption is one of the simplest way to investigate transient species, but its sensitivity is rather poor. A technique based on holography was developed by Eichler¹² that gives at least a 100 time better signal to noise ratio (S/N). It is called Transient Grating (TG).

To perform such an experiment, two time coincident light pulses, called pump pulses, have to cross in the sample. Their interference results in a light intensity grating, a succession of dark and bright fringes. The ensuing photochemical changes in the sample mimic this intensity grating, and result in a population grating. This alters the sample absorption and/or refractive index in a periodic manner.

A third pulse, called probe pulse, strikes the sample and is partially diffracted by these gratings. The diffraction efficiency is proportional to the square of the grating amplitude and reflects the chemical changes in the sample.

Doing such an experiment with short laser pulses allows the investigation of kinetic properties of the sample. This is called time resolved TG.

1.2.2. Principle of Holography

To obtain a conventional photography, the scattered light from an object needs to be accumulated on a photoactive medium. A spatial representation of the intensity of the scattered light is stored and is called an image.

In holography, the phase of the light is also important, as it allows depth information to be stored. The object needs to be irradiated with a coherent light source (i.e. a laser). A second coherent beam, with a known phase, is used as a reference beam, and interferes with the scattered one on the photoactive medium. Information on the phase front of the scattered beam is stored as a complicated interference pattern.

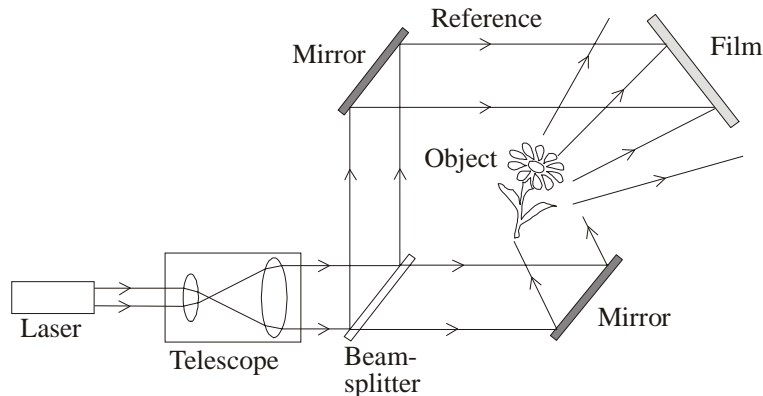


Figure 1.1: Typical geometry to write a hologram. The scattered beam interferes with the reference beam, and the resulting interference pattern is recorded.

A coherent beam is also necessary to read the hologram. It is diffracted at the hologram and the ensuing diffracted beam reconstruct the 3D image (real and virtual) of the object (Figure 1.2).

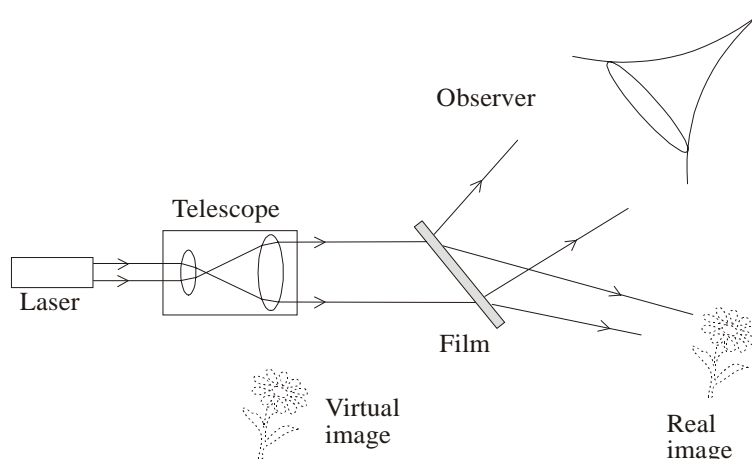


Figure 1.2: Typical geometry to read a hologram. The reference beam is diffracted by the stored interference pattern to produce the real image.

We can distinguish two types of holograms:

- 1) Absorption or amplitude holograms absorb a part of the reconstruction beam to produce the diffraction. Their efficiency cannot be higher than 3.7%.
- 2) Phase or refractive index holograms are made in the same way as amplitude holograms. A further chemical reaction bleaches the remaining absorbing part of the photoactive medium, producing regions of different refractive index. The image is no longer formed due to the attenuation of a part of the probe beam (absorption), but to the dephasing originating from the variation of refractive index in the medium.

To unify those two types of interaction with matter, physicists use a so-called complex refractive index, which contains the conventional refractive index and the attenuation (or absorbance) K of the system:

$$\tilde{n} = n + iK \quad (1.1)$$

Of course in TG, one does not work with scattered light from an object, but the interference pattern is produced by two plane waves.

Light Intensity Grating

When two electromagnetic waves cross in a medium, they interfere, and if they are plane waves with the same wavelength, a harmonic grating is obtained.

This can be easily understood by looking at the crossing of two plane waves with an angle 2φ .

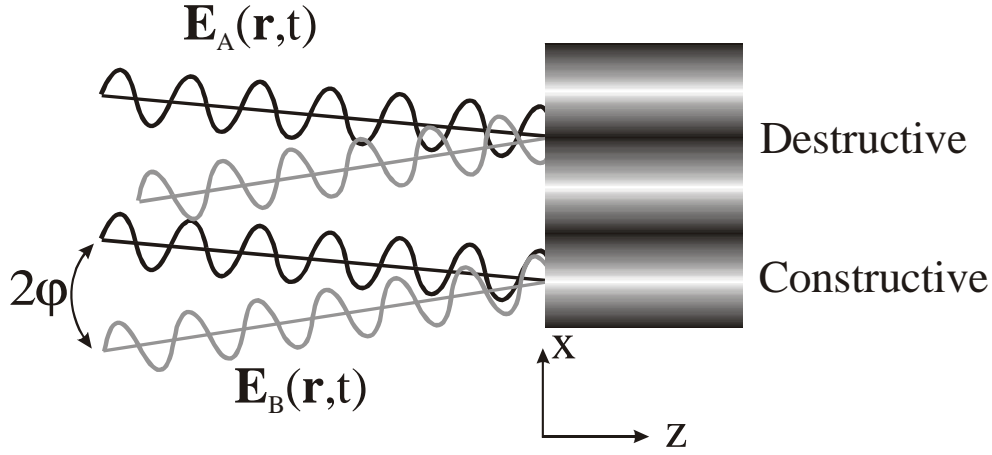


Figure 1.3: Grating formation. Two plane waves with the same wavelength cross with a 2ϕ angle to produce an harmonic grating. Constructive and destructive interference are illustrated.

The two electromagnetic plane waves can be described by their electric field vectors \mathbf{E}_A and \mathbf{E}_B :

$$\begin{aligned}\mathbf{E}_A(\mathbf{r}, t) &= \mathbf{A}_A \cdot e^{i[\mathbf{k}_A \cdot \mathbf{r} - \omega t]} \\ \mathbf{E}_B(\mathbf{r}, t) &= \mathbf{A}_B \cdot e^{i[\mathbf{k}_B \cdot \mathbf{r} - \omega t]}\end{aligned}\quad (1.2)$$

where \mathbf{A}_A and \mathbf{A}_B are the amplitudes (defined as complex quantities) of \mathbf{E}_A and \mathbf{E}_B respectively, \mathbf{k}_A and \mathbf{k}_B their wavevector of length k , t the time, \mathbf{r} the position vector and ω the angular frequency.

At the interference region, i.e. at $z = 0$, the spatial dependence of the wave is:

$$\begin{aligned}\mathbf{k}_A \cdot \mathbf{r} &= k(z \cdot \cos\phi - x \cdot \sin\phi) = -k \cdot x \cdot \sin\phi \\ \mathbf{k}_B \cdot \mathbf{r} &= k(z \cdot \cos\phi + x \cdot \sin\phi) = k \cdot x \cdot \sin\phi\end{aligned}\quad (1.3)$$

and the total electric field amplitude becomes:

$$\mathbf{A} = \mathbf{A}_A \cdot e^{i[k \cdot \sin\phi \cdot x]} + \mathbf{A}_B \cdot e^{i[-k \cdot \sin\phi \cdot x]}\quad (1.4)$$

As the intensity of a light beam can be expressed as:

$$\mathbf{I} = \frac{nc}{2\pi} (\mathbf{A} \cdot \mathbf{A}^*)\quad (1.5)$$

the intensity distribution can finally be described as:

$$\begin{aligned}
I(x) &= \frac{nc}{2\pi} (\mathbf{A} \cdot \mathbf{A}^*) \\
&= \frac{nc}{2\pi} \left[\begin{aligned} &\mathbf{A}_A \cdot \mathbf{A}_A^* + \mathbf{A}_B \cdot \mathbf{A}_B^* \\ &+ \mathbf{A}_A \cdot e^{i[k \cdot \sin \phi \cdot x]} \cdot \mathbf{A}_B^* \cdot e^{i[k \cdot \sin \phi \cdot x]} \\ &+ \mathbf{A}_B \cdot e^{-i[k \cdot \sin \phi \cdot x]} \cdot \mathbf{A}_A^* \cdot e^{-i[k \cdot \sin \phi \cdot x]} \end{aligned} \right] \\
&= \frac{nc}{2\pi} \left[|\mathbf{A}_A|^2 + |\mathbf{A}_B|^2 + \left(\mathbf{A}_A \cdot e^{i[k \cdot \sin \phi \cdot x]} \cdot \mathbf{A}_B^* \cdot e^{i[k \cdot \sin \phi \cdot x]} + c.c. \right) \right] \\
&= I_A + I_B + 2\sqrt{I_A \cdot I_B} \cdot \cos(2 \cdot k \cdot \sin \phi \cdot x)
\end{aligned} \tag{1.6}$$

From this equation, it is clear that the resulting intensity grating is harmonic. Its amplitude varies as a cosine function in the x direction and is constant in the y direction.

This result is correct for plane waves. In practice, Gaussian pulses are often used and the x, y dependence of the grating amplitude is shown in Figure 1.4.

It is interesting to notice that if both beams have the same intensity, the maximum amplitude of the grating is 4 times higher than that of a single pump beam.

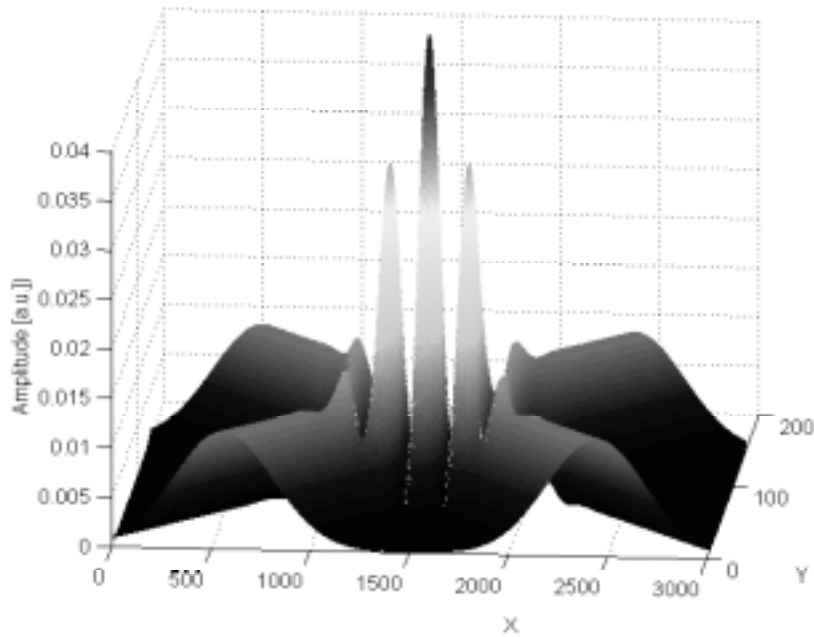


Figure 1.4: Simulation of an intensity grating formation with two Gaussian beams crossing at 90° . Note that the grating amplitude is four times higher than that of a single pump beam.

Such an harmonic grating can be described by two parameters: the **fringe spacing** (Λ) and the **fringe visibility** (Z).

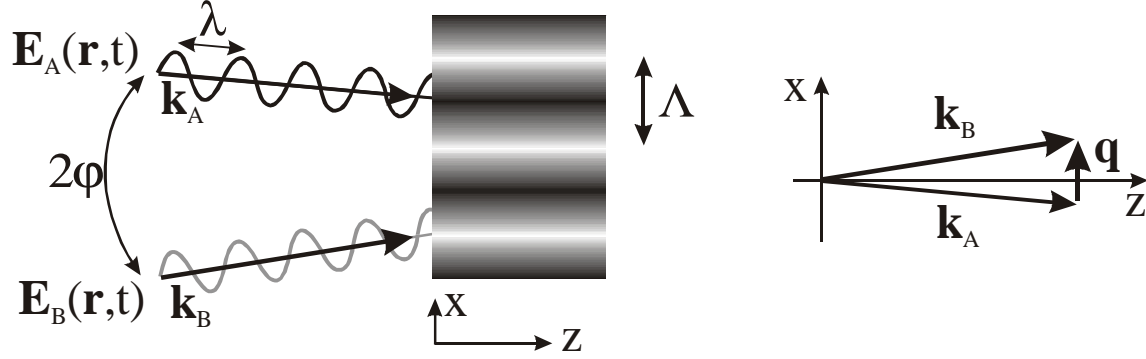


Figure 1.5: Schematic representation of grating formation with two plane waves of wavevectors k_A and k_B . The fringe spacing Λ is the distance between two interference maxima and \mathbf{q} is the grating vector.

The fringe spacing is the distance between two maxima of the interference pattern in the x direction (see Figure 1.5). It can be expressed as:

$$\Lambda = \frac{2\pi}{q} \quad (1.7)$$

with

$$q = |\mathbf{q}| = 2 \cdot k \cdot \sin \varphi \quad (1.8)$$

$$k = \frac{2\pi}{\lambda} \quad (1.9)$$

\mathbf{q} being the **grating vector** and corresponds to $\pm(\mathbf{k}_A - \mathbf{k}_B)$.

One obtains finally:

$$\begin{aligned} \Lambda &= \frac{2\pi}{q} = \frac{2\pi}{2 \cdot k \cdot \sin \varphi} = \frac{\pi}{\frac{2\pi}{\lambda} \cdot \sin \varphi} \\ &= \frac{\lambda}{2 \cdot \sin \varphi} \end{aligned} \quad (1.10)$$

where λ is the wavelength of the pump beams and 2φ their crossing angle.

The fringe visibility Z is the contrast of the hologram and can vary from 0 to 1. It can be expressed as:

$$Z = 2 \frac{\sqrt{I_A \cdot I_B}}{I_A + I_B} \quad (1.11)$$

It reaches its maximal value when both beams have the same intensity.

Approximations

The theory developed above considers plane waves with parallel polarization. In practice, this is not true and Gaussian laser beams of varying polarization are often used. These modifications affect the grating in the following ways:

A) The use of Gaussian beams induces many changes in the theory because the waves are no longer infinite in the x and y directions. Furthermore, the divergence of the beam leads to a phase mismatch of the wave-front, and plane wave theory is in principle no longer applicable.

Fortunately, a Gaussian beam can be approximated to a plane wave if the three following conditions are fulfilled:

- 1) The interaction region must be large compared to the fringe spacing. This implies that many fringes have to be formed in the sample. When working at 532 nm with a crossing angle $2\phi = 5^\circ$, the fringe spacing is $\Lambda = 6 \mu\text{m}$. A Gaussian beam of 6 mm of diameter produces thus 1000 fringes and can then be considered as a plane wave.
- 2) The overlap length in the z direction must be larger than the sample thickness. Here again, for 6 mm diameter beams and $2\phi = 5^\circ$, the two beams overlap (more than 90%) on about 15 mm in the z direction, that is much larger than the sample thickness (usually 1 or 2 mm).

- 3) The attenuation K of the excitation beams by the sample must be negligible. This implies to work with low absorbing samples (typical absorbance 0.3).

B) The polarization problem will be treated in detail in following sections (chapter 1.2.7 and 1.3.2).

Real Time Holography

In order to perform kinetic measurements with the holographic technique described above, the time dependence of such a grating needs to be examined. In time resolved grating experiment, also called real time holography, a grating is created with two laser pulses. These pump pulses have typically a Gaussian temporal intensity profile with a half width τ_p ¹³. The interference term can then be described as¹⁴:

$$\sqrt{I_A I_B} = \sqrt{\hat{I}_A \hat{I}_B} \cdot e^{-(\Delta t/\tau_p)^2} \cdot e^{-(t/\tau_p)^2} \quad (1.12)$$

where $\hat{I}_{A,B}$ are the peak intensities of the pulses, and Δt the time delay between them¹. We can note from this equation that the interference intensity do also have a Gaussian time dependence (the same as the pulses), but decreases exponentially when the two pulses are not time coincident.

¹ The above equation is only valid if the coherence time τ_c (i.e. the reciprocal of the spectral width) is equal to the pulse duration. With incoherent light, which can be considered as a succession of ultrafast coherent pulses with random phases, the pulse duration τ_p has to be replaced by the coherence time τ_c .

Creating a grating with laser pulses is then a suitable method to investigate time resolved processes. The response time is the same as in flash photolysis for instance.

1.2.3. Photophysical Grating

Until now, only the light interference arising from two crossing, time coincident, laser pulses was described. However, our goal is to use this technique to study chemical processes. Thus, the interaction of the medium with the light intensity grating has to be considered.

It was shown previously that the interference intensity was decreasing exponentially with increasing time delay between the two pulses (eq. 1.12). If one considers the electronic dephasing time of the medium, this principle is not absolutely true. In fact, if the two pulses are not time coincident, a small population grating can nevertheless be formed. This is explained by the fact that the electric field of the first pulse forces the electrons to oscillate coherently between two states. When the light is switched off, the electronic oscillation is still coherent for some more time, called the dephasing time. At low temperature, this coherence can have a long lifetime, but in liquids it is usually lost after a few tens of fs. If the second pulse arrives before this coherence is lost, interference between the new electric field and the coherent electronic oscillation occurs, allowing a partial grating to be formed. This property is mainly used in photon echo spectroscopy¹⁵. In our case, we will nevertheless optimize the time coincidence of the two pump pulses to obtain the deepest grating.

A grating being a succession of dark and bright regions, it is clear that photochemistry only occurs in the bright fringes (see Figure 1.6). Consequently, the maximum of the product concentration, corresponding to the minimum of the reactant concentration, matches the light intensity pattern. The modulation of concentration can be expressed as:

$$C(x) = C_0 + C_{\text{mod}} \cdot \cos\left(\frac{2\pi x}{\Lambda} + \theta\right) \quad (1.13)$$

with C_0 being the average concentration of the population and C_{mod} , its modulation amplitude. The θ dephasing allows both product and reactant to be expressed with the same equation.

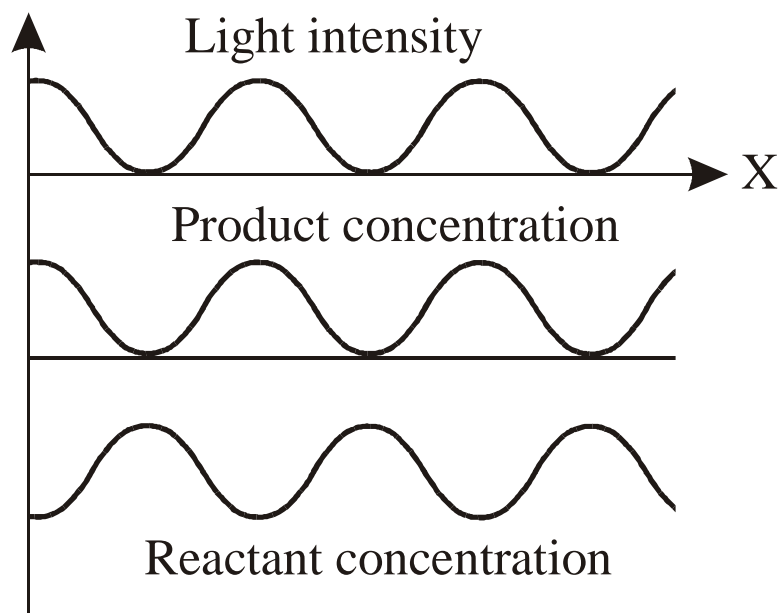


Figure 1.6: Modulation of the light intensity, concentration of photoproduct and reactant in the grating region formed by two time coincident laser pulses of the same intensity. Note that the reactant concentration modulation is out of phase relative to the product one.

In most cases, the reactant and the products do not have the same optical properties. Changing their concentrations modifies the properties of the sample and leads to a material grating.

To describe these optical changes, one can express the dielectric constant of the medium ϵ , which interacts with the electric field of the light, as:

$$\epsilon(x) = \epsilon_0 + \epsilon_1 \cdot \cos\left(\frac{2\pi x}{\Lambda}\right) \quad (1.14)$$

$$\epsilon = \tilde{n}^2 = n^2 + 2i \cdot nK - K^2 \quad (1.15)$$

As the complex refractive index also contains the attenuation of the sample, two types of gratings are produced:

- 1) The amplitude grating is due to modulation of absorbance of the product. This grating is easy to understand, as each species has its own absorption spectrum.
- 2) The phase grating is a variation of the real part of the refractive index, the dispersion. This grating can have three different origins:
 - A) As the product does not possess the same absorption spectrum as the reactant, it also has a different dispersion spectrum. This dispersion spectrum is related to the absorption spectrum through the Kramers-Kronig relation¹⁶. The dispersion spectrum can be calculated by a Hilbert-transformation of the absorption spectrum:

$$n_{pop}(\omega) = \frac{2}{\pi} \cdot \int_0^{\infty} \frac{\omega' K(\omega')}{\omega'^2 - \omega^2} d\omega' \quad (1.16)$$

Where n_{pop} is the refractive index due to population changes.

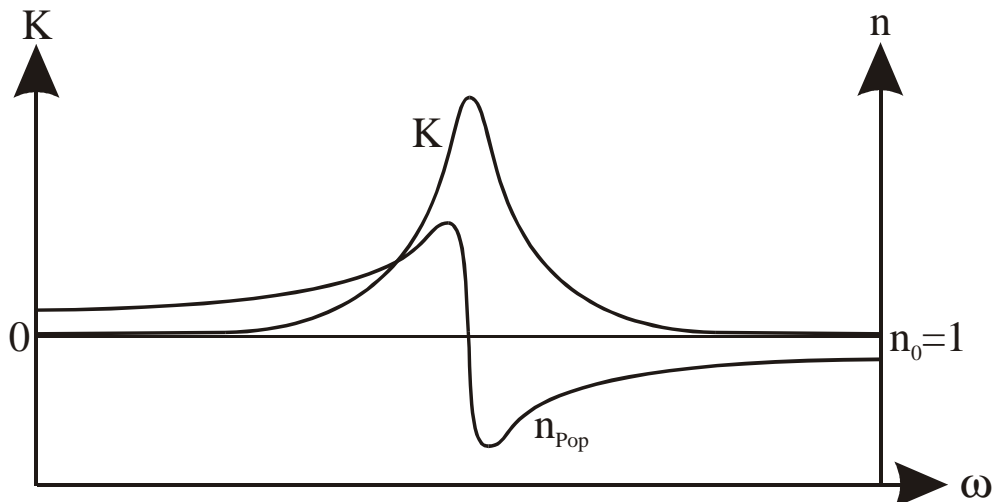


Figure 1.7: Kramers-Kronig relation between dispersion (n_{Pop}) and absorption (K). Note that for frequency higher than the absorption maximum the dispersion is smaller than n_0 ^{II}.

- B) If the volume of the product is not equal to that of the reactant, a change in density in the bright fringes is observed. This is the case, mainly, for formation or dissociation of a complex, or electrostriction. This produces a density grating that results in a phase grating.
- C) During the excitation, an excess energy is often used. This excess energy is relaxed in the medium as heat. A temperature grating is then formed and produces a thermal expansion. That leads to a density grating, called thermal phase grating¹⁷⁻²². Such a grating can also be produced with any systems that deactivates through non-radiative transitions. This specific case will be studied in the next section.

^{II} The refractive index can be understood as an electronic absorption-emission to a virtual state. Each of these cycles taking a few fractions of fs, the light is slowed down in the media and the refractive index is always greater than one. However, near an absorption band, the virtual state has a longer lifetime, and the refractive index increases with increasing frequency. In the center of the absorption band, absorption takes place, and an anomalous dispersion is present (the refractive index decreases with increasing frequency).

In most cases both gratings are present, but it is also possible to selectively study one without the other (by changing the detection wavelength or the polarization conditions for instance) as shown in chapter 1.2.7 and 1.3.2.

1.2.4. Thermal Grating

As mentioned in the previous section, a thermal grating can be produced upon exothermic reaction or non-radiative relaxation. Such a grating can be seen as the interference of a temperature-volume grating with an acoustic grating.

When heat is released, the temperature changes in the fringes. This change in temperature is accompanied by a change in volume. This volume change takes place in an acoustic period τ_{ac} , which is defined as the time needed for an acoustic wave to travel one grating fringe Λ . It can be expressed as:

$$\tau_{ac} = \frac{\Lambda}{v_{ac}} = \frac{2\pi}{\omega_{ac}} \quad (1.17)$$

where v_{ac} is the speed of sound in the medium and ω_{ac} the acoustic frequency.

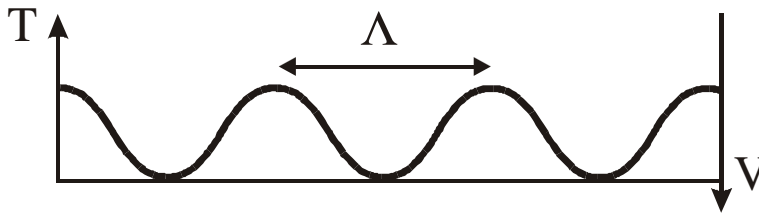


Figure 1.8: Temperature-volume grating formed by heat release in the fringes.

The temperature-volume grating thus formed is lasting for μs , as the diffusion of temperature and molecules is slow.

On the other hand, the sudden change of temperature is like an explosion and molecules are compressed in the dark fringes. This expansion launches two counter-propagating acoustic waves.

This density, or acoustic, grating can be seen as the superposition of two counter-propagating waves, as described in Figure 1.9.

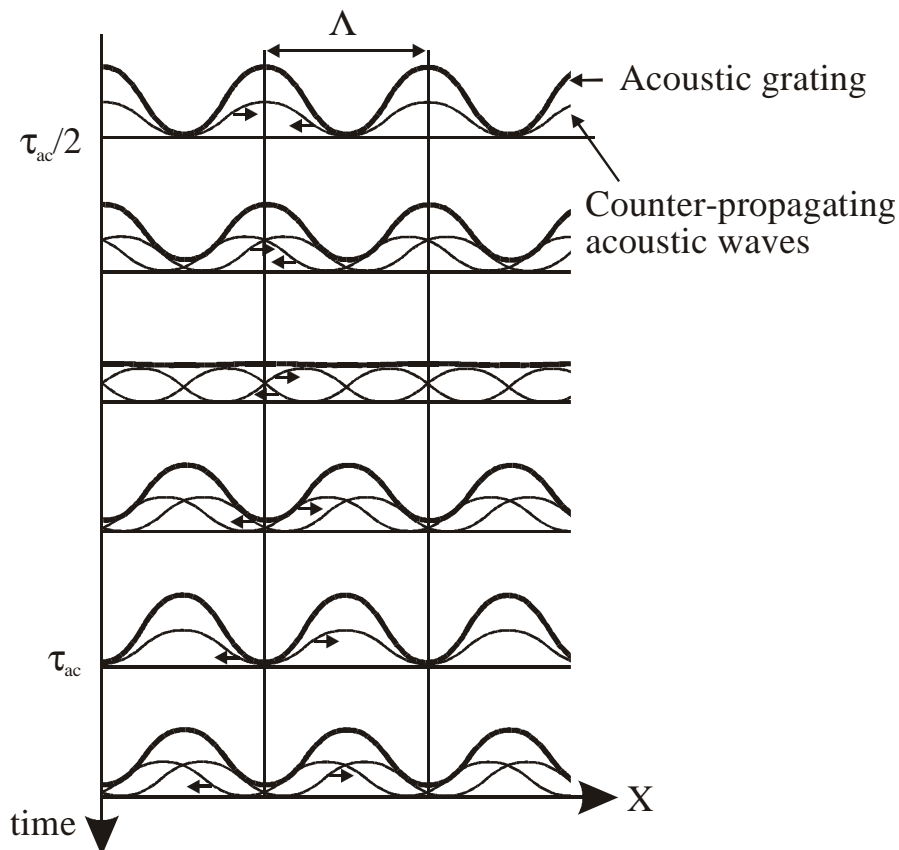


Figure 1.9: Counter-propagation of acoustic waves in a thermal phase grating. The resulting acoustic grating oscillates in time and changes its phase after each half acoustic period. Note that the first maximum of grating amplitude is reached only a half acoustic period after the light intensity grating generation.

Each time two maxima of density, produced from different fringes, met, a maximum of acoustic grating amplitude is achieved. Note that at each half acoustic period, the phase of the acoustic grating is shifted by π .

As the acoustic grating changes its phase at each half acoustic period, the interference of both temperature-volume and acoustic grating leads to an oscillatory behavior of the resulting density grating. The overall grating amplitude thus oscillates in time between zero (destructive interference) and four times the temperature modulation amplitude (constructive interference).

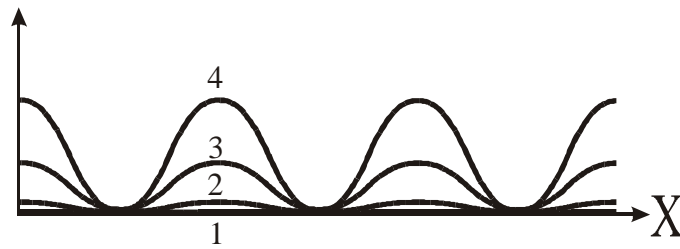


Figure 1.10: Time evolution (1-2-3-4-3-2-1-...) of the density grating, resulting from the interference of the two counter-propagating acoustic waves and the temperature-volume grating. The amplitude of the density grating oscillates between 0 and four times the temperature-volume grating amplitude.

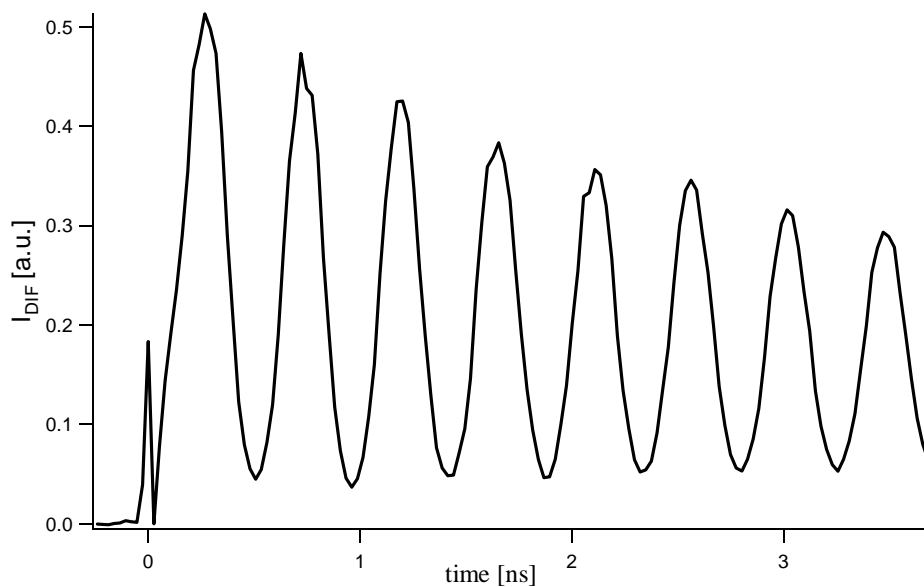


Figure 1.11: Time profile of the diffracted intensity from a thermal grating formed by a suspension of 20 nm diameter colloidal TiO_2 , excited at 355 nm and probed at 532 nm. Note the initial spike at time zero, which is due to the population grating.

This oscillation lasts until the acoustic waves are attenuated by the medium. Thermal diffusion being much slower than acoustic attenuation, the equilibrium intensity corresponds to $\frac{1}{4}$ of the maximum amplitude. The time dependence of the refractive index change, due to density, Δn_p can thus be expressed as:

$$\Delta n_p = Cst \cdot e^{-\Gamma_{ac}t} \cdot (1 - \cos(\omega_{ac}t)) \quad (1.18)$$

where Γ_{ac} is the acoustic attenuation.

If the heat release is slower than the acoustic period, acoustic waves are not produced impulsively, and temporal resolution of the heat release is possible (see Figure 1.12). The advantage of this technique over thermal lensing, is that the time resolution, corresponding to the acoustic period, is determined by the fringe spacing, and can thus be as short as 100 ps for 355 nm pulses. In comparison, the resolution of thermal lensing is in the μs time scale for 2 mm diameter irradiation spot.

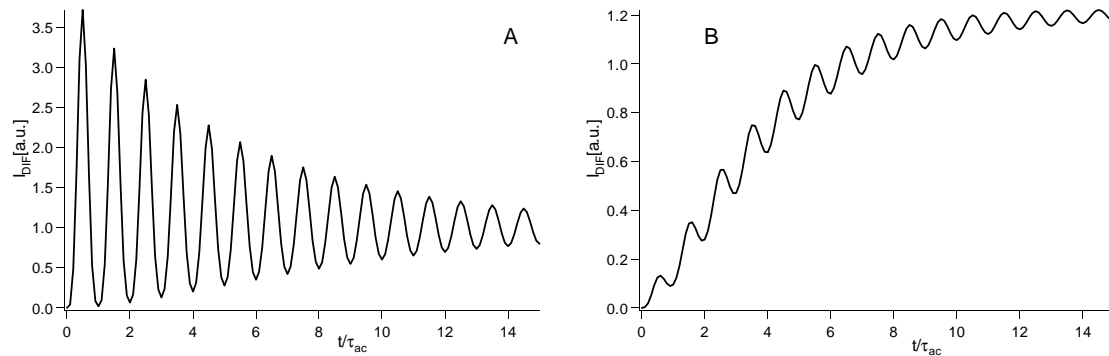


Figure 1.12: Simulation of the time profile of the intensity diffracted from a density grating. A) All the heat is released instantaneously. B) 80% of the heat is released slowly and 20% instantaneously.

We will show in eq.(1.39), that the density grating is in phase with the population phase grating, but do not interact with the amplitude grating. Constructive interference between both phase gratings can then strongly enhance the dispersive signal^{23, 24}.

1.2.5. Grating Detection

Two pump beams that cross in the sample interfere and produce a light grating. This grating modulates the population of the medium and a physical grating is formed (amplitude and phase gratings).

To detect such a grating, a third beam is needed, called probe beam or reference beam (by analogy with holography). It will interact with the spatially modulated dielectric constant of the medium and be diffracted. To understand this phenomenon, the efficiency of the grating has to be determined.

This efficiency can be expressed as:

$$\eta_{eff} = \frac{I_{dif}}{I_{pr}} = \frac{\mathbf{E}_{dif}^2}{\mathbf{E}_{pr}^2} \quad (1.19)$$

Kogelnik has developed a coupled wave theory for holography²⁵. This theory is based on the following ideas:

- 1) The wave propagation obeys the time dependent wave equation derived from Maxwell's relations.
- 2) In the grating, the electric fields of the probe and diffracted beams are superimposed.

From the Maxwell's relation, Helmholtz has derived the following equation, assuming that $\mathbf{E} = \mathbf{E}(\mathbf{r}) \cdot \exp(i\omega t)$:

$$\left[\nabla^2 + \frac{\omega^2}{c^2} \epsilon(x) \right] \cdot \mathbf{E} = 0 \quad (1.20)$$

where $\nabla^2 = \nabla \cdot \nabla$ is the Laplacian operator (second partial derivation in the three directions).

Assuming a x, z -polarized beam, the vectorial representation of the electric field can be reduced to its scalar expression:

$$E(x, z) = A \cdot e^{i\mathbf{k} \cdot \mathbf{r}} + c.c. \quad (1.21)$$

with

$$\mathbf{r} = \sin \varphi \cdot x + \cos \varphi \cdot z \quad (1.22)$$

φ being the angle of incidence of the probe beam.

As the electric field in the grating is the sum of the probe and diffracted ones, it is expressed as:

$$E(x, z) = A_{pr}(z) \cdot e^{i\mathbf{k}_{pr} \cdot \mathbf{r}} + c.c. + A_{dif}(z) \cdot e^{i\mathbf{k}_{dif} \cdot \mathbf{r}} + c.c. \quad (1.23)$$

The conservation of momentum implies that:

$$\mathbf{k}_{dif} = \mathbf{k}_{pr} + \mathbf{q} \quad (1.24)$$

where \mathbf{q} is the grating vector.

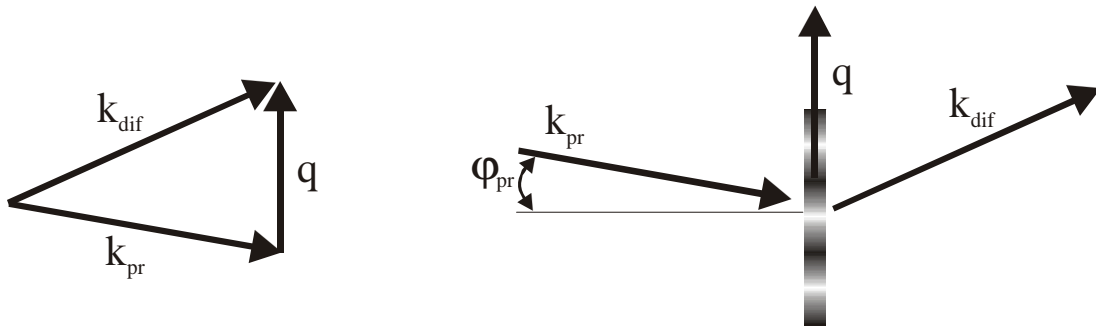


Figure 1.13: Conservation of momentum for diffraction at a grating and experimental geometry.

Using eq.(1.14), the equation (1.20) becomes:

$$\left[\nabla^2 + k^2 \cdot \left(\epsilon_0 + \epsilon_1 \cdot \cos\left(\frac{2\pi x}{\Lambda}\right) \right) \right] \cdot E = 0 \quad (1.25)$$

With the approximation $\epsilon_1 = \Delta\epsilon \approx 2\tilde{n}\Delta\tilde{n} \approx 2n(\Delta n + i\Delta K)$, based on eq.(1.15), and the following definitions:

$$a = \frac{2\pi K}{\lambda} \quad \text{and} \quad \kappa = \frac{1}{2}(k_1 + ia_1) \quad (1.26)$$

where a is the **amplitude absorption constant** and κ the **coupling constant**, a_1 and k_1 are the modulation amplitudes of the absorption and **propagation constant**, respectively. The resolution of eq.(1.25) gives two coupled wave equations:

$$\frac{d^2}{dz^2} [A_{pr}(z)] + 2ik_z \cdot \frac{d}{dz} [A_{pr}(z)] + 2iak \cdot A_{pr}(z) + 2\kappa k A_{dif}(z) = 0 \quad (1.27)$$

$$\begin{aligned} \frac{d^2}{dz^2} [A_{dif}(z)] + 2ik_z \cdot \frac{d}{dz} [A_{dif}(z)] + 2iak \cdot A_{dif}(z) + 2\kappa k A_{pr}(z) \\ + 2k\vartheta \cdot A_{dif}(z) = 0 \end{aligned} \quad (1.28)$$

where $k_z = k \cdot \cos(\varphi)$ is the z -component of the reference and signal wavevectors and ϑ is the dephasing expressed as:

$$\vartheta = q \cdot \sin(\varphi) - \frac{q^2 \cdot \lambda_{pr}}{4\pi} \quad (1.29)$$

λ_{pr} being the probe wavelength.

Note that the angle φ is assumed to be identical for the probe and pump beams.

As seen in chapter 1.2.2, the absorbance of the sample is small and the exchange of energy between the probe and pump beams is slow. This implies that, over an optical wavelength, the amplitude of both waves can be considered to be constant. With this assumption, the second derivative of A_{pr}

and A_{dif} (in eq. 1.27 and 1.28) can be neglected. Inserting eq.(1.29), and multiplying by $(-i)$, the coupled wave equations (1.27 and 1.28) become:

$$\cos(\varphi) \cdot \frac{d}{dz} [A_{pr}(z)] + a \cdot A_{pr}(z) = i\kappa A_{dif}(z) \quad (1.30)$$

$$\cos(\varphi) \cdot \frac{d}{dz} [A_{dif}(z)] + a \cdot A_{dif}(z) - \vartheta \cdot A_{dif}(z) = i\kappa A_{pr}(z) \quad (1.31)$$

The general solution for these coupled equations is:

$$A_{dif}(z) = r_1 \cdot e^{\gamma_1 z} + r_2 \cdot e^{\gamma_2 z} \quad (1.32)$$

$$A_{pr}(z) = s_1 \cdot e^{\gamma_1 z} + s_2 \cdot e^{\gamma_2 z} \quad (1.33)$$

Inserting these solutions and solving for the boundary conditions $A_{pr}(0) = 1$ and $A_{dif}(0) = 0$, one obtains:

$$A_{dif} = ie^{\left(\frac{ad}{\cos\varphi}\right)} \cdot e^{\xi} \cdot \frac{\sin\left(\sqrt{v^2 - \xi^2}\right)}{\left(1 - \frac{\xi^2}{v^2}\right)} \quad (1.34)$$

with $v = \frac{\kappa d}{\cos\varphi}$ and $\xi = i \frac{\vartheta d}{2\cos\varphi}$, d being the grating thickness.

At this point it is important to notice that if ϑ is different from 0, the diffracted wave is not in phase with the probe wave. In this case, the energy exchange is not efficient and no diffraction is obtained. Consequently, a signal is only produced if the **Bragg condition** is achieved:

$$\sin(\varphi_{Pr}) = \sin(\varphi_B) = \frac{q}{2nk_0} = \frac{\lambda_{pr} \sin(\varphi_{Pu})}{\lambda_{pu}} \cdot m \quad (1.35)$$

where $m = 0, \pm 1, \pm 2, \dots$, φ_B is the Bragg angle, φ_{Pu} is half the angle between the two pump beams and $\lambda_{pr,pu}$ are the probe and pump wavelength.

The diffracted amplitude formed by a probe beam at Bragg angle simplifies to:

$$A_{dif} = i \cdot e^{-\frac{ad}{\cos \varphi_B}} \cdot \sin\left(\frac{\kappa d}{\cos \varphi_B}\right) \quad (1.36)$$

Under the Bragg condition, the grating efficiency can be calculated, assuming a probe wave amplitude of unity, as:

$$\begin{aligned} \eta_{eff} &= \frac{I_{dif}}{I_{pr}} = \frac{A_{dif} \cdot A_{dif}^*}{A_{pr} \cdot A_{pr}^*} = A_{dif} \cdot A_{dif}^* \\ &= \left[\sin^2\left(\frac{k_1 d}{2 \cos \varphi_B}\right) + \sinh^2\left(\frac{a_1 d}{2 \cos \varphi_B}\right) \right] \cdot e^{-\left(\frac{2ad}{\cos \varphi_B}\right)} \end{aligned} \quad (1.37)$$

In this equation, both the phase and the amplitude gratings are characterized.

The first term represents the modulation of the propagation constant k and corresponds to the diffraction efficiency due to the phase grating. The second one is a modulation of the absorption coefficient a , and is the diffraction efficiency due to the amplitude grating. The last term, decreasing exponentially with d , represents the attenuation of the diffracted beam by the sample. This term is responsible for the low maximum diffraction efficiency, which cannot be higher than 3.7% in a pure amplitude grating.

Usually, the diffraction efficiency is even lower than 1%. In such cases, the simplifications $\sin(\alpha) = \alpha$ and $\sinh(\alpha) = \alpha$ are valid. Furthermore, with $k_1 = k_0 \cdot \Delta n$, Δn being the modulation amplitude of the refractive index, eq.(1.37) becomes:

$$\begin{aligned} \eta_{eff} &= \left[\left(\frac{k_1 d}{2 \cos \varphi_B}\right)^2 + \left(\frac{a_1 d}{2 \cos \varphi_B}\right)^2 \right] \cdot e^{-\left(\frac{2ad}{\cos \varphi_B}\right)} \\ &= \left[\left(\frac{\pi d \cdot \Delta n}{\lambda \cos \varphi_B}\right)^2 + \left(\frac{d \cdot \Delta a}{2 \cos \varphi_B}\right)^2 \right] \cdot e^{-\left(\frac{2ad}{\cos \varphi_B}\right)} \\ &= \left[\left(\frac{\pi d}{\lambda \cos \varphi_B}\right)^2 \cdot (\Delta n^2 + \Delta K^2) \right] \cdot e^{-\left(\frac{2ad}{\cos \varphi_B}\right)} \end{aligned} \quad (1.38)$$

This expression demonstrates that the diffracted **signal is proportional to the sum of the square of the absorption and refractive index changes**. As a direct consequence, if one measure η_{eff} as a function of time and if the population changes decay exponentially, the observed **signal decays two times faster than the related population**.

Another important observation is that, remembering the double possible origin of dispersion changes (population or density changes), a cross term describes the interference between these two contributions:

$$\begin{aligned}\eta_{eff} &\propto \Delta n^2 + \Delta K^2 \\ &\propto \Delta n_p^2 + \Delta n_d^2 + \Delta K^2 \\ &\quad + 2 \cdot \Delta n_p \cdot \Delta n_d\end{aligned}\tag{1.39}$$

Introducing the frequency dependence of the diffracted efficiency allows the spectral properties of the TG signal to be understood. In fact, shortly after the grating formation, the diffracted spectrum is similar to the absorption spectrum (only slightly broadened), as long as the Δn_p contribution is small. But after half an acoustic period, the thermal phase grating interferes with the dispersion spectrum, and an intense inverse dispersion spectrum is observed²⁴. The diffracted spectrum changes then in time from an absorption to an inverse dispersion one.

1.2.6. Thin and Thick Gratings

The derivation described previously is only valid for thick gratings, i.e. when the grating thickness is larger than the grating fringe spacing Λ .

The Bragg condition is not essential for diffraction in a thin grating. In the latter case, the angle of incidence of the probe beam is of minor importance.

This is due to the fact that the phase difference of a wave diffracted at the entrance ($z = 0$) and at the back ($z = d$) of the grating is small:

$$|\vartheta d| = \left| \frac{2\pi\lambda_{pr} \cdot d}{\Lambda^2 \cdot n} \right| \ll 1 \quad (1.40)$$

Raman-Nath diffraction is then observed²⁶. The diffraction efficiency must be specified for each diffraction order j . For an angle of incidence of 0° , it can be expressed as:

$$\eta_j = \left| J_j \left(\frac{2\pi\Delta\tilde{n}d}{\lambda_{pr}} \right) \right|^2 \quad (1.41)$$

where J_j is the Bessel function of order j , and $\Delta\tilde{n}$ the complex refractive index change.

If the modulation amplitude is small, this equation can be simplified to:

$$\eta_j \propto \Delta\tilde{n}^2 \quad (1.42)$$

Here again, the diffraction efficiency is proportional to the square of the refractive index.

Thick grating can be considered as a succession of thin gratings. The different orders of diffraction interfere with each other. All these diffracted beams interfere constructively only if the angle of incidence satisfies the Bragg condition²⁷.

The sample thickness usually amounts to 1 or 2 mm. In these cases, the thick grating theory have to be applied and only one diffraction order is observed. Nevertheless, when working at very small angles ($<0.2^\circ$), other orders of diffraction can be observed. The efficiency of $\pm 1^{\text{st}}$ orders diffraction being proportional to the square of the complex refractive index, conventional data analysis can be applied also in these cases.

1.2.7. Beams Polarization

The polarization of the beams involved in TG is another interesting parameter that can be varied. A complete determination of the various polarizations and their effect will be discussed within the nonlinear formalism (chapter 1.3.2), but some specific configurations can already be described here.

Intensity Grating

When the polarization of both pump beams is linear and parallel, an intensity grating is formed as described above. The interference of the two beams leads to an harmonic light grating that modifies the properties of the sample. It is important to realize that only molecules that possess a transition dipole moment in the direction of polarization are excited²⁸.

A probe beam of the same polarization will give information, not only on the population dynamics (ground-state recovery or excited-state lifetime), but also on the orientational dynamics. In fact, if the rotational dynamics of the probed system is faster than its relaxation time, the first part of the diffracted dynamics reflects these orientational motions while the final part corresponds to the population dynamics.

The use of a probe beam with perpendicular polarization is also very useful to study the rotational properties of the sample. In this case the diffracted signal increases in the first part of the kinetics. Near time zero, all excited molecules have a parallel orientation (relative to the polarization of the pump beams), and the perpendicular probe beam is almost not diffracted. After some time, orientational changes will increase the number of perpendicularly oriented

molecules, increasing the diffracted intensity. Of course, this only appears if rotational dynamics is faster than the relaxation one.

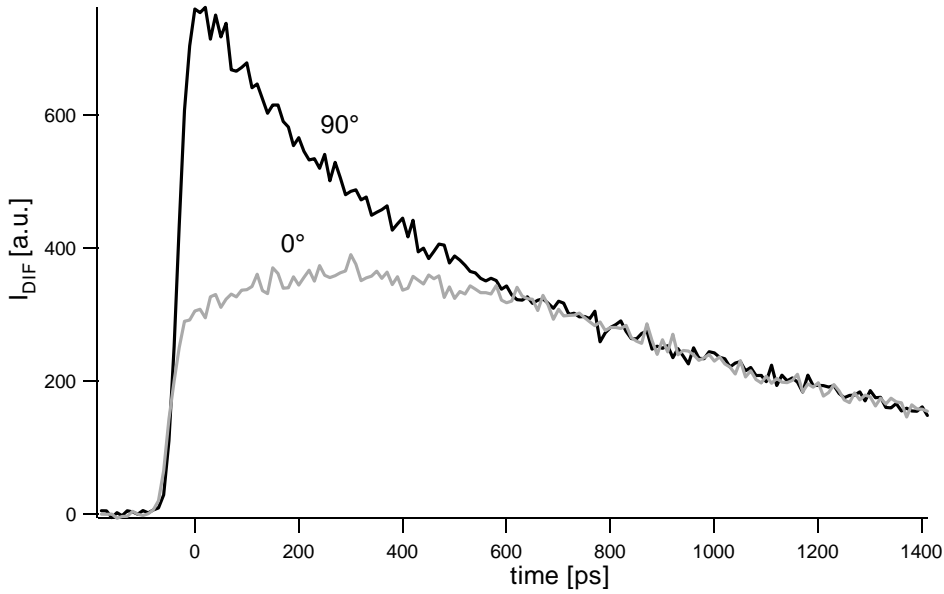


Figure 1.14: Time profile of the diffracted intensity obtained by probing rhodamine 6G in ethanol with a parallel and perpendicular polarization. Pump and probe beams are at 355 nm and 532 nm respectively. Note that as the transition dipole at 355 nm and 532 nm are perpendicular, it is the parallel geometry that gives an initial rise.

The anisotropy of the system can be determined by²⁹:

$$\mathbf{r}(t) = \frac{N_{\parallel} - N_{\perp}}{N_{\parallel} + 2N_{\perp}} = \frac{\sqrt{I_{dif}^{\parallel}(t)} - \sqrt{I_{dif}^{\perp}(t)}}{\sqrt{I_{dif}^{\parallel}(t)} + 2 \cdot \sqrt{I_{dif}^{\perp}(t)}} = r_0 \cdot e^{-\frac{t}{\tau_{rot}}} \quad (1.43)$$

where $I_{dif}^{\parallel,\perp}(t)$ are the diffracted intensities obtained with probe pulse polarization parallel and perpendicular to the pump one and τ_{rot} the rotational relaxation time of the solute molecule. The initial anisotropy r_0 gives informations on the orientation of the transition dipole. If the probed dipole is parallel to the excitation one, $r_0 = 0.4$ and if it is perpendicular, $r_0 = -0.2$.

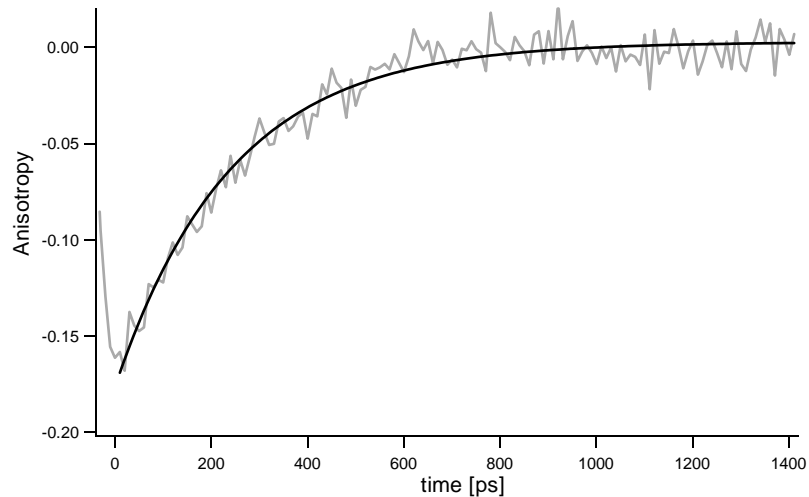


Figure 1.15: Anisotropy decay of rhodamine 6G in ethanol obtained by eq.(1.43) and best exponential fit.

To obtain a pure population dynamic, one can work with two parallel pump pulses and a probe beam polarized at **the magic angle: 54.73°** ^{III}. With this geometry, the contributions due to rotation compensate and population relaxation time can be directly determined, even if rotational reorientation is faster.

Another way of investigating orientational properties is to create a polarization grating.

Polarization Grating

When the polarization of both pump beams is perpendicular, the term $A_A \cdot A_B^*$ in eq.(1.6) vanishes, and the total intensity is no longer modulated. In this

^{III} As $N_{\parallel} \propto \cos^2 \theta$ and $N_{\perp} \propto \sin^2 \theta$, the magic angle is obtained by resolution of $N_{\perp} = 2N_{\parallel}$ which gives $\sin^2 \theta = 2 \cos^2 \theta$ that simplifies to $\tan^2 \theta = 2$.

case, an intensity grating is no longer formed, but a polarization grating is created.

The polarization grating can be decomposed as the sum of four intensity gratings contributions: two circularly (rcp and lcp) and two linearly polarized (m and p) gratings³⁰.

If the investigated sample does not exhibit an optical activity, only the two linearly polarized at $+45^\circ$ (p) and -45° (m) gratings have to be considered.

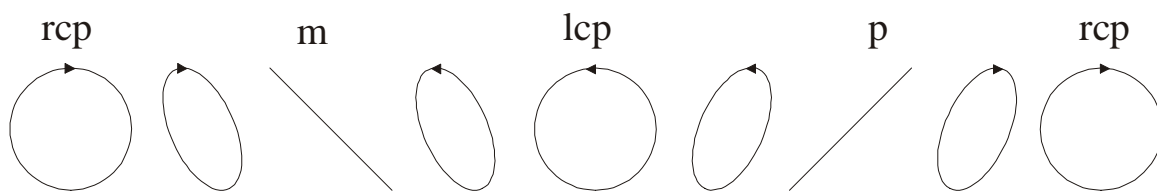


Figure 1.16: Polarization of the electric field along a grating fringe formed by two perpendicular linearly polarized beams.

The sum of these two, out of phase, linear gratings is constant and thus the light intensity is no longer modulated. The sample is excited in all the interacting region, but this excitation is anisotropic in polarization, thus in orientation of population.

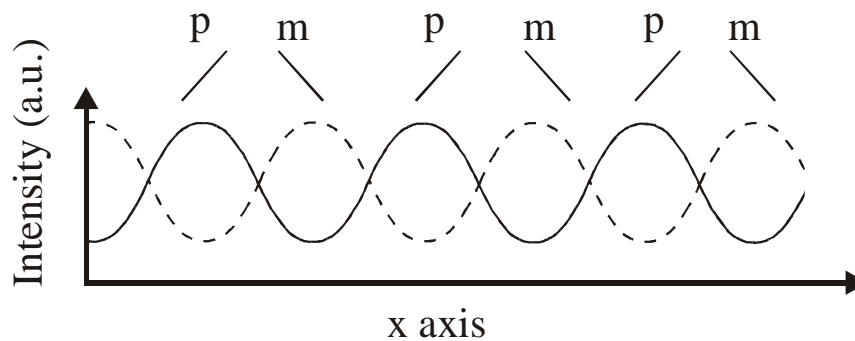


Figure 1.17: Spatial dependence of the two linear contribution of the electric field at $+45^\circ$ (p) and -45° (m) in a polarization grating experiment. Note that their sum is no longer oscillating along x direction and thus there is no light intensity modulation.

The electric field of the probe beam, having the same polarization as one of the pump beams, can be decomposed in two components, each parallel to one grating orientation (see Figure 1.18).

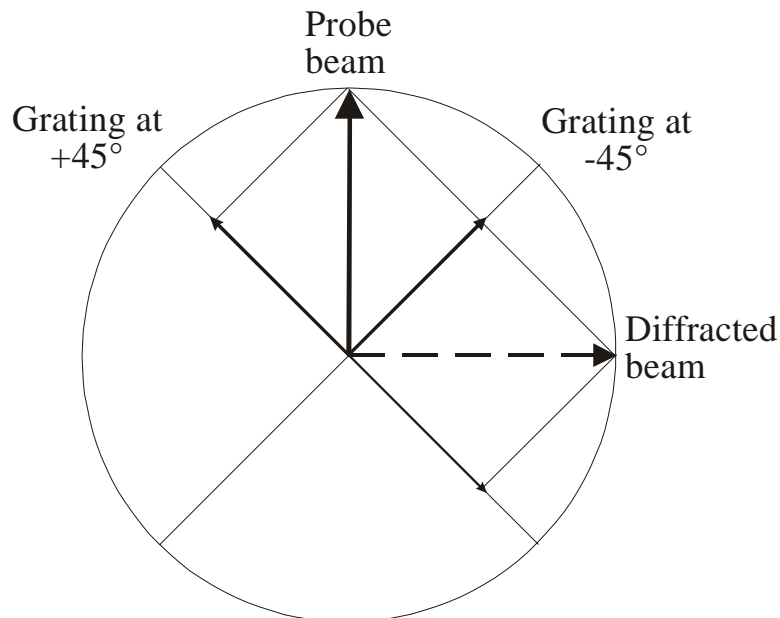


Figure 1.18: Schematic representation of the diffraction at a polarization grating. The 90° rotation of the diffracted beam is due to the π dephasing between both intensity gratings.

The probe beam contribution polarized at $+45^\circ$ only feels the p grating and is not affected by the m one. It is then partially diffracted. The other contribution (at -45°) is also diffracted, but by the m grating. The two gratings being 180° out of phase, their respective diffracted components are also π out of phase. Their recombination leads to a 90° rotation of the diffracted beam polarization, relatively to the probe one.

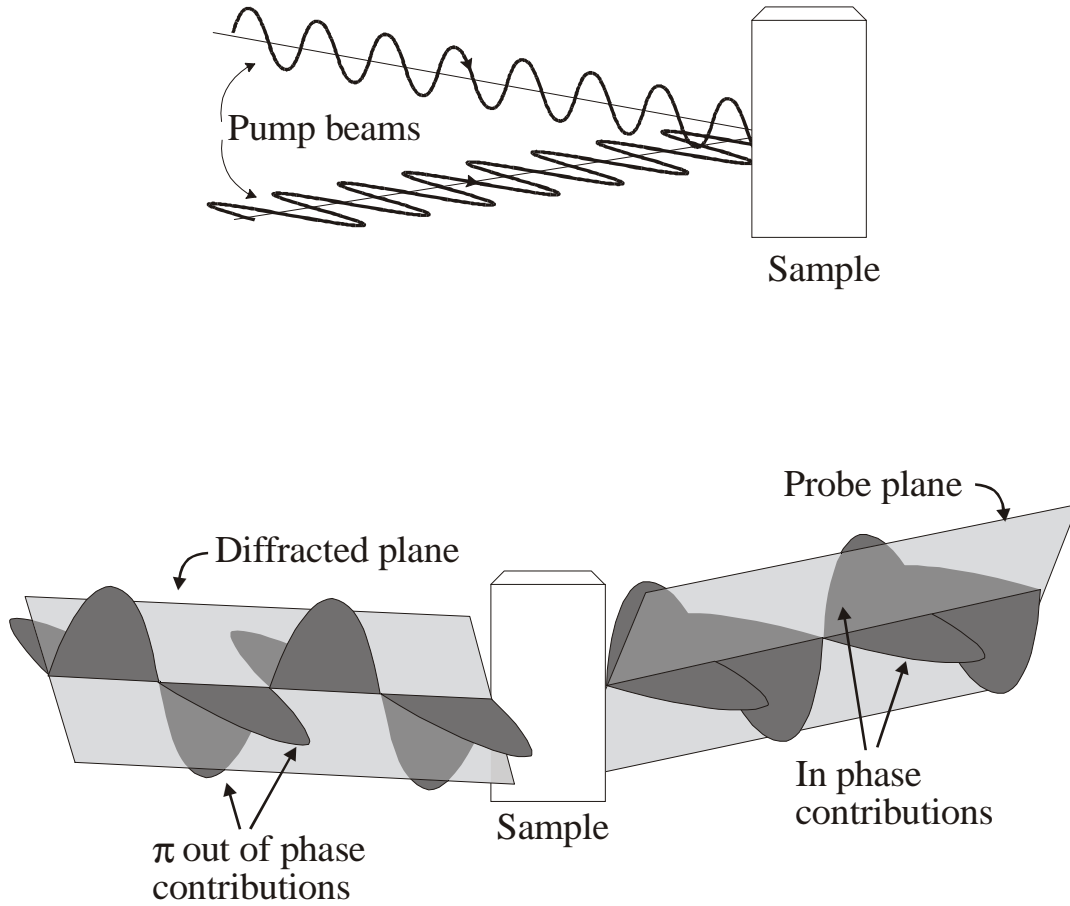


Figure 1.19: Creation and detection of a polarization grating. The plane of polarization of the diffracted beam is rotated by 90° compared to that of the probe beam. This is due to the 180° dephasing between the m and p intensity gratings.

The decay of the m and p intensity gratings is due to the population relaxation and to the reorientation of the transition dipoles. The time dependence of the diffracted intensity is expressed as:

$$I_{\text{dif}}(t) = I_{\text{dif}}(0) \cdot e^{-2(k_{\text{rot}} + k_{\text{pop}})t} \quad (1.44)$$

where $k_{\text{rot, pop}}$ are the rate constant of rotational reorientation and population relaxation respectively. The origin of the factor 2 has already been discussed in eq.(1.38).

This technique is very useful for investigating:

- 1) The reorientational dynamics of molecule whose population relaxation is known³¹. A single measurement allows the anisotropy decay to be obtained directly.
- 2) The lifetime of slow rotating molecule or their solvation dynamics, without producing thermal gratings. As shown in chapter 3.5.2, this is very useful when working with high repetition rate lasers where accumulation of thermal phase grating limits the use of TG technique.
- 3) The energy hopping between chromophores. Such an experiment was performed for instance with multiporphyrin arrays³².

1.2.8. Advantages of TG over TA

Compared to TA, TG spectroscopy has many advantages:

- 1) TG is a zero background technique. In TA, the transmitted pulse is measured and small changes in its intensity have to be detected. However, in TG, the signal is spatially separated from the transmitted light. In this case no background light is present. It is then possible to use very sensitive photomultipliers to increase the sensitivity. The signal to noise ratio is about hundred times better in TG spectroscopy than in TA.

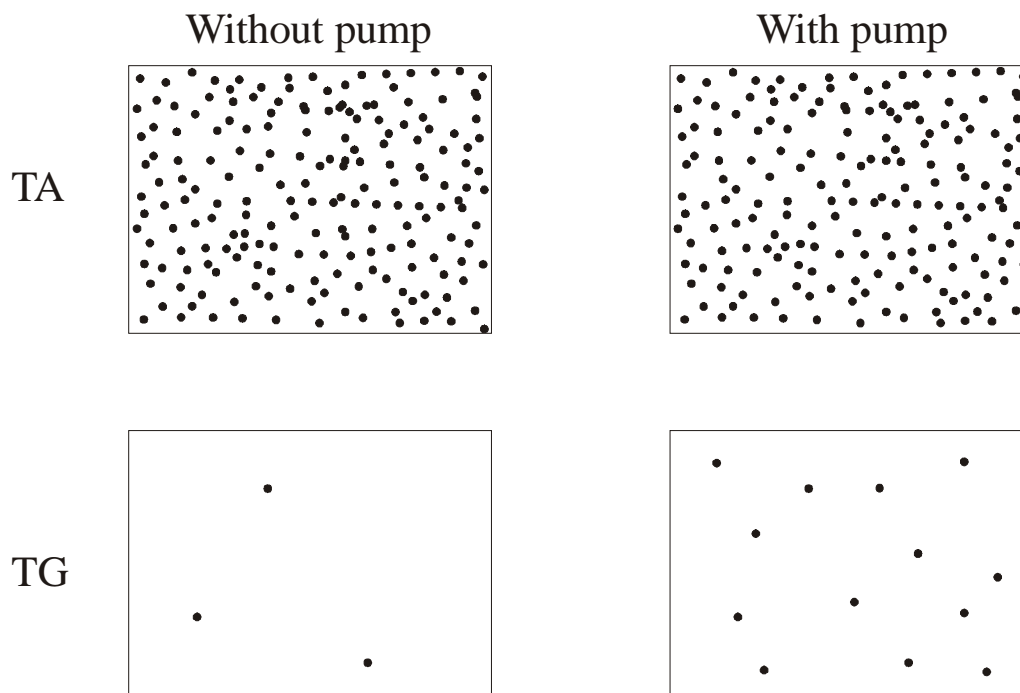


Figure 1.20: Illustration of the zero background detection. In TA the detector has to measure a difference of 10 photons, with and without the pump pulse. In the TG case, the same intensity change is much easier to detect.

- 2) The very high sensitivity of TG allows lower laser intensities to be used. Multiphoton absorption is thus less probable and the photochemical system is better defined (no unwanted species formed).
- 3) The irradiation region is also reduced due to this high sensitivity. Degradation problems are then limited.
- 4) Density gratings and all related energetics investigations can be performed^{17,22}. Furthermore, transient thermal phase grating can be used to investigate species that do not absorb in an accessible region or have small absorption coefficient. This can be achieved by detection of the heat dissipation dynamics, arising from their decay^{33,34}.
- 5) Reorientational properties can be investigated through polarization selective TG^{29,31}. Such an experiment will be described in detail in section 4.5.

1.3. Nonlinear Optics

The nonlinear optics theory has been developed right after the realization of the first laser, when phenomena such as Second Harmonic Generation (SHG) were observed³⁵. This theory allows all processes dealing with electromagnetic waves to be described within a unique formalism. After the basic principles and the definition of tensors, the transient grating and other spectroscopies, such as time resolved resonant CARS, will be described.

1.3.1. Basic Principles

The interaction of light with matter is known as the light induced polarization. It corresponds to the dipole moment per unit volume induced by the electric field of the optical wave.

In conventional optics, the induced polarization (\mathbf{P}) depends linearly on the electric field (\mathbf{E}). It is thus called **linear optics**.

$$\tilde{\mathbf{P}}(t) = \chi^{(1)} \tilde{\mathbf{E}}(t) \quad (1.45)$$

where $\tilde{\mathbf{E}}(t)$ is the fast oscillating electric field of the light and $\chi^{(1)}$ the first-order susceptibility or linear susceptibility. $\chi^{(1)}$ is a second rank tensor.

A tensor is a multidimensional vector. For instance $\chi^{(1)}$ is a second rank tensor that describes the different orientations of the polarization (in the 3 directions x, y, z) of the two electric fields involved (the incident and created fields). It possesses $3^2 = 9$ polarization arrangements. $\chi^{(1)}$ is thus composed of 9 elements:

$$\chi_{x,x}^{(1)} \quad \chi_{x,y}^{(1)} \quad \chi_{x,z}^{(1)} \quad \chi_{y,x}^{(1)} \quad \chi_{y,y}^{(1)} \quad \chi_{y,z}^{(1)} \quad \chi_{z,x}^{(1)} \quad \chi_{z,y}^{(1)} \quad \chi_{z,z}^{(1)}$$

Another way to write these tensor elements is:

$$\chi_{i,j}^{(1)} \quad (1.46)$$

with i and j standing for the 3 Cartesian coordinates of the fields.

Equation (1.45) is only a limit valid for low light intensity (pre-laser era). More generally, the polarization can be expressed as a power series of the electric field:

$$\begin{aligned} \tilde{\mathbf{P}}(t) &= \tilde{\mathbf{P}}^{(1)}(t) + \tilde{\mathbf{P}}^{(2)}(t) + \tilde{\mathbf{P}}^{(3)}(t) + \dots \\ &= \chi^{(1)} \tilde{\mathbf{E}}(t) + \chi^{(2)} \tilde{\mathbf{E}}^2(t) + \chi^{(3)} \tilde{\mathbf{E}}^3(t) + \dots \end{aligned} \quad (1.47)$$

where $\chi^{(2)}$ and $\chi^{(3)}$ are the second and third order nonlinear susceptibility tensors, containing $3^3 (= 27)$ and $3^4 (= 81)$ elements respectively.

The polarization being proportional to higher orders of the electric field, one speaks of **nonlinear optics**.

Due to the small magnitude of their related susceptibility, the higher order polarizations are only important with intense laser beams:

$$\chi^{(1)} \approx 1 \quad \chi^{(2)} \approx 10^{-12} \text{ m/V} \quad \chi^{(3)} \approx 10^{-23} \text{ m}^2/\text{V}^2$$

Furthermore, in centro-symmetric media (such as liquids), every even order vanishes. This can be easily demonstrated by looking at the polarization for the two opposite directions of the electric field:

$$\begin{aligned} \tilde{\mathbf{P}}^{(2n)} &= \chi^{(2n)} \tilde{\mathbf{E}}^{(2n)} \\ \text{and } -\tilde{\mathbf{P}}^{(2n)} &= \chi^{(2n)} (-\tilde{\mathbf{E}})^{(2n)} = \chi^{(2n)} \tilde{\mathbf{E}}^{(2n)} \end{aligned} \quad (1.48)$$

then

$$\tilde{\mathbf{P}}^{(2n)} = -\tilde{\mathbf{P}}^{(2n)} \quad \Rightarrow \quad \chi^{(2n)} = 0 \quad (1.49)$$

When working in liquids with peak power of MW to GW, one only needs to look at the first and third order susceptibilities to account for the various phenomena encountered.

Second Order Susceptibility

For reason of completeness, it is nevertheless interesting to look first at the second order polarization. It is responsible for SHG in non centro-symmetric crystals for instance.

Using an incident field of the form:

$$\tilde{\mathbf{E}}(t, z) = \mathbf{E}_1 \cos(\omega_1 t - k_1 z) + \mathbf{E}_2 \cos(\omega_2 t - k_2 z) \quad (1.50)$$

with $k_{1,2}$ the wavevector components in the z direction and $\omega_{1,2}$ the wave frequencies, the second order polarization, which is proportional to \mathbf{E}^2 , is expressed at the sample ($z = 0$) as:

$$\tilde{\mathbf{E}}^2(t) = \mathbf{E}_1^2 \cos^2(\omega_1 t) + \mathbf{E}_2^2 \cos^2(\omega_2 t) + 2\mathbf{E}_1 \mathbf{E}_2 \cos(\omega_1 t) \cos(\omega_2 t) \quad (1.51)$$

Remembering the trigonometric relations:

$$\cos^2(\alpha) = \frac{1}{2}(1 + \cos(\alpha)) \quad (1.52)$$

$$\cos(\alpha) \cdot \cos(\beta) = \frac{1}{2} \cos(\alpha + \beta) + \frac{1}{2} \cos(\alpha - \beta) \quad (1.53)$$

Equation (1.51) becomes:

$$\begin{aligned} \tilde{\mathbf{E}}^2(t) = & \frac{1}{2}(\mathbf{E}_1^2 + \mathbf{E}_2^2) + \frac{1}{2}(\mathbf{E}_1^2 \cdot \cos(2\omega_1 t)) + \frac{1}{2}(\mathbf{E}_2^2 \cdot \cos(2\omega_2 t)) \\ & + \mathbf{E}_1 \mathbf{E}_2 [\cos(\omega_1 + \omega_2)t + \cos(\omega_1 - \omega_2)t] \end{aligned} \quad (1.54)$$

The first term is time independent and corresponds to the optical rectification in the sample. The second and third terms oscillate at the double input frequencies. This corresponds to the SHG (in usual case ω_1 and ω_2 are identical). The last term possesses contributions at sum and difference frequencies.

Thus a system with $\chi^{(2)} \neq 0$ will exhibit polarization at the frequencies:

$$2\omega_1 \qquad 2\omega_2 \qquad \omega_1 + \omega_2 \qquad \omega_1 - \omega_2$$

Nevertheless, these different phenomena will not take place simultaneously. To selectively obtain one of them, their specific **phase matching condition** has to be fulfilled.

For instance, the sum frequency generation is only possible when:

$$\mathbf{k}(\omega_1 + \omega_2) = \mathbf{k}(\omega_1) + \mathbf{k}(\omega_2) \quad (1.55)$$

$$n_3\omega_3 = n_1\omega_1 + n_2\omega_2 \quad (1.56)$$

In a dispersive medium, the refractive index increases with the frequency. The previous condition can therefore only be achieved in birefringent crystals. In this case the refractive index depends on the direction of polarization of the optical radiation. The highest-frequency wave ω_3 has to be polarized in the direction of the lower refractive index (the extraordinary polarization in a negative uniaxial crystal). Note that it implies a $\pi/2$ rotation of the polarization of the wave at 2ω relatively to that at ω . Two arrangements can be used:

- 1) If an angle ϕ between the incident beams is adjusted, the conversion efficiency is small, but spatially separated from the incident beams.

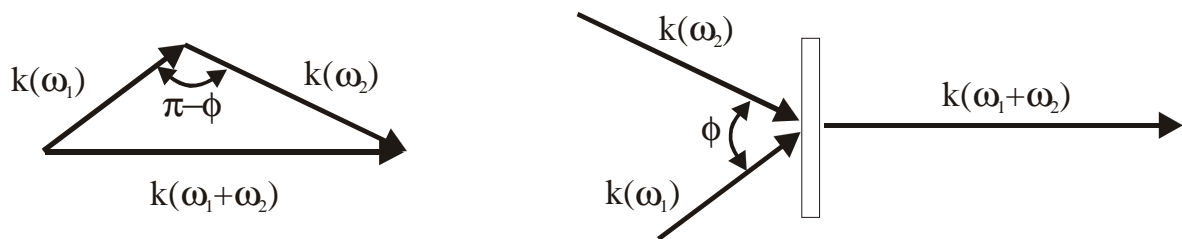


Figure 1.21: Phase matching condition for the sum frequency generation in a birefringent medium. The angle ϕ between the two incident pulses limits the interaction length, but allows an easy spatial separation of the new field.

- 2) Collinear geometry. In this case the interaction length is maximal, and rotation of the birefringent crystal allows the phase matching condition to be fulfilled.

Nevertheless, the notation of nonlinear phenomena is rather complicated. In the study of third order processes, a general resolution of the equations is almost impossible to obtain, and each case of interest has to be studied with its own approximations and symmetry properties.

1.3.2. TG in the Framework of NLO

Transient grating spectroscopy is a four wave mixing (FWM) technique: two pump and one probe beams are mixing together to produce a fourth diffracted beam. This technique depends on the third order nonlinear susceptibility:

$$P_i^{(3)}(\omega_4) = \chi_{ijkl}^{(3)} E_j(\omega_3) \cdot E_k(\omega_2) \cdot E_l(\omega_1) \quad (1.57)$$

where $P_i^{(3)}(\omega_4)$ is the third order polarization amplitude at frequency ω_4 and along the polarization direction i (i standing for the x , y , and z directions). E_j , E_k , E_l are the amplitude of the incident electric fields along the j , k , and l directions, and $\chi_{ijkl}^{(3)}$ is the $ijkl$ element of the third order susceptibility tensor.

The polarization resulting from the mixing of the three input waves oscillates at a frequency ω_4 , and produces a new electromagnetic wave at this frequency, when the phase matching condition is fulfilled.

In the case of the TG experiment, the general expression described above can be simplified, due to the fact that both pump pulses possess the same frequency ω_{pu} .

Furthermore, the diffracted wave oscillates at the same frequency as the probe one. It is then possible to express the generated field frequency as:

$$\begin{aligned} \omega_{dif} &= \omega_{pr} \\ &= \omega_{pr} + \omega_{pu} - \omega_{pu} \end{aligned} \quad (1.58)$$

The negative frequency is a mathematical trick to express an electric field as a complex quantity. As it is a physical measurable quantity, it must be purely real and hence a conjugated complex must exist. It has then been defined as:

$$E_i^*(\omega) = E_i(-\omega) \quad (1.59)$$

Combining eq.(1.57) with the above simplifications gives:

$$P_i^{(3)}(\omega_{dif} = \omega_{pr} + \omega_{pu} - \omega_{pu}) = \chi_{ijkl}^{(3)} E_j(\omega_{pr}) \cdot E_k(\omega_{pu}) \cdot E_l^*(\omega_{pu}) \quad (1.60)$$

Here again, phase matching condition is essential to allow this new wave to grow in the sample. It can be expressed as:

$$|\mathbf{k}_{dif}| = |\mathbf{k}_{pr} + \mathbf{k}_{pu1} - \mathbf{k}_{pu2}| \quad (1.61)$$

Note that this condition is equivalent to the Bragg condition.

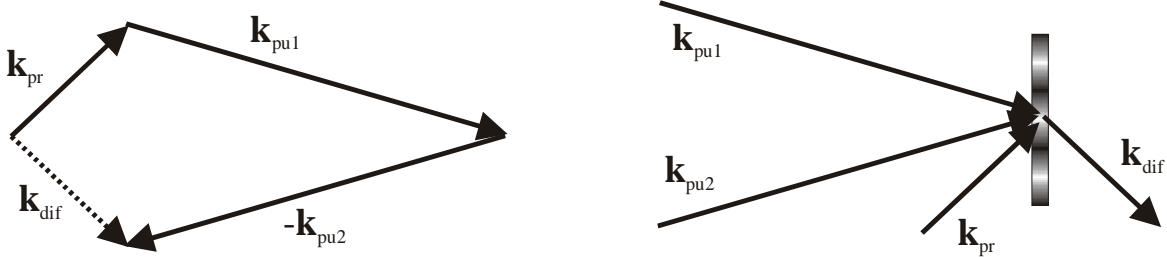


Figure 1.22: Vectorial phase matching diagram and experimental geometry for an in-plane transient grating experiment. The phase matching condition is $\mathbf{k}_{dif} = \mathbf{k}_{pr} + \mathbf{k}_{pu1} - \mathbf{k}_{pu2}$.

The new electromagnetic wave formed at frequency ω_4 originates from the third order polarization of the sample. It can thus be expressed by the wave equation adapted for polarization:

$$\left[\nabla^2 + \frac{\omega^2}{c^2} \epsilon(x) \right] \cdot \mathbf{E} = -\frac{4\pi\omega^2}{c^2} \mathbf{P}_i^{(3)}(\omega) \quad (1.62)$$

The following simplifications can be made to solve this equation:

- 1) The input beams are not depleted or attenuated in the sample.

- 2) The electric field is considered to be only slowly varying in space and time compared to its exponential periodicity. This is known as the slow-varying approximation.

The diffracted intensity is obtained by solving eq.(1.62) with eq.(1.60):

$$I_{dif} = \left(\frac{2\pi}{nc}\right)^4 \cdot \frac{\omega_{dif}^2}{\epsilon(\omega_{dif})} \cdot |\chi_{ijkl}^{(3)}|^2 \cdot I_{pr} \cdot I_{pu1} \cdot I_{pu2} \cdot \frac{\sin^2(\Delta k \cdot d/2)}{(\Delta k \cdot d/2)^2} \quad (1.63)$$

where c is the speed of light in vacuum, d the length of the interacting region and Δk the phase mismatch ($\Delta k = k_{pr} + k_{pu1} - k_{pu2} - k_{dif}$).

If the phase matching condition is not satisfied ($\Delta k \neq 0$), the intensity of the diffracted beam varies periodically with the interaction length. Here again the thin and thick grating can be represented:

In a thick grating, diffraction is only possible if the coherence length, defined as $L_c = 2/\Delta k$, is longer than the sample thickness. This implies that the phase matching condition is fulfilled and thus, the Bragg geometry is used.

In a thin grating, the sample thickness is smaller than the coherence length, even when $\Delta k \neq 0$. In this case, the Bragg condition is no longer necessary for diffraction and many orders of diffraction are present.

Time Dependence

In order to look at the time dependence of the diffracted intensity, the time dependence of the polarization has to be determined.

The Fourier transformation allows $P(\omega)$ to be converted in the time domain.

The polarization described in eq.(1.60) can then be expressed as:

$$P_i^{(3)}(t) = \int_{-\infty}^t dt_1 \int_{-\infty}^t dt_2 \int_{-\infty}^t dt_3 \left[F_{ijkl}^{(3)}(t-t_3, t-t_2, t-t_1) \cdot E_j(t_3) \cdot E_k(t_2) \cdot E_l^*(t_1) \right] \quad (1.64)$$

where $F^{(3)}$ is the Fourier transform of $\chi^{(3)}$ ($\omega_4 = \omega_1 + \omega_2 - \omega_3$), and $t_{1,2,3}$ are the arrival time of the pulses on the sample. In the TG technique, the two pump pulses are time coincident at time τ and equation (1.64) can be rewritten as³⁶:

$$P_i^{(3)}(t) = E_j^{pr} \cdot \int_{-\infty}^t d\tau \left[F_{ijkl}^{(3)}(t-\tau) \cdot E_k^{pu1}(\tau) \cdot E_l^{*pu2}(\tau) \right] \quad (1.65)$$

$$P_i^{(3)}(t) = \int_{-\infty}^t d\tau \cdot \left[\delta(t-t_3) E_j^{pr}(t-t_3) \right] \cdot \int_{-\infty}^t d\tau \left[F_{ijkl}^{(3)}(t-\tau) \cdot E_k^{pu1}(\tau) \cdot E_l^{*pu2}(\tau) \right]$$

where the pump and probe processes have been separated and $\delta(t-t_3) = F_{ijkl}^{(3)}(t-t_3)$ is the Kronecker delta. Solving the wave equation (1.62), with this polarization expression, gives the diffracted intensity at the probing time t_d ³⁶:

$$I_{dif}(t_d) = \left(\frac{2\pi}{nc} \right)^4 \cdot \frac{\omega_{dif}^2}{\epsilon(\omega_{dif})} \cdot \int_{-\infty}^{+\infty} dt \cdot I_{pr}(t_d - t) \cdot \left[\int_{-\infty}^{+t} d\tau \cdot F_{ijkl}^{(3)}(t-\tau) \cdot I_{pu}(\tau) \right]^2 \quad (1.66)$$

where it is assumed that the two time coincident pump pulses have the same intensity. The two integrals represent the convolution of the sample response with both pump pulses (last term) and with the probe pulse (first integral).

Symmetry Properties

To calculate the diffracted intensity, the tensor $\chi_{ijkl}^{(3)}$ (or its Fourier transform $F_{ijkl}^{(3)}(t)$) has to be known. As described previously, a fourth rank tensor contains 81 elements. Fortunately, symmetry consideration allows many simplifications.

In isotropic media, such as liquids, 60 tensor elements are zero. This is due to the fact that the elements must possess an even number of similar Cartesian index. With an odd number, as with χ_{1222} , a wave polarized in the x direction should be produced by 3 waves polarized in the y direction. This is not possible in isotropic media as the response should be in both the $+x$ and $-x$ direction and thus vanish.

Furthermore, symmetry properties allow the indices to be permuted. The 21 remaining elements can only have four different values:

$$\begin{aligned}
 \chi_{1111} &= \chi_{2222} = \chi_{3333} \\
 \chi_{1122} &= \chi_{1133} = \chi_{2211} = \chi_{2233} = \chi_{3311} = \chi_{3322} \\
 \chi_{1212} &= \chi_{1313} = \chi_{2121} = \chi_{2323} = \chi_{3131} = \chi_{3232} \\
 \chi_{1221} &= \chi_{1331} = \chi_{2112} = \chi_{2332} = \chi_{3113} = \chi_{3223}
 \end{aligned} \tag{1.67}$$

These values are also related by the following equation:

$$\chi_{1111} = \chi_{1122} + \chi_{1212} + \chi_{1221} \tag{1.68}$$

In the special case of TG, both pump pulses have the same frequency and can thus be permuted. A further simplification is possible:

$$\chi_{1212} = \chi_{1221} \tag{1.69}$$

From the 81 elements of the third order nonlinear tensor, only 21 are nonzero and only two (χ_{1122} and χ_{1212}) are independent in a TG experiment:

$$\chi_{1111} = \chi_{1122} + 2 \cdot \chi_{1212} \tag{1.70}$$

To calculate these elements, it is necessary to look at the physical process they depend on. In a condensed phase TG, the nonlinear susceptibility can originate from four different physical processes. The tensor can then be expressed as the sum of these four contributions³⁶:

$$\chi_{ijkl}^{(3)} = \chi_{ijkl}^{(3)}(e) + \chi_{ijkl}^{(3)}(n) + \chi_{ijkl}^{(3)}(d) + \chi_{ijkl}^{(3)}(p) \tag{1.71}$$

Electronic Contribution $\chi_{ijkl}^{(3)}(e)$

When an electric field propagates through a dielectric medium, the bound electrons respond to this field and become aligned to it. The electronic anisotropy thus created induces a birefringence in the medium^{IV}. This effect is known as the *electronic Optical Kerr Effect* (eOKE). The response can be considered as instantaneous, even with fs pulses, and does not last after the electric field has left the sample. This contribution corresponds to the convolution of the two pump pulses with the probe pulse.

Within the Born-Oppenheimer approximation, the related susceptibility $\chi_{ijkl}^{(3)}(e)$, have the following additional symmetry property³⁶:

$$\begin{aligned}\chi_{1111}^{(3)}(e) &= 3 \cdot \chi_{1122}^{(3)}(e) \\ &= 3 \cdot \chi_{1212}^{(3)}(e)\end{aligned}\tag{1.72}$$

Nuclear Contribution $\chi_{ijkl}^{(3)}(n)$

The nuclei of the sample cannot oscillate at the optical frequency to reorient. However, two beams are interacting in the media, and the optical field has to be squared. Therefore, as described in eq.(1.54) a component of the electric field independent of the optical frequency is also present. This is responsible for the *optical rectification*. This constant electric field will last as long as the beams cross the sample. The reorientation time of organic solvents being in

^{IV} As already mentioned in section 1.2.3, the refractive index can be understood as an electronic absorption-emission to a virtual state. When an anisotropy is induced in the electron orientation by a pump pulse, the refractive index becomes also anisotropic, and thus polarization dependent. One speaks of induced birefringence.

the order of ten ps (for benzene for instance), a 30 ps laser pulse induces an alignment of the molecules along the optical electric field²⁶. This is of course only possible with molecules having a permanent dipole moment or an anisotropic polarizability.

This effect is known as the *nuclear Optical Kerr Effect* (nOKE) and is lasting as long as the anisotropy is present. In general, this contribution vanishes by reorientation a few ps after the pulses have left the sample.

Due to its symmetry property, the following relationship can be deduced for the nuclear susceptibility³⁶:

$$\begin{aligned}\chi_{1111}^{(3)}(n) &= -2 \cdot \chi_{1122}^{(3)}(n) \\ &= \frac{4}{3} \cdot \chi_{1212}^{(3)}(n)\end{aligned}\tag{1.73}$$

Density Contribution $\chi_{ijkl}^{(3)}(d)$

As already mentioned in section 1.2.4, heat release, due to excess excitation energy or fast non-radiative conversion, is responsible for acoustic wave production. The density contribution of the nonlinear susceptibility accounts for this phenomenon. Its time dependence is the same as that of the density refractive index (eq. 1.18). With small crossing angle, this contribution only appears ns after the excitation and can last for μ s.

Its specific symmetry property is:

$$\chi_{1212}^{(3)}(d) = 0\tag{1.74}$$

$$\chi_{1111}^{(3)}(d) = \chi_{1122}^{(3)}(d)\tag{1.75}$$

Equation (1.74) corresponds to the case when two perpendicular polarized pump beams are used and no intensity grating, and thus no density grating is formed.

Population Contribution $\chi_{ijkl}^{(3)}(p)$

The population changes modify the optical properties of the sample. For simplicity, it is convenient to consider a two-level system with a ground, g , and excited, e , state population. In this case the total linear polarization is the sum of both contributions:

$$\begin{aligned}\mathbf{P} &= \mathbf{P}_g + \mathbf{P}_e \\ &= \boldsymbol{\chi}_g \cdot \mathbf{E}_g + \boldsymbol{\chi}_e \cdot \mathbf{E}_e\end{aligned}\quad (1.76)$$

For isotropic media, the linear susceptibility is defined as²⁶:

$$\boldsymbol{\chi}_{g,e}^{(1)} = N_{g,e} \cdot f \cdot \boldsymbol{\alpha}_{g,e} \quad (1.77)$$

where N is the molecular density, $\boldsymbol{\alpha}$ the orientationally averaged polarizability of the molecules and f the Lorentz local field correction factor:

$$f = \frac{n^2 + 2}{3} \quad (1.78)$$

The excited-state population density following a fast laser excitation can be assumed to be:

$$N_e(x, t) = \sigma \cdot N_{tot} \cdot I_{pu}(x) \cdot e^{-k \cdot t} \quad (1.79)$$

where σ is the molecular absorption cross section, k the rate constant of deactivation of the excited-state, I_{pu} the spatially modulated pump intensity and N_{tot} the total population.

$$N_{tot} = N_g(x, t) + N_e(x, t) \quad (1.80)$$

The polarization can then be rewritten, assuming $N_g \approx N_{tot}$ as:

$$\mathbf{P} = \chi_g^{(1)} \cdot \mathbf{E}_g + [\boldsymbol{\sigma} \cdot N_{tot} \cdot f \cdot (\alpha_e - \alpha_g) \cdot e^{-k \cdot t}] \cdot I_{pu}(x) \cdot \mathbf{E}_e \quad (1.81)$$

or as

$$\mathbf{P}_i = \chi_{ij}^{(1)} \cdot \mathbf{E}_j(\omega_{pr}) + \chi_{ijkl}^{(3)}(p) \cdot \mathbf{E}_j(\omega_{pr}) \cdot \mathbf{E}_k(\omega_{pu}) \cdot \mathbf{E}_l(\omega_{pu}) \quad (1.82)$$

with

$$\chi_{ijkl}^{(3)}(p) = \frac{nc}{2\pi} \cdot \boldsymbol{\sigma} \cdot N_{tot} \cdot f \cdot \Delta\alpha \cdot e^{-k \cdot t} \quad (1.83)$$

The third order nonlinear susceptibility can thus be calculated from the polarizability difference between the ground and excited-states.

The symmetry property of this contribution is more complicated. In fact it depends on the angle between the transition dipoles involved in the pump ($\boldsymbol{\mu}_{pu}$) and the probe ($\boldsymbol{\mu}_{pr}$) processes. Myers and Hochstrasser³⁷ have expressed the susceptibility taking into account the polarization anisotropy r .

$$\chi_{1122}^{(3)}(p) = \frac{1-r}{3} \quad (1.84)$$

$$\chi_{1212}^{(3)}(p) = \frac{r}{2} \quad (1.85)$$

and thus with eq.(1.70):

$$\chi_{1111}^{(3)}(p) = \frac{1+2r}{3} \quad (1.86)$$

where the anisotropy is described by:

$$r = \frac{2}{5} (P_2 [\boldsymbol{\mu}_{pu} \cdot \boldsymbol{\mu}_{pr}]) \quad (1.87)$$

with P_2 being the second Legendre polynomial and the brackets standing for the average angle between the transition dipoles.

Three main cases can be considered:

- A) There is no correlation between μ_{pu} and μ_{pr} . In this case, the probe pulse arrives in the sample after all information about the polarization has disappeared. This means that the sample is isotropic. As $r = 0$ the relations between the susceptibility tensors are:

$$\chi_{1212}^{(3)}(p, r = 0) = 0 \quad (1.88)$$

$$\chi_{1111}^{(3)}(p, r = 0) = \chi_{1122}^{(3)}(p, r = 0) \quad (1.89)$$

- B) μ_{pu} and μ_{pr} are parallel. The Legendre polynomial is 1 and the anisotropy is thus $r = 2/5$. The relations between the susceptibility tensors are:

$$\begin{aligned} \chi_{1111}^{(3)}(p, r_{\parallel}) &= 3 \cdot \chi_{1122}^{(3)}(p, r_{\parallel}) \\ &= 3 \cdot \chi_{1212}^{(3)}(p, r_{\parallel}) \end{aligned} \quad (1.90)$$

- C) μ_{pu} and μ_{pr} are perpendicular. In this case the Legendre polynomial is $-1/2$ and thus the anisotropy $r = -1/5$. The following relations are valid:

$$\begin{aligned} \chi_{1111}^{(3)}(p, r_{\perp}) &= \frac{1}{2} \cdot \chi_{1122}^{(3)}(p, r_{\perp}) \\ &= -2 \cdot \chi_{1212}^{(3)}(p, r_{\perp}) \end{aligned} \quad (1.91)$$

The symmetry properties of the tensor elements for the six physical processes mentioned above are different. They can thus be separated by selective polarization TG measurements. By choosing the appropriate arrangement of polarization of the pump, probe and signal waves, one can eliminate one of these processes.

The easiest example of this selective polarization TG has already been mentioned in section 1.2.7, where the polarization grating (corresponding to $\chi_{1212}^{(3)}$) had no density grating contribution ($\chi_{1212}^{(3)}(d) = 0$) and decays with the rotational time of the molecule, i.e. the loss of anisotropy ($\chi_{1212}^{(3)}(p, r = 0) = 0$).

More generally, one can calculate for a specific pump-probe polarization, the detection polarization, ξ , needed to eliminate the contribution of each specific process. For instance for the geometry:

Pump1: 0° , Pump2: 0° , and Probe: 45°

the values of ξ are summarized in Table 1.1^{38,39}.

Physical mechanism	$\chi_{1111}^{(3)}$	$\chi_{1122}^{(3)}$	$\chi_{1212}^{(3)}$	ξ
Electronic OKE	1	1/3	1/3	-71.6°
Nuclear OKE	1	-1/2	3/4	63.4°
Population :				
$\mu_{pu} \parallel \mu_{pr}$	1	1/3	1/3	-71.6°
$\mu_{pu} \perp \mu_{pr}$	1	2	-1/2	-26.6°
$r = 0$	1	1	0	-45°
Density, Acoustic wave	1	1	0	-45°

Table 1.1: Relative values of the tensor elements of the third order nonlinear susceptibility originating from the different physical processes taking place in a TG experiment and signal beam polarization angle ξ which suppresses the contribution of the given process for the set of polarization ($\xi, 45^\circ, 0^\circ, 0^\circ$).

Note that the eOKE and the parallel population contributions have the same symmetrical properties and thus can not be separated geometrically. Nevertheless, time dependence of these physical processes is often different and separation is easy, as long as the population lifetime is greater than the laser pulse duration.

1.4. CARS

As seen in the previous section, TG can be used to obtain many information on a photophysical system, such as population dynamics, energetic or reorientational time. However, unless working in the IR, no information about structure and time resolved structural changes can be obtained. Such information can be determined by *Time Resolved Resonance Coherent Anti-Stokes Raman Scattering* (TR²-CARS) spectroscopy.

Spontaneous Raman scattering does also gives the same information, but CARS spectroscopy possesses the following advantages:

- 1) Its sensitivity is orders of magnitude higher (typically 10^4 to 10^{10} for the resonant and double resonant case).
- 2) Its signal is not hidden by the fluorescence of the sample.
- 3) Its signal is well collimated (as a laser beam) and can thus be easily separated from the ambient-light background.

This technique is also a four wave mixing process and can thus be expressed in the NLO and grating formalisms.

1.4.1. CARS in the NLO Formalism

Looking at the following energy level diagram, one can interpret the CARS spectroscopy as a succession of absorption and emission of light.

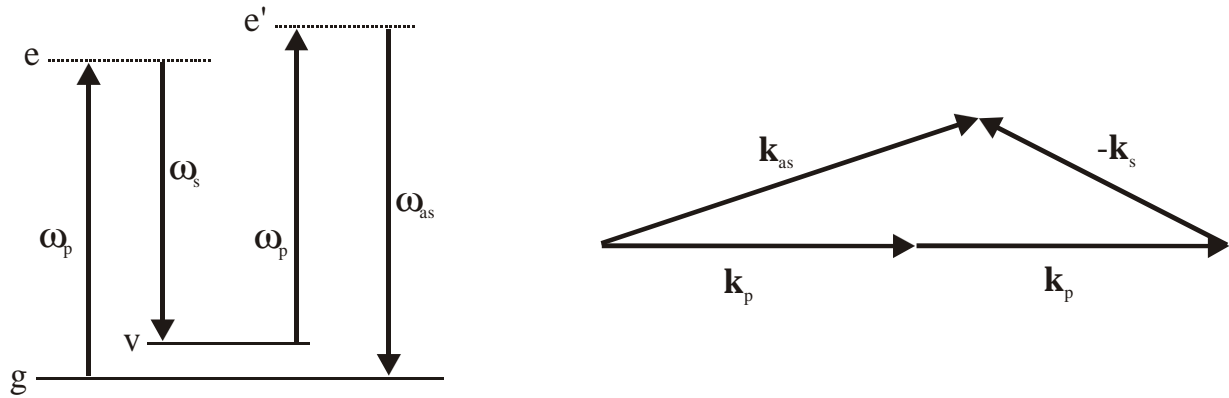


Figure 1.23: Four-level energy diagram and phase matching conditions for CARS experiment. g is the ground-state and v the first vibrational excited-state. In double resonant CARS, e or e' can be electronically excited-states, otherwise they are virtual states.

First, an electromagnetic wave of frequency ω_p interacts with the sample, bringing it in a virtual state e . The second beam at frequency ω_s induces the "emission" to the first vibrational excited-state v . The sample is excited again by the pulse ω_p to an e' state that goes back to the initial state upon emission of an anti-Stokes radiation at ω_{as} .

Of course, this sequential representation is not correct as all four beams are simultaneously in the sample, but it facilitates the physical comprehension of the CARS spectroscopy.

The phase matching condition has also to be satisfied:

$$|\mathbf{k}_{as}| = |\mathbf{k}_p + \mathbf{k}_p - \mathbf{k}_s| \quad (1.92)$$

However, a new difficulty arises from the fact that, for a given geometry, this condition can only be fulfilled for a single Stokes frequency. In practice, a broadband pulse is used as Stokes pulse and the geometry has to be adapted for each of the vibration investigated.

CARS can thus be seen as a four wave mixing process involving 4 different electronic states. Note that the states e and e' can be virtual (in CARS and resonant CARS) or electronic states (in double resonant CARS). The polarization is:

$$P_i^{(3)}(\omega_{as} = \omega_p + \omega_p - \omega_s) = \chi_{ijkl}^{(3)} E_j(\omega_p) \cdot E_k(\omega_p) \cdot E_l^*(\omega_s) \quad (1.93)$$

As in TG, we have the following relation between the non-vanishing terms of $\chi^{(3)}$:

$$\chi_{1111} = \chi_{1122} + \chi_{1212} + \chi_{1221} \quad (1.94)$$

but with

$$\begin{aligned} \chi_{1122} &= \chi_{1212} \\ &\neq \chi_{1221} \end{aligned} \quad (1.95)$$

Solving the wave equation (1.62) with this polarization allows the CARS intensity to be determined as⁴⁰:

$$I_{CARS} \propto |\chi_{ijkl}^{(3)}|^2 \cdot I_p \cdot I_p \cdot I_s^* \cdot L^2 \cdot \text{sinc}^2\left(\frac{\Delta k \cdot L}{2}\right) \quad (1.96)$$

where L is the interaction length and Δk the phase mismatch. Note that this equation is the same as eq.(1.63), as $\text{sinc}^2(\alpha) = \frac{\sin^2(\alpha)}{\alpha^2}$.

In a four-level system, such that shown in Figure 1.23, the nonlinear susceptibility is described as 48 permutations of a 8 terms summation expression. $\chi^{(3)}$ is thus the sum of 384 elements⁴¹.

Most of these elements are negligible and working near the Raman resonant frequency ($\omega_{as} = 2\omega_p - \omega_s$) allows 16 of the terms to be strongly enhanced. Assumption as been made that only the level g is initially populated (no thermal population in v).

The nonlinear susceptibility can thus be split in a Raman resonant and a nonresonant contribution.

$$\chi_{ijkl}^{(3)} = \chi_{ijkl}^{(3)}(R) + \chi_{ijkl}^{(3)}(NR) \quad (1.97)$$

with the Raman resonant part of the susceptibility written as⁴²:

$$\begin{aligned} \chi_{ijkl}^{(3)}(R) &= \frac{N}{\hbar^3} \cdot \frac{1}{\omega_{gv} - \omega_p + \omega_s - i\gamma_{gv}} \\ &\times \sum_{e'} \left[\frac{\mu_{ge'} \cdot \mu_{e'v}}{\omega_{e'v} + \omega_{as} + i\gamma_{e'v}} + \frac{\mu_{ge'} \cdot \mu_{e'v}}{\omega_{e'g} - \omega_{as} - i\gamma_{e'g}} \right] \\ &\times \sum_e \left[\frac{\mu_{ve} \cdot \mu_{eg}}{\omega_{eg} + \omega_s - i\gamma_{eg}} + \frac{\mu_{ve} \cdot \mu_{eg}}{\omega_{eg} - \omega_p - i\gamma_{eg}} \right] \end{aligned} \quad (1.98)$$

where γ_{ij} are the spectral bandwidth^V and μ_{ij} the transition dipoles.

Contrarily to the nonresonant susceptibility which is purely real, the resonant one is complex, and eq.(1.97) can thus be given by:

$$\chi_{ijkl}^{(3)} = \chi_r^{(3)}(R) + i\chi_i^{(3)}(R) + \chi_{ijkl}^{(3)}(NR) \quad (1.99)$$

The imaginary part being 90° out of phase compared to both real parts, it cannot interfere with them and the CARS intensity can be expressed with $\Delta k = 0$ as:

$$I_{CARS} \propto \left\{ \left| \chi_{ijkl,i}^{(3)}(R) \right|^2 + \left| \chi_{ijkl,r}^{(3)}(R) + \chi_{ijkl}^{(3)}(NR) \right|^2 \right\} \cdot I_p \cdot I_p \cdot I_s^* \quad (1.100)$$

^V One has to remember that the spectral bandwidth is related to the decay rate accounting for the damping phenomenon as shown by the expression: $\gamma = \frac{1}{2\pi \cdot T_1} + \frac{1}{\pi \cdot T_2}$, where T_1 is the population lifetime of the states, and T_2 the vibrational dephasing time.

The nonresonant contribution of the CARS signal interferes with the real part of the resonant contribution. The CARS signal is thus rather difficult to interpret. The nonresonant part being always present, the signal shape changes with the amplitude of the resonance and thus with the concentration of the species studied⁴².

By grouping together the nonresonant term of $\chi^{(3)}$ with the background susceptibility of the solvent in a term B , Lotem and Lynch⁴³ have rewritten $\chi^{(3)}$ as:

$$\chi^{(3)}(\omega_{as} = \omega_p + \omega_p - \omega_s) = B + \sum_r \frac{R_1}{\omega_r - (\omega_p - \omega_s) - i\Gamma_r} \quad (1.101)$$

with

$$R_1 = 2C \cdot \left[\sum_e \left(\frac{\mu_{ge} \mu_{er}}{\omega_e - \omega_{as} - i\Gamma_e} + \frac{\mu_{ge} \mu_{er}}{\omega_e + \omega_p - i\Gamma_e} \right) \right] \\ \times \left[\sum_e \left(\frac{\mu_{re} \mu_{eg}}{\omega_e - \omega_p - i\Gamma_e} + \frac{\mu_{re} \mu_{eg}}{\omega_e + \omega_s - i\Gamma_e} \right) \right] \quad (1.102)$$

where $\omega_{r,e}$ is a Raman and electronic allowed frequency of half width Γ_r , Γ_e respectively. The summation is made over all the Raman bands of the system.

One can rewrite eq.(1.101) using the Raman half width at half maximum Γ_r , the real and imaginary parts of R_l , R_r and I_r , and the detuning from a particular Raman frequency, $\delta_r = \omega_r - (\omega_p - \omega_s)$ as:

$$\chi^{(3)}(\omega_{as} = \omega_p - \omega_s + \omega_p) = B + \sum_r \frac{R_r + iI_r}{\delta_r - i\Gamma_r} \quad (1.103)$$

The line-shape is related to the CARS intensity and thus to the square of the absolute susceptibility.

$$\begin{aligned}
|\chi^{(3)}|^2 &= B^2 + B \cdot \sum_r \frac{R_r + iI_r}{\delta_r - i\Gamma_r} + B \cdot \sum_r \frac{R_r - iI_r}{\delta_r + i\Gamma_r} \\
&\quad + \sum_r \frac{R_r + iI_r}{\delta_r - i\Gamma_r} \cdot \sum_r \frac{R_r - iI_r}{\delta_r + i\Gamma_r}
\end{aligned} \tag{1.104}$$

For simplicity, let's consider an isolated Raman line. In such a case, the summation over r can be dropped and one obtains:

$$|\chi^{(3)}|^2 = B^2 + \frac{2BR\delta}{\delta^2 + \Gamma_r^2} + \frac{2BI\Gamma_r}{\delta^2 + \Gamma_r^2} + \frac{R^2 + I^2}{\delta^2 + \Gamma_r^2} \tag{1.105}$$

The first term is the background signal arising mainly from the solvent. It is only slowly varying in the frequency domain. The second one is a dispersion-shape cross term depending on the sign of R and increasing linearly with concentration. Its contribution is important for low concentration solutions as it interferes with the constant background. The third term possesses a Lorentzian shape centered at $\delta = 0$, and scales linearly with concentration. Its sign depends on that of I . Here again its contribution influences the signal mainly at low concentration. The last term is a positive Lorentzian centered at $\delta = 0$. It scales as the square of the solute concentration and becomes dominant at high concentrations of the solute molecule.

Depending on the magnitude and on the sign of R and I and also on the concentration of the solute, the CARS spectrum can change from a negative Lorentzian to a dispersive shape and finally to a positive Lorentzian for higher concentration.

Note that both Lorentzian contributions are centered at $\delta = 0$ and can thus not be separated. It is then possible to express eq.(1.105) with only three terms:

$$|\chi^{(3)}|^2 = W + \frac{A}{\delta^2 + \Gamma_r^2} + \frac{C\delta}{\delta^2 + \Gamma_r^2} \tag{1.106}$$

where

$$W = B^2 \qquad A = R^2 + I^2 - 2BI\Gamma_r \qquad C = 2BR \tag{1.107}$$

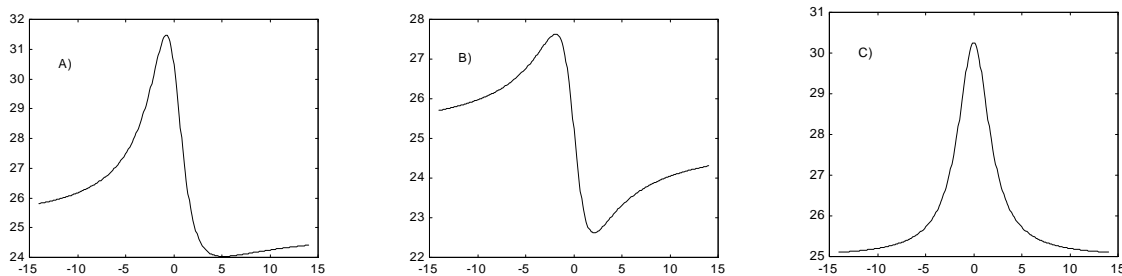


Figure 1.24: Simulation of a typical CARS spectrum near a resonant Raman vibration frequency (A) and its real (dispersive, B) and imaginary (Lorentzian, C) contributions.

Further enhancement of the CARS signal by a factor 10^4 can be achieved by double resonance. In such a case, frequencies are adjusted so that the e or e' state corresponds to an electronic excited-state.

$$\omega_p = \omega_{ge} = \omega_{S_0-S_n} \quad \text{and} \quad \omega_p - \omega_s = \omega_{gv} = \omega_{V_0-V_n} \quad (1.108)$$

In this case, electronic resonance is also achieved and specific elements of the susceptibility are enhanced. This second resonance allows dilute molecules down to 10^{-5} M to be studied⁴².

1.4.2. CARS In the Grating Formalism: Moving Gratings

It is also possible to understand the CARS spectroscopy within the holographic formalism. In this case, the grating is formed by the interaction of the pump and the Stokes pulses, and is read by the second pulse at ω_p .

The major difference with the TG technique is that the two pulses that creates the grating are not at the same frequency. As a consequence a moving grating is formed and the diffracted beam is shifted in frequency.

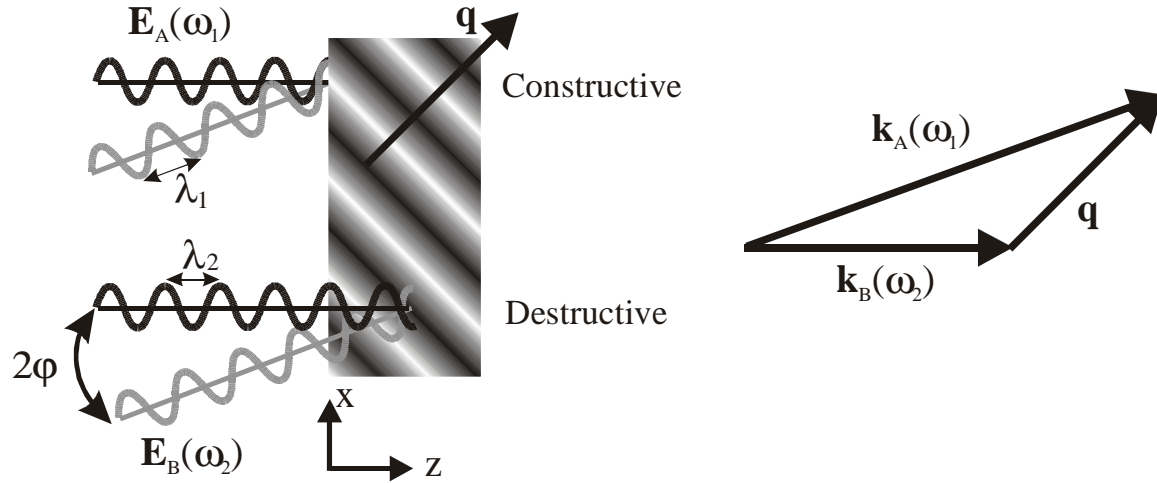


Figure 1.25: Moving grating formation with two pump beams at different frequencies. The grating vector is perpendicular to the grating direction. The diffracted beam is shifted in frequency by $\Omega = \omega_p - \omega_s$.

Moving Grating

When two beams arrive on a sample with an angle 2ϕ , they interfere. In the case of two identical frequencies, this results in a stationary grating. However, if the frequencies are different ($\omega_A \neq \omega_B$), the maxima of interference move with time in the x direction. This grating possess a so-called sweeping frequency Ω :

$$\Omega = \omega_A - \omega_B \quad (1.109)$$

and the intensity of the light on the sample is:

$$I = \frac{nc}{2\pi} \left[|A_A|^2 + |A_B|^2 + A_A \cdot A_B^* \cdot e^{i((\mathbf{k}_A - \mathbf{k}_B) \cdot \mathbf{r} - \Omega t)} + c.c. \right] \quad (1.110)$$

producing a similar photophysical grating. It is interesting to notice that if the photogenerated species lives longer than the sweeping time ($k_{pop} \ll \Omega$), no diffraction is present. For instance, a moving grating formed with two pulses

at 530 and 540 nm, have a sweep frequency of 10^{13} Hz. Thus, processes slower than 100 fs do not contribute to the diffracted signal, as they don't generate any modulation in the x direction. In such a case, only electronic and vibrational properties can be investigated.

This technique can also be used to study short living species with long pulses. The temporal resolution is no longer limited by the pulse duration, but by the frequency shift. Using a broadband ns pulse, one can investigate ps excited lifetime, by analyzing the diffracted spectrum. A broad diffracted spectrum corresponds to a fast deactivation and vice versa. A high-resolution spectrometer is needed as a 10 ps lifetime corresponds to a 5 cm^{-1} bandwidth around 500 nm.

Coherent Vibrations

As the moving grating has a sweeping frequency $\Omega = \omega_p - \omega_s$, the vibration of the molecule is driven by a force²⁶:

$$\tilde{F}(z, t) = \left(\frac{\partial \alpha}{\partial q} \right)_0 \tilde{E}_p \cdot \tilde{E}_s \quad (1.111)$$

where $\tilde{E}_{p,s}$ are the oscillating electric fields of the probe and Stokes beams, q the vibrational coordinate and α the optical polarizability of the molecule. The vibration being driven by the electric field is coherent and thus creates a well defined modulation of the refractive index. The probe beam that strikes this moving grating in the phase matching geometry is diffracted and frequency shifted by $\pm \Omega$. The contribution at $\omega_p + \Omega$ is the CARS signal.

1.5. Transient Dichroism (TD)

The transient dichroism is based on the same principle as the transient birefringence, and allows the investigation of orientational anisotropy of absorbing molecules.

As only 2 beams are needed, TD is experimentally easier to achieve than polarization grating. Nevertheless, further treatment of the signal is needed to extract the anisotropy decay rate constant from heterodyne TD.

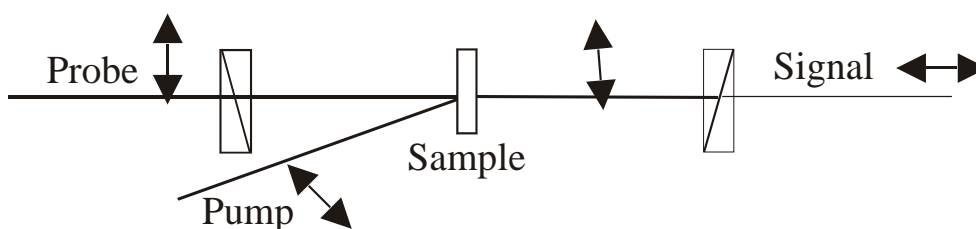


Figure 1.26: Scheme of a TD experiment. Dichroism, induced by the pump pulse in the sample, rotates the polarization of the probe pulse, that is thus partially transmitted through the crossed analyzer.

A linearly polarized pump pulse induces a linear dichroism in the sample.

In other words, only molecules having their transition dipole oriented parallel to the electric field are excited^{VI}.

The probe pulse is also linearly polarized, but at 45° relatively to the pump pulse. It can be decomposed in two components, one parallel and one perpendicular to the pump orientation.

^{VI} Note that the excitation probability is proportional to $\cos^2\theta$ when θ is the angle between the transition dipole and the pump pulse polarization. Nevertheless, for simplicity one speaks of parallel and perpendicular orientations.

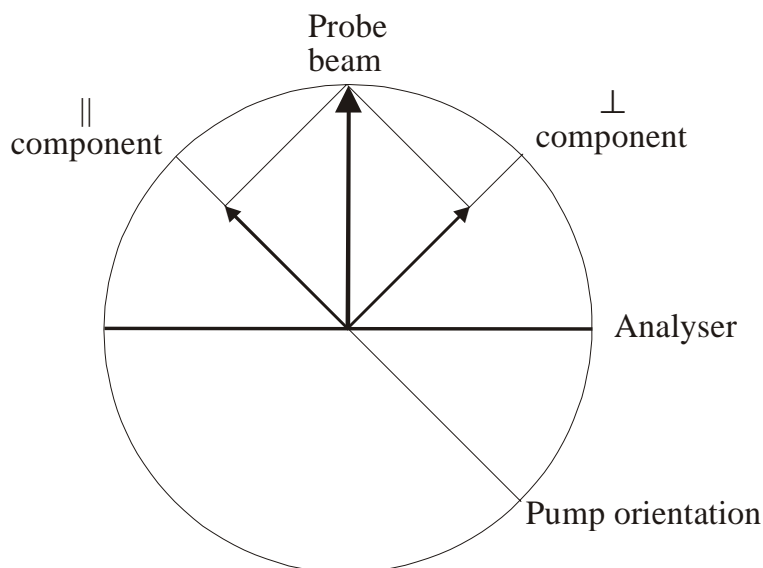


Figure 1.27: Transient dichroism geometry. The probe beam can be decomposed in two components, one being parallel and the other perpendicular to the pump polarization. Without any anisotropy in the sample, the probe beam is completely blocked by the crossed analyzer.

If anisotropy is present, the two components are not transmitted identically. In the case where the probe wavelength is the same as the pump one, the parallel component is less absorbed than the perpendicular component, due to the bleaching of the ground-state. This is known as transient dichroism. The reconstruction of the probe pulse leads to a rotation of its polarization.

A similar experiment, known as nuclear OKE, can be performed with non-absorbing samples. In this case the population of the ground-state is not anisotropic, but the orientation of molecules is driven by the electric field. The change in refractive index along the direction of the electric field induces a transient birefringence. The dephasing between the parallel and perpendicular components of the probe beam leads to the rotation of the overall polarization.

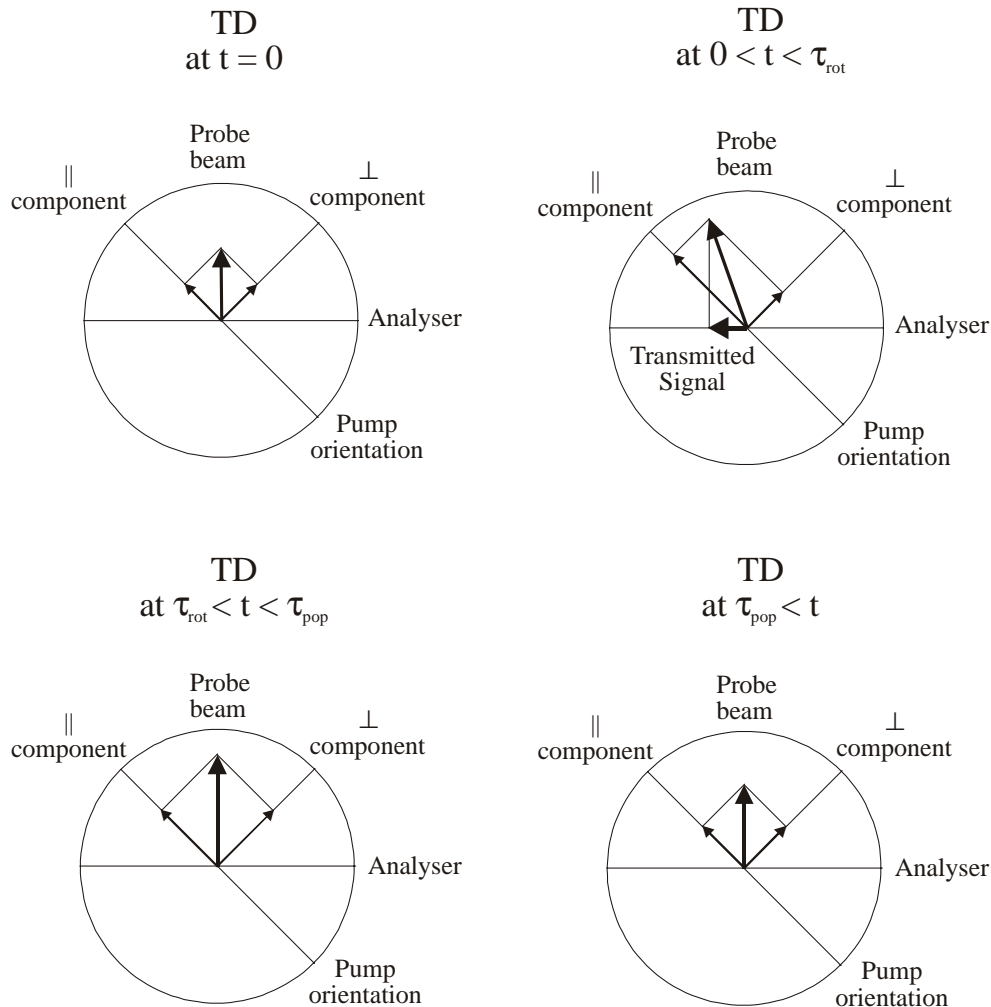


Figure 1.28: Time evolution of the transmitted pulse in a TD experiment. At time 0, both components are equally absorbed. When anisotropy is present, the component parallel to the pump polarization is less absorbed, due to the bleaching of ground-state absorption. This induces a rotation of the polarization of the probe pulse and thus a part of the beam can go through the analyzer. After rotational motions have washed out the anisotropy, both components have again the same intensity and no signal is detected any more. Finally, the ground-state is repopulated and the sample returns to its initial absorbance.

To detect this rotation, a crossed Glan Taylor polarizer is placed in front of the detector and adjusted so that no light goes through without pump beam. When the anisotropy is formed, a part of the probe beam is transmitted and is detected. The anisotropy vanishes due to reorientation of the transition dipole,

and the probe polarization returns to its initial orientation. The signal comes back to zero and further deactivation of the excited species is not detected.

1.5.1. TD in the NLO Formalism

It may be surprising to express the TD, that only uses two beams, as a FWM technique, but in fact four electric field interactions are occurring, even in this simple experiment. Two of them come from the pump beam, one from the probe and the last is the signal.

For an optical excitation, the light intensity must be different from zero. As the intensity is defined as the square of the electric field, it is already clear that excitation of the sample need two electric fields. In TD, as in transient absorption for instance, these two electric fields come from a single pump beam.

As TD is a FWM technique, it can be described in the NLO formalism. To avoid too many repetitions of this formalism in this thesis, only the detected intensity is shown, but a complete description of this phenomenon can be found in the literature⁴⁴.

$$\mathbf{E}_{TD} = \frac{6\pi i}{n} \cdot \frac{\omega \cdot l}{c} \left\{ \chi_{1111}^{(3)} - \chi_{1122}^{(3)} \right\} \cdot \mathbf{E}_{pu}^2 \cdot \mathbf{E}_{pr} \frac{(\hat{x} - \hat{y})}{\sqrt{2}} \quad (1.112)$$

where n is the refractive index, l the sample length, ω the pump and probe frequency, \hat{x} and \hat{y} the unit vectors in x and y direction.

Note that, in the case of TD (change in absorbance), only the real part of \mathbf{E}_{TD} has to be considered, and that the imaginary part corresponds to transient birefringence (change in refractive index).

1.5.2. Homodyne and Heterodyne

In the previous description, it has been postulated that in absence of anisotropy, no light goes through the crossed analyzer. This corresponds to an *homodyne TD*. Nevertheless, it is often very difficult to adjust the Glan Taylor polarizer so that it completely switches off the probe beam. Furthermore, optical elements, such as lenses, might be slightly birefringent. A leak is thus often present and interacts with the signal.

Homodyne TD

This case is easier to interpret, as the signal is directly proportional to the square of the changes of absorbance ΔA and refractive index (due to population) Δn_p , and thus to the square of the concentration difference (ΔC).

$$I_{TD} \propto \Delta A^2 + \Delta n_p^2 \propto \Delta C^2 \quad (1.113)$$

Nevertheless, it is almost impossible to avoid leaks through the analyser. Furthermore, their presence can change the previous relation as described in the following section. It is therefore better to induce artificially a leak than trying to work with an unknown one.

Heterodyne TD

This technique requires more experimental work, but has the advantage of being completely controlled. Furthermore, a linear relation between I_{TD} and ΔC is achieved.

To induce a leak through the analyzer, different methods are possible:

- 1) One can slightly rotate ($< 1^\circ$) the detection polarizer. In this case, part of the light is detected, even in absence of anisotropy in the sample.
- 2) A similar result can be obtained by adding a $\lambda/4$ plate. In this case the polarization of the probe beam is no longer linear, but slightly elliptic. The part parallel to the analyzer is always detected.

As a consequence, the artificial leak interferes with the transmitted signal due to anisotropy, and the detected intensity is:

$$\begin{aligned}
 I_{TD} &\propto \mathbf{E} \cdot \mathbf{E}^* \\
 &\propto (\mathbf{E}_{LO} + \mathbf{E}_{HTD}) \cdot (\mathbf{E}_{LO}^* + \mathbf{E}_{HTD}^*) \\
 &\propto \mathbf{E}_{LO}^2 + \mathbf{E}_{HTD}^2 + 2 \cdot \text{Re} \left\{ \mathbf{E}_{LO}^* + \mathbf{E}_{HTD} \right\}
 \end{aligned} \tag{1.114}$$

where \mathbf{E}_{LO} is the electric field of the local oscillator (leak), and \mathbf{E}_{HTD} that of the Homodyne Transient Dichroism (HTD) signal. \mathbf{E}_{LO} being constant, it only appears as a background signal and do not vary with time.

In the case where $\mathbf{E}_{LO} \gg \mathbf{E}_{HTD}$, the crossed term is dominant, and the detected variation of intensity is:

$$\begin{aligned}
 I_{TD} &\propto 2 \cdot \text{Re} \left\{ \mathbf{E}_{LO}^* + \mathbf{E}_{HTD} \right\} \\
 &\propto \mathbf{E}_{HTD}
 \end{aligned} \tag{1.115}$$

In a more general case, the contribution from \mathbf{E}_{HTD}^2 can be eliminated by performing two different measurements. By changing the experimental conditions, it is possible to force the interaction between the leak and the homodyne signal to be constructive or destructive.

For instance, if the leak comes from a misalignment of the analyzer, changing the polarization of the pump beam of 90° will also change the phase between

the leak and the HTD signal. The interaction is once constructive, and once destructive. This behavior can be illustrated as follows:

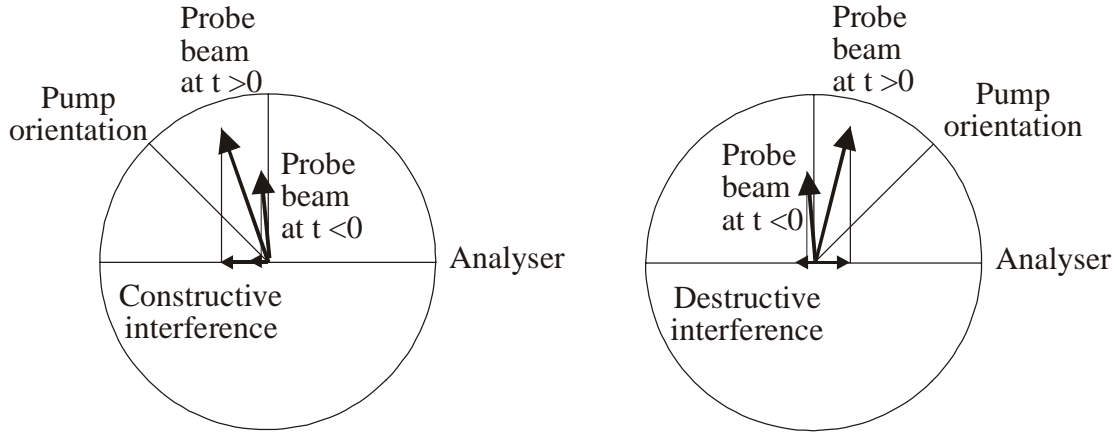


Figure 1.29: Constructive and destructive interference in heterodyne TD. The leak is constant and the pump polarization is turned by 90° to induce either constructive or destructive interference between the leak and the homodyne signal.

By subtracting the two signals obtained, one can eliminate the \mathbf{E}_{HTD}^2 contribution:

$$\begin{aligned}
 I_{Constr} - I_{Destr} &\propto \mathbf{E}_{LO}^2 + \mathbf{E}_{HTD}^2 + 2 \cdot \text{Re} \left\{ \mathbf{E}_{LO}^* + \mathbf{E}_{HTD} \right\} \\
 &\quad - \left[\mathbf{E}_{LO}^2 + \mathbf{E}_{HTD}^2 - 2 \cdot \text{Re} \left\{ \mathbf{E}_{LO}^* + \mathbf{E}_{HTD} \right\} \right] \\
 &\propto 4 \cdot \text{Re} \left\{ \mathbf{E}_{LO}^* + \mathbf{E}_{HTD} \right\}
 \end{aligned} \tag{1.116}$$

A similar result can be obtained by keeping the pump polarization fixed and changing the direction of the analyzer. In the last case however, a rotation of only 2° is necessary and experimental imprecision is important.

The heterodyne TD signal has a linear dependence with concentration changes. A time resolved experiment gives thus directly the anisotropy rate constant.

In a homodyne TD, this time dependence should be two time faster, but due to frequent uncontrolled leaks, complicated relations are often obtained⁴⁵. This technique should then not be used, to avoid misleading results to be observed.

2. Experiment with ps Pulses

2.1. Introduction

Femtochemistry is of course the ultimate limit to chemistry, but many phenomena can be investigated in the ps time scale. For instance Electron Transfer (ET) reactions^{19,33}, energy transfer^{32,46}, rotational dynamics of dyes^{31,47}, and many others can often be studied with ps resolution.

Furthermore, working with ps pulses is a very good way to acquire the skill needed for fs experiments.

It was then logical to begin this thesis with two different types of ps experiments: determination of the lifetime of excited-state radical ions and time resolved CARS experiment.

2.2. Investigation of the Excited-State Dynamics of Radical Ions in the Condensed Phase Using the Picosecond Transient Grating Technique

2.2.1. Introduction

According to the Marcus theory⁴⁸, the rate constant of intermolecular ET depends on the energy gap between the initial and final states of the reaction. The relation between the ET rate constant and the free energy (ΔG_{ET}) being Gaussian, highly exergonic reactions should be in the so-called inverted region, and thus be slow. However, as shown in Figure 2.1, this inverted behavior has not been shown experimentally for these reactions.

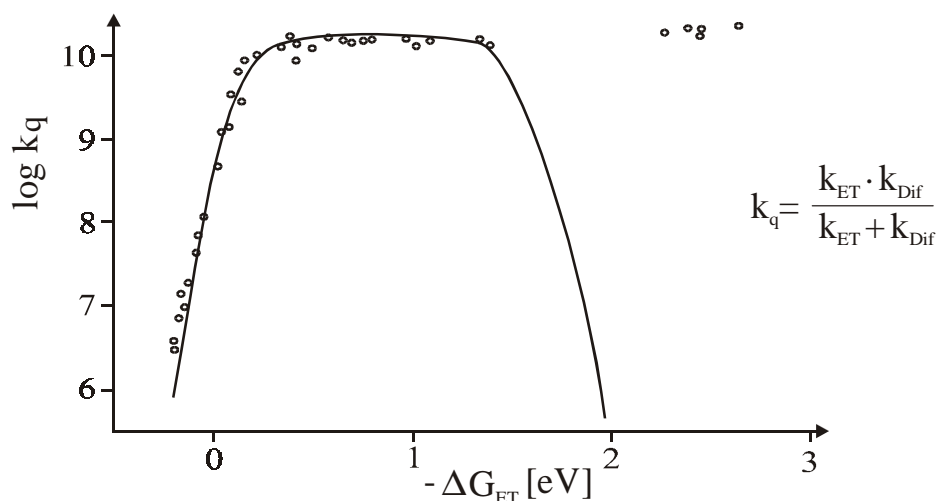


Figure 2.1: Experimental ET quenching rate constants as a function of the free energy and fit using Marcus theory for the ET rate constant⁴⁹. Highly exergonic ET reactions are faster than predicted for the inverted region.

To account for this discrepancy, two explanations have been advanced:

- 1) In highly exergonic reactions, the ET can take place over a long distance⁵⁰. Inserting this parameter in the Marcus equation, the observed data can be fitted⁴⁹. This hypothesis has one major drawback, as the intermolecular distance needed to correct the Marcus curve becomes huge. The ET should take place over distances as long as 10 ångströms (Å) for free energy differences of 2 eV⁵⁰.
- 2) Ions are formed in an electronic excited-state. In this hypothesis, a two steps mechanism leads to the formation of the ions in their ground-state. The free energy that has to be considered in the Marcus theory is no longer ΔG_{CS}^0 , but ΔG_{CS}^{0*} (see Figure 2.2), that can be significantly smaller⁵¹. The problem of this assumption is that the excited-state of the radical ions was never observed. An explanation for this lack of experimental evidence could be due to a very short lifetime of such species.

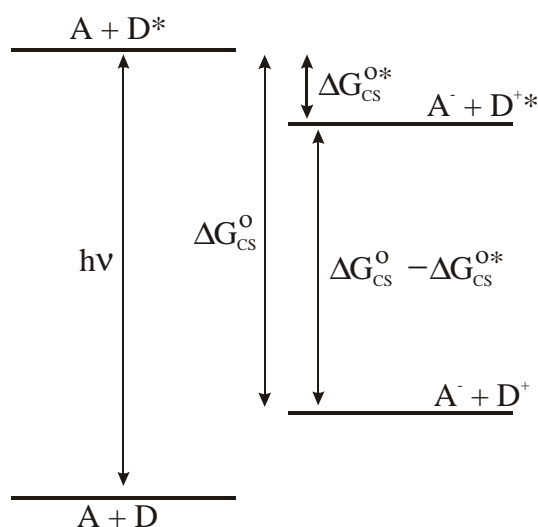


Figure 2.2: Energy level diagram for photoinduced ET reaction⁵². The formation of the ions in the excited-state may explain the absence of the inverted behavior for highly exergonic reactions.

Few years ago, Majima and co-workers⁵³ used an indirect technique based on the rate constant of electron transfer quenching, to determine the lifetime of excited radical ions. They found a lifetime as long as 4 ns for anthraquinone radical anion (AQ^{•-}).

This value is surprising, because no fluorescence is observed with this ion in solution, suggesting a much shorter lifetime. Therefore, we have performed direct measurements to determine the excited-state dynamics of radical ions. The higher sensitivity of TG over TA, shown previously, leads us to use ps time resolved TG to study perylene radical cation (PE^{•+}) and anion (PE^{•-}). For AQ^{•-} however, a new technique, based on a calorimetric detection, has been developed. Finally an indirect measurement of 9-10 dicyanoanthracene (DCA^{•-}) radical anion is also presented.

2.2.2. Picosecond Time Resolved TG

This technique has already been extensively described in chapter 1. Two ps pump pulses of same wavelength cross in the sample and create a light intensity grating. This results in a photophysical grating that lasts as long as the associated process (electrostriction, anisotropy, population, acoustics) has not vanished. In this specific case, we are interested in ground-state population recovery and thus the χ_{1111} element has to be considered.

Experimentally, the following setup has been used:

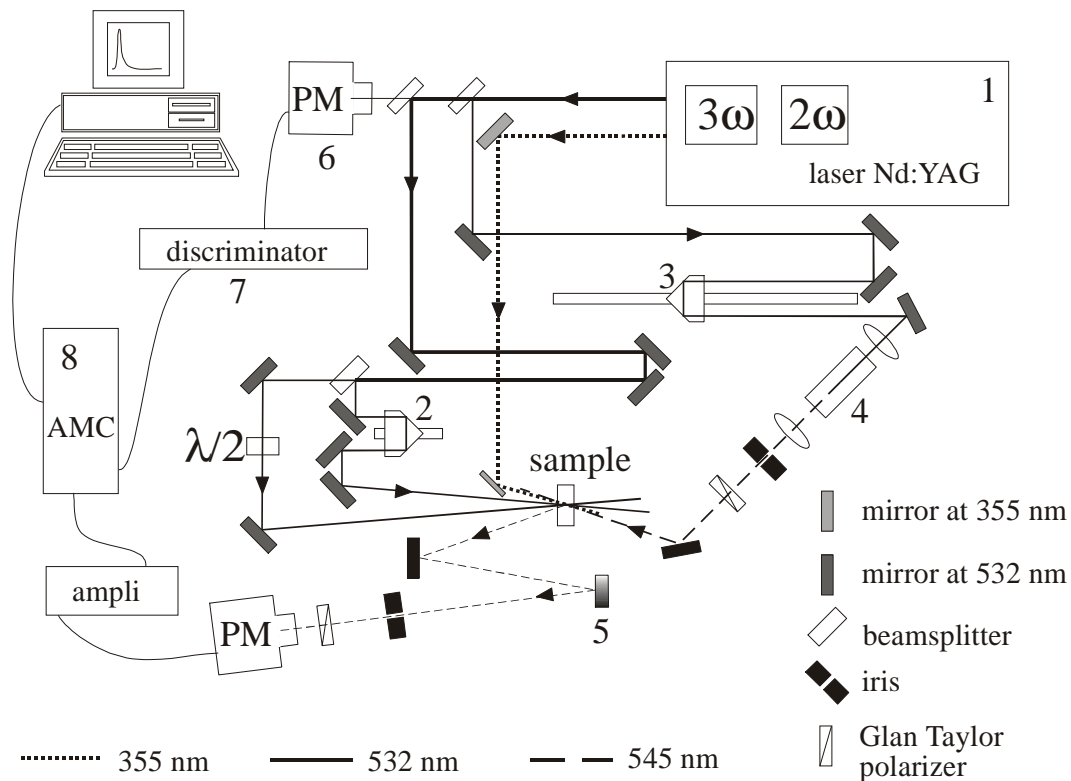
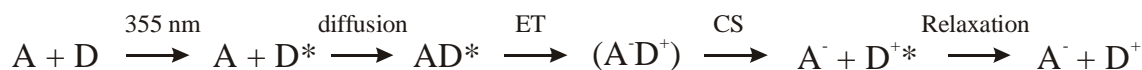


Figure 2.3: Experimental setup for a ps time resolved TG experiment with Raman shifted probe beam. For explanation, see text.

The 532 nm output of the laser is split in two parts of 90% and 10%. The major part is split again in two equal portions to produce the pump pulses, which cross in the sample to form the grating. The time coincidence is optimized by a translation stage in the path of one of the pump pulse (2 in Figure 2.3).

The 10% portion is used as probe pulse. It is time delayed by the computer controlled delay line (3 in Figure 2.3) before striking the sample at Bragg angle. For changing the probe wavelength, the probe pulse is focused in a CCl_4 cell (4 in Figure 2.3) located after the translation stage. The separation of the Raman wavelength can be achieved by a filter or a grating located either before or after the sample (5 in Figure 2.3).

To form the ion in situ, an additional 355 nm pulse is needed.



In order to allow a large ion yield, two conditions are necessary:

- 1) A high concentration of quencher has to be used (>0.1 M) in order to allow the diffusional quenching to be fast.
- 2) The actinic pulse at 355 nm has to arrive on the sample at least 7 ns before the grating formation to allow the quenching and ET to be achieved. The optical path-length of the actinic pulse has to be 2 m shorter than that of the 532 nm pulses.

Diffusional ET can then take place, and ions yields as high as 70% can be obtained, depending on the acceptor-donor system. Detection is achieved by a vacuum photodiode. Its signal is sent to the acquisition board (Canberra Accuspec NaI multi-channel analyzer, 8 in Figure 2.3) and stored by the computer only if the discriminator triggers it.

2.2.3. Experimental Conditions

Laser Pulses

To produce ps-pulses, a passive/active mode-locked and Q-switched Nd:YAG laser from Continuum™ (PY-61-10) was used (1 in Figure 2.3). It produces 25 ps pulses of 30 mJ at 1064 nm that can be doubled and tripled to produce 532 and 355 nm pulses.

Other wavelengths are also available through Raman-shift in organic solvents. For instance 545 nm is produced by focusing a mJ pulse at 532 nm in a 5 cm CCl₄ cell (4 in Figure 2.3).

It is sometimes important to use a probe wavelength different from the pump beams to avoid hybrid gratings (formed with one pump pulse and the probe pulse) to be formed, which lead to the formation of a coherence spike in the time profile.

Optical Delays

In order to insure the time coincidence of the two pump pulses, one of them have to go along a variable optical delay. In practice, this consists of a corner cube prism mounted on a translation stage (2 in Figure 2.3).

Furthermore, to allow time resolved experiment, the probe beam has to be delayed by a motorized optical delay line (3 in Figure 2.3) that can be precisely moved by computer.

For ps measurement, the length of the delay line used is of 0.8 m long to achieve a total measurement of 5.3 ns, and allow steps as small as 0.3 mm (corresponding to 2 ps) to obtain a good time resolution. This very precise translation stage has been built at the Engineer School of Fribourg.

Discriminator

As the laser stability is not perfect, we had to develop a discriminator to limit the fluctuation of the diffracted signal. A portion of the pump beam is sent to a photomultiplier tube (PM, 6 in Figure 2.3) and its signal is transmitted to the electronic discriminator (7 in Figure 2.3). If the pulse intensity differs

significantly from the average intensity (defined by the user), the diffracted signal is ignored. In other cases, a triggering pulse is sent to the acquisition computer and the signal is recorded.

2.2.4. TG with Calorimetric Detection

To investigate weakly absorbing species such as AQ^{\bullet} , high pulse intensities are needed. Unfortunately, increasing the pulse energy also increases the nonresonant contribution of $\chi^{(3)}$. In particular the electronic contribution from the solvent cannot be separated by polarization selective TG. As the ground-state recovery time of AQ^{\bullet} is very short, temporal separation is also not possible. To solve this problem, we developed a new pulse sequence that can be seen as TG with calorimetric detection.

Instead of varying the time delay between the pump and probe pulses, we kept it fixed at 7 ns. The diffracted signal is thus no longer due to nonresonant contributions (that last a few ps) or population decay (less than 100 ps in this case), but only to the density contribution. Adjusting the incident angle at 2° allows the formation of strong density grating after 7 ns (half the acoustic period). As thermal grating is due to non-radiative deactivation of $AQ^{\bullet*}$, its contribution to the diffracted signal is proportional to the square of the excited-state population. A calorimetric detection of the excited population is thus obtained.

The time resolution is achieved by a time varying bleaching pulse that precedes the grating formation. If the bleaching pulse arrives far before the pump pulses, the excited molecules have come back to their ground-state, and an intense thermal grating is formed. However, when it arrives just before,

almost no ground-state is left as the pump pulses strikes the sample, and only a weak thermal grating is formed.

This technique has two major advantages:

- 1) Nonresonant contributions are not detected as the probing is done 7 ns after the grating formation. The signal is then only due to non-radiative population relaxation.
- 2) The thermal grating is more intense than the corresponding population grating signal, due to its thermal and acoustic contributions. This detection is a kind of amplification of population signal.

2.2.5. Paper

ARTICLES

Investigation of the Excited-State Dynamics of Radical Ions in the Condensed Phase Using the Picosecond Transient Grating Technique

Jean-Claude Gomy and Eric Vauthey*

Institute of Physical Chemistry of the University of Fribourg, Pérolles, CH-1700 Fribourg, Switzerland

Received: June 25, 1997; In Final Form: August 26, 1997[⊗]

A study of the dynamics of ground-state recovery of the perylene radical cation ($\text{Pe}^{\bullet+}$), of perylene radical anion ($\text{Pe}^{\bullet-}$), and of anthraquinone radical anion ($\text{AQ}^{\bullet-}$) is reported. In boric acid glass, the excited-state lifetime of $\text{Pe}^{\bullet+}$ is 35 ± 3 ps, while in concentrated sulfuric acid, it is smaller than 15 ps, the time resolution of the experimental setup. The excited-state lifetime of $\text{Pe}^{\bullet+}$, $\text{Pe}^{\bullet-}$, and $\text{AQ}^{\bullet-}$ generated by photoinduced intermolecular electron-transfer reaction in MeCN is shorter than 15 ps. In the case of $\text{Pe}^{\bullet-}$, the uncomplete ground-state recovery is ascribed to the occurrence of electron photoejection. The free ion yield in the intermolecular electron-transfer reaction between 9,10-dicyanoanthracene (DCA) and two electron acceptors was measured in a two-pulse experiment, where the second pulse excited the ensuing $\text{DCA}^{\bullet-}$. This excitation has no influence on the magnitude of the free ion yield, indicating a short excited-state lifetime of $\text{DCA}^{\bullet-}$ relative to the time scale of back electron transfer and ionic dissociation. A red emission, ascribed to the fluorescence of protonated Pe, was detected in boric acid glass and sulfuric acid. No fluorescence that could be clearly ascribed to $\text{Pe}^{\bullet+}$ could be observed.

Introduction

Open-shell organic radical ions play a crucial role in a large variety of chemical processes. Although the photochemistry of these species has been intensively studied, especially in solid matrixes at low temperature,¹ little is known about the dynamics of their excited states. The absence of the inverted region for highly exergonic bimolecular electron transfer (ET) quenching reactions in solution has sometimes been explained by the production of electronically excited ions.¹⁻³ However, the formation of such excited ions could not be confirmed experimentally with either absorption or fluorescence techniques.^{2,3} Fluorescence from radical cations has been observed in the gas phase^{4,5} and in matrixes at low temperature.⁶ In the condensed phase at room temperature, there have been only very few

reports of fluorescence from radical ions.⁷⁻⁹ Recently, Breslin and Fox¹⁰ have shown that, among those reported emissions in solution, several were not genuine. For example, the fluorescence ascribed to anthraquinone radical anion ($\text{AQ}^{\bullet-}$) was actually due to bianthrone dianion and that assigned to 9,10-dicyanoanthracene anion ($\text{DCA}^{\bullet-}$) originated from 10-cyanoanthrolate. Moreover, no transient with nanosecond lifetime could be observed upon excitation of $\text{AQ}^{\bullet-}$ at wavelengths above 500 nm. The absence of luminescence and of transient with nanosecond lifetime is generally explained by a fast nonradiative transition to the ground state favored by the small energy gap between the D_1 - D_0 states.

Very recently, Majima and co-workers¹¹ reported excited-state lifetimes of $\text{AQ}^{\bullet-}$, $\text{DCA}^{\bullet-}$, and phenazine radical ions of the order of 4 ns. These lifetimes were not measured directly but were estimated from the rate constant of ET quenching of the excited ions by an electron acceptor using a combination

* Corresponding author. E-mail: Eric.Vauthey@unifr.ch.

⊗ Abstract published in *Advance ACS Abstracts*, October 15, 1997.

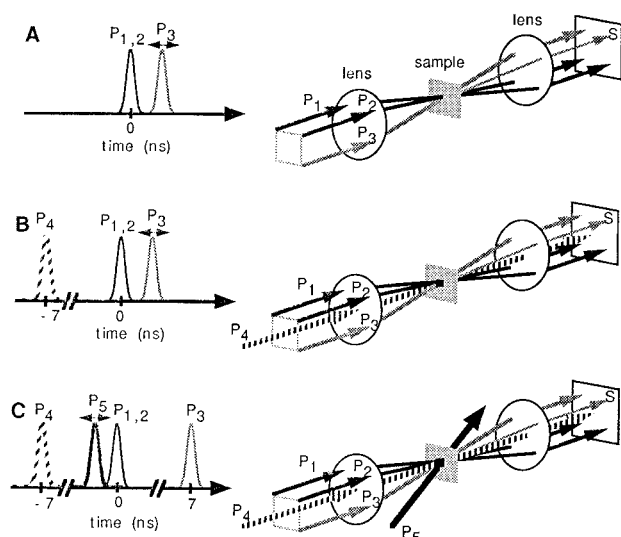


Figure 1. Pulse sequences and geometries (A) for the transient grating experiments with Pe^{*+} in boric acid glass and H_2SO_4 , (B) for the transient grating experiments with ions generated by photoinduced ET, and (C) for probing the density grating formed at different time delays after a bleaching pulse ($P_{1,2}$, transient grating pump pulses; P_3 , probe pulse; P_4 , UV pulse; P_5 , bleaching pulse; S, signal pulse).

of pulse radiolysis and nanosecond flash photolysis. In this case as well, no transient was observed upon excitation of the radical ions.

In this paper, we report on the investigation of the dynamics of ground-state recovery of the radical cation of perylene (Pe^{*+}) in a boric acid glass, in sulfuric acid, and in acetonitrile (MeCN), of perylene radical anion (Pe^{*-}), and of AQ^{*-} in MeCN, using the picosecond transient grating technique. This method was preferred to the more conventional transient absorption spectroscopy because of its superior sensitivity. A simple experiment allowing an indirect estimate of the excited-state lifetime of radical ions is also described.

Experimental Section

Transient Grating. The transient grating setup has been described in detail elsewhere.^{12,13} Briefly, the second harmonic output at 532 nm of a passive/active mode-locked and Q-switched Nd:YAG laser (Continuum PY-61-10) was split into three parts. Two parts of equal intensity (P_1 and P_2) were time coincident and were crossed on the sample with an angle of 2° to generate the grating. The third part (P_3) was sent along a time delay line before striking the grating in a folded BOXCARS geometry (see Figure 1a). For probing at 545 nm, this time-delayed pulse was Raman-shifted in CCl_4 . The energy of the pump pulses was about $20 \mu\text{J}$, and that of the probe pulse was at least 10 times smaller. The beam radii on the sample were around 1 mm, and the pulse duration was about 25 ps. The polarization of each pulse could be controlled with a combination of Glan-Taylor polarizers and half-waveplates.

For experiments in MeCN, the ET reaction was initiated with a 25 ps pulse at 355 nm with an energy between 0.5 and 1 mJ. This UV pulse (P_4) arrived on the sample 7 ns before the two 532 nm transient grating pulses. Its radius on the sample was around 2 mm.

Free Ion Yields. The free ion yields were determined using photoconductivity. The photocurrent cell has been described in detail elsewhere.¹⁴ Excitation was carried out with a Q-switched Nd:YAG laser (JK Laser Model 2000) generating 10 mJ pulses at 355 nm with 20 ns duration.

Fluorescence. Fluorescence spectra were measured using a CCD camera (Oriol Instaspec IV) connected to a $1/4$ m imaging

spectrograph (Oriol Multispec). All the emission spectra were corrected for the spectral sensitivity of the CCD camera.

Samples. Perylene (Pe) and anthraquinone (AQ) were recrystallized from benzene. Tetracyanoethylene (TCNE) was recrystallized from chlorobenzene and sublimed. Fluorene (FLU) was recrystallized from ethanol. Anisol (ANI) and *N,N*-dimethylaniline (DMA) were vacuum-distilled. 9,10-Dicyanoanthracene (DCA, Aldrich) and 1,4-diazabicyclo[2.2.2]octane (DABCO) were sublimed. Crystal violet (CV), boric acid (puriss.), sulfuric acid (95–97%, Merck, pro analysi), acetonitrile (MeCN, UV grade), and methanol (MeOH, UV grade) were used without further purification. Unless specified, all products were from Fluka.

The Pe-doped boric acid glass was prepared by melting at $210\text{--}220^\circ\text{C}$ a mixture of boric acid and Pe between two quartz plates. The resulting metaboric acid glass was 0.1 mm thick and was of good optical quality. The Pe concentration was measured spectroscopically to be around 5×10^{-4} M. The Pe^{*+} was prepared by irradiating the doped glass with nanosecond laser pulses at 355 nm.¹⁵ The absorption spectrum of the ensuing pink glass exhibited the bands of Pe as well as those of Pe^{*+} , i.e., a strong band at 543 nm and weaker bands between 580 and 765 nm.¹⁶ The absorbance of the sample at 532 nm was 0.09.

In sulfuric acid, Pe^{*+} was readily prepared by adding Pe to the acid. Solutions with various Pe^{*+} concentration were used, and the optical path length was adjusted to achieve an absorbance at 532 nm between 0.1 and 0.2.

In MeCN, the concentration of the parent neutral compound was adjusted to obtain an absorbance at 355 nm between 0.1 and 0.2 on 1 mm, the cell thickness. With Pe and AQ, the quencher concentration was 0.2 and 0.1 M, respectively.

Data Analysis. The transient grating technique is a four-wave mixing method, and therefore the signal intensity depends on the third-order nonlinear optical susceptibility tensor $\chi^{(3)}$ of the sample.¹⁷ The intensity of the diffracted signal, $I_d(t)$, can be expressed as^{18,19}

$$I_d(t) = \int_{-\infty}^{+\infty} I_{P_3}(t - t'') \times \sum_m \{ C_m \chi_{ijkl}^{(3)}(m) \int_{-\infty}^t \exp[-(t'' - t')/\tau_m] I_{P_{1,2}}(t') dt' \}^2 dt'' \quad (1)$$

where I_{P_3} and $I_{P_{1,2}}$ are the intensities of the probe and pump pulses, respectively. $\chi_{ijkl}^{(3)}(m)$ is a tensor element of the nonlinear optical susceptibility due to the process m with a decay time τ_m and a weighting factor C_m . These processes are the electronic ($m = e$) and the nuclear ($m = n$) optical Kerr effects (OKE) from the matrix or the solvent, the formation of a population grating ($m = p$), and the generation of a density grating due to heat releases ($m = d$).¹⁹ These four processes lead to four $\chi^{(3)}(m)$ tensors with different symmetry properties which can in principle be distinguished by using various combinations of polarization for the three pulses and by selecting a given polarization component of the signal.^{18,19} The second integral in eq 1 represents the convolution of the nonlinear response with the pump pulses, while the first integral is the convolution with the probe pulse.

The time profiles of the diffracted intensity were analyzed by iterative reconvolution using eq 1. The temporal width of the pump and probe pulses was determined by performing measurements with a solution of CV in MeOH. The ground-state recovery of CV in MeOH is known to take place in less than 3 ps, i.e., much faster than the response time of the experiment.²⁰ With our experimental setup and with a careful

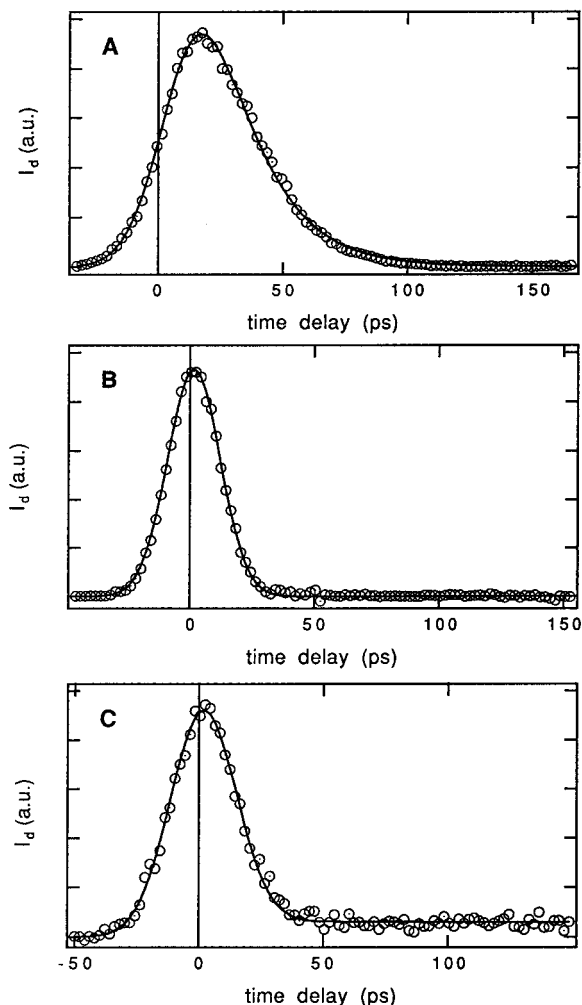


Figure 2. Time profiles of the diffracted intensity measured at 532 nm and best fits of eq 1 with (A) Pe^{*+} in boric acid glass, (B) Pe^{*+} in H_2SO_4 , and (C) Pe^{*+} generated by photoinduced ET with DMA.

analysis of the time profile, the smallest resolvable decay time was of the order of 15 ps.

Results and Discussion

Pe^{*+} in Boric Acid Glass. Figure 2a shows the time dependence of the diffracted intensity obtained by pumping and probing Pe^{*+} in boric acid glass at 532 nm using the configuration described in Figure 1a. This time profile could be satisfactorily fitted using eq 1 assuming the contribution of a single process to the signal with a decay time of 35 ± 3 ps. This process corresponds to the ground-state recovery of Pe^{*+} after excitation from D_0 to D_5 .²¹ To check for a possible contribution of the Kerr effect to this signal, the experiment was repeated on a region of the sample that had not been previously irradiated with UV light, i.e., that had no absorbance at 532 nm. With the pump-probe pulse intensity used previously, no signal could be detected. A signal could only be observed by increasing substantially the laser pulse intensity. Finally, the contribution of a density grating due to the heat released upon nonradiative transition to the ground state could only be observed at much larger time delays ($t > 3$ ns). Indeed, with a crossing angle of 2° , the acoustic period is of the order of 15 ns. Even at these time delays, the diffracted intensity due to the density grating was very small compared to that shown in Figure 2a. This can be understood by considering that the thermal expansion coefficient of boric acid glass must be similar to that of other glasses, i.e., about 100 times smaller

than that of organic solvents.²² For measuring the time profile shown in Figure 2a, the three pulses were polarized in the same direction, and therefore this profile reflects the dynamics of $\chi_{1111}^{(3)}(p)$. Other polarization combinations were used to probe $\chi_{1122}^{(3)}$ and $\chi_{1212}^{(3)}$ and resulted in a weaker signal but with the same temporal shape. Finally, to eliminate the possible contribution of gratings formed between one of the pump pulse and the probe pulse at time zero, the ground-state recovery of Pe^{*+} was also probed at 545 nm. The decay of the time profile was the same, within the experimental error, as that measured at 532 nm.

Pe^{*+} in Sulfuric Acid. The absorption spectrum in sulfuric acid depends on the concentration of Pe. At low concentration ($[\text{Pe}] = 10^{-5}$ M), the absorption spectrum was similar to that observed in boric acid glass, with the intense band located at 538 nm.²³ At higher concentration ($[\text{Pe}] = 10^{-3}$ M), a band with a maximum at 505 nm could also be observed. This band had previously been assigned to the dimer $(\text{Pe}^{*+})_2$ which is in equilibrium with Pe^{*+} .²⁴ The time profile of the diffracted intensity depicted in Figure 2b shows that the ground-state recovery of Pe^{*+} in H_2SO_4 is faster than the response of the instrument and must therefore take place in less than 15 ps. For this measurement the concentration of Pe was 2×10^{-5} M. The experiment was repeated with a 10^{-2} M Pe solution using a 0.01 mm optical path length. At this concentration, the absorbance at 532 nm was mainly due to $(\text{Pe}^{*+})_2$. In this case as well, the decay time of the diffracted intensity was shorter than 15 ps.

Pe^{*+} , Pe^{*-} , and AQ^{*-} in MeCN. These radical ions were generated by photoinduced intermolecular ET reaction. The pulse sequence is illustrated in Figure 1b. A UV pulse at 355 nm (P_4) excited either Pe or AQ dissolved in MeCN in the presence of either an electron donor (D) or an electron acceptor (A) with a concentration lying between 0.1 and 0.2 M. At this quencher concentration, the ET quenching takes place in less than a nanosecond, the reaction being diffusion controlled. Mataga and co-workers²⁵ have shown that for the Pe/TCNE pair, where TCNE is the electron acceptor, free Pe^{*+} and TCNE^{*-} ions are formed within less than 5 ns with a yield of about 50%. Similarly, with the Pe/DMA pair, where DMA is the electron donor, free Pe^{*-} and DMA^{*+} ions are generated in the same time scale with a yield of about 70%. Finally, AQ^{*-} was generated by photoinduced ET between ${}^3\text{AQ}^*$ and DABCO with a resulting free ion yield close to unity.²⁶ These free ion populations decay in the microsecond time scale by homogeneous recombination.²⁷ As shown in Figure 1b, the transient grating experiment was performed on the free ion population 7 ns after the starting of the ET reaction by P_4 . At this time delay, the transient absorbance at 532 nm was of the order of 0.1 and remained constant within the time window of the transient grating experiment. The transient gratings were probed at both 532 and 545 nm. At those wavelengths, the absorption is due to either Pe^{*+} or Pe^{*-} or AQ^{*-} but not to the corresponding quencher radical ion.¹⁶ Figure 2c shows the time profile measured at 545 nm with the Pe/DMA pair. After a decay that is too fast to be resolved, the diffracted intensity remained constant and larger than zero even at time delays larger than 1 ns (not shown). The nature of this very slow component will be discussed below. With Pe/TCNE, only the very fast decay was observed, indicating that the lifetime of Pe^{*+} in MeCN is shorter than 15 ps.

For the AQ/DABCO pair, the time profile of the diffracted intensity was similar to that observed with the Pe/TCNE pair. However, a higher pulse intensity at 532 nm had to be used as the extinction coefficient of AQ^{*-} at this wavelength is

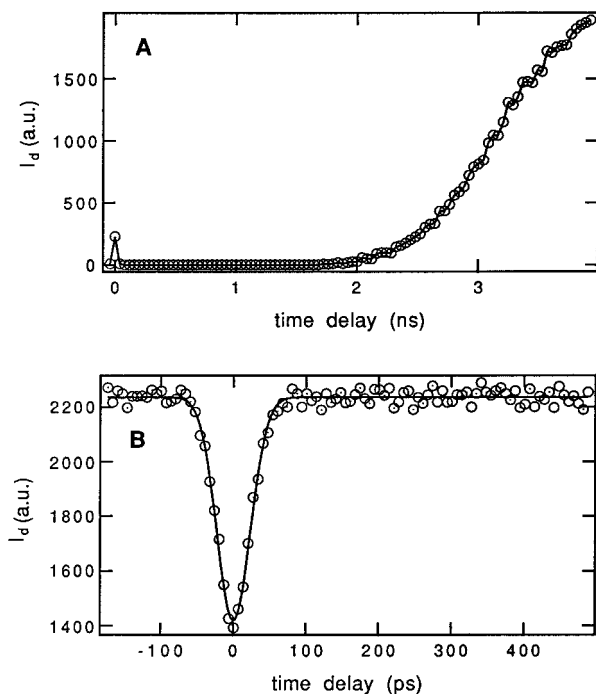


Figure 3. (A) Time profiles of the diffracted intensity measured at 532 nm with $AQ^{\bullet-}$ generated by photoinduced ET reaction with DABCO. (B) Dynamics of ground-state recovery of $AQ^{\bullet-}$ obtained by probing the density grating formed at different time delays after the bleaching pulse P_5 and best fit of a Gaussian function.

substantially smaller than that of Pe^+ . For this reason, a diffracted signal could already be observed without the UV pulse, indicating the contribution from other processes than the population grating. This unwanted signal could not be totally eliminated even by using a combination of polarization to suppress the contribution of the nuclear OKE,^{18,19} indicating the occurrence of electronic OKE. In a polarization selective transient grating experiment, the contribution of electronic OKE cannot be distinguished from that of the population grating when the transition dipole involved in the pumping process is parallel to that involved in the probing process, as in the present case.¹⁹ Consequently, a different experiment was performed to measure the contribution of the population grating only, without those due to nonresonant nonlinear processes.

Dynamics of Ground-State Recovery by Monitoring $\chi_{ijkl}^{(3)}(d)$. Figure 3a shows the time profile of the diffracted intensity measured with the AQ/DABCO pair on a long time scale using parallel polarization. The slow rise of the diffracted intensity originates from $\chi_{1111}^{(3)}(d)$, i.e., from the density grating, which is itself caused by the thermal expansion following the nonradiative deactivation of $AQ^{\bullet-}$ to D_0 . The amplitude of this density grating and thus the diffracted intensity oscillate at a frequency $\omega = 4\pi \sin(\theta/2)v_s/\lambda_{pu}$,²⁸ where θ is the crossing angle of P_1 and P_2 at the wavelength λ_{pu} and v_s is the velocity of sound. In MeCN and with $\theta = 2^\circ$, the maximum of the first oscillation appears at a time delay of about 7 ns. The magnitude of this maximum is proportional to the square of the population of ions that have undergone photoexcitation and relaxation to the D_0 state and does not depend on any nonresonant processes. Therefore, the ground-state recovery dynamics of the ions was measured by monitoring $\chi_{1111}^{(3)}(d)$ using pulse sequence depicted in Figure 1c. The photoinduced ET reaction was triggered by the UV pulse, P_4 , and approximately 7 ns later, the absorbance at 532 nm due to free ion population was bleached by a single intense pulse at 532 nm (P_5 , 500 μ J, 2 mm beam radius). The dynamics of ground-state recovery was

monitored by measuring with P_3 the amplitude of the density grating, i.e., $\chi_{1111}^{(3)}(d)$, generated by the P_1 and P_2 pulses on the remaining ground-state ion population. The time delay between the $P_{1,2}$ pulses and the probe pulse P_3 was 7 ns. The bleaching pulse P_5 arrived on the sample at a variable time delay relative to the three transient grating pulses. This technique can be considered as flash photolysis with calorimetric detection.⁴² The advantage of monitoring the density grating instead of using a photoacoustic detector is that the heat generated by P_4 and P_5 does not contribute to the signal.^{30,31} Figure 3b shows the diffracted intensity measured with the AQ/DABCO pair as a function of the time delay between P_5 and the grating pulses, $P_{1,2}$. When the latter pulses arrive on the sample before P_5 , the absorbance at 532 nm is the highest and the amplitude of the density grating is the highest as well. When P_5 and $P_{1,2}$ are time coincident, the amplitude of the density grating is smaller, because the absorbance at 532 nm has been reduced by P_5 . Once the ground-state population of the ions and the absorbance at 532 nm have been restored, the amplitude of the density grating recovers its initial value. The continuous line in Figure 3b is the best fit of a Gaussian function. Time profiles with the same widths were obtained with CV in MeOH and with Pe/TCNE in MeCN. These measurements indicate that the lifetime of $AQ^{\bullet-}$ in MeCN is also shorter than the response time of the experiment. This result contrasts remarkably with the lifetime of 4 ns obtained indirectly by Fujita et al.¹¹ The origin of this discrepancy is not understood and might be due to the complexity of the system used by these authors.

Origin of the Incomplete Ground-State Recovery of $Pe^{\bullet-}$.

With the Pe/DMA system, the ground-state recovery of $Pe^{\bullet-}$ is not complete, indicating that a fraction of the anion population has undergone an irreversible photoreaction. By comparing the square root of the intensity of the fast and of the slow components of the time profile shown in Figure 2c, the quantum yield of this reaction is about 0.15, and therefore the time constant for this process must be shorter than 85 ps. As the overall concentration of Pe stays unchanged even after intense laser irradiation, the process responsible for the uncompleted recovery of the $Pe^{\bullet-}$ population must lead to the formation of neutral parent. Considering the time constant of this reaction and the concentrations of both $DMA^{\bullet+}$ and DMA, bimolecular processes such as $Pe^{\bullet-} + DMA^{\bullet+} \rightarrow Pe + DMA$ or $Pe^{\bullet-} + DMA \rightarrow Pe + DMA^{\bullet-}$ can be excluded. Consequently, the most probable process is electron photoejection from $Pe^{\bullet-}$, which is known to be a major deactivation pathway of photoexcited radical anions in the gas phase and in nonpolar solvents.⁶ For example, a photoejection yield of 0.46 has been reported for $Pe^{\bullet-}$ in tetramethylsilane.³² In the gas phase, photoejection takes place when the excitation energy is larger than the electron affinity of the neutral parent molecule. In the case of $Pe^{\bullet-}$ and $AQ^{\bullet-}$, this should take place upon excitation at wavelengths below 1400 and 780 nm, respectively.^{32,33} In solution and particularly in polar solvents, the ions are stabilized, and the threshold energy for photoejection, E_{th} , can be expressed as^{11,32}

$$E_{th} = E_{red} + V_0 + C \quad (2)$$

where E_{red} is the reduction potential of the parent neutral in MeCN ($E_{red}(Pe) = -1.66$ V vs SCE,³⁴ $E_{red}(AQ) = -0.894$ V vs SCE³⁵), V_0 is the lower edge of the conduction band of an electron in the solvent relative to vacuum ($V_0 = -0.14$ eV in MeCN³⁶), and C is the oxidation potential of a reference calomel electrode ($C = 4.56$ V). From this equation, E_{th} is equal to 2.7 eV for $Pe^{\bullet-}$ and to 3.5 eV for $AQ^{\bullet-}$. Comparison between these values and the energy of a photon at 532 nm ($E_{hv} = 2.33$ eV)

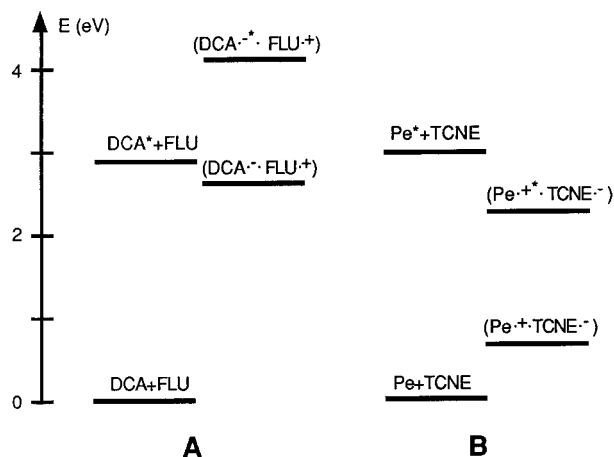


Figure 4. Energy levels involved in the photoinduced ET reaction in MeCN between (A) DCA and FLU and (B) perylene and TCNE.

shows that photoejection with a single photon is not possible with AQ^{*-} . On the other hand, considering the uncertainties of the values used in the calculation, the threshold for Pe^{*-} is close to the energy of a 532 nm photon. For Pe^{*-} in nonpolar solvents, the time constant for photoejection has been estimated to be smaller than 100 fs.³² Therefore, a time constant shorter than 85 ps is reasonable, even for an electron ejection with a photon close to the threshold energy. However, the occurrence of biphotonic ejection cannot be excluded.

ET Dynamics with Excited Ions. The free ion yield in an intermolecular ET reaction in solution depends on the competition between back ET within the ion pair and diffusion of the ions. In MeCN, diffusion of the ions out of the reaction volume, where geminate recombination is still possible, occurs within a couple of nanoseconds, whereas the rate constant of back ET is very sensitive to the energy gap between the ion pair state and the neutral ground state.^{25,37–39} Consequently, if one of the ions within the geminate ion pair is in an electronic excited state, the energy gap for back ET is substantially larger than the energy gap with both ions in the ground state. Of course, this additional free energy can only influence the free ion yield if the excited-state lifetime of the ion is not too small compared with the time scale of ion diffusion. For example, if the excited-state lifetime of DCA^{*-} is around 5 ns, as determined by Fujita et al.,¹¹ excitation of DCA^{*-} within the geminate ion pair ($DCA^{*-} \cdot D^{+}$) formed after ET quenching should influence the free ion yield. Such an experiment was performed with two electron donors, FLU and ANI. The free energy for back ET from the ion pair in the ground state amounts to about -2.63 and -2.74 eV for FLU and ANI, respectively (see Figure 4a). Upon excitation at 355 nm with a 20 ns laser pulse of a solution of a DCA containing 0.2 M donor in MeCN, the free ion yield was around 20% and 14% with FLU and ANI, respectively. The absorbance at 532 nm after 355 nm excitation was of the order of 0.1. The same experiment was repeated with an additional, time coincident, 20 ns laser pulse at 532 nm to excite DCA^{*-} . Back ET within ($DCA^{*-} \cdot D^{+}$) to the neutral ground state is more negative by 1.56 eV²¹ than back ET within ($DCA^{*} \cdot D^{+}$) and should consequently be much slower. On the other hand, back ET to $DCA^{*} + D$ is not possible from ($DCA^{*-} \cdot D^{+}$) but is energetically feasible from ($DCA^{*-} \cdot D^{+}$), the corresponding free energy being equal to -1.30 and -1.41 eV for FLU and ANI, respectively (see Figure 4a). Consequently, this very different situation for recombination within ($DCA^{*-} \cdot D^{+}$) should have a strong repercussion on the free ion yield, as long as the lifetime of DCA^{*-} is long enough. The intensity ratio of the 532 nm/355 nm laser pulse intensity was varied from 0.2 to 2. With this additional excitation, the

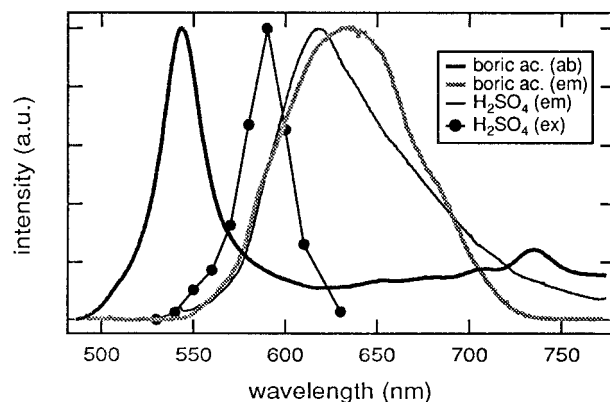


Figure 5. Absorption spectrum of Pe-doped boric acid glass after UV irradiation (thick black line), emission spectrum measured with the same sample upon excitation at 532 nm (thick gray line), emission spectrum measured with a solution of Pe in H_2SO_4 excited at 532 nm (thin black line), and corresponding excitation spectrum (black dots).

free ion yields were identical with those obtained without the 532 nm pulse. No effect was observed with the Pe/TCNE pair either (see Figure 4b). The latter result was expected as the lifetime of Pe^{*+} has been measured to be shorter than 15 ps. The result with DCA strongly suggests that the lifetime of DCA^{*-} is much smaller than 5 ns.

Emission from Radical Ions. Upon laser irradiation at 532 nm, the Pe^{*+} -doped boric acid glasses exhibited a weak red luminescence which is shown in Figure 5. Its intensity was too small to perform an excitation spectrum. However, Pe^{*+} in H_2SO_4 exhibited a similar emission which was intense enough to measure an excitation spectrum which is also shown in Figure 5. This spectrum coincides very well with the absorption spectrum of protonated perylene, PeH^+ , measured in HF solution.²³ Recently, similar absorption and emission spectra were observed with Pe in zeolites and were indeed ascribed to PeH^+ .⁴⁰ As the absorption band of PeH^+ around 600 nm is completely hidden by those of Pe^{*+} , the concentration of the protonated Pe in both boric acid glass and in H_2SO_4 must be very small compared to that of the radical cation. Moreover, the absorbance of PeH^+ at 532 nm is close to zero, and therefore this species does not play any role in the ground-state recovery measurements.

The fluorescence of Pe^{*+} has been reported in BF_3 -trifluoroacetic acid solution, on surfaces⁹ and in rare gas matrixes at low temperature.⁴¹ The solution and surface fluorescence spectra consist of two bands, one located around 800–820 nm and a second one at 910 nm. In H_2SO_4 and in boric acid glass, the presence of the emission band of PeH^+ and of other bands observed with undoped boric acid glass did not allow a unequivocal detection of fluorescence from Pe^{*+} . The intensity of $Pe^{*+} D_1 \leftarrow D_0$ absorption band is very weak and corresponds to an oscillator strength of the order of 5×10^{-3} .²¹ From this value, the natural radiative lifetime of Pe^{*+} can be calculated to be of the order of 1 μs . Such a very long natural radiative lifetime, together with a nonradiative decay time in solution of a few picoseconds, indicates a fluorescence quantum yield of the order of 10^{-6} . Similar fluorescence quantum yields are predicted for Pe^{*-} and AQ^{*-} , which should fluoresce above 1100 nm. The detection of such weak emissions is certainly possible, but only with samples of well-known composition and that do not contain other fluorescing species. The systems studied here are therefore not well suited for such measurements.

Concluding Remarks

The very fast ground-state recovery of the ions measured here must be due to a very efficient internal conversion favored by

a small D_1-D_0 energy gap. This property seems to be a general characteristic of almost all organic radical ions, and therefore short excited-state lifetimes have to be expected for most of them. Coincidentally, the oscillator strength of the $D_1 \leftarrow D_0$ transition of many radical ions is small, indicating a long natural radiative lifetime. Consequently, the detection of the fluorescence of most radical ions requires laser excitation and also near-IR detection. This certainly explains why so few genuine emission from radical ions in the condensed phase at room temperature have been reported so far.

The different lifetimes of Pe^{*+} measured in boric acid glass and liquid solutions must be due to the fact that the coupling between the vibrational modes of the ions and the phonons of the medium is less efficient in the glass than in the liquids. In rare gas matrixes at low temperature, this coupling is so weak that vibrationally unrelaxed fluorescence has been observed for substituted benzene cations.⁶ The same effect might explain the observation of the fluorescence of Pe^{*+} on surfaces.⁹

Considering the small $D_1 \leftarrow D_0$ energy gap of most aromatic radical ions involved in ET quenching experiments, the formation of excited radical ions in exergonic processes is not only energetically feasible (see for example Figure 4b) but also should be favored by a superior vibronic coupling with respect to the formation of the ions in the ground state. However, the very short lifetime of excited radical ions makes the detection of such intermediates extremely difficult.

Acknowledgment. This work was supported by the Fonds national suisse de la recherche scientifique through Project No. 20-49235.96 and by the program d'encouragement à la relève universitaire de la Confédération. Financial support from the Fonds de la recherche and the Conseil de l'Université de Fribourg is also acknowledged.

References and Notes

- Haselbach, E.; Bally, T. *Pure Appl. Chem.* **1984**, *56*, 1203.
- Mataga, N.; Kanda, Y.; Asahi, T.; Miyasaka, H.; Okada, T.; Kakitani, T. *Chem. Phys.* **1988**, *127*, 239.
- Kikuchi, K.; Katagiri, T.; Niwa, T.; Takachi, Y.; Suzuki, T.; Ikeda, U.; Miyashi, T. *Chem. Phys. Lett.* **1992**, *193*, 155.
- Miller, T. A. *Annu. Rev. Phys. Chem.* **1982**, *33*, 257.
- Klapstein, D.; Maier, J. P.; Misev, L. In *Molecular Ions: Spectroscopy, Structure and Chemistry*; Miller, T. A., Bondibey, V. E., Eds.; North-Holland: Amsterdam, 1983; p 175.
- Bondibey, V. E.; Miller, T. A. In *Molecular Ions: Spectroscopy, Structure and Chemistry*; Miller, T. A., Bondibey, V. E., Eds.; North-Holland: Amsterdam, 1983; p 125.
- Eriksen, J.; Lund, H.; Nyvad, A. *Acta Chem. Scand.* **1983**, *B37*, 459.
- Eriksen, J.; Jorgensen, K. A.; Lindenberg, J.; Lund, H. *J. Am. Chem. Soc.* **1984**, *106*, 5084.
- Pankasem, S.; Iu, K. K.; Thomas, J. K. *J. Photochem. Photobiol. A* **1991**, *62*, 53.
- Breslin, D. T.; Fox, M. A. *J. Phys. Chem.* **1994**, *98*, 408.
- Fujita, M.; Ishida, A.; Majima, T.; Takamuka, S. *J. Phys. Chem.* **1996**, *100*, 5382.
- Vauthey, E. *Chem. Phys. Lett.* **1993**, *216*, 530.
- Högemann, C.; Pauchard, M.; Vauthey, E. *Rev. Sci. Instrum.* **1996**, *67*, 3449.
- von Raumer, M.; Suppan, P.; Jacques, P. *J. Photochem. Photobiol. A* **1997**, *105*, 21.
- Andreev, O. M.; Smirnov, V. A.; Alifimov, M. V. *J. Photochem.* **1977**, *7*, 149.
- Shida, T. *Electronic Absorption Spectra of Radical Ions*; Elsevier: Amsterdam, 1988; Vol. Physical Sciences Data 34.
- Shen, Y. R. *The Principles of Nonlinear Spectroscopy*; J. Wiley: New York, 1984.
- Etchepare, J.; Grillon, G.; Chambaret, J. P.; Hamoniaux, G.; Orzag, A. *Opt. Commun.* **1987**, *63*, 329.
- Deeg, F. W.; Fayer, M. D. *J. Chem. Phys.* **1989**, *91*, 2269.
- Sundström, V.; Gillbro, T. In *Picosecond Chemistry and Biology*; Doust, T. A. M., West, M. A., Eds.; Science Review: Northwood, 1983; p 148.
- Negri, F.; Zgierski, M. Z. *J. Chem. Phys.* **1994**, *100*, 1387.
- Handbook of Chemistry and Physics*, 66th ed.; CRC Press: Boca Raton, FL, 1985.
- Aalbersberg, W. I.; Hooijink, G. J.; Mackor, E. L.; Weiland, W. P. *J. Chem. Soc.* **1959**, 3049.
- Kimura, K.; Yamazaki, T.; Katsumata, S. *J. Phys. Chem.* **1971**, *75*, 1768.
- Mataga, N.; Asahi, T.; Kanda, Y.; Okada, T.; Kakitani, T. *Chem. Phys.* **1988**, *127*, 249.
- Haselbach, E.; Vauthey, E.; Suppan, P. *Tetrahedron* **1988**, *44*, 7335.
- Haselbach, E.; Jacques, P.; Pilloud, D.; Suppan, P.; Vauthey, E. *J. Phys. Chem.* **1991**, *95*, 7115.
- Nelson, K. A.; Fayer, M. D. *J. Chem. Phys.* **1982**, *79*, 5202.
- Terazima, M. *J. Phys. Chem.* **1997**, *101*, 3227.
- Rothberg, L. J.; Bernstein, M.; Peters, K. S. *J. Chem. Phys.* **1983**, *79*, 2569.
- Siegmán, A. E. In *Applications of Picosecond Spectroscopy to Chemistry*; Eisenthal, K. B., Ed.; D. Reidel: Dordrecht, 1983; p 325.
- Sowada, U.; Holroyd, R. A. *J. Phys. Chem.* **1981**, *85*, 541.
- Kebarle, P.; Chowdhury, S. *Chem. Rev. (Washington, D.C.)* **1987**, *87*, 513.
- Parker, V. D. *J. Am. Chem. Soc.* **1976**, *98*, 98.
- Peover, M. E. *J. Chem. Soc.* **1962**, 4541.
- Peover, M. E. *Electrochim. Acta* **1968**, *13*, 1083.
- Marcus, R. A.; Sutin, N. *Biochim. Biophys. Acta* **1985**, *811*, 265.
- Gould, I. R.; Ege, D.; Mattes, S. L.; Farid, S. *J. Am. Chem. Soc.* **1987**, *109*, 3794.
- Vauthey, E.; Suppan, P.; Haselbach, E. *Helv. Chim. Acta* **1988**, *71*, 93.
- Iu, K. K.; Liu, X.; Thomas, J. K. *Chem. Phys. Lett.* **1991**, *186*, 198.
- Joblin, C.; Salama, F.; Allamandola, L. *J. Chem. Phys.* **1995**, *102*, 9743.
- This technique is very similar to a method described by Terazima²⁹ in a paper which was published while we were writing this one.

2.3. Picosecond Resonance CARS Investigation of Intermolecular ET Reactions in Solution

2.3.1. Introduction

Many optical techniques based on transient absorption or emission can be used to study intermolecular electron transfer reactions. However, when the studied species are very similar, as for instance exciplex and ion pairs, their spectroscopic characteristics are often not very different. Structural information are therefore needed to differentiate them⁵⁴. Furthermore, when fluorescent samples are studied, Raman spectroscopy is not possible and Coherent Anti-Stokes Raman Scattering (CARS) spectroscopy has to be used. In this experiment, we wanted to study the structure of the intermediates formed upon photoinduced intermolecular electron transfer reaction between perylene and different acceptors.

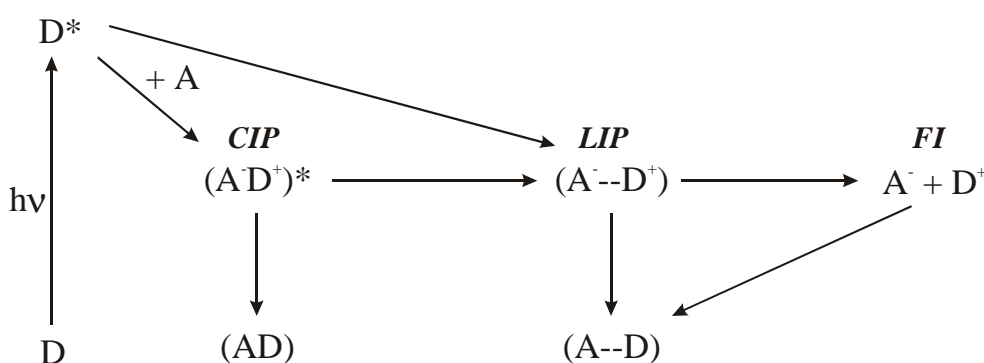


Figure 2.4: Scheme of a photoinduced ET reaction⁵⁵. The excited donor can be quenched to lead to a CIP or to a LIP . Both of them can recombine or lead to FI . CIP , LIP and FI have similar absorption spectra, but their structure should be somewhat different.

In the presence of an electron acceptor, excited PE is quenched, leading to ions pairs. Depending on the quenching distance, this ET can either lead to Contact Ions Pairs (CIP) or to Loose Ions Pairs (LIP). Furthermore, if charge recombination does not take place, the CIP separates to LIP and finally to Free Ions (FI). In order to confirm the presence of the CIP, time resolved structural changes have to be investigated.

Unfortunately, as shown in the following sections, double resonance CARS was hard to achieve and results were not reproducible.

Therefore only the solvent and highly concentrated species have been accurately observed. The probable formation of the PE radical cation is also shown, and hints on its formation dynamics are given.

2.3.2. Experimental Conditions

Laser Pulses

In order to achieve time resolved CARS spectroscopy of ET reactions, four ps-pulses are needed.

- 1) A 355 nm pulse: this 30 ps pulse, directly produced by the third harmonic of an active/passive mode-locked Q-switched Nd:YAG laser (Continuum model PY61-10), is used to initiate the photoinduced intermolecular ET. In order to achieve a time resolved experiment, this pulse is time delayed by a motorized translation stage. The delay between the ET initiation and the CARS probing can thus be varied.

- 2) Two 532 nm pulses: directly produced by the Nd:YAG laser, they are used as pump pulses in the CARS experiment. It is also possible to Raman shift them to 543 nm or 519 nm in CCl_4 . This is useful to:
- Optimize resonance conditions.
 - Obtain different resonance spectral window without changing ω_{Stokes} .
Frequency shifts as small as 500 cm^{-1} can be thus achieved.

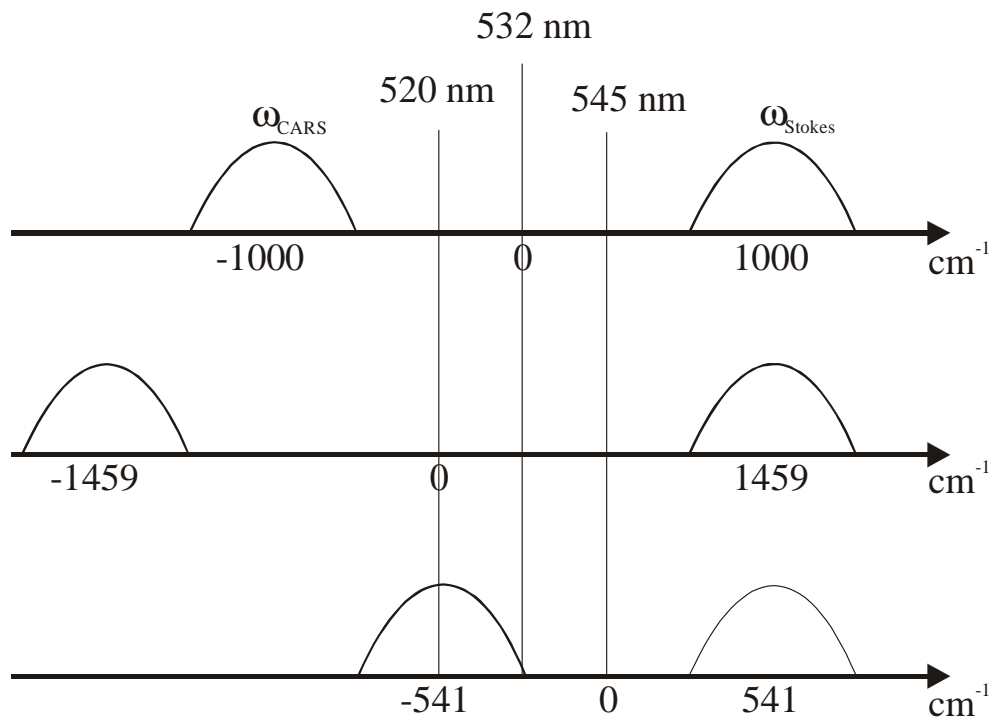


Figure 2.5: Shift of the CARS frequency obtained by changing the pump wavelength. Raman shifting in CCl_4 leads to a $\pm 459 \text{ cm}^{-1}$ shift in the CARS frequency.

Nevertheless, as it is not possible to perfectly eliminate unwanted Raman shifted lines, CARS spectra obtained in this way become very complicated and each vibration band may appear three times in the spectrum.

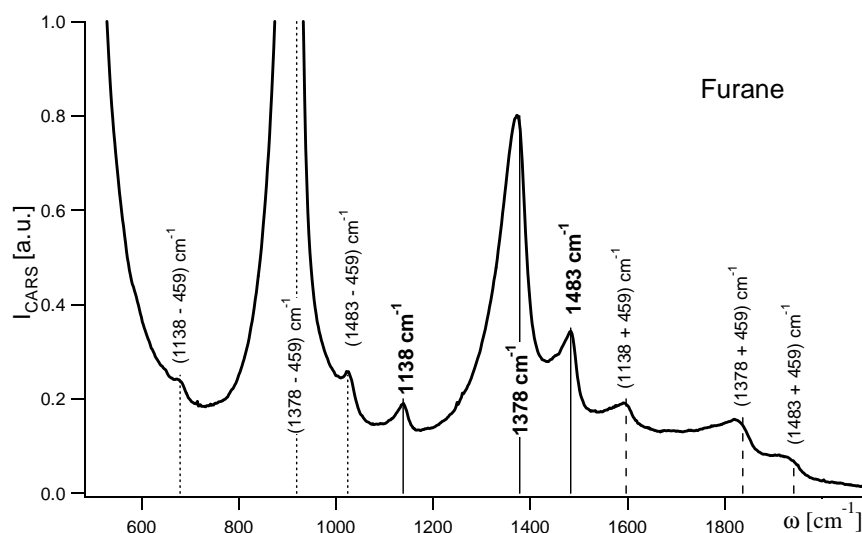


Figure 2.6: CARS spectrum of pure furane obtained with pump pulses that are Raman-shifted in CCl_4 (Stokes and anti-Stokes). The vibrations at 1138 cm^{-1} , 1378 cm^{-1} , and 1483 cm^{-1} are present three times on the spectrum, leading to a complex analysis of the data.

- 3) A 540-570 nm pulse: this Stokes pulse has to possess a broad spectrum in order to perform multiplex CARS experiment. It can therefore not be directly produced by the laser. Twelve mJ of the fundamental of the Nd-YAG laser (1064 nm) are focused in a cell containing a 70:30 (v/v) $\text{D}_2\text{O}/\text{H}_2\text{O}$ mixture, to produce a white light continuum pulse. This phenomenon, mainly due to Self Phase Modulation (SPM) has already been extensively described in the literature^{26,56}. A spectral portion of this low energy continuum is amplified by a two stage dye amplifier, pumped at 532 nm. A 10-15 nm broad pulse is thus obtained. Its central frequency can be varied by changing the corresponding dye, leading to shifts from 500 cm^{-1} (fluoresceine) to 1700 cm^{-1} (kiton red).

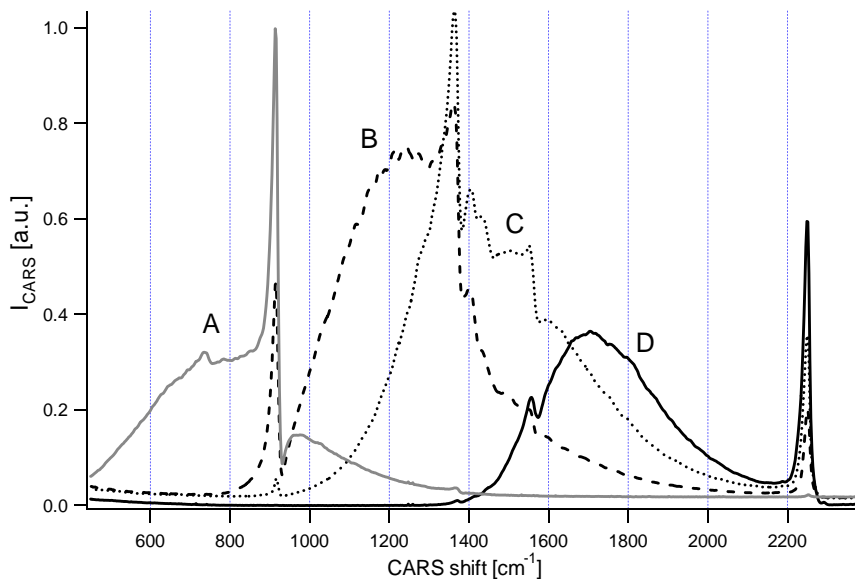


Figure 2.7: CARS signal from PE/TCNE in acetonitrile investigated with different ω_{Stokes} , amplified in fluoresceine (A), rhodamine 6G (B), kiton red (D) and mixture (C). Phase matching conditions allows only a 700 cm^{-1} spectral window to be investigated without adapting the geometry.

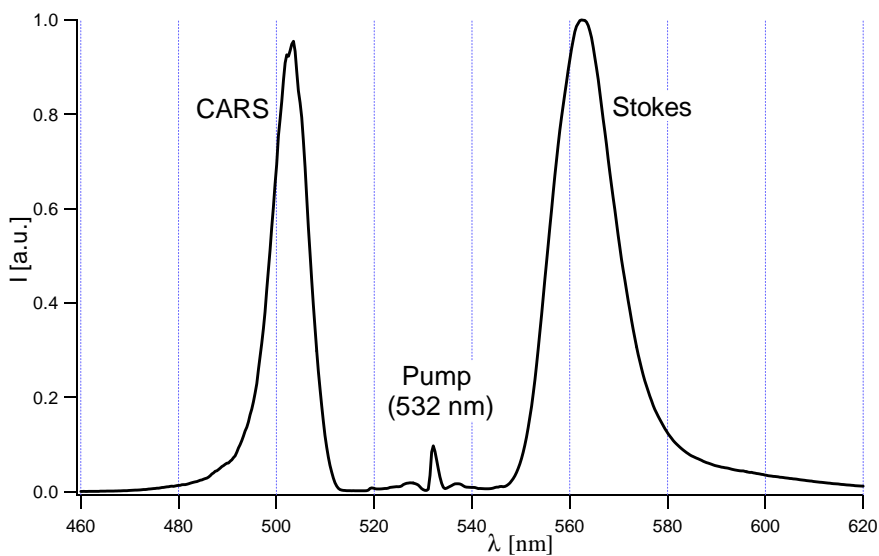


Figure 2.8: Wavelength used in a CARS experiment performed in pure CCl_4 . Stokes pulse is amplified in a rhodamine 6G/fluoresceine mixture, leading to a maximal shift of 1000 cm^{-1} relatively to λ_{pump} . The CARS signal appears around 505 nm .

Samples

In order to investigate ET reactions dynamics, one first need to be sure that ions are formed.

To obtain the transient spectra of $\text{PE}^{\bullet+}$, we used white light TG spectroscopy described in details by Högemann⁵⁶. This technique allows ps time-resolved TG spectra (similar to transient absorption spectra²³) to be obtained with a very good signal to noise ratio.

Upon excitation with a UV pulse, PE is excited to its S_1 state, which absorbs at 700 nm in propionitrile (PrCN)⁵⁷. By adding different electron acceptors, this state can be quenched to produce $\text{PE}^{\bullet+}$.

For instance a PE solution with 0.15 M Tetracyanoethylene (TCNE) that is irradiated with a 3 mJ, 355 nm pulse, leads to the formation of the $\text{PE}^{\bullet+}$. This can be shown in the TG spectra by the appearance of a new band at 540 nm with a long lifetime. The $\text{PE}^{\bullet+}$ formed by γ irradiation in 77K matrices has the same spectrum⁵⁸.

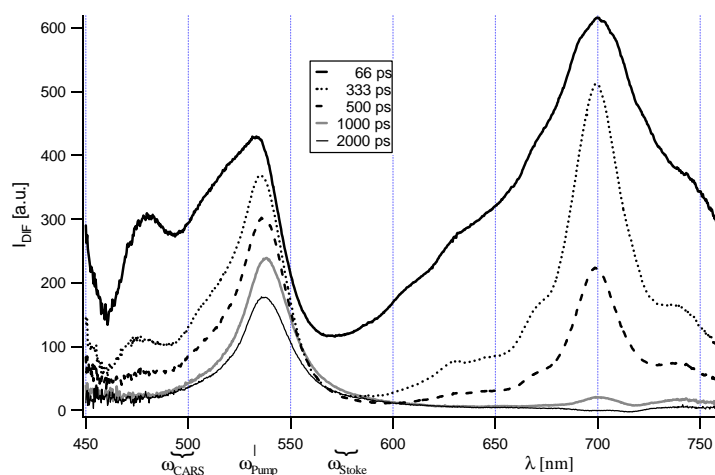


Figure 2.9: TG spectra of PE with 0.15M TCNE in PrCN at different delays after UV excitation. The S_1 excited-state of PE (at 700 nm) decays in 680 ps. The wavelength used for CARS experiments are also indicated to show that the electronic resonance condition is fulfilled.

Weaker electron acceptors also lead to ion formation, but with a slower formation dynamics, as shown with 1,2-dicyanobenzene (1,2-DCB).

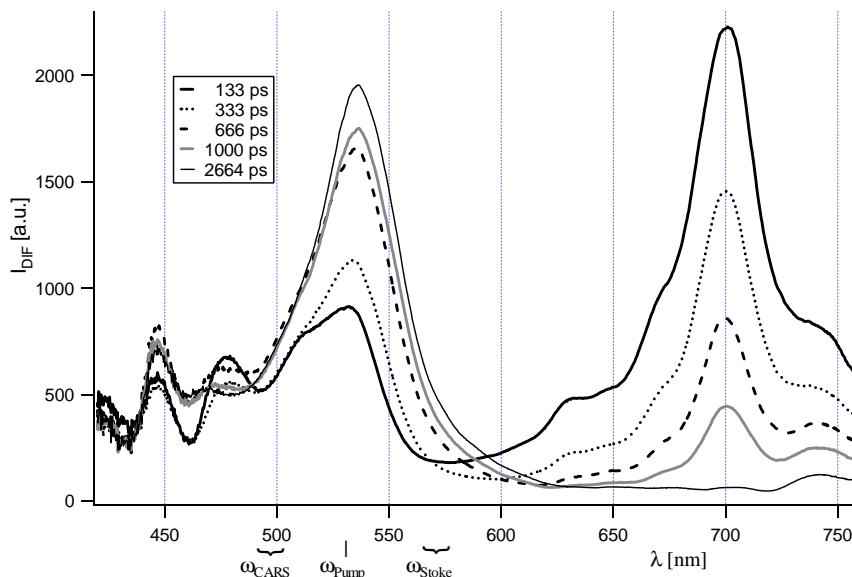


Figure 2.10: TG spectra of PE with 0.2M 1,2-DCB in PrCN at different delays after UV excitation. The ion formation is, in this case, slower than that with TCNE as shown by the increase of the PE^{*+} absorption with time. Note that the anion of 1,2-DCB does not absorb between 400 nm and 1100 nm.

Similar results were also obtained for the fluorescence quenching of PE by 1,4-DCB, 1,3-DCB, fumaronitrile or Phthalic Anhydride (PA), in PrCN (not shown).

As shown in eq.(1.98), single resonance is achieved when $\omega_{gv} = \omega_p - \omega_{Stokes}$. To allow double resonance CARS, the pump and/or CARS frequencies have to be in the absorption band of the species studied, to minimize the denominator of eq.(1.98), and thus to enhance the signal. In other words, the following conditions have to be satisfied:

$$\omega_p = \omega_{eg} \quad (2.1)$$

$$\text{and/or} \quad \omega_{CARS} = \omega_{e'g} \quad (2.2)$$

In the case of PE^{*+} , the CARS pump intensity corresponds to the maximum of the absorption band and should thus lead to a strong resonance (Figure 2.9).

Another difficulty with multiplex CARS spectroscopy arises from the phase matching condition. As the Stokes beam is broadband, phase matching conditions cannot be satisfied for all wavelengths without changing the angle of incidence on the sample. To minimize this problem, one has to use a very thin sample (less than a half millimeter). In this case, the moving grating formed is almost a thin grating and Bragg condition is no longer so restrictive (see section 1.2.6).

Furthermore, the cell windows give a CARS signal that can be measured even with an empty sample cell. Flowing the sample in a jet eliminates these two problems. With the 300 μm thick jet used here, no windows effect take place and phase matching can be achieved over 700 to 800 cm^{-1} (Figure 2.7).

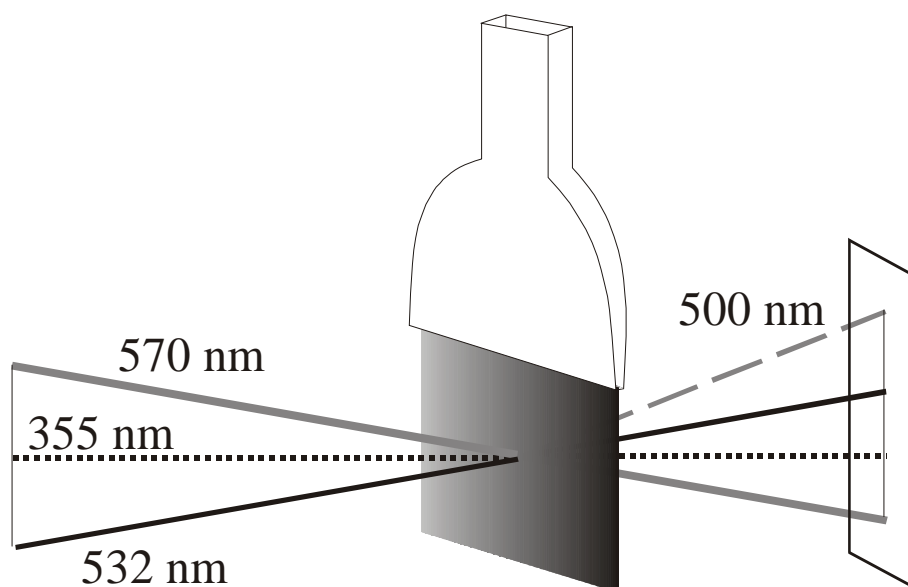


Figure 2.11: Scheme of a CARS experiment in a 300 μm thick sample flowing jet. With thin samples, the phase matching condition is not too restrictive and allows 700 cm^{-1} multiplex CARS to be performed around 500 nm. Signal from the windows is also eliminated with a jet. Note that both 532 nm pumping photons come from the same pulse.

All the solvents used were from Fluka with the highest purification grade available. Only propionitrile was provided by Rathburn in a highly purified grade (200 nm grade). PE, 1,2-DCB, 1,3-DCB, 1,4-DCB, fumaronitrile and PA were also from Fluka and were recrystallized and sublimed. Special care was taken with TCNE that was, after purification, kept in the fridge under Ar-atmosphere.

Detection

Performing multiplex CARS allows investigating many vibrations simultaneously. As many wavelengths are present in the signal, a PM tube can no longer be used, and a spectral resolution has to be achieved. Furthermore, vibrational bands may have narrow width, and a high resolution spectrograph is needed in order to resolve all the bands.

In this experiment a ¼-m imaging spectrograph (Oriel Multispec 257) equipped with a 1200 groove/mm grating was coupled to a 1024 × 256 pixels water-cooled Charge Coupled Device (CCD) camera (Oriel Instaspec IV). The resolution thus obtained is 2.5 cm⁻¹ for an overall bandwidth of 2500 cm⁻¹.

The CARS spectra were averaged over 1000 laser shots in order to minimize the noise. As the fluorescence of the sample, due to the actinic pulse, is emitted isotropically and the CARS signal is collimated, spatial isolation of the signal with an iris is possible, and no background correction has to be performed.

The bandwidth of the CARS signal is nevertheless limited by the phase matching conditions, the thinner the sample, the broader the signal. In our jet experiment, phase matching conditions were achieved over 700 to 800 cm⁻¹ without having to change the geometry.

Experimental Setup

In order to perform double resonance multiplex CARS spectroscopy, the setup depicted in Figure 2.12 is used. The laser directly produces the pump and excitation pulses. A spectral portion of white light continuum, formed in a D_2O/H_2O containing cell, is amplified by a two stages dye amplifier and used as Stokes pulse. The pump and Stokes pulses are focused in the sample by a 100 mm focal lens, and the CARS signal, that is spatially isolated (iris) is focused in an optical fiber coupled to the spectrograph, itself connected to the CCD camera. A translation stage is used for the UV pulse, to allow time resolution of the ET to be investigated. A combination of half-wave plates and polarization filters were used in order to achieve polarization sensitive CARS spectroscopy.

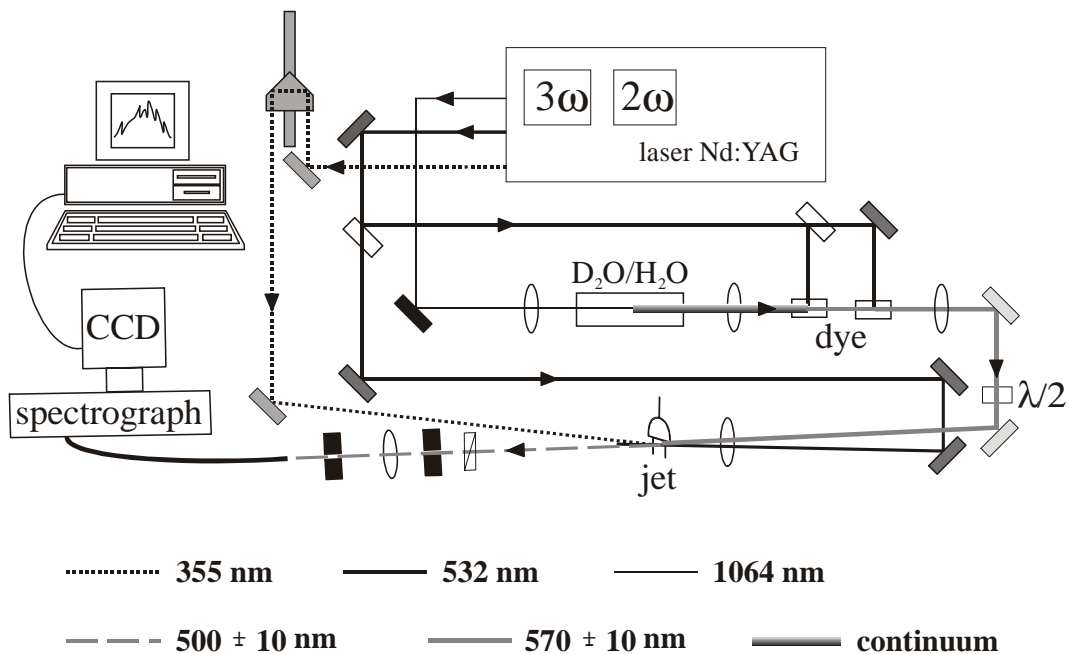


Figure 2.12: Experimental setup for a multiplex CARS experiment. The broadband Stokes pulse is obtained by amplification of a spectral portion of the continuum formed in a D_2O/H_2O mixture. The sample is flowing in a 300 μm thick jet in order to avoid window signal and too restrictive Bragg condition. Time delay is achieved by changing the UV path-length with a translation stage.

2.3.3. Nonresonant CARS Spectroscopy

In order to show that the CARS technique is suitable to characterize species through their vibrational spectra, we first applied this spectroscopy to solvents. In this case only single resonance (i.e. vibrational resonance) is achieved as no electronic transition is taking place near the working frequencies.

The nonresonant electronic background is also present and can be easily characterized with pure CCl_4 , where only one weak Raman band is present above 850 cm^{-1} . The same spectrum is recorded in the presence of a preceding UV pulse, and as expected, no structural changes are visible.

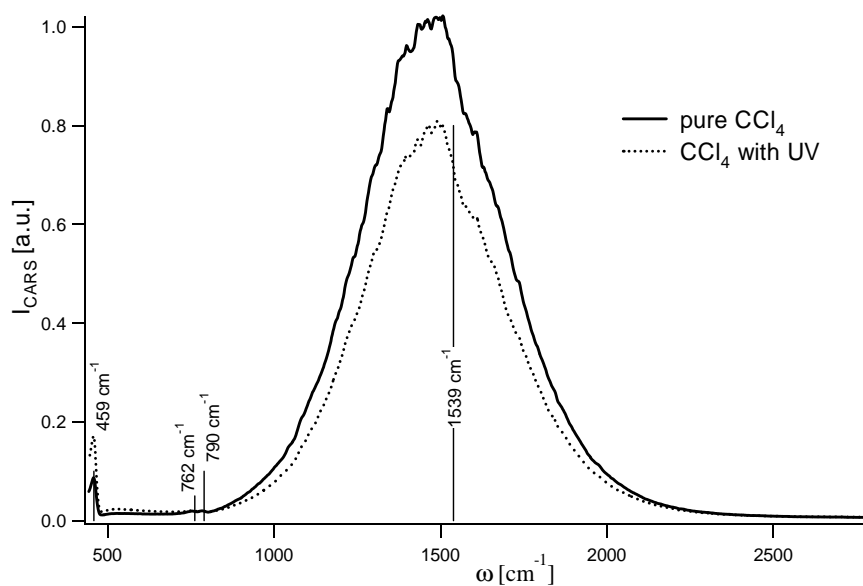


Figure 2.13: CARS spectrum of pure CCl_4 obtained with and without previous UV irradiation. No structural differences are induced by the UV pulse. Note that the 459 cm^{-1} band is so intense that it is visible even if the phase matching conditions are not fulfilled for this frequency. Above 800 cm^{-1} the CARS signal is only due to the electronic nonresonant contribution and contains only one weak band at 1539 cm^{-1} .

Once the nonresonant electronic signal is determined, other solvents can be investigated. As described in section 1.4.1, the CARS line-shapes depend on the nonresonant background. A complex data analysis has to be performed in order to extract their line-shape parameters. Nevertheless, a simple observation of the line-shape (Lorentzian or dispersive) is sometimes sufficient to find the central frequency of the vibration. In the following examples, values obtained from the CARS spectra are in perfect agreement with the literature⁵⁹. The relative intensities of the Raman bands, taken from the same literature, are mentioned in brackets.

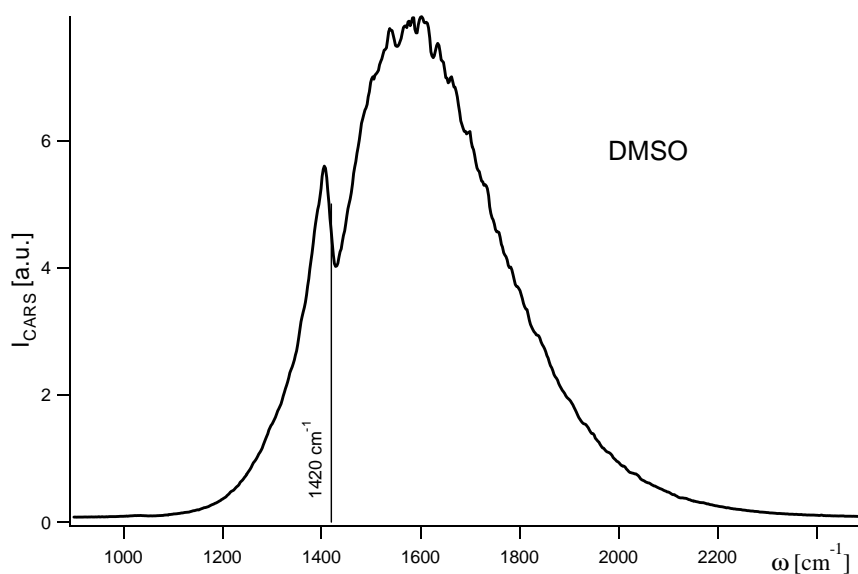


Figure 2.14: CARS spectrum of pure dimethylsulfoxide (DMSO). The weak 1420 cm^{-1} (5) band is in the phase matching region, and thus appears as dispersive.

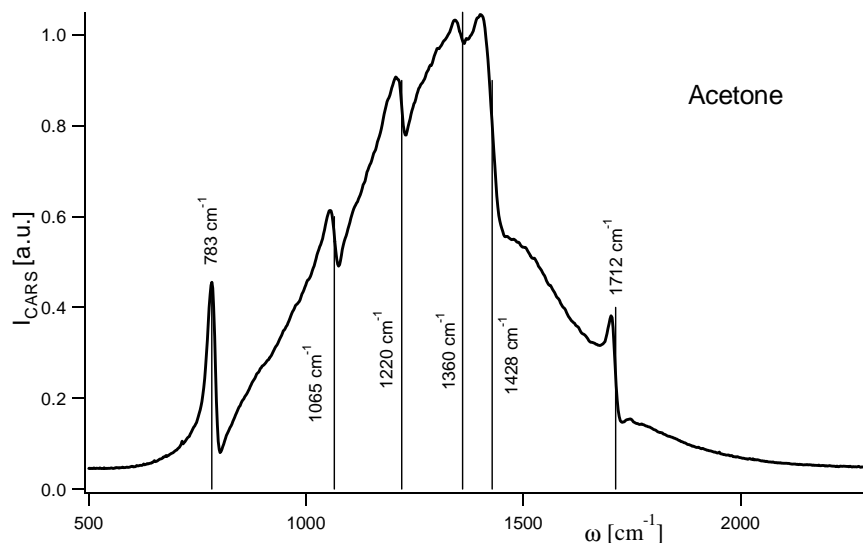


Figure 2.15: CARS spectrum of pure acetone. Vibration at 783 cm^{-1} (60) is almost Lorentzian due to its high intensity and the small nonresonant background. The other bands at 1065 cm^{-1} (5), 1220 cm^{-1} (5), 1360 cm^{-1} (weak), 1428 cm^{-1} (8.5) and 1712 cm^{-1} (15) exhibit dispersive line-shapes.

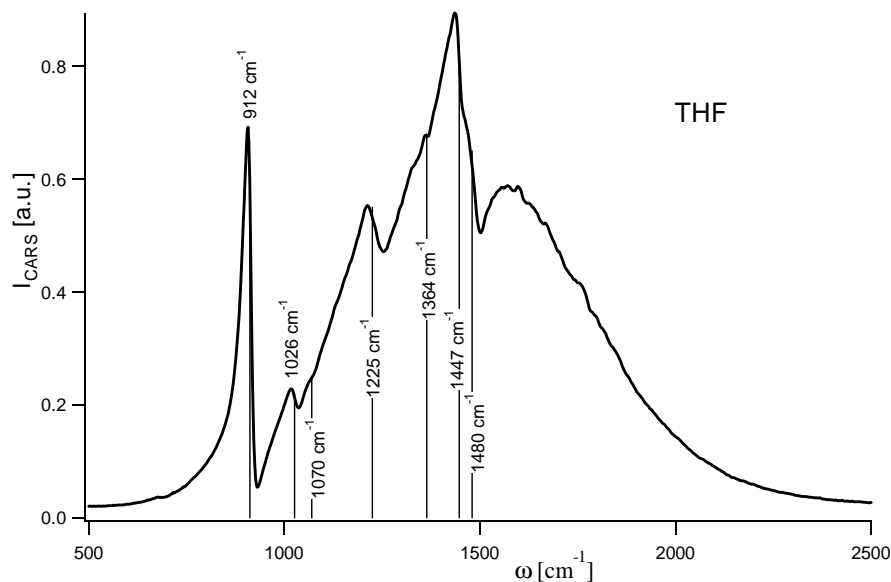


Figure 2.16: CARS spectrum of tetrahydrofurane (THF). Vibrations are at 912 cm^{-1} (45), 1026 cm^{-1} (5), 1070 cm^{-1} (1.5), 1225 cm^{-1} (4.5), 1364 cm^{-1} (0.5) and a broad one with two maxima at 1447 cm^{-1} and 1480 cm^{-1} (5.5). Only the 912 cm^{-1} band is almost Lorentzian.

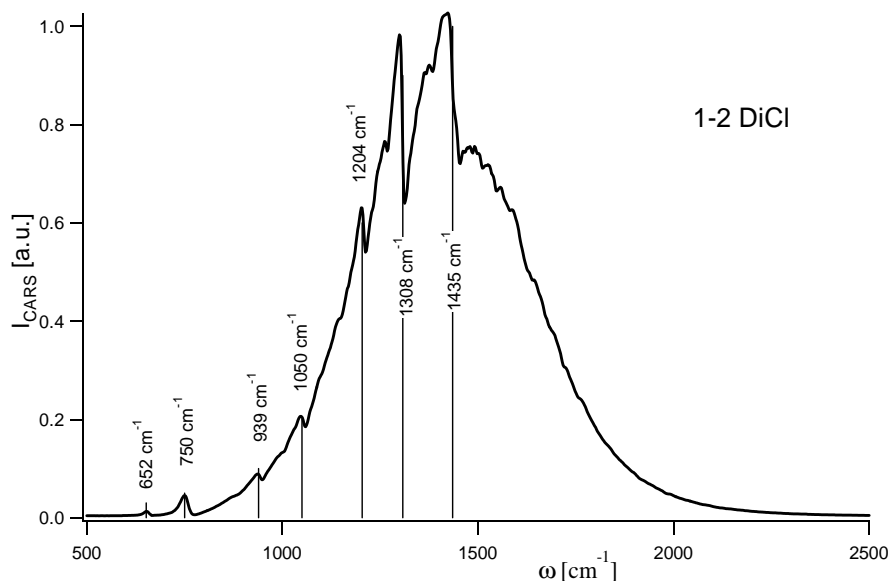


Figure 2.17: CARS spectrum of pure 1-2 dichloroethane (1-2 DiCl). With the exception of the bands at 652 cm^{-1} (45) and 750 cm^{-1} (40), all other bands have intensities smaller than 7. Furthermore, the band at 1435 cm^{-1} is due to two very close bands that cannot be resolved with a simple analysis.

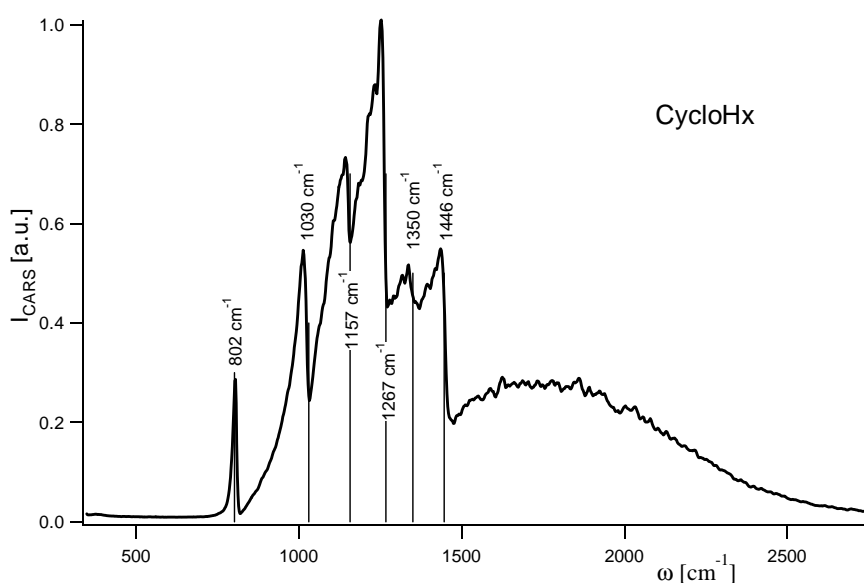


Figure 2.18: CARS spectrum of pure cyclohexane (CycloHx). The strong band at 802 cm^{-1} (90) is Lorentzian while the others at 1030 cm^{-1} (13), 1157 cm^{-1} (5.5), 1267 cm^{-1} (11), 1350 cm^{-1} (2) and 1446 cm^{-1} (10) are dispersive.

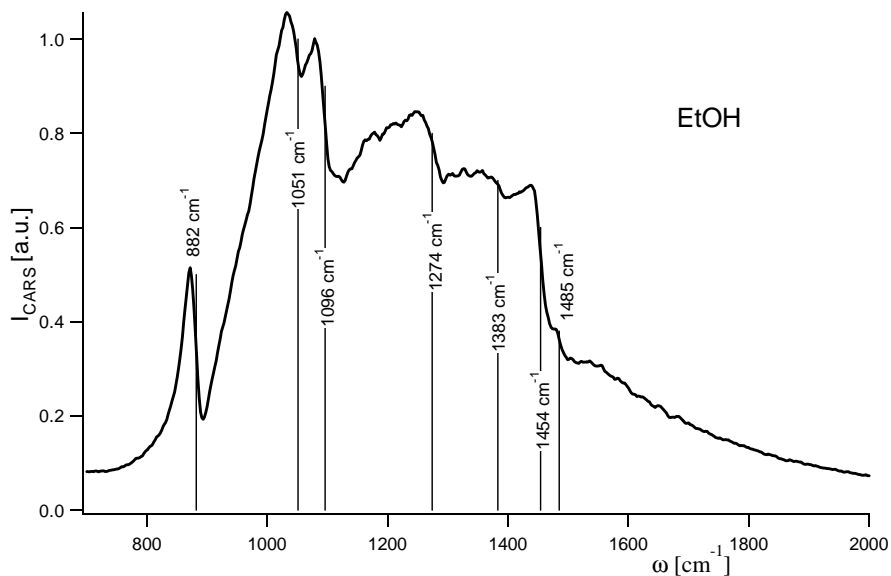


Figure 2.19: CARS spectrum of pure ethanol (EtOH). Bands are very intense and the overall nonresonant shape is highly distorted. Vibrations have the following intensities from 882 cm^{-1} to 1454 cm^{-1} : 53, 14, 14, 6, weak, 19 (broad with a shoulder at 1485).

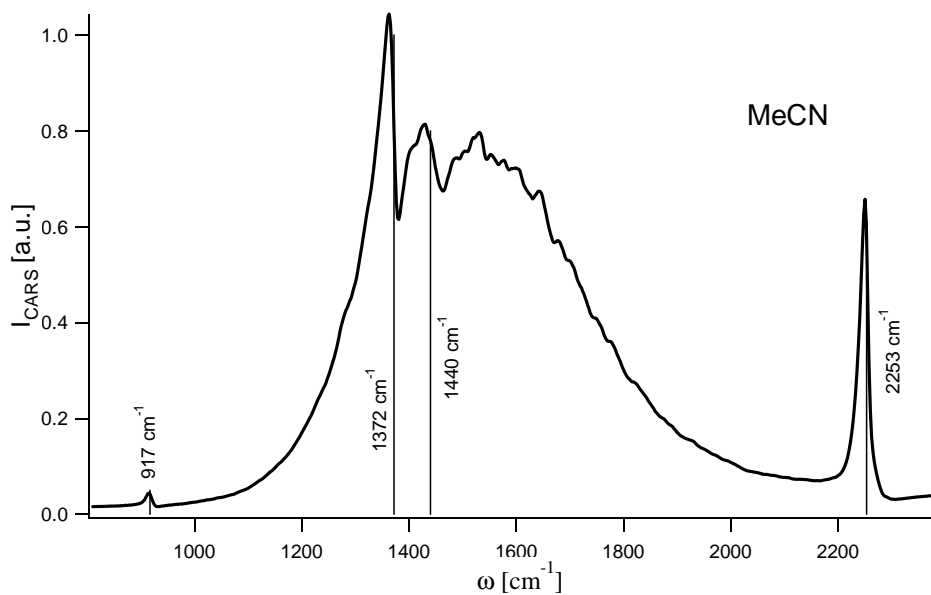


Figure 2.20: CARS spectrum of pure acetonitrile (MeCN). Only few bands are present, but that centered at 1440 cm^{-1} (weak) is broad (from 1350 to 1600 cm^{-1}). Other bands are at 917 cm^{-1} (15), 1372 cm^{-1} (3.5) and 2253 cm^{-1} (31).

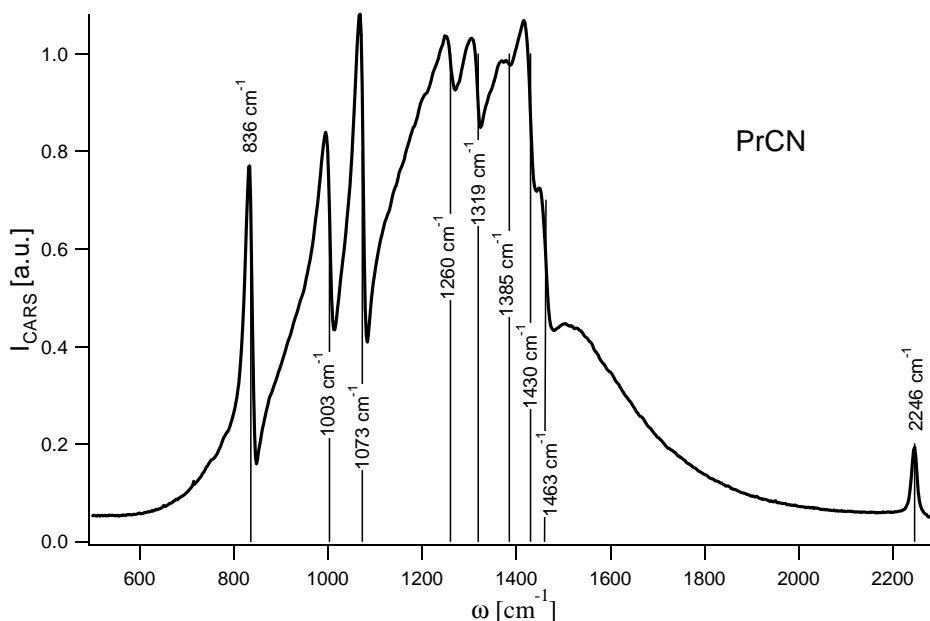


Figure 2.21: CARS spectrum of pure propionitrile (PrCN). Many bands are present below 1470 cm^{-1} : 836 cm^{-1} (9.5), 1003 cm^{-1} (4), 1073 cm^{-1} (5), 1260 cm^{-1} (weak), 1319 cm^{-1} (1.5), 1385 cm^{-1} (weak), 1430 cm^{-1} (3) and 1463 cm^{-1} (3). A last band at 2246 cm^{-1} (39) is visible. Nevertheless, the region from 1500 cm^{-1} to 2200 cm^{-1} gives a nice window without any solvent vibrations.

In order to completely characterize the solvent, equation (1.106) was used to perform a full simulation of the solvent bands and of the nonresonant electronic background. An example of such a fit is presented for pure propionitrile:

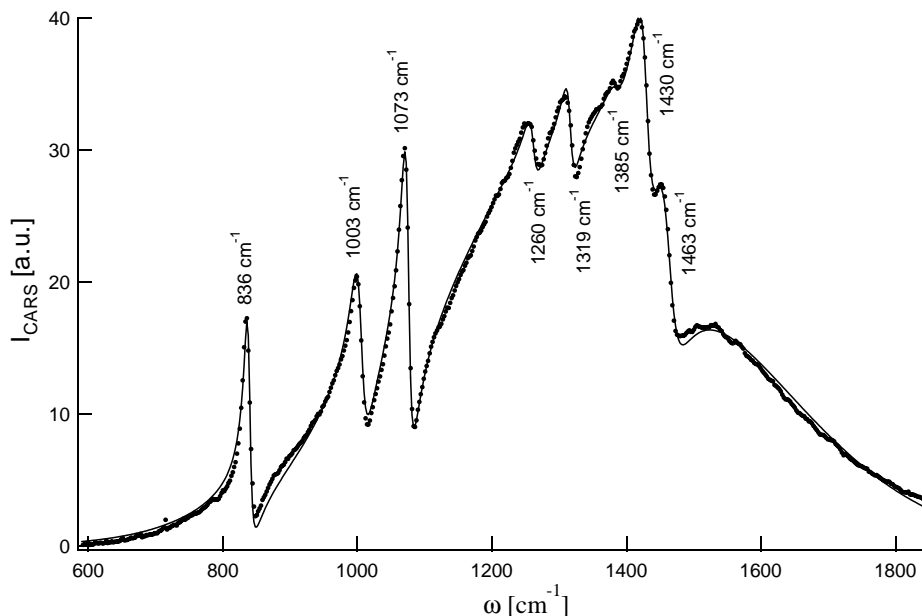


Figure 2.22: CARS spectrum of pure propionitrile (dots) and best fit (thin line) obtained with 8 vibrational modes interacting with the nonresonant electronic background.

This fitting procedure allows not only the central position of the vibration bands to be determined, but also their relative intensities. Comparison of the CARS values obtained with those from Raman spectroscopy⁵⁹ is very good in the central part of the CARS signal and slightly imprecise in the low frequency domain. It can be noticed that in Figure 2.22, this part of the fit is not optimal. This is probably due to an asymmetry in the nonresonant electronic background, which is not taken into account in the fit.

Vibration [cm^{-1}]	836	1003	1073	1260	1319	1385	1430	1463
Raman intensity	9.5	4	5	weak	1.5	weak	3	3
CARS intensity	14.7	4.8	6.3	0.88	1.2	0.3	2.7	2.7

2.3.4. Time Resolved CARS Spectroscopy of $\text{PE}^{\bullet+}$

In order to investigate intermolecular ET reactions in the condensed phase, we focused on $\text{PE}^{\bullet+}$, due to its high absorption coefficient in the wavelength domain available (see Figure 2.9). It is produced by photoinduced ET with TCNE. This very efficient electron acceptor absorbs neither at 355 nm nor in the visible and is thus suitable for this experiment. Furthermore, its anion absorbs only below 470 nm⁵⁸.

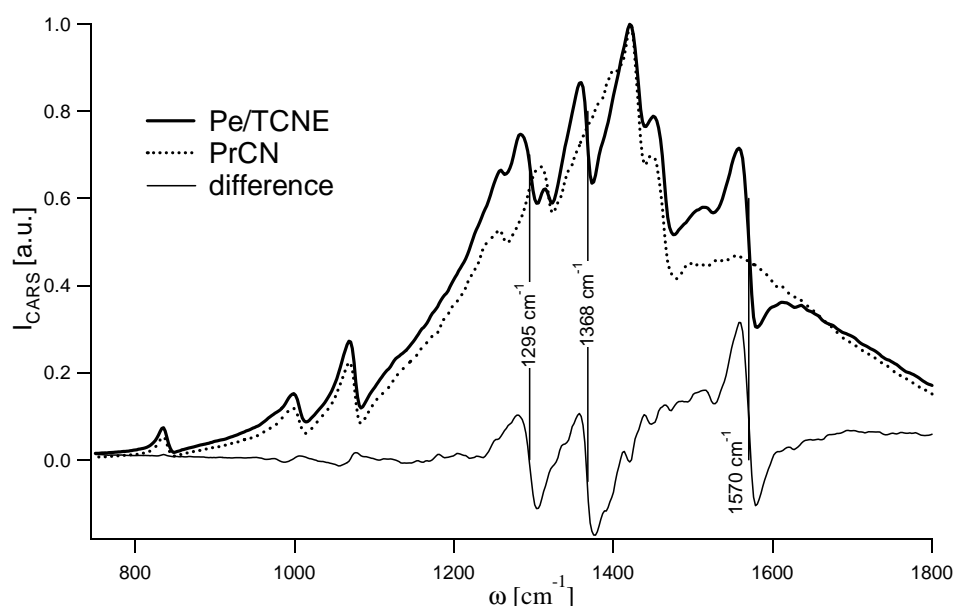


Figure 2.23: CARS spectrum of pure PrCN and of a 10^{-3}M solution of PE with 0.15M TCNE in PrCN. Difference spectrum (thin line) shows three new bands at 1295 cm^{-1} , 1368 cm^{-1} , and 1570 cm^{-1} , that can be attributed to the ground-state of the PE.

Three new bands appear by adding 10^{-3}M PE and 0.15M TCNE in PrCN. In order to determine the origin of these new bands (PE or TCNE), the same measurement was performed with a solution $3 \cdot 10^{-3}\text{M}$ of PE and 0.2M 1,2-DCB in THF. As shown in Figure 2.24, the same three new bands are present at 1295, 1368 and 1570 cm^{-1} allowing their attribution to the ground-state of

PE⁶⁰. Furthermore, no bands due to TCNE or to 1,2-DCB are visible in this spectral window.

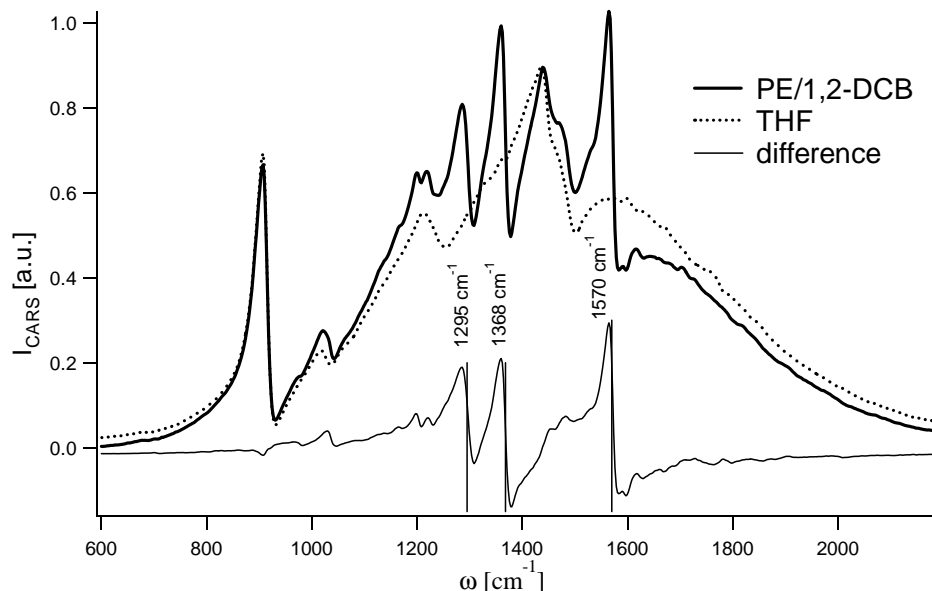


Figure 2.24: CARS spectrum obtained with pure THF and with a solution of 10^{-3}M PE and 0.2M 1,2-DCB in THF. The three new bands of the PE are visible at 1295, 1368 and 1570 cm^{-1} .

Upon irradiation with a 3 mJ UV pulse at various time delays before the CARS experiment with the PE/TCNE solution, intermolecular ET is induced, leading to the formation of $\text{PE}^{\bullet+}$ and $\text{TCNE}^{\bullet-}$. The absorption spectrum of $\text{TCNE}^{\bullet-}$ being out of the resonance domain, its contribution should be much smaller than that of $\text{PE}^{\bullet+}$. One can thus expect the band of PE to be bleached and new ones from $\text{PE}^{\bullet+}$ to be formed.

Furthermore, as the double resonance condition is only fulfilled for perylene cation, the new bands should be larger than that of its ground-state, even if its concentration is smaller.

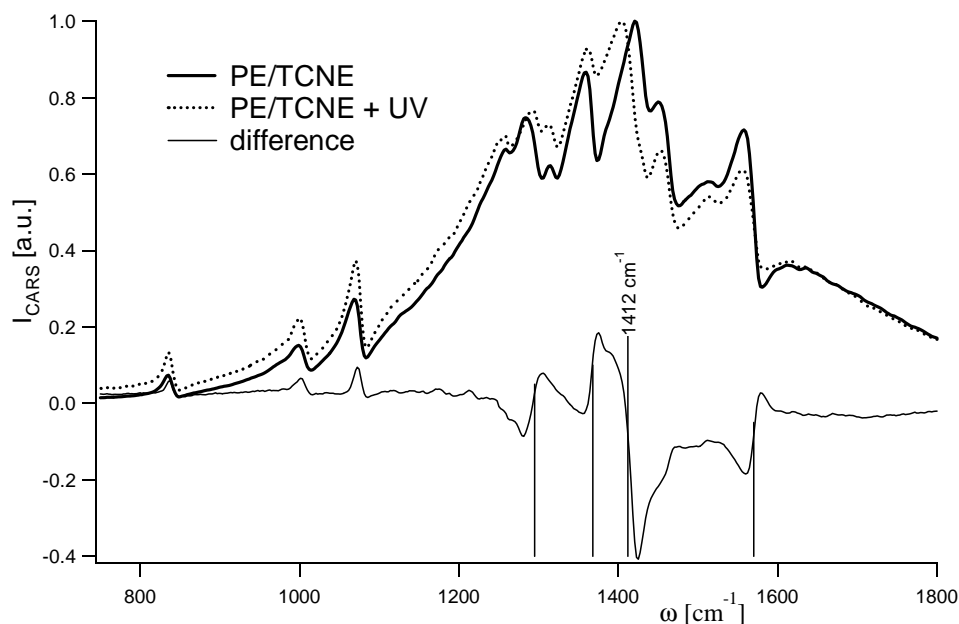


Figure 2.25: CARS spectra of a PE/TCNE solution in PrCN with and without UV excitation and difference spectrum. The UV pulse arrived 2.7 ns before the pump and Stokes pulses. The new band at 1412 cm^{-1} is assigned to the $\text{PE}^{\bullet+}$. Note that the bands of PE that is depleted, have inverse dispersive-shapes.

As expected, with actinic UV excitation, a new intense band is formed, which is assigned to a specific vibration of the radical cation of the PE.

Changing the delay between the UV pulse and the CARS experiment allows investigation of the rate constant of formation of the cation and thus of the intermolecular ET rate constant.

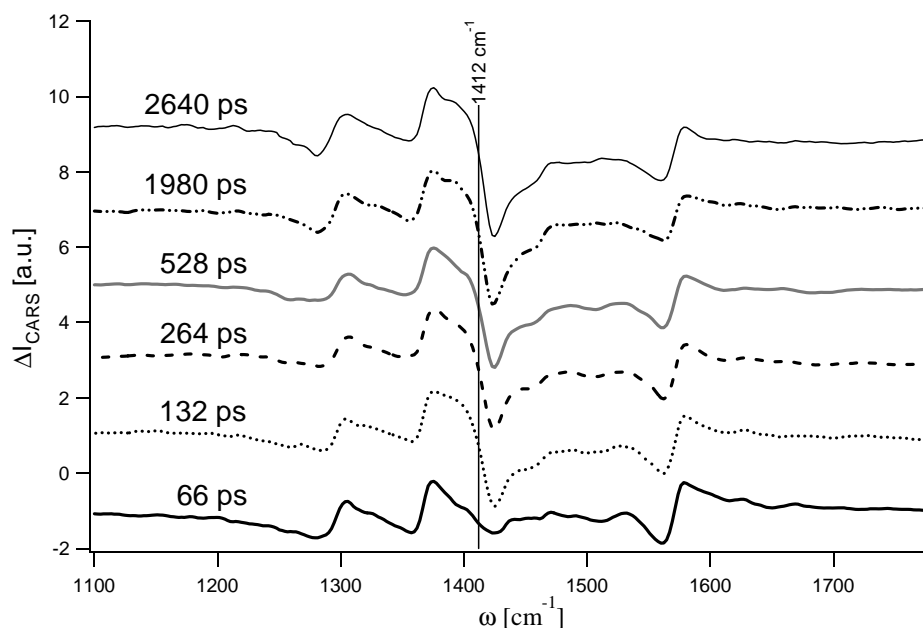


Figure 2.26: Time evolution of the difference CARS spectrum obtained with and without UV excitation. The $\text{PE}^{\bullet+}$ formation is shown by the increase of the 1412 cm^{-1} band.

In this experiment, the ET is already completely achieved after 132 ps. The rate constant can thus be estimated to be less than 100 ps.

Unfortunately, it was impossible to reproduce the above results, and therefore this time constant has to be taken with caution.

Even with newly purified (recrystallized and sublimed) PE and TCNE, this double resonance CARS signal of $\text{PE}^{\bullet+}$ was no longer achieved. Great care was taken to optimize the geometry and change the power of each beam, but this 1412 cm^{-1} band was no longer observed with this system.

When an experiment is not reproducible, one immediately thinks of an impurity problem. Nevertheless, the hypothesis of an impurity present in the PE, TCNE or the solvent is improbable as it would have need to satisfy the following conditions:

- 1) The impurity must absorb at 355 nm.
- 2) Its transient spectrum must be around 500 to 600 nm.

- 3) Its concentration has to be larger than that of $\text{PE}^{\bullet+}$.
- 4) It has to possess a vibration frequency of 1412 cm^{-1} .

The condition 1 allows to eliminate a contamination of the solvent, as the absorption spectrum of PrCN (Rathburn 200 nm grade) did not show any band above 220 nm.

Conditions 1 and 3 limits the possibility of an impurity in the PE as its ion yield with TCNE is 0.5⁵⁷. The impurity should then represent more than 40% of the total amount in order to compete with the cation. Such an impurity concentration would strongly modify the absorption spectrum in the UV, which was not observed.

The TCNE is the most probable source of problems, as it is known to slowly degrade. However, it is probably not the case, as the transient absorption spectra of the PE/TCNE in PrCN (Figure 2.9) does not show any long living species other than $\text{PE}^{\bullet+}$. Nevertheless, in order to demonstrate it, we performed the same CARS experiment with a different electron acceptor: Phthalic Anhydride (PA).

The CARS signal of a solution 10^{-3}M PE with 0.2M PA in propionitrile was measured. As shown in Figure 2.27, irradiation with a UV pulse 133 ps before the CARS experiment leads to a slight change at four frequencies: 1295 cm^{-1} , 1368 cm^{-1} , 1570 cm^{-1} and 1412 cm^{-1} . Three of them correspond to the bleaching of PE and the last one is ascribed to the formation of its radical cation.

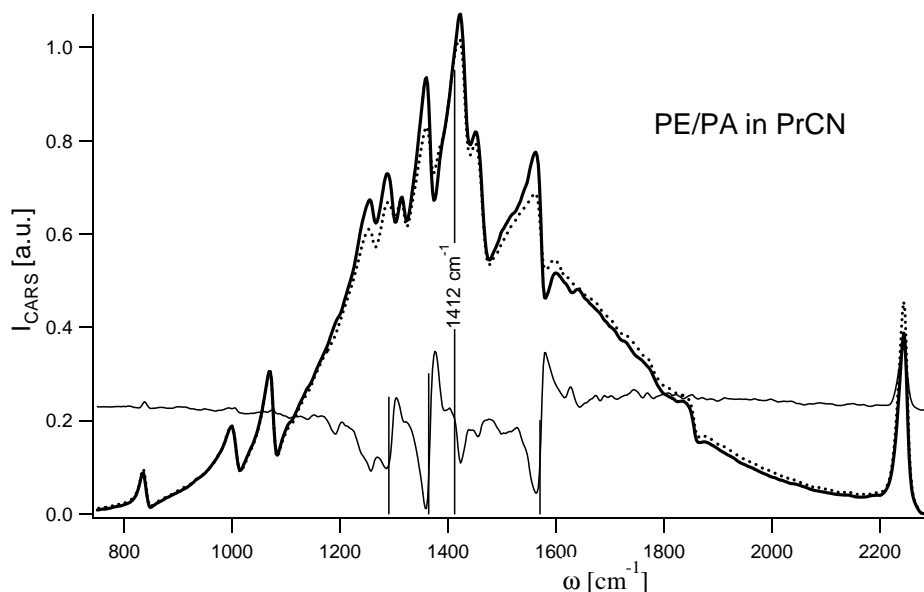


Figure 2.27: CARS spectra of a 10^{-3} M PE solution with 0.2 M PA in propionitrile with and without UV excitation and difference spectrum. It can be noticed that the 1412 cm^{-1} band is accounting for the presence of $\text{PE}^{\bullet+}$. The UV pulse arrived 133 ps before the pump and Stokes pulses.

The presence of this small band at 1412 cm^{-1} , even in absence of TCNE, eliminates the hypothesis of dirty TCNE.

Unfortunately, the signal intensity is much smaller than that obtained in the previous experiment and kinetic measurements were impossible to perform accurately.

The most probable reason for this reproducibility problem is that resonant CARS is sensitive to many parameters and especially to saturation. When intense pulses are used, the resonance signal saturates and is overwhelmed by the nonresonant contribution.

Most of the CARS experiments reported in the literature were performed with low power pulses at high repetition rate (kHz or MHz), and with single

wavelength detection^{61,62}. This allows the detector to be a high sensitivity PM tube and thus to use low power pulses in order to avoid saturation problems. It is thus probable that the band at 1412 cm^{-1} really corresponds to a PE^{*+} vibration. Unfortunately, working at 10 Hz and with a CCD camera detection implies high intensities to be used, probably leading to saturation of the resonance. The signal shown in Figure 2.25 is the proof of the feasibility of such an experiment, but the experimental conditions are very complex and hard to reproduce.

In the case of PE/PA, conditions were probably not perfect, and the signal intensity from the ion band was only partially enhanced.

It is also interesting to notice that the papers dealing with resonance CARS spectroscopy are mostly obtained with only few molecules such as 1,2-diphenylbutadiene⁶³, t-stilbene⁶³⁻⁶⁵, rhodopsine^{66,67}, β -carotene^{61,68} or retinal⁶⁹. It seems that double resonance CARS spectroscopy is only efficient with those molecules.

Such a behavior is odd, but one has to admit that, even if the basic theory of CARS is known, there are still many other nonlinear phenomena that can take place simultaneously. Competition between them should be investigated in more details by the theoretician, in order to predict the CARS behavior of a specific molecule.

It is also probable that only vibrational modes that are strongly coupled to the electronic transition can really be enhanced by double resonance conditions. This would explain the small number of molecules studied so far with this technique.

2.3.5. Conclusion

Double resonance multiplex CARS spectroscopy is a very attractive technique to investigate transient molecules through their specific vibrational modes.

In principle, CARS is an ideal technique for studying transients showing similar absorption in the UV/VIS domain. For instance exciplexes and ions pairs having different structures, they should be distinguishable through their CARS spectra.

Unfortunately, if this technique is suitable for highly concentrated species, it seems that only polyene molecules give rise to intense double resonance signals, allowing low concentration analysis to be performed.

In this work, we have observed the first CARS spectra for intermolecular electron transfer reaction between PE and two different electron acceptors. As shown in Figure 2.25, a new band at 1412 cm^{-1} has been assigned to the PE cation. Kinetic measurements could not be performed accurately, but as shown by the TG spectrum (Figure 2.9), the ion formation takes place in less than 100 ps, in complete agreement with the CARS data. Furthermore, no spectral shifts were observed in longer time domain. If ET would have produced CIP prior to LIP, a vibrational shift should have been observed⁷⁰. The direct formation of the LIP is consistent with the important free energy of the reaction ($\Delta G < -0.7\text{ eV}$)³⁴, which allows the ET to take place over a few ångströms.

Saturation problems are probably responsible for the very bad reproducibility of such experiment. Working at 10 Hz in a multiplex way, implies high intensities to be used and thus saturation problems to be important. Working with a high repetition tunable laser would probably leads to better results, as lower peak power could be used. Furthermore, a precise control of the pulses

polarization should allow the nonresonant background to be suppressed, and thus enhance the sensitivity of the technique.

On the other hand, theoreticians have still to explain why, even with optimized setup, some molecules lead to intense double resonance signal and others to very weak one. This is especially interesting as most molecules give rise to an intense resonance Raman signal. It is only then that TR²-CARS will really be a powerful, complementary technique to other spectroscopies, and become a common tool for species characterization.

3. Experiment with Unamplified fs Pulses

3.1. Introduction

As shown in the previous chapter, pulses of 25 ps duration are too long to investigate excited-state lifetime of radical ions in liquids. Measurements in boric acid³⁴ or in low temperature matrixes⁷¹ lead to values from 35 ps to 100 ps, but in the liquid phase, their lifetime has been shown to be shorter than 15 ps, our ps experiment resolution.

In order to obtain accurate values of ultrafast processes, sub-picosecond time resolution has to be achieved. For this reason, the group of Eric Vauthey acquired in 1997 a laser producing low energy pulses (nJ) of about 60 fs.

This chapter describes the interfacing of a complete fs experiment, the pulse duration measurement and of course a photophysical application in the fs time scale.

3.2. The fs Ti:sapphire Laser

Without going too deeply in the laser theory, which can be found in the literature^{72,73}, it is important to review the basic principle of ultrashort pulses production.

3.2.1. Production of fs Pulses

A linear cavity of length L only allows wave frequency multiples of $c/2L$ to oscillate. The electric field in the cavity is thus quantified, and all possible frequencies are called the longitudinal cavity modes.

Furthermore, the laser media possess a specific gain spectrum, and only photons in this spectral window can be amplified and thus lead to *Light Amplification by Stimulated Emission of Radiation (LASER)*.

Due to losses in the cavity, modes that are not amplified enough in the medium, lose intensity at each round trip and vanish.

In conclusion, for a light mode to be amplified, three conditions have to be fulfilled:

- 1) The mode must have a frequency

$$\nu = n \frac{c}{2L} \quad \text{with } n = 1, 2, 3, \dots \quad (3.1)$$

- 2) It must be in the gain spectrum of the lasing medium
- 3) Its gain has to be greater than its losses.

In the following Figure, only three modes oscillating in the cavity lead to laser output.

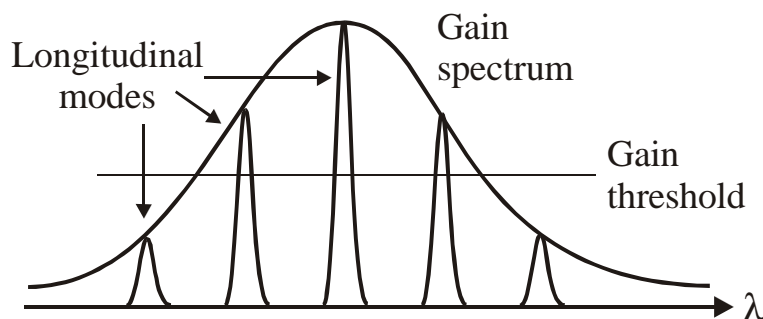


Figure 3.1: Modes oscillating in a cavity with a lasing medium. Only the three central modes satisfy the conditions for amplification.

In order to create a pulse of light, many frequencies have to interfere in phase and thus create a wavepacket.

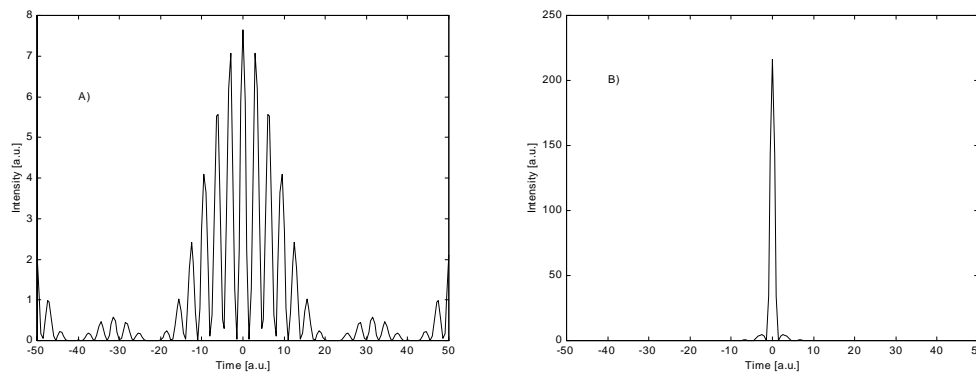


Figure 3.2: Simulation of pulse formation by increasing the number of in-phase modes (Gaussian distribution of intensity with constant frequency shift between the modes). A) With 3 modes and B) with 40 modes.

In other words, to produce ultrashort pulses one needs:

- 1) To increase the number of amplified modes in the cavity
- 2) To phase-lock them.

Amplified Modes in a Cavity

To increase the number of amplified modes in a cavity, it is possible to limit the losses, to increase the cavity length or to use broadband gain medium.

- A) Losses being usually already minimized in all lasers, this factor is not suited to shorten the pulse duration.
- B) The length of the cavity has only a small impact on the pulse duration as increasing by a factor of two is already experimentally difficult.
- C) The best way to enlarge the number of oscillating modes is to use a broadband gain medium. Working with organic dye solutions instead

of crystals was the first way to achieve fs pulses, as laser dyes possess fluorescence bands as broad as 80 nm (for R6G). Nevertheless, working with crystals is more convenient and the discovery of the Ti:sapphire properties made a real revolution in the laser world. This material possesses a gain bandwidth of 200 nm FWHM. In comparison, Nd:YAG crystal only emits over few wavenumbers.

Cavity Mode-locking

In order to obtain short pulses, the intracavity modes have to oscillate in phase. To phase-lock them, many techniques can be used:

- A) Active mode-locking: the cavity length being known, it is possible to calculate the round trip time of the light in the cavity (usually between 7 and 15 ns). It is then possible to add a fast gate in the cavity, working at the corresponding frequency (around 100 MHz), so that only one wavepacket can oscillates without being attenuated. Acousto-optic modulators are used for this purpose, as they can work at these frequencies. All wavepackets not in phase with the modulator are partially diffracted by the induced acoustic grating. This technique is used as well for ps than for fs pulses mode-locking.
- B) Passive mode-locking: for ultrashort pulses production, saturable absorbers are often used. They increase the losses in the medium by absorbing the oscillating wavelength. When a wavepacket is intense enough, its leading edge bleaches the saturable dye, and the main part of the pulse can go through with low losses. All the light modes that are not in phase with the wavepacket are too weak to bleach the dye, and thus vanish.

For Ti:sapphire fs pulses, passive mode-locking is performed with a slit inserted in the cavity. This slit increases the losses, and cw lasing is more difficult. By perturbing the laser cavity, its length changes slightly, and a few modes begin to oscillate in phase. This initial wavepacket thus formed has a high peak power and induces a nonlinear process called Self Focusing (SF) in the Ti:sapphire crystal. The refractive index of a nonlinear medium being sensitive to the light intensity, a spatial Gaussian distribution of light intensity induces refractive index distribution similar to that of a converging lens. This is known as Kerr lensing.

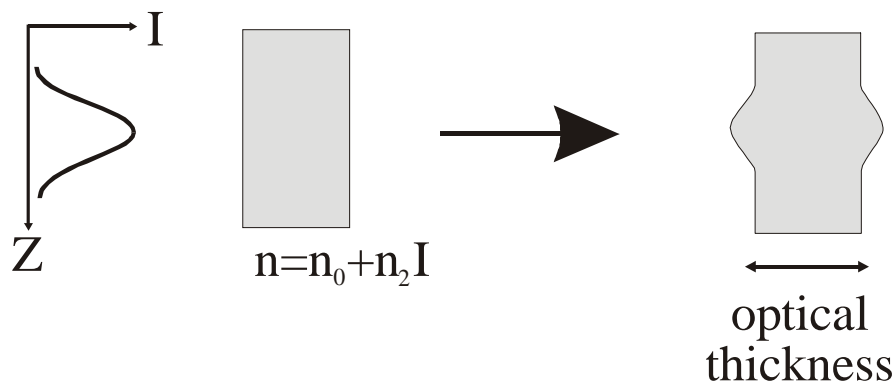


Figure 3.3: Principle of a Kerr lens. In nonlinear media, the refractive index depends on the light intensity and thus a Gaussian pulse induces changes in the optical thickness of the sample. A Kerr lens is produced.

The wavepacket being focused, the beam radius becomes smaller, and the losses induced by the slit decreases. At each round trip, the wavepacket is amplified and is thus more focused. Finally, the fs wavepacket can go through the slit with very few losses.

In the ps Nd:YAG laser described in chapter 2.3.2, mode-locking is achieved through combination of an acousto-optic modulator (active) and of a saturable absorber (passive).

In our Ti:sapphire fs laser, mode-locking is a combination of active (acousto-optic modulator) and passive (Kerr lens) mode-locking.

3.2.2. Characteristics

The laser used in this work is a TsunamiTM Ti:sapphire provided by Spectra PhysicsTM. It is pumped by the frequency doubled output of a 5W cw Nd:YVO₄ laser also from Spectra PhysicsTM (MilleniaTM V). The latter is pumped by two arrays of laser diodes providing 40 W of cw light around 816 nm. Cooling is achieved by an internal water circuit with a air/water heat exchanger. A laboratory with efficient air-conditioning is thus necessary to keep the room temperature constant between 19 and 20°C.

The minimal pulse duration is 60 fs, but it can be varied by changing the slit size in the cavity, up to hundred fs.

The output power is 1W, and as the laser is working at 82 MHz, this corresponds to an energy per pulse of 12.2 nJ, produced every 12.2 ns.

The peak power obtained with the minimal pulse duration is 0.25 MW.

The central wavelength is 800 nm, but it can be easily tuned from 750 nm (0.4W) to 840 nm (0.4W), by changing the slit position.

3.3. Pulse Duration Measurements

In order to perform fs measurements, one needs to be sure of the duration of the pulses used.

For pulses longer than 500 ps, combination of a fast photodiode detector and a modern oscilloscope allows a direct measurement of the pulse duration. With shorter pulses, pure optical methods have to be used, as the response of the electronic detectors is too slow.

3.3.1. Fourier-Transform-Limited Pulses

According to the Heisenberg uncertainty principle, it is not possible to know simultaneously the frequency and the pulse duration of a wavepacket, with infinite precision.

$$\delta t \cdot \delta E \geq \frac{1}{2} \hbar \quad (3.2)$$

$$\delta t \cdot \delta \omega \geq \frac{1}{2} \quad (3.3)$$

where δ represents the half width of the Gaussian profile.

This can also be understood by considering that a wavepacket is formed by in-phase interaction of waves of different frequencies. In other words, a short pulse has a broad spectrum.

One has to remember that the opposite is not true, as broadband pulses have not to be short. For instance, switching on and off a lamp does not give fs pulses even if the spectrum is very broad (white light).

It is nevertheless possible to find the shortest limit of the pulse duration by studying its spectrum. If the pulse reaches this limit, it is called "Fourier-transform-limited" ⁷⁴.

An easy way to quantify the width of a spectrum is to measure its Full Width at Half Maximum (FWHM). Equation (3.3) can then be rewritten as:

$$\Delta t \cdot \Delta \nu \geq K \quad (3.4)$$

where Δt and $\Delta \nu$ are the temporal and spectral widths at half maximum. K depends on the shape of the pulse. For a Gaussian pulse, $K = 0.441$ and for a squared hyperbolic secant, $K = 0.315$.

FWHM spectrum [nm]	0.02	12	14	16	18	100
Gaussian pulse duration [fs]	47000	78	67	59	52	9.4
Sech ² pulse duration [fs]	34000	56	48	42	37	6.7

Table 3.1: Fourier-transform-limited pulse durations for different spectral bandwidths around 800 nm, assuming a Gaussian or a squared hyperbolic secant pulse shape.

As shown in table Table 3.1, the assumption on the pulse shape has a great influence on the calculated pulse duration. For instance a spectrum of 14 nm FWHM centered at 800 nm, leads to a Fourier-transform-limited pulse duration between 67 and 48 fs, depending on the pulse shape used.

Furthermore, the central wavelength is also important in the pulse duration calculation. For a given pulse duration, the corresponding spectrum width can be calculated with:

$$\Delta \lambda = 2 \cdot \left(\lambda - \frac{c}{\frac{c}{\lambda} + \frac{1}{2} \cdot \pi \cdot \Delta t} \right) \quad (3.5)$$

where λ is the central wavelength, c the speed of light and Δt the pulse duration. For instance, assuming a sech² pulse shape, a 50 fs duration has the following FWHM spectrum for the given central wavelength:

Central wavelength [nm]	760	780	800	820	840
FWHM spectrum [nm]	12.2	12.8	13.5	14.1	14.8

Table 3.2: Fourier-transform-limited pulse bandwidths (FWHM) for different central wavelengths, assuming a squared hyperbolic secant pulse shape.

3.3.2. Autocorrelation

A second way to determine the pulse duration, is the measure of the intensity autocorrelation function. The key idea is to duplicate the laser pulse, and time delay one copy relative to the other. Looking at their interference allows information about the pulse duration to be extracted.

Second order autocorrelation can be easily achieved by choosing a detector that is only sensitive to two-photon processes. The cheapest way is to use a Light Emitting Diode (LED) of band gap greater than the photon energy^{75,76}. In this case the two-photon process, corresponding to the overlap of the two time delayed pulses, lead to an increase of the observed voltage. Pulse duration can be directly extracted, assuming a known pulse shape.

Performing a collinear recombination of the two electric fields leads to an interference pattern, unless the sweeping of the delay is faster than the detection time constant. In the latter case, the autocorrelation analysis is easier to perform.

As in the case of Fourier transform of the spectrum, the pulse shape has to be assumed and influences strongly the results.

For instance, FWHM pulse duration (Δt) can be calculated from the FWHM $\Delta\tau$ of an intensity autocorrelation trace:

$$\Delta t = \Delta\tau / 1.414 \quad \text{for a Gaussian pulse shape} \quad (3.6)$$

$$\Delta t = \Delta\tau / 1.54 \quad \text{for an squared hyperbolic secant pulse shape} \quad (3.7)$$

Another important point to mention is that an autocorrelation function is always symmetrical, even if the pulses are asymmetric. It can thus not be used for pulse shape characterization.

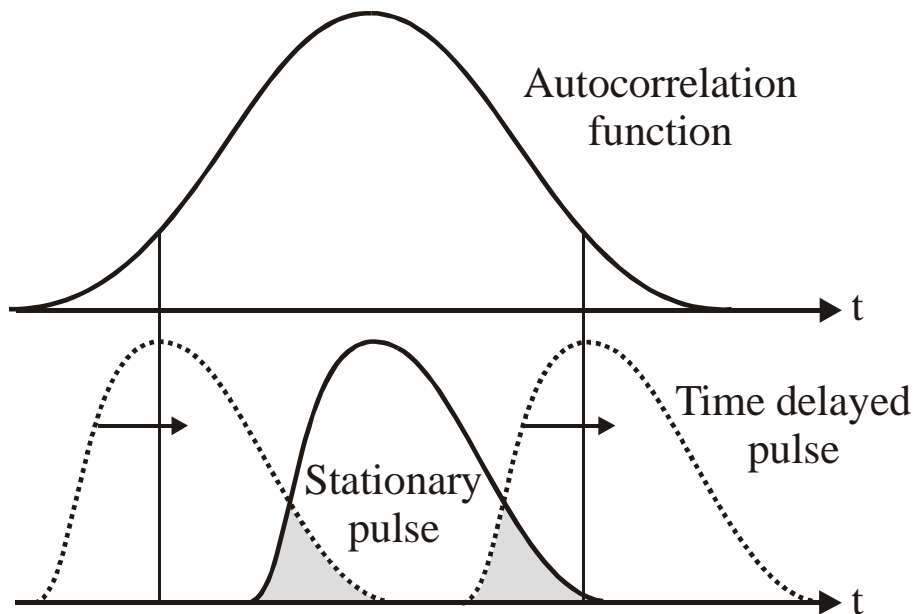


Figure 3.4: Symmetrical autocorrelation trace produced by interaction of two time delayed portions of an unsymmetric pulse.

Setup

In order to build up an autocorrelator, one needs a fast scanning translation stage. A loudspeaker is a cheap and efficient way to achieve this goal.

Mounting a mirror right on the middle of the membrane and feeding the loudspeaker with triangular electric signal, allows good linearity of translation to be achieved over 0.1 mm, corresponding to an optical delay of 600 fs.

As a detector, a simple LED emitting above 700 nm can be used. Two-photon absorption is necessary for a current to be generated, and thus second order autocorrelation is readily measured. Experimentally, one needs to eliminate the polymeric front part of the diode to allow a good focalization of the laser pulses on the very small emitting zone.

As the laser operates at 82 MHz, a 70-80 Hz oscillation of the loudspeaker membrane gives a continuous signal that can be recorded on an oscilloscope or by a computer acquisition board.

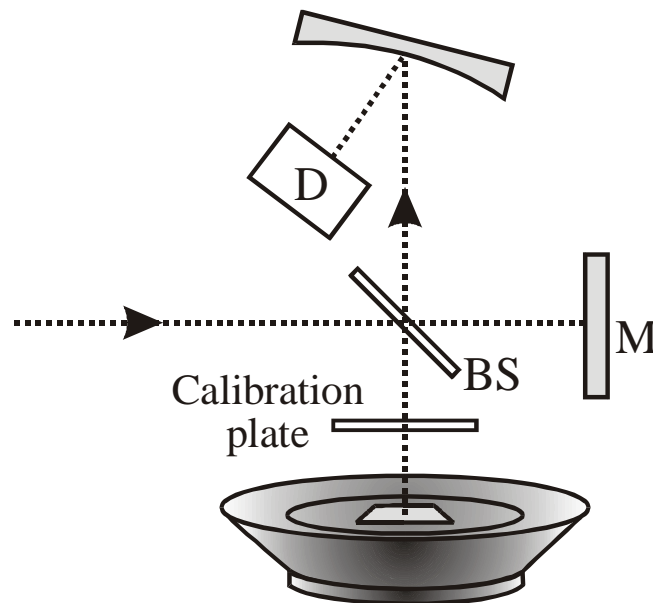


Figure 3.5: Scheme of an autocorrelator formed by a loudspeaker and a LED as a nonlinear medium and detector (D). The beamsplitter (BS) has to be as thin as possible in order to limit pulse chirping. Time calibration is achieved by removing the calibration plate.

Results

As described previously, the shortest pulse duration is achieved by increasing the slit size in the cavity. It is possible to reach pulses spectrum of FWHM as large as 14 to 16 nm. Further increase of the intra-cavity slit eliminates its mode-locking function, and cw light is produced.

Note that the pulse spectrum is measured by a diode array placed after a large slit monochromator. The reading sweeping leads to a continuous trace on an analogic oscilloscope. The calibration of the wavelength axis is performed by changing the central value of the monochromator.

Pulse duration obtained by Fourier transform of the spectrum:

from 60 to 70 fs if Gaussian shape is assumed

from 40 to 50 fs for squared hyperbolic secant shape

Second order autocorrelation trace of such pulse is shown in Figure 3.6.

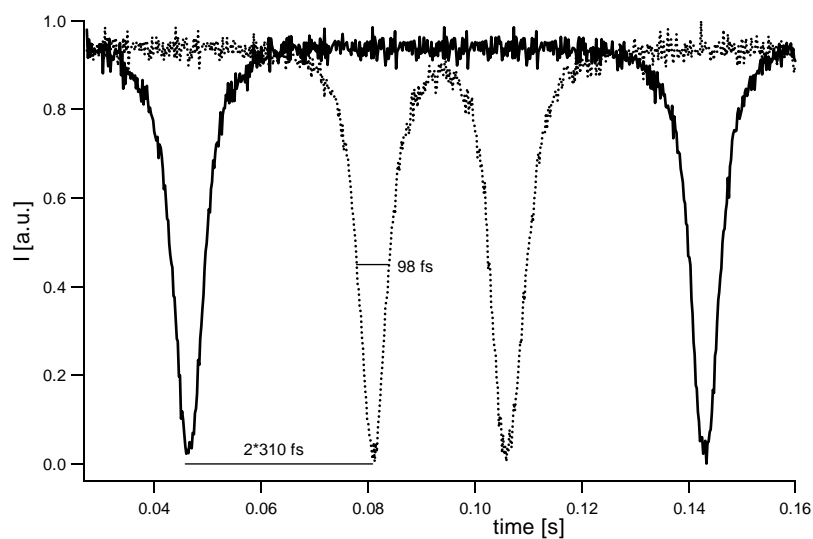


Figure 3.6: Autocorrelation trace of a Gaussian pulse of 69 fs (98/1.414) obtained with (dots) and without (continuous line) a 310 fs calibration window.

Its FWHM is of 98 fs, leading to pulses duration of:

$$98/1.414 = 69 \text{ fs if Gaussian shape is assumed}$$

$$98/1.54 = 64 \text{ fs for squared hyperbolic secant shape}$$

As long as the pulse shape is not known, the pulse duration cannot be determined precisely. More complicated methods such as Frequency-Resolved Optical Gating (FROG)⁷⁷ or Spectral Phase Interferometry for Direct Electric-field Reconstruction (SPIDER)⁷⁸ gives information on the amplitude and the phase of the pulse, allowing complete pulse characterization to be performed. Nevertheless, for our purpose it is sufficient to have an approximate value of the pulse duration, and we can assume the pulses to have minimal duration of 65 to 70 fs.

3.4. Interfacing of the fs Experiment

In order to perform a fully automated experiment, interfacing between the mechanical and electronic devices and the computers has to be achieved. For instance, the translation stage must be computer controlled in order to ensure a good reproducibility of the measurements. Furthermore, detection parameters such as amplification, acquisition time and averaging level have to be easily accessible. This is achieved by the programs, written in Fortran and Pascal, and the specific interfacing described in this chapter.

3.4.1. Real Time Measurements

As our laser produces pulses every 12.2 ns, we first build up a real time experiment. By real time, one means that the acquisition is made with a time axis in seconds, that has to be converted in fs by mean of the calibrated speed of the delay line.

This kind of measurement is easy to perform, as both computers (the one that controls the delay line and the one that makes the acquisition) can work separately. A trigger pulse is necessary for both to begin simultaneously.

3.4.2. Computer Controlled Delay Line

To perform a fs-experiment, a μm -precision delay line has to be used. The 25 mm translation stages from Micro Control™ are optimal for this purpose as the translation motion is achieved by the rotation of a screw. New Focus™ motorized screws have very small thread, and one complete turn leads to a translation of 320 μm , corresponding to a delay of 2.12 ps (controlled with a μm caliber over more than 10 rotations).

These screws can be controlled by a multi-axis picomotor driver (model 8610 from New Focus™), allowing up to 8 three-axis devices to be analogically (remote) or digitally (computer) controlled. The digital command needs 12000 pulses to complete one screw turn, allowing a maximal theoretical resolution of 0.2 fs per step.

For each step, the CTM-05 board from Metrabyte™ mounted in the controlling computer (Compaq™ 486 DX2 prolinea) has to send a 1 ms TTL pulse to the delay controller. This is achieved by a Fortran program, using


```

03      nrdl=int(acp(2))                                ! acquisition length in steps
        continue
        write(*,30) acp(2)
        write(*,40) acp(3)
        write(*,52) ic
        write(*,*)'*****'
30      format(' 1) length of one scan [steps]:      ',f10.1)      ! displayed on the screen
40      format(' 2) init. pos. optical delay [mm]:  ',f10.2)      ! displayed on the screen
52      format(' 3) number of scans:                ',i5)         ! displayed on the screen
        ix=0
        write(*,*)'to change a parameter, just strike his #'      ! displayed on the screen
        write(*,*)'to keep the values unchanged, strike "enter"'  ! displayed on the screen
        read(*,120) ix
120     format(i1)
60     format(i5)
70     format(f10.5)
        if(ix.ne.0) then
            if(ix.eq.1) then
                write(*,*)' length [steps]'          ! changing the acquisition length
                read(*,60) nrdl
                acp(2)=float(nrdl)
            endif
            if(ix.eq.2) then
                write(*,*)' init. pos. [steps]'      ! changing the initial position
                read(*,70) acp(3)
            endif
            if(ix.eq.3) then
                write(*,*)' number of scan '        ! changing the number of scans
                read(*,60) ic
                acp(5)=float(ic)
            endif
            call clsc
            goto 3
        else
            goto 2
        endif
2      continue
        open(1,file='param.txt',status='unknown',access='sequential',
            +form='formatted')
        do 4 i=1,6
            write(1,100) acp(i)                      ! write the parameter in a file
4      continue
100     format(1x,f10.1)
        close(1)
        nstep=acp(1)+1                                ! send the values in the parameters
        rdl=acp(2)
        rlo=acp(3)*10
        avlev=ib
        kscans=ic
        cor=acp(6)
end

```

Once the parameters have been entered, the program calculates the number of steps needed to reach the final position.

```

subroutine movto(rmm)
  $include:'tg2.fcm'
  integer*4 ithnew,istep
  ithnew=int4(rmm)
  istep=(ithnew-itheta)           ! compare the actual position with the final one.
  call move(istep)
end

```

It is now ready to start the acquisition. In the 'move' procedure, the program determines the direction of the displacement (up or down), and generates, through the acquisition board, the TTL pulses. Note that prior to the 'move' subroutine, a TTL-trigger pulse is sent to the acquisition computer (not shown).

```

subroutine move(istep)
  $include:'tg2.fcm'
  integer*4 istep, denomi
  character erase*5, pos1*8
  erase='\033[2j'c
  pos1='\033[1;27h'c
  if(istep.eq.0) then
    goto 136
  endif
  if(istep.gt.0) then           ! prepare up direction motion
    call up
    isgn=1
    corrup=1.05
    istepc=(int4(istep*corrup))
  endif
  if(istep.lt.0) then         ! prepare down direction motion
    call down
    isgn=-1
    corrup=1
    istepc=abs(istep)
  endif
  istep=abs(istep)
  call clsc
  if (istepc.lt.250) then
    denomi=10
  else
    if (istepc.lt.2500) then denomi=100
    else denomi=1000
    endif
  endif
  do 134 i=1,istepc           ! begin of the steps loop
    i2=nint(i/corrupt)
    if ((i2/denomi).ne.((i2+1)/denomi)) then   ! write the evolution of the acquisition
      write (*,*) i2+1
    endif
    do 135 j=1,100           ! 100 TTL pulses for each step
      call upbit(2)         ! change state of output 2
      call qwait(5)        ! wait 1 ms
    enddo
  enddo

```

```
        call dbit(2)           ! close the pulse by changing the state of output 2
        if (isgn.eq.-1) then
            if (inbit(0).eq.1) then
                itheta=0       ! check if TZD indicates position 0
                goto 136
            endif
        endif
        call qwait(20)        ! make a ms stop between each TTL pulses
135     continue
134     continue
        itheta=itheta+(isgn*istep) ! calculate the new actual position
136     end
```

Many other options have been programmed, such as a mouse control to modify the delay position. It would take too much space to rewrite the integrality of the program (more than 20 pages) and only the main points have been described here.

In our experiment, the time needed to perform one screw rotation is 18.3 seconds. As it corresponds to a delay of 2.12 ps, the time axis conversion is of 116 fs/sec.

Linearity of the Translation Stage

In a real time measurement, one has to be sure that the delay line is perfectly linear. If not, the acquisition time axis is wrong, and data analysis is not possible.

The time needed for one step to be accomplished can be assumed to be constant, as it is defined by the computer. The control of the linearity can thus be performed by controlling the number of steps needed for each screw rotation.

The following results were obtained:

Screw turns	1	2	3	4	5	6	7
# of steps	128	127	126	125	122	120	120

Screw turns	8	9	10	11	12	13	14
# of steps	119	119	119	119	120	120	122

The delay is highly linear over height screw rotations (turn 6 to 13), corresponding to an optical delay of 17 ps. Over longer range, nonlinearity is present, and acquisitions have to be considered with at least 10% intrinsic error.

A second way to check the linearity of the delay line is to perform twice a similar measurement, but once with a known induced delay. For instance addition of a quartz calibration plate of known thickness, allows to delay the probe beam by a known amount. We used a 310 fs calibration plate from Spectra Physics™ to induce the delay, and check the linearity of our delay line.

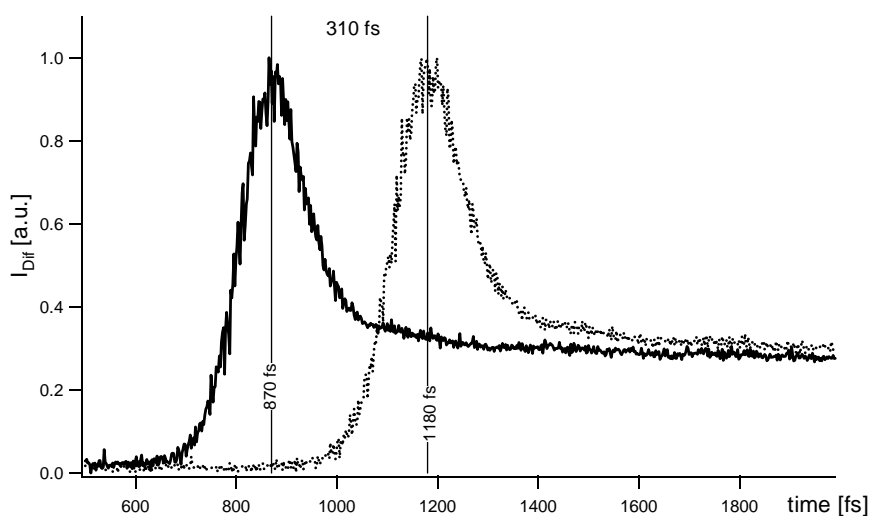


Figure 3.7: Calibration of the delay line by performing a similar measurement with and without a known calibration window of 310 fs.

As a conclusion, real time measurement can be performed over 15 ps with a very good precision. Longer acquisition should be avoided.

Usually translation stages possess springs to force the stage to stay against the screw. Unfortunately, the strength of the spring is not linear, and the probability of screw-slipping of the piezo motor is not constant over the delay line. In order to avoid this problem, we placed the delay line, without springs, vertically. The force used in this case is the gravity, which is independent of the position of the translation stage.

Nevertheless, it is clear that it is more difficult for the screw to push the mirrors up than down, and the screw sliding is different for up and down motions. In order to ensure good measurements, we only acquired data during the up motion, and we used a Turn Zero Detector (TZD) to ensure the correct back position of the translation stage.

Turn Zero Detector

The key idea is to place a reference on the screw, and detect it at each turn by a magnetic detector from SyrelecTM/CrouzetTM (D in Figure 3.8). The TZD increments a counter at each up-turn, and decreases it when down motion is performed. When the zero position is reached, the TZD produces a pulse that stops the down motion of the delay line.

The Figure 3.8 shown how the TZD works with a computer controlled delay line. The computer sends TTL pulses to the screw controller, which transforms them in high voltage peaks. An up or down pulse is also sent to the TZD, so that it can increase or decrease its counter, according to pulses from the magnetic detector. Finally, when the turn zero is reached during a down

motion, the TZD stops the computer, and thus the screw controller. This system ensures that each acquisition begins exactly at the same position.

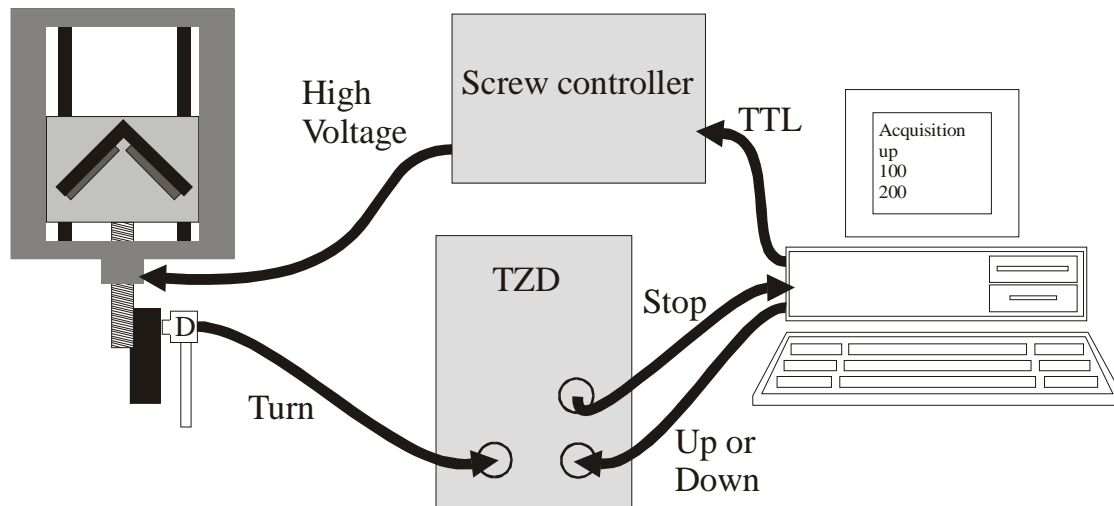


Figure 3.8: Scheme of a computer controlled delay line, using a Turn Zero Detector for higher acquisition reproducibility. Information flow is represented by arrows.

To take the TZD stop pulse into account, the program is modified for the down motion in the following way:

- 1) The down step loop has to be longer (by $rTZD = 1.1$), in order to ensure that TDZ signal is the only way to end down motion.
- 2) The TDZ state has to be checked to exit the loop.

```

do 134 i=1,istepc*rTZD                                ! rTZD = 1 for up, but 1.1 for down
  i2=nint(i/corrupt)
  if ((i2/denomi).ne.((i2+1)/denomi)) then             ! write the evolution of the acquisition
    write (*,*) i2+1
  endif
  do 135 j=1,100                                       ! 100 pulse for each step
    if (isgn.eq.-1) then                                ! down motion
      call upbit(2)                                    ! produce pulses for
      call qwait(5)                                    ! the delay controller
      call dbit(2)
      if (inbit(0).eq.1) then                           ! Test if TZD stop state is produced
        call qwait(1)                                  ! during down motion
        if (inbit(0).eq.1) then
          itheta=0
          goto 136                                     ! if stop pulse is present, the loop ends
        endif
      endif
    endif
  else ...

```

3.4.3. Data Acquisition

In a real time measurement, the acquisition computer is almost independent of the delay line controller. The only common part is a trigger pulse produced by the delay computer at the beginning of the translation stage motion. Of course, the acquisition parameters, such as the number of steps and scans, have to be consistent for both computers.

Acquisition Board

As described previously, a 2 ps acquisition takes more than 17 seconds. Thus, the acquisition board has not to have a fast response. For this reason, an acquisition 12-bit A/D board Axiom™ AX 5210 is sufficient.

This board possesses 16 analogic inputs, 8 digital inputs and 8 digital outputs. Its maximal working frequency is 30 kHz in analogic mode, as A/D conversion has to be performed. This allows a theoretical resolution for the experiment of fractions of fs. Experimentally, time loss in the program loops limits this acquisition frequency to 1 kHz.

For real time measurement, even a simple acquisition board is sufficient, as only two inputs are needed, with time resolution in the 100 ms range (≈ 10 fs resolution).

The vertical resolution of the Axiom™ board is of 4096 points for a ± 5 V input range. The card gain can be increased up to 16, in order to achieve a maximal resolution of 0.15 mV per point. The signal being usually greater than 100 mV, a vertical resolution above 700 points is achieved.

The Axiom™ board can be computer controlled, by mean of a set of compiled procedure given with the board⁷⁹. The acquisition frequency, the gain and the number of channels read, can be easily adapted.

Program

The acquisition program is written in Turbo Pascal™ version 5.5.

As the entire program takes more than 12 pages, only key parts are discussed below.

Parameters

A fundamental difference with the delay-controlling program arises from the fact that the speed of the acquisition card is defined in frequency.

As a consequence the number of points stored is kept fixed, and the acquisition time is adapted by changing the acquisition frequency.

For instance, performing a 5 ps measurement takes around 40 seconds, and thus for a 1000 points time resolution, the frequency has to be set to 25 Hz.

In practice, one first defines the acquisition frequency and adapts the time of the controlling delay. For convenience, both programs indicate in seconds the acquisition time needed for the experiment to be performed. One only has to ensure that the delay moves during all the acquisition time.

Parameters, saved in a text file, are separated in two categories:

- 1) Conventional parameters. These parameters have to be adapted for each experiment. They include the amplification *gain factor* of the acquisition card, the *acquisition frequency*, the *number of scans* averaged and the minimal *spike height* to be withdrawn.

- 2) Advanced parameters. They should normally not be changed as they allow compatibility with the specific computer. Only the *zoom* and *number of steps* (usually set to 1000 points) could be modified, if the signal is too weak or if the acquisition resolution has to be changed. Note that the *zoom* parameter does not improve the vertical resolution, but only amplify the signal display.

```

procedure param;                                {read and rewrite parameters }
type p=array[1..10] of integer;                 {from the text file: param.spi}
var
  p_array: p;
  i, rep2, rep3: integer;
  k: text;
begin
  repeat
    assign(k, 'param.spi');
    reset(k);
    for i:=1 to 10 do
      read(k, p_array[i]);                       {read the parameter from the file}
    close(k);
    clrscr;
    writeln('      parameters');
    writeln;
    writeln('1) gain factor          : ', p_array[1]);
    write('2) acquisition frequency [hz]  : ', p_array[2]);           {convert the acquisition}
    writeln('  acquisition time [s] = ', p_array[6]/p_array[2]:4:1);   {frequency in seconds}
    writeln('3) number of scans          : ', p_array[3]);
    writeln('4) spike height [full screen=4000]: ', p_array[4]);
    writeln;
    writeln('5) advanced parameters ');
    writeln;
    writeln('0) quit  ');
    writeln;
    write('to change a parameters, type its number : ');
    readln(rep2);
    writeln;
    case rep2 of
      1: begin                                     {change the gain}
          write('gain factor (1 (=10V), 2 (=5V), 4 (=2,5V), 8 (=1,25V), 16 (=0.625V)) : ');
          readln(p_array[1]);
        end;
      2: begin                                     {change the frequency}
          write('acquisition frequency in Hz (1-300): ');
          readln(p_array[2]);
        end;
      3: begin                                     {change the # of scans}
          write('number of scans : ');
          readln(p_array[3]);
        end;
      4: begin                                     {change the spike height}
          write('spike height [full screen = 4040] : ');
    end;
  end;
end;

```

```

        readln(p_array[4]);
    end;
5: begin
    repeat
        clrscr;
        writeln('    advanced parameters');
        writeln;
        writeln('1) number of steps           : ',p_array[6]);
        writeln('2) fs per sec [116 steps = 2.12 ps = 18.3 s] : ',p_array[7]);
        writeln;
        writeln('3) sign of signal [1 = positive]');
        writeln('    [2 = negative]');
        writeln('    [3 = both   ]           : ',p_array[8]);
        writeln;
        writeln('4) number of adc conversion per second   : ',p_array[9]);
        writeln;
        writeln('5) axis zoom [1 to 16]                 : ',p_array[10]);
        writeln;
        writeln('0) quit   ');
        writeln;
        write('to change a parameters, type its number : ');
        readln(rep3);
        writeln;
        case rep3 of
            1: begin
                    { change the # of steps }
                    write('number of steps [max:1000] : ');
                    readln(p_array[6]);
                end;
            2: begin
                    { change the time conversion factor }
                    write('fs per sec [old=116] : ');
                    readln(p_array[7]);
                end;
            3: begin
                    { change the signal type }
                    write('sign of input signal [1=+, 2=-, 3=both] : ');
                    readln(p_array[8]);
                end;
            4: begin
                    { change the computer speed }
                    write('number of adc conversion per second [old=3050]: ');
                    readln(p_array[9]);
                end;
            5: begin
                    { amplify graphically the signal }
                    write('axis zoom [full axis = 1] : ');
                    readln(p_array[10]);
                end;
        end;
        until rep3=0;
    end;
end;
assign(k,'param.spi');
rewrite(k);
for i:=1 to 10 do
    writeln(k, p_array[i]);
close(k);
gain:=p_array[1];
frequenc:=p_array[2];
scans:=p_array[3];
spike:=p_array[4];
steps:=p_array[6];
fs_s:=p_array[7];

```

```

    sign:=p_array[8];
    adc_freq:=p_array[9];
    zoom:=p_array[10];
until rep2=0;
end;

```

Oscilloscope mode

When looking for a signal, it is convenient to have a continuous display during the optimization. For this purpose an "oscilloscope mode" of the acquisition board has been developed. This program allows a continuous display of the DC signal from the PM tube, with the amplification parameter described above. It is thus possible to optimize the signal by slightly changing the delay by hand. Once the signal is optimized, one only needs to turn to acquisition mode to acquire the data.

```

procedure real_time;                                     {oscilloscope mode}
var
    trash:char;
    i,j:integer;
    ok2:boolean;
begin
    channel(start_ch);
    fun := set_timer;           {set timer rate = 1M/(divisor1 * divisor2) }
    dio[1] := 10;              {divisor 1 }
    dio[2] := 10;              {divisor 2 }
    flag := ax5210(fun,dio);

    repeat
        axes;                  {display the acquisition window,
        for i:=1 to 500 do      {500 points and clear the screen}
            begin
                fun := nadc_ary;           {perform A/D conversion}
                dio[1] := 1;
                dio[2] := ofs(dat1);       {destination of acquired data: dat1 }
                dio[3] := timer_trg;
                flag := ax5210(fun,dio);
                putpixel(trunc(80+i),trunc(175-(dat1)/16*zoom),white);
                for j:=1 to 5000 do
                    ok2:=keypressed;
                if ok2 then begin
                    i:=500;
                    trash:=readkey;
                end;
            end;
        until ok2;
    end;
end;

```

Acquisition mode

Once the signal is optimized, the acquisition is performed. This procedure has mainly five differences with the oscilloscope mode:

- 1) A scan only begins when a trigger pulse is produced by the delay controller computer. The trigger detection is achieved in less than a ms, allowing starting precision of 0.1 fs between two scans. A manual initiation is also possible, by pressing a keyboard key.
- 2) The scanning frequency defined in the parameters is used to adapt the acquisition time to the length of the desired measurement.
- 3) The data are averaged over the number of scans. Only the averaged value is displayed and improvement of the S/N is thus readily visible.
- 4) Averaged data are save in an ASCII file. This is performed by a specific procedure not described here.
- 5) A spike detection allows peak noise to be withdrawn. Working with flowing or rotating cells often gives rise to signal peaks in the acquisition. In order to eliminate this specific noise, a three consecutive points comparison is made. If the difference between these consecutive points (taken every ms) is greater than the limit defined in parameter, a new series of three points is taken and tested. As experiments are usually not performed at frequencies higher than 50 Hz (corresponding to a 2.3 ps measurement), six spike detection tests can be achieved for each step, allowing most of the parasitic spikes to be withdrawn.

```

procedure conversion;                               {acquisition mode}
  var
    xx, yy, xx1, yy1, j, sp:integer;
    trash:char;
    ok2, trig:boolean;
begin

```

```

axes;
spik:=0;
trig:=false;
frequency (10000,100);
repeat
    channel(trig_ch);
    fun := nadc_ary;
    dio[1] := 1;
    dio[2] := ofs(trigger);
    dio[3] := timer_trg;
    flag := ax5210(fun,dio);
    if (abs(trigger)>=1000) then trig:=true;
    for i:=1 to 500 do
        if keypressed then begin
            trash:=readkey;
            trig:=true;
        end;
    until trig;

circle (80,300,2);
frequency (adc_freq+frequenc,100);
channel(start_ch);
for k:=1 to steps do
    begin
        sp:=3;
        for i:=1 to (round(1000/frequenc)) do
            begin
                fun := nadc_ary;
                dio[1] := 1;
                dio[2] := ofs(dat0);
                dio[3] := timer_trg;
                flag := ax5210(fun,dio);
                if i =(sp-2) then dat1:=dat0;
                if i=(sp-1) then dat3:=dat0;
                if i = sp then
                    begin
                        dat2:=dat0;
                        if (abs(dat3-dat1) > spike) or (abs(dat2-dat3)> spike) then
                            begin
                                sp:=i+3;
                                spik:=spik+1;
                                putpixel((80+3*spik),343,white);
                                outtextxy (10,340,'spikes :');
                            end
                        else
                            sp:=0;
                    end;
                for j:=1 to 100 do
                    ok2:=keypressed;
                if ok2 then begin
                    k:=(steps-1);
                    i:=round(1000/frequenc)-1;
                    trash:=readkey;
                    sca:=scans;
                end;
            end;
        xx:=80+trunc((500/(steps-1))*(k-1));
        xx1:=80+trunc((500/(steps-1))*(k-2));
        case sign of
    
```

{ wait for the trigger pulse
to initiate the acquisition }

{ set trigger level to 2 V }

{ manual initiation }

{ set the acquisition frequency }

{ acquisition for 1000 steps }

{ destination of acquired data: dat1 }

{ spike detection test }

{ data averaging }

```

1: begin                                {positive signal}
    dat[k]:=dat2+dat[k];
    yy:=300-trunc(dat[k]/8/sca);
    yy1:=300-trunc(dat[k-1]/8/sca);
end;
2: begin                                {negative signal}
    dat1:=-dat2;
    dat[k]:=dat1+dat[k];
    yy:=300-trunc(dat[k]/8/sca);
    yy1:=300-trunc(dat[k-1]/8/sca);
end;
3: begin                                {both positive and negative}
    dat1:=2048+dat2;
    dat[k]:=dat1+dat[k];
    yy:=175-trunc(((dat[k]/sca)-2048)/16*zoom);
    yy1:=175-trunc(((dat[k-1]/sca)-2048)/16*zoom);
end;
end;
if k>1 then line (xx1,yy1,xx,yy);      {display the data}
end;
end;

```

A last mode, called Optimization mode, has also been developed in order to keep ten successive scans displayed on the screen. It is thus possible to compare the signal obtained by changing one parameter, and thus to optimize it. This is specially interesting when the lifetime of the observed species is short, and moving the delay with the hand, does not allow the maximum amplitude of the signal in the oscilloscope mode to be determined.

3.5. Investigation of the Solvation Dynamics of an Organic Dye in Polar Solvents Using the Femtosecond Transient Grating Technique

Due to its characteristics (65 fs pulse and maximal acquisition time of 17 ps) this setup is perfectly adapted to study ultrafast processes such as solvation dynamics.

Until recently, solvation dynamics was assumed to be a pure diffusive process^{80,81}. Solvent motions were only considered as global motions, involving the neighbor molecules. It was thus viscosity dependent, and taking place in the ps time regime. The model used to describe the rotation of molecules as a function of the solvent viscosity is described in the chapter 4.5.1.

Nevertheless, this model was unable to explain some observations such as the sub-ps electron transfer reactions^{82,83}. An inertial contribution to the solvation dynamics was postulated by molecular dynamics simulations^{84,85}. Inertial contributions are due to librational motions of solvent molecule taking place in their own cavity. No neighbor molecules are involved and this inertial contribution is thus viscosity independent.

Using a time resolved fluorescence Stokes shift measurement with 120 fs pulses, Fleming was able to observe a fast inertial contribution taking place in less than 200 fs in MeCN⁸⁶.

The technique being based on fluorescence, the number of probe molecules is limited⁸⁷. Furthermore, only excited-state solvation dynamics can be investigated, and wavelength dependent measurement cannot be achieved.

In order to overcome these limitations, we have performed a transient grating experiment that can be understood in terms of spectral hole burning spectroscopy.

3.5.1. Transient Spectral Hole Burning Spectroscopy

In a liquid, the energy of a solute molecule may be stabilized by the solvent. If the solvent configuration do not stabilize the ground and the corresponding

electronic excited-state in the same manner, the energy gap between the two states changes, and thus the absorption spectrum changes as well. As a solution is a dynamic system, the surrounding of a specific molecule changes very rapidly. As a consequence, looking at the spectrum of a single solute molecule in the ns time regime give a broad band.

Doing the same experiment in the femtosecond time regime is different, as the solution can be considered as frozen, and the solvent configuration cannot change in this time scale. The absorption spectrum of a single molecule is thus much narrower. In this case, the overall absorption spectrum of the solution can be seen as the superposition of many narrow bands corresponding to different solvent configurations.

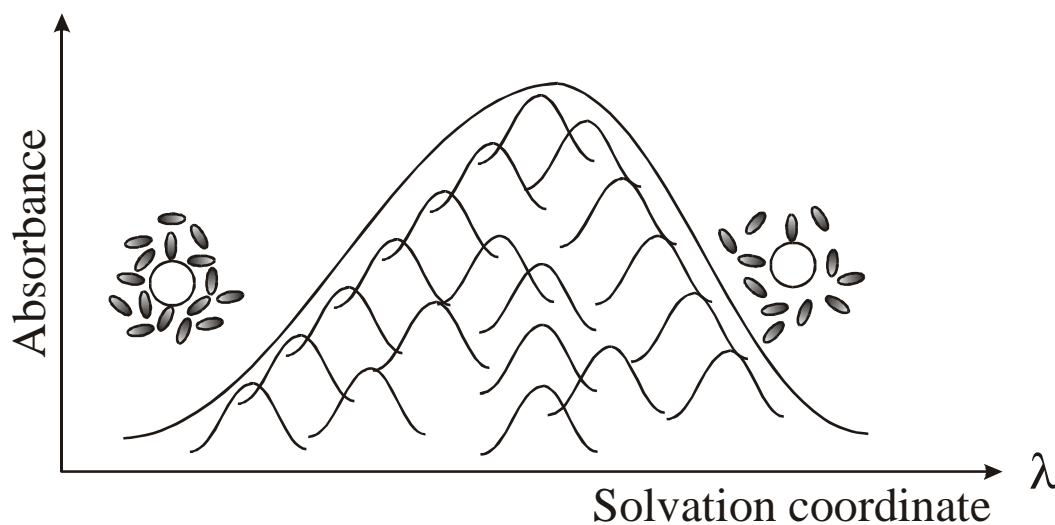


Figure 3.9: In the liquid phase, the overall absorption spectrum is due to the superimposition of the spectra of many solute molecules having specific solvation. For hypsochromic behavior, the solvation increases from the red to the blue part of the spectrum.

If the solute molecule shows a blue spectral shift when dissolved in a more polar solvent, one speaks of hypsochromic solvent shift. In such a case, the polarity of the solvent stabilizes more the ground than the excited-state of the

solute molecule. One can thus assume that the best ground-state solvated molecules absorb in the blue part of the spectrum, while the ones with loose solvation absorb in the red part.

In order to investigate the inertial solvation dynamics, the laser pulse has to be short enough to allow sufficient time resolution (< 200 fs), but also to possess a spectrum narrower than the absorption band (> 20 fs).

Excitation with such a pulse induces a hole in the absorption band, which corresponds to the depletion of molecules having a specific solvent configuration. Probing the refilling of this hole gives information on the solvation dynamic, as long as the ground-state recovery is slow.

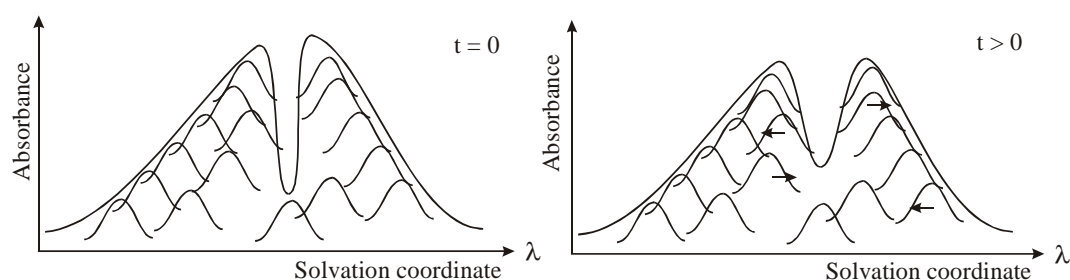


Figure 3.10: Hole burning spectroscopy investigates the time evolution of a spectral hole created in the absorption band of the sample, which corresponds to a specific solvation configuration. With time, the hole depth decreases due to solvation dynamics and ground-state recovery.

3.5.2. Experimental Conditions

The transient grating technique was used to probe the refilling of the solvation hole. As the fs laser produces pulses every 12.2 ns, a thermal grating accumulates (see chapter 1.2.4). To avoid it, polarization gratings were used in order to get rid of the intensity grating, and thus of the thermal grating. This

can be seen in Figure 3.11, by the use of a half-wave plate on one of the pump beams.

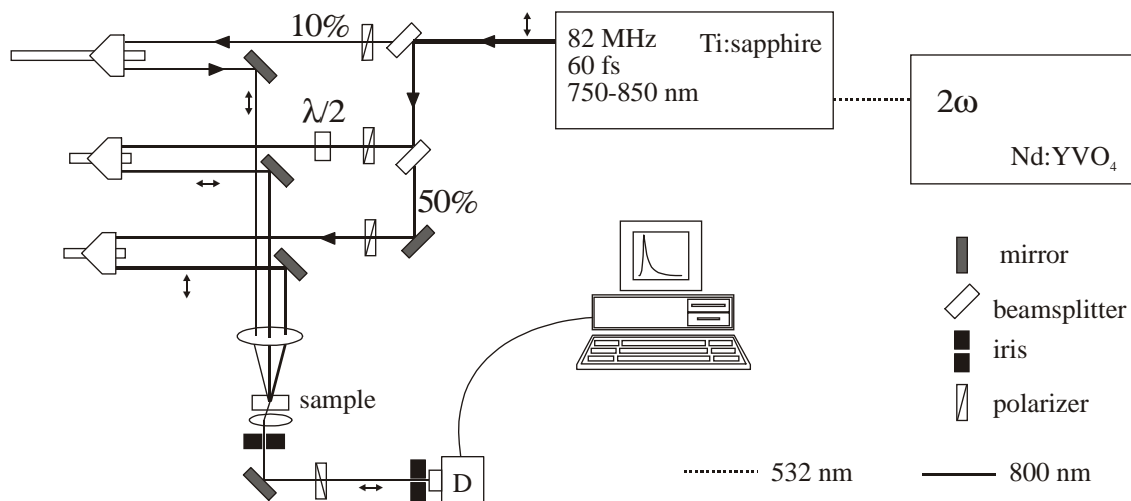


Figure 3.11: Setup for a transient polarization grating experiment with fs pulses.

Working at high repetition rate may also lead to sample degradation problems, as the total amount of heat released is not negligible ($\approx 0.1\text{W}$ in $0.1\ \mu\text{l}$ of solution). It is thus necessary to flow the sample in a circulation cell.

Circulation Cell

We have asked the mechanics workshop of the Chemistry department to build a circulation cell of 1mm sample thickness with two Suprasil windows. As the windows are discs of 1" diameter, the flow is turbulent on the sides and laminar in the middle (see Figure 3.12). This allows the central portion of the cell to be used with a minimum of scattered light.

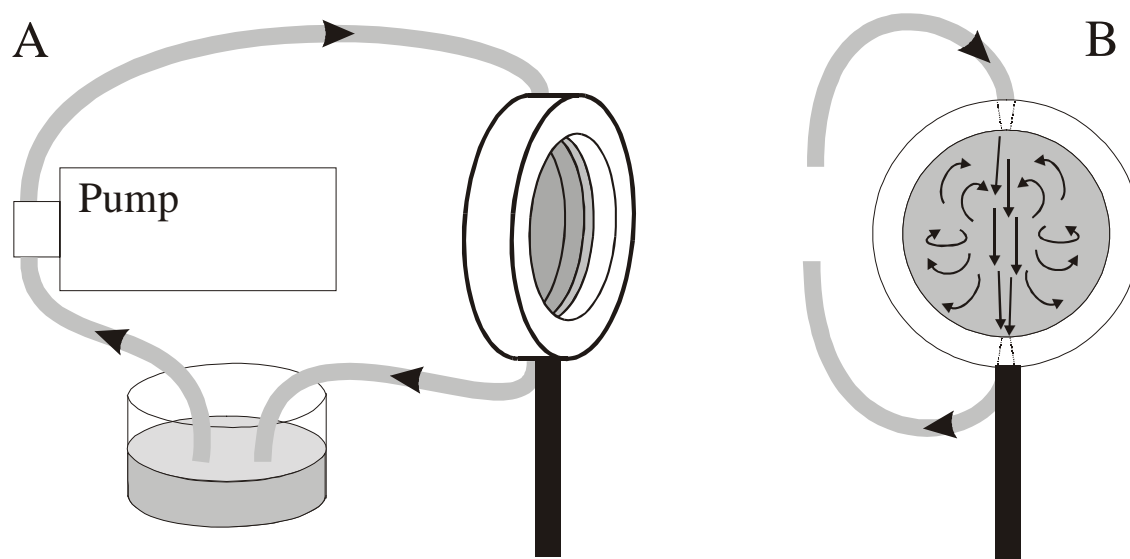


Figure 3.12: Home made circulation system with 1mm thick sample cell. A) general view of the cell with the circulation pump and the 40 ml tank. B) front scheme of the turbulences in the cell.

The magnetic drive gear circulation pump used is a Series 120 model from Micropump™. It allows a maximal flow rate of 53 ml/s, but due to the small radius of the teflon tubes (1 mm), it was working at a 3 ml/s maximal flow rate. The irradiated sample volume is thus renewed every 30 μ s, leading to a maximum local heating of 7°C. As the sample is in contact with metallic parts of the pump, highly corrosive solvents have to be avoided. With alcohols and nitriles, no contamination problems were observed.

Great care has to be taken when changing the sample. To avoid solvent mixing (leading to an undefined viscosity and an increase of turbulences), the system is washed twice with acetone and dried with nitrogen. It is then rinsed three times with the new solvent and once with the sample solution.

The use of a circulation cell has three major limitations:

- 1) Only non-corrosive solvents can be used in order to avoid destruction of the circulation pump and contamination of the sample.
- 2) Forty milliliters of sample solution are needed. It is thus not adequate to work with high concentrations species such as weakly absorbing molecules or quenchers.
- 3) The head of the pump heats the solution when working at high flow rate. It is thus difficult to perform temperature dependent experiments, such as rotational dynamics⁸⁸.

Sample: IR140

The IR140 organic dye was chosen for its availability (ExcitonTM), its high stability, and its absorption spectrum that perfectly matches the TsunamiTM output range.

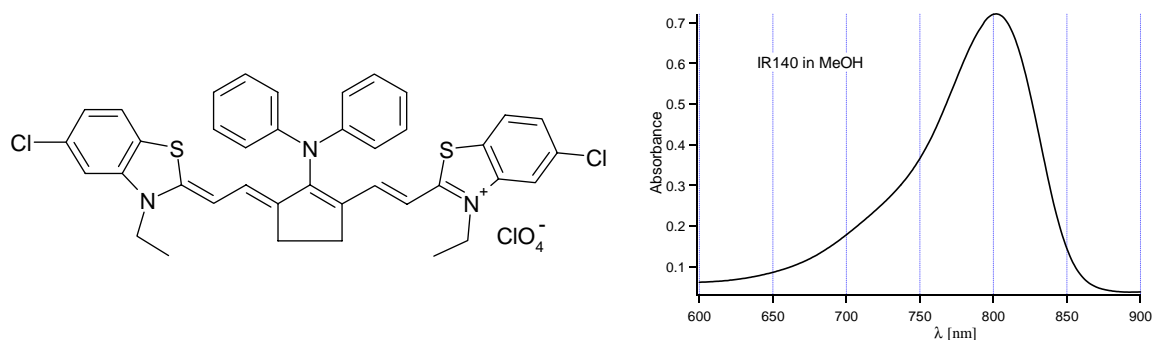


Figure 3.13: Structure of IR140 organic dye from ExcitonTM and its absorption spectrum in methanol (MeOH).

Its solvatochromic behavior was studied through the shift of the maximum of absorption in a series of alcohols and nitriles. Drawing the maximum position

as a function of the Onsager function $f(D)$ allows to determine the solvatochromic behavior of IR140^{2,89}.

Solvent	Dielectric constant ϵ^{90}	$f(D) = \frac{2 \cdot (\epsilon - 1)}{2\epsilon + 1}$	λ_{\max} [nm]	λ_{\max} [cm^{-1}]
MeOH	32.7	0.9548	802	12468
BuOH	20.33	0.928	810	12345
PentOH	13.9	0.896	811.5	12323
MeCN	37.5	0.9605	802	12469
PrCN	27.2	0.946	805	12422
BuCN	20.3	0.928	807	12391
OcCN	13.9	0.896	810.5	12338

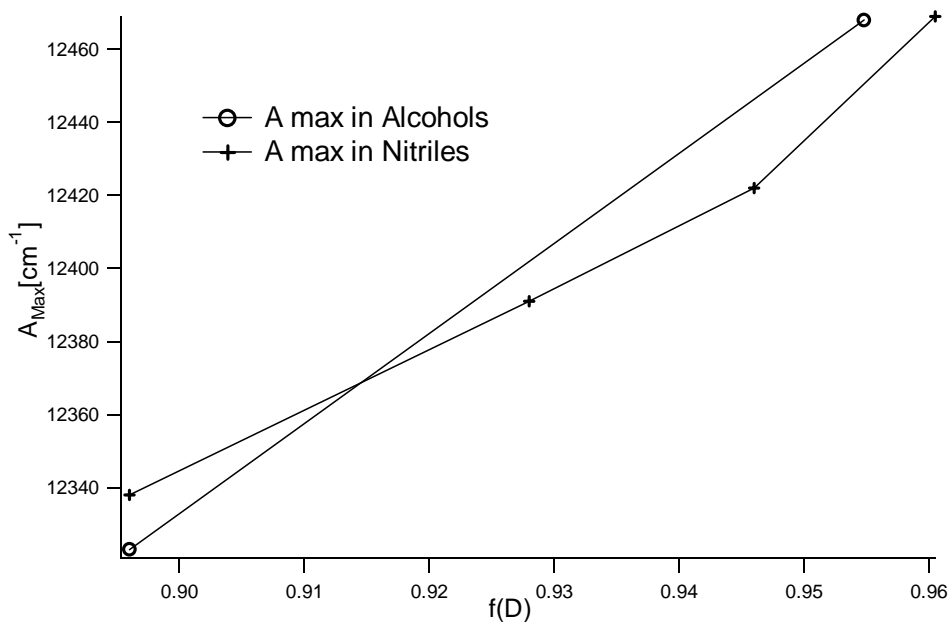


Figure 3.14: Solvatochromic plot for IR140 dye in series of alcohols and nitriles. The positive slope indicates that the excited-state is less stabilized by the solvent than its ground-state².

From this solvatochromic plot, one can determine that the dipole moment of the excited-state is smaller than that of the ground-state. As a consequence, polar solvents stabilize more the ground than the excited-state of the IR140 dye. Highly solvated molecules are well stabilized by the solvent and absorb in the blue part of the spectrum. On the other hand, molecules with a loose solvation shell are less stabilized and thus represent the red part of the absorption spectrum.

3.5.3. Paper

Investigation of the Solvation Dynamics of an Organic Dye in Polar Solvents Using the Femtosecond Transient Grating Technique

Jean-Claude Gummy, Olivier Nicolet, and Eric Vauthey*

Institut de Chimie-Physique de l'Université de Fribourg, Pérolles, CH-1700 Fribourg, Switzerland

Received: July 1, 1999; In Final Form: October 11, 1999

The solvation dynamics of an organic dye, IR140, in methanol, ethanol, and in a series of six alkanenitriles has been investigated using the transient grating technique. In all solvents, the dynamics exhibit ultrafast, almost solvent-independent, components ascribed to inertial solvation, and a slower viscosity-dependent component, due to diffusive solvation. The relative amplitudes of these components depend on both the solvent and on the wavelength at which the experiment is performed. The contribution of inertial motion increases with decreasing size of the solvent molecules and with decreasing wavelength. It appears that diffusive motion is associated with a loose solvent shell, while inertial motion dominates when the solvation layer is dense.

Introduction

The role of the solvent is of primary importance for the chemical reactivity. First, the solvent can favor chemical reaction by transferring momentum to the reactive species. Second, solvent offers efficient channels to dissipate energy as heat. Indeed, many exoergic chemical reactions taking place in the condensed phase do not occur in the gas phase due to the lack of such energy dissipation channels. Third, the solvation energy is often a decisive factor for the occurrence of a given chemical process. In photochemistry, the nature of the lowest excited state can be switched by varying the polarity of the solvent.¹ Moreover, in the condensed phase, spectral features are broader in comparison to the gas phase. This is due to the fact that the measured spectrum corresponds to an ensemble averaging over many solute–solvent configurations.

The response of the nuclear contribution to the dielectric constant does not follow instantaneously a variation of the electric field, such as that accompanying a chemical reaction or an electronic transition. Until recently, it was thought that this solvation dynamics was a purely diffusive process.^{2–4} This hypothesis was corroborated by measurement of the dynamics of the fluorescence Stokes shifts performed with picosecond laser pulses. The resulting solvation times were found to be of the same order of magnitude of the longitudinal dielectric relaxation times of the solvents. This parameter corresponds to the reorientational time of the solvent molecules under the influence of a constant charge and ranges from a few ps to several hundreds of ps, depending on the viscosity.⁵ However, molecular dynamics simulations of dipolar solvation have revealed the importance of the inertial motion of the solvent molecules, which takes place on a time scale of a few tens to a few hundreds of femtoseconds and which can contribute to up to 80% of the solvent relaxation.⁶ This prediction was verified afterward by Fleming and co-workers who performed time-resolved fluorescence Stokes shift measurements in acetonitrile with 125 fs pulses and later in water with 50 fs pulses.^{7,8} Four and six wave-mixing techniques have also been shown to give insight into the solvation dynamics.^{9–13} When the pulse duration is shorter than the electronic dephasing time of the probe

molecule, photon echo techniques allow the disentanglement of homogeneous and inhomogeneous contributions to line broadening.^{13,14} Fainberg and Huppert have shown that transient grating measurements with pulses longer than the dephasing time of the probe molecule can give information equivalent to those obtained from fluorescence Stokes shifts.⁹ This can be understood in terms of transient hole-burning spectroscopy: by exciting the probe molecule with pulses which are shorter than the solvation time but longer than the dephasing time, i.e., which have a narrower spectrum than the absorption band of the probe molecule, only a subset of the ground state population is excited. This subset corresponds to probe molecules experiencing similar interactions with the solvent. Assuming that the ground-state recovery time of the probe molecule is much longer than the solvation processes, the spectral hole broadens as the thermal equilibrium distribution of solvent configurations is restored. Experimentally, this broadening can be monitored by measuring the decrease of the hole depth. While the fluorescence Stokes shift technique is limited to a few numbers of probe molecules, the transient grating technique approach can be carried out with any probe molecule. This is also valid for any other spectroscopy sensitive to absorbance changes, such as transient absorption or transient dichroism. Another important advantage of this method is that these measurements can be performed at various wavelengths, and thus various subsets of the ground-state population can be investigated. Low-temperature spectral hole-burning studies have shown that processes such as spontaneous hole refilling¹⁵ or pressure-induced¹⁶ and electric-field-induced¹⁷ hole broadening are strongly dependent on the position of the hole in the inhomogeneous absorption band. Such investigations have revealed important information on the origin of line broadening in solids.

We report here on the study of the solvation dynamics of a dye, IR140, in methanol, ethanol and in a series of six alkanenitriles, from acetonitrile to decanenitrile, using the transient grating (TG) technique. While the solvation dynamics in alcohols and acetonitrile has been the subject of several investigations,^{4,7,9,18–23} there is much less information on the solvation dynamics in longer alkanenitriles in a time scale less than 1 ps. Moreover, an investigation of the influence on the

* Corresponding author. E-mail: Eric.Vauthey@unifr.ch.

solvation dynamics of the wavelength at which the experiment is performed is also reported.

Experimental Section

Apparatus. The pulses used for the TG measurements were generated by a cw mode-locked Ti:sapphire laser (Spectra-Physics, Tsunami) pumped by a Nd:YVO₄ laser (Spectra-Physics, Millennia V). The average output power at 800 nm was 900 mW at 82 MHz. The pulse duration measured at the sample position was between 65 and 75 fs fwhm. The output pulses were split into three parts, one probe and two pump pulses, with an intensity ratio of 1:10:10. The three pulses were sent along variable optical delay lines, before being focused onto the sample with a 90 mm achromatic lens. The three beams were arranged in a box configuration with a crossing angle of 5°. The delay lines for the pump pulses were only varied to optimize the temporal overlap and remained fixed during the measurements. The diffracted pulse was spatially isolated from the three other pulses with an iris located directly after the sample and recollimated with a 90 mm lens, before being sent to a photomultiplier tube (Hamamatsu R928). Its output was then directed to a computer board for digitization (Axiom AX5210 A/D board). The polarization of the pump and probe pulses was controlled with combinations of Glan-Taylor polarizers (Laser Components) and achromatic half-wave plates (Newport). A Glan-Taylor polarizer was also placed in front of the photomultiplier tube to select a precise polarization component of the signal.

To measure the dynamics at time delays longer than 50 ps, the picosecond TG setup described in ref 24 was used. In this case, the pump and probe wavelength was at 532 nm.

Samples. IR140 (Exciton) was used as received. Methanol (MeOH) and ethanol (EtOH) as well as acetonitrile (ACN) were of spectroscopic grade and used without further purification. Propionitrile (PrCN), butyronitrile (BuCN), valeronitrile (VaCN), octanenitrile (OcCN), and decanenitrile (DeCN) were washed twice with half the volume of concentrated HCl, then washed with saturated aqueous NaHCO₃, dried with MgSO₄, and distilled.²⁵ Unless specified, all products were from Fluka. For femtosecond TG, the concentration of IR140 was adjusted to obtain an absorbance at the pump wavelength of about 0.25 on 1 mm, the sample thickness. This corresponds to a concentration of about 1.5×10^{-5} M. The sample solutions were flowed at 3 mL/s in a home-built cell with 1.2 mm thick Suprasil windows (Helma 202-QS). The time required to replace the solution in the irradiated zone was of the order of 30 μ s.

For the ps TG measurements at 532 nm, the concentration amounted to 2×10^{-4} M.

Results

Solvent Dependence. Slow dynamics. Figure 1A shows the TG signal measured at 532 with IR140 in PrCN. For these measurements, the crossed grating geometry was used, i.e., the pump pulses had perpendicular linear polarization, the polarization of the probe pulse was parallel to that of one pump pulse, and the signal polarizer was perpendicular to the probe polarizer.²⁴ This geometry prevents the formation of a density phase grating and a distortion of the time profiles at longer time delays.²⁶ The decrease of the diffracted intensity corresponds to the decay of the polarization grating via both rotational diffusion and ground-state recovery (GSR),²⁷

$$I_{\text{TG}}^{\text{CG}} = I_0 \exp[-2k_{\text{CG}}t] k_{\text{CG}} = k_{\text{rot}} + k_{\text{GSR}} \quad (1)$$

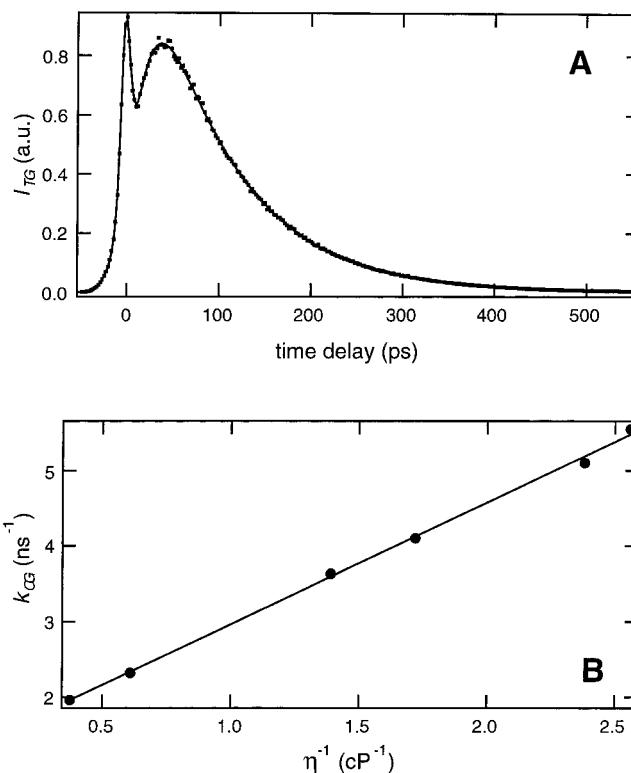


Figure 1. (A) Time profile of the diffracted intensity measured at 532 nm in PrCN using the crossed grating geometry (dots) and best fit of eqs 1 and 2 with an additional Gauss function (see text). (B) Viscosity dependence of the crossed grating decay rate constant, k_{CG} , in alkanenitriles.

where k_{rot} and k_{GSR} are the rate constants for rotational diffusion and GSR, respectively. The peak at time zero is the so-called coherence spike. It is due to the diffraction of one pump pulse off the grating formed between the probe pulse and the other pump pulse at time zero.^{28,29} This spike occurs in any pump–probe experiments when the probe and pump pulses are at the same wavelength and derived from the same pulse.

The TG intensity, I_{TG} , can be expressed as^{30,26}

$$I_{\text{TG}}(t) \propto \int_{-\infty}^{+\infty} I_{\text{pr}}(t-t') \left[\int_{-\infty}^t \chi^{(3)}(t''-t') I_{\text{pu}}(t') dt' \right]^2 dt'' \quad (2)$$

where I_{pr} and I_{pu} are the probe and pump intensities and $\chi^{(3)}$ is the third-order nonlinear susceptibility of the sample. $\chi^{(3)}$ is a third rank tensor whose elements correspond to various orientations of the four electric fields. The crossed grating geometry is therefore sensitive to $\chi_{1212}^{(3)}$. Various processes can contribute to $\chi^{(3)}$:²⁶ the electronic and the nuclear Kerr effects (OKE) from the solvent, the formation of population gratings, and the generation of a density phase grating due to heat releasing processes. In all the TG data presented here, there is no contribution from the OKE of the solvents. Moreover, the contribution of the density phase grating to $\chi_{1212}^{(3)}$ is zero, as such a grating is not formed in the crossed grating geometry, the pump intensity not being spatially modulated. Consequently, the signal intensity is only due to population gratings.

To fit properly eq 2 to the data shown in Figure 1A, $\chi_{1212}^{(3)}$ had the following functional form:

$$\chi_{1212}^{(3)}(t) = I \exp(-k_{\text{CG}}t) \quad (3)$$

To account for the coherent spike, an additional Gaussian function centered at time zero was used. This Gaussian was

TABLE 1: Best Fit Parameters of Eqs 2 and 4 with an Additional Gaussian to the Measured TG Profiles Measured at 800 nm in Various Solvents^a

solvent	A_G	$\Delta\tau_G$ (fs)	A_1	τ_1 (fs)	A_2	τ_2 (ps)	A_3	τ_3 (ps)
MeOH	0.180	65	0.166	256	0.197	5.7	0.444	240
EtOH	0.196	66	0.151	225	0.227	10.5	0.415	434
ACN	0.141	47	0.230	180	0.141	2.0	0.472	179
PrCN	0.135	45	0.227	190	0.140	2.7	0.483	196
BuCN	0.137	50	0.226	195	0.164	3.8	0.457	243
VaCN	0.151	49	0.191	203	0.180	4.7	0.462	285
OcCN	0.163	45	0.174	187	0.176	6.4	0.471	430
DeCN	0.194	56	0.144	196	0.172	8.9	0.474	510

^a A_4 , τ_4 , and ω are essentially independent on the solvent and amount to 0.02, 500 fs, and 23 ps⁻¹, respectively. The τ_3 values have been determined from the fit of eqs 2 and 3 to the slow dynamic data ($\tau_3 = k_{CG}^{-1}$).

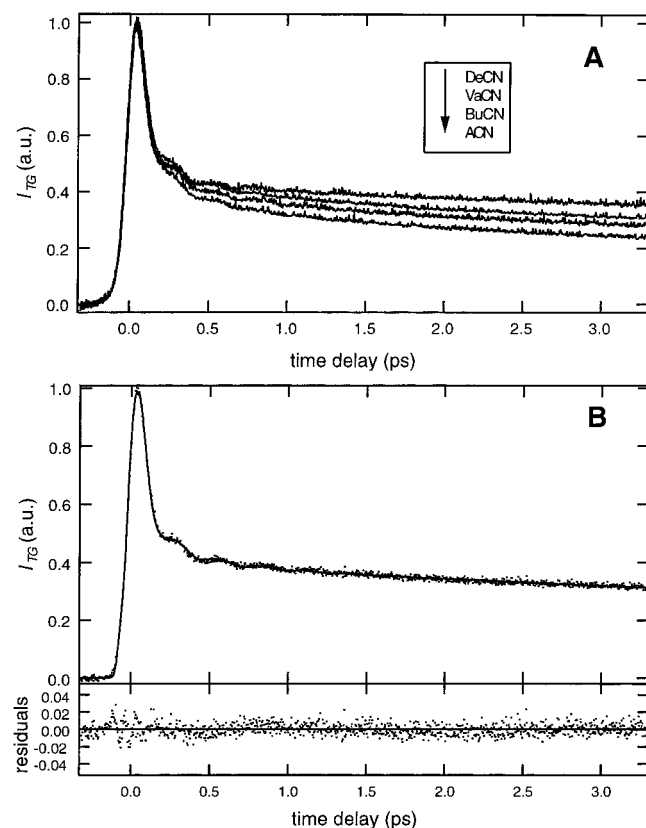


Figure 2. (A) TG decays at 800 nm measured in several alkanenitriles using the crossed grating geometry. (B) TG decay at 800 nm measured in EtOH using the crossed grating geometry, best fit of eqs 2 and 4 with an additional Gauss function and residuals.

simply added to the convolution of $\chi_{1212}^{(3)}(t)$ with the pump pulse profile. The result was then squared and convoluted with the probe pulse profile. It can be seen that this simple treatment of the coherent coupling spike results in a good fit. Moreover, the relative intensities of the coherent spike and incoherent signal at time zero have a ratio close to 4:1, as predicted by theory.^{28,29} The k_{CG} values obtained from the fit are listed in Table 1. Figure 1B shows a plot of k_{CG} in alkanenitriles as a function of $1/\eta$, where η is the solvent viscosity. From the intercept of the linear fit, the rate constant of GSR, k_{GSR} , amounts to 1.35 ± 0.6 ns⁻¹.

Fast Dynamics. Figure 2 shows TG decays measured at 800 nm in nitriles and in EtOH with the femtosecond setup using the crossed grating geometry. The time profiles look biphasic, with an initial spike and a slower decay. The initial part of the decay does not exhibit a strong solvent dependence. Moreover, an oscillation with a solvent-independent frequency is observed.

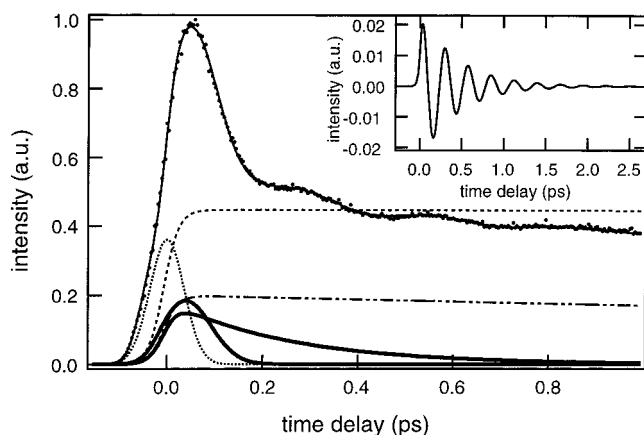


Figure 3. Relative contributions to the diffracted intensity measured at 800 nm in MeOH (dots): inertial solvent motion (Gaussian and exponential functions, bold), diffusive solvent motion (exponential function, dotted-dashed), population and rotational relaxation (exponential function, dashed), wave packet motion (damped cosine function, insert), and coherent coupling spike (Gaussian function, dotted). For the fit, the five contributions are added and squared and the result is convoluted with the probe pulse profile.

These decays are qualitatively very similar to those reported by Fleming and co-workers²² as well as Huppert and co-workers⁹ using the same technique. To fit properly eq 2 to these data, the following functional form has to be used for $\chi_{1212}^{(3)}(t)$:

$$\chi_{1212}^{(3)}(t) = A_G \exp[-(t/\Delta\tau_G)^2] + \sum_{i=1}^3 A_i \exp(-t/\tau_i) + A_4 \exp(-t/\tau_4) \cos(\omega t + \phi) \quad (4)$$

where the first term is the Gaussian function reproducing the initial peak and the last term is a damped cosine function reproducing the oscillation of the TG intensity. At least three exponentials are required for a proper fit, the slowest one having a lifetime $\tau_3 = k_{CG}^{-1}$. For the fit, the pump and probe pulses were taken as Gaussian. The best fit was obtained by letting the pulse duration vary during the fit. However, the resulting duration was substantially larger than that measured by auto-correlation at the sample position. When the measured duration was kept fixed, the fit was very good in the decaying part of the signal but was poorer on the rising edge. We attribute this effect to the contribution of coherent coupling spike to the signal. This coherent coupling effect has been invoked by Cong et al. to explain the initial spike in GSR measurements such as those shown in Figure 2.³¹ However, Fleming and co-workers have shown that this spike arises almost entirely from the ultrafast solvation dynamics.²² An excellent fit to the data is obtained with the measured pulse duration, if an additional Gaussian function centered at time zero is used, as described above for the ps TG signals. The various contributions to the signal are shown in Figure 3. The parameters obtained from the fit are listed in Table 1 together with the fixed parameter τ_3 . The oscillation amplitude, A_4 , frequency, ω , and the damping time, τ_4 , amount to about 0.02, 23 ps⁻¹, and 500 fs, respectively, in all solvents investigated.

Without going into detail, this table shows that the width of the Gaussian function, $\Delta\tau_G$, is in both solvent series less than 70 fs, i.e., close to the pulse duration ($\Delta\tau(\text{fwhm}) = 1.66\Delta\tau_G$). A fast exponential with a lifetime, τ_1 , around 250 and 200 fs is observed in alcohols and in nitriles, respectively. Neither $\Delta\tau_G$ nor τ_1 shows any viscosity dependence. However, the lifetime, τ_2 , associated with the second exponential exhibits a marked

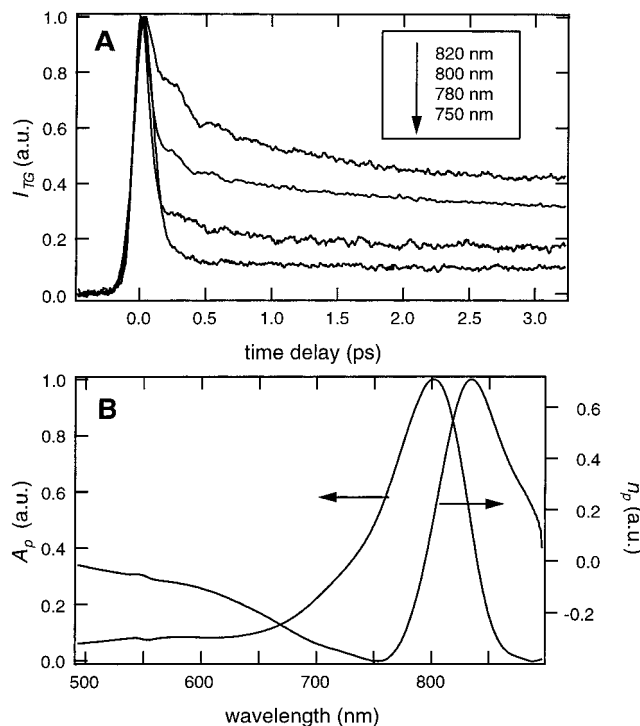


Figure 4. (A) TG decays measured at various wavelengths in MeOH with parallel polarization of the four beams. (B) Absorption and calculated dispersion spectra of IR140 in MeOH.

viscosity dependence and goes from 2 ps in ACN to about 10 ps in EtOH and in DeCN.

Wavelength Dependence. The variation of the TG decay with wavelength strongly depends on the polarization of the four interacting beams. TG decays recorded at various wavelengths with all parallel polarization of the beams are shown in Figure 4A. Two types of changes can be observed: (i) the intensity ratio of the initial spike to the slow decay increases by going from the red to the blue wavelength and (ii) the lifetimes associated with the various components vary substantially with the wavelength. A slow rise is even observed at 750 nm.

This spectacular effect is ascribed to the interference of the population phase grating with an accumulated density phase grating. This density phase grating is due to the thermal expansion following nonradiative deactivation of the excited state.³² The lifetime of the grating depends on the fringe spacing, around 9 μm in the present case, and on the thermal diffusivity of the sample solutions, which is of the order of 10^{-7} m^2/s . This results in a density grating lifetime of about 20 μs . With parallel polarizations, the diffracted intensity is proportional to $|\chi_{1111}^{(3)}|^2$, where $\chi_{1111}^{(3)}$, which contains contributions from population gratings and density grating, is a complex quantity:

$$\text{real}(\chi_{1111}^{(3)}) = \chi_{1111}^{(3)}(\Delta n_p) + \chi_{1111}^{(3)}(\Delta n_d) \quad (5a)$$

$$\text{imag}(\chi_{1111}^{(3)}) = \chi_{1111}^{(3)}(\Delta A_p) \quad (5b)$$

where $\chi_{1111}^{(3)}(\Delta n_p)$ and $\chi_{1111}^{(3)}(\Delta n_d)$ are responsible for variation of refractive index due to population, Δn_p , and density changes, Δn_d , respectively, while $\chi_{1111}^{(3)}(\Delta A_p)$ is connected to the variation of absorbance due to population changes, ΔA_p . From eqs 2 and 5a, it is clear that the signal generated by both phase gratings can interfere. The intensity and the nature of the interference depend on the relative magnitude and sign of Δn_p and Δn_d and on the associated tensor elements, $\chi_{1111}^{(3)}$.^{32–34} The

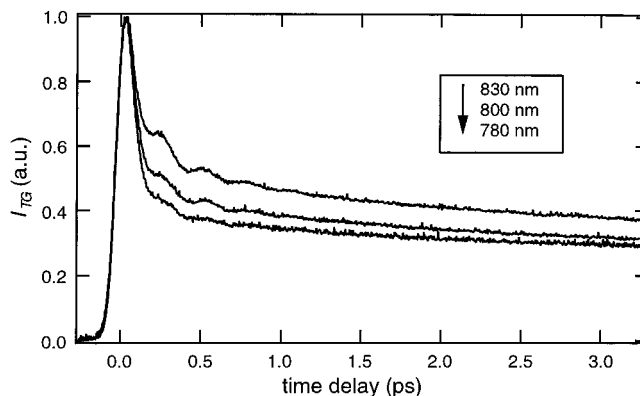


Figure 5. TG decays measured at various wavelengths in MeOH using the crossed grating geometry.

change of refractive index is caused by thermal expansion following heat release, and thus Δn_d is negative. On the other hand, Δn_p can be obtained by Kramers–Kronig transformation of ΔA_p . Figure 4B shows the absorption spectrum, $A_p(\lambda)$, and the calculated dispersion spectrum, $n_p(\lambda)$, of IR140 in MeOH. If we assume that, the photoinduced absorbance change in this spectral region is only due to the bleaching of IR140 ground state absorption, ΔA_p and Δn_p are simply proportional to $-A_p$ and $-n_d$, respectively. From this figure, it appears that Δn_p is negative on the red side of the absorption band and positive on the blue side. Thus, the interference between the density and the population phase gratings should be constructive at wavelengths longer than 800 nm and destructive at lower wavelengths. Moreover, there should be no interference at 800 nm, where Δn_p vanishes. This is in perfect agreement with the observation. Indeed, the light diffracted by the accumulated density phase grating acts as a local oscillator, in phase with the light diffracted by the population phase grating, but in quadrature with the light diffracted from the population amplitude grating. The resulting signal is a mixture of heterodyne and homodyne signals. The heterodyne signal scales linearly with Δn_p and contains information on its sign, while the homodyne signal scales quadratically with ΔA_p and is always positive. For these reasons, the signal at 800 nm ($\Delta n_p = 0$) is identical to the signal measured with the crossed grating configuration ($\Delta n_d = 0$). Similarly, this explains why the apparent decay of the signal at $\lambda > 800$ nm (constructive interference) is slower than at 800 nm and why the decay at $\lambda < 800$ nm is faster (destructive interference).

These results also confirm that the absorbance changes around 800 nm are due to the bleaching of the ground state absorption only. If the excited-state absorption were also involved, the resulting absorption change spectrum would be different from $-A_p$, displayed in Figure 4B, and Δn_p would not vanish at 800 nm. Consequently, the TG decay at this wavelength would not be the same in the crossed grating and in the all parallel polarization geometry.

Figure 5 shows the TG decays measured at several wavelengths between 830 and 780 nm in MeOH using the crossed grating geometry, i.e., without the formation of an accumulated density grating. For these measurements, great care was taken to keep the pulse duration, the pulse energy, and the sample absorbance constant. These decays were analyzed using eqs 2 and 4 with the additional Gauss function. In this case, the lifetimes τ_1 to τ_3 , the width of the Gaussian $\Delta\tau_G$, as well as the parameters pertaining to the oscillation, A_4 , τ_4 , and ω , obtained from the fit were independent of the wavelength. The effect of wavelength appears only in the relative amplitudes A_G to A_3 , as shown in Table 2.

TABLE 2: Best Fit Parameters of Eqs 2 and 4 with an Additional Gaussian to the Measured TG Time Profiles Measured in MeOH at Various Wavelengths^a

λ (nm)	A_G	$\Delta\tau_G$ (fs)	A_1	τ_1 (fs)	A_2	τ_2 (ps)	A_3
830	0.107	58	0.169	260	0.239	6.3	0.471
820	0.115	60	0.158	259	0.256	6.3	0.465
800	0.184	66	0.148	254	0.197	6.4	0.450
780	0.240	64	0.138	231	0.150	6.5	0.454

^a A_4, τ_4, ω are essentially independent on λ and amount to 0.02, 500 fs, and 23 ps⁻¹, respectively. τ_3 has been fixed to 240 ps.

This table shows that the amplitude of the Gaussian component increases with decreasing wavelength, while A_1 decreases only weakly. On the other hand, the amplitude of the slower, viscosity-dependent component, A_2 , shows a strong decrease from the red to the blue, and the relative amplitude associated with the long decay time, τ_3 , decreases weakly.

Discussion

The GSR signals contains four contributions.

(i) The contribution due to the decay of the polarization grating with a lifetime τ_3 determined with the picosecond TG experiment at 532 nm ($\tau_3 = k_{CG}^{-1}$).

(ii) The contribution due to solvation, i.e., the restoration of the equilibrium distribution of solvent configurations after depletion of a subset of these configurations. This contribution is phenomenologically described by a Gaussian and two exponential functions with decay time τ_1 and τ_2 , respectively.

(iii) The contribution from the propagation of a ground state wave packet generated via impulsive stimulated Raman scattering. This contribution is described by a frequency, ω , and a damping time, τ_4 , which are independent of both the solvent and the wavelength.

(iv) The contribution of the coherence coupling spike at zero time delay, which is present in all pump-probe experiments performed at a single wavelength.

The latter contribution is of course unwanted but cannot be avoided. As discussed in the previous section, we think that this spike has been accounted for by adding a Gaussian function centered at time zero. As this procedure gives good results with the picosecond TG data shown in Figure 1, it should work as well for the ultrafast TG data. Consequently, the contribution of the coherent coupling to A_G must be negligible. This is in agreement with the wavelength dependence of the GSR signal. According to Cong et al., the amplitude of the coherence coupling spike increases as the wavelength at which the experiment is performed is located further apart from the absorption band maximum.³¹ This means that, if A_G was dominated by the coherent coupling, it should decrease from 830 nm to about 810 nm, and then increase again when going to a shorter wavelength. As shown in Table 2, this behavior is not observed, A_G increasing continuously from 830 to 780 nm. However, the amplitude of the added Gaussian function decreases weakly from 830 to 800 nm (from 0.44 to 0.41) and increases again at 780 nm to 0.42, in agreement with the prediction of Cong et al.³¹ Nevertheless, this variation is close to the error limit and could be coincidental.

Solvent Dependence. As shown in Table 1, the total contribution of solvation to the signal, $A_s = A_G + A_1 + A_2$, is almost constant in a given solvent series. The contribution of solvation to the GSR signal can be separated into two parts: the contribution of inertial motion, which does not depend on viscosity, and the contribution of diffusive motion, which is viscosity dependent. The inertial contribution is accounted for

by the initial Gaussian and the fastest exponential decay, while the diffusive solvation is described by the single exponential with a decay time τ_2 . These τ_2 values in MeOH and EtOH are in good agreement with those reported in the literature.^{4,21} In ACN, the τ_2 value is very similar to that of 2.23 ps reported recently by Passino et al.²³ The solvation times in PrCN, BuCN, and VaCN are also of the same order of magnitude as those previously published, i.e., between 2 and 4 ps.⁴ To our knowledge, there are no data on the solvation dynamics in OoCN and DeCN.

There is also less data concerning the faster contributions to solvation. In the alcohols, the width of the Gaussian amounts to about 65 fs. The lifetime of the first exponential, τ_2 , is also the same in both alcohols and lies around 240 fs. Lifetimes of the order of 400 fs have been reported by Goldberg et al.⁹ Horng et al. have observed an exponential with a similar time constant in the solvation dynamics of a coumarin in a series of alcohols.²¹ Moreover, recent three pulse stimulated photon echo peak shift (3PEPS) measurements performed on DTCl in MeOH showed a 260 fs component.³⁵ On the other hand, similar 3PEPS investigations of the solvation dynamics of IR144 did not reveal any component between 100 fs and 1 ps in both MeOH and EtOH.²³ The origin of these differences is not understood and could be related to the nature of the probe molecule.

Although τ_G and τ_1 do not exhibit an apparent solvent dependence in a given series, the situation is different if the amplitudes A_G , A_1 , and A_2 are considered. In alcohols, A_G and A_1 are almost constant while A_2 increases by going from MeOH to EtOH.

In the nitriles, the width of the initial Gaussian is somewhat smaller than in the alcohols and is of the order of 50 fs. Similarly, τ_1 is smaller than in the alcohols and lies around 190 fs. A 90 fs and a 630 fs component have been reported for coumarin in ACN by Horng et al.,²¹ while Passino et al. have found 73 fs and 2.23 ps components with IR144.²³ Finally, Lee et al. have reported 219 fs and 2.1 ps components with DTCl in ACN,³⁵ in good agreement with the present results. Concerning the amplitudes, A_G increases with increasing length of the solvent molecule, while A_1 exhibits the opposite behavior. A similar trend can be found in the data reported by Horng et al. The relative amplitude of the component around 300 fs decreases from 0.34 to 0.07 by going from MeOH to decanol.²¹ The sum of the amplitudes related to inertial solvation, $A_G + A_1$ decreases with increasing length of the solvent molecules. This effect is confirmed by the increases of A_2 with increasing chain length. Molecular dynamics simulations of solvation indicate that the inertial contribution is largely due to the molecules located in the first solvation shell.³⁶ For small solvent molecules, inertial motion can involve the rotation of the whole molecule. For longer molecules, only the polar heads must contribute to the inertial motion. Consequently, it is reasonable to assume that inertial solvation is more efficient in solvents such as ACN or MeOH, where the number of polar heads around the solute molecule is large, than in long nitriles and alcohols, where substantial reorientation of the solvent molecules cannot occur without diffusional motion.

Wavelength Dependence. The wavelength dependence measured with parallel polarization is due to a large extent to interference between the signals originating from the population and density phase gratings. However, the wavelength dependence measured in the crossed grating configuration is not "contaminated" by this effect. This is confirmed by the fact that the dynamics parameters obtained from the fit, $\Delta\tau_G$ to τ_2 ,

did not show significant wavelength dependence. Table 2 shows that the total contribution of solvation to the signal, $A_s = A_G + A_1 + A_2$, increases weakly with decreasing wavelength. This is in agreement with theoretical prediction by Joo et al.²² This effect can be explained by the dynamic Stokes shift in the GSR process. Indeed, the minima of the ground and excited potentials are not located at the same position. Thus, GSR occurs from the minimum of the excited state potential to the edge of the ground state potential, which corresponds to the red side of the absorption spectrum.

Larger wavelength effects can be observed in the relative amplitudes related to the solvation dynamics. Indeed, A_G exhibits a strong increase, by a factor larger than 2, with decreasing wavelength. As explained above, this confirms that the coherent coupling spike does not contribute significantly to A_G . On the other hand, A_1 shows only a very weak decrease, by a factor 1.2, by going from 830 to 780 nm. Finally, the amplitude of the diffusive solvation, A_2 , shows a decrease by a factor 1.6.

There are only very few reports on the wavelength dependence of solvation dynamics. Such an investigation is not possible with fluorescence Stokes shift measurements. Moreover, the spectrum associated with pulses shorter than 25 fs, as used in some groups, is so large ($\Delta\lambda > 36$ nm around 800 nm) that it almost entirely overlaps with the absorption band of the probe molecule. Heterodyne transient dichroism measurements with rhodamine 800 (R800) in H₂O at two wavelengths have been reported by Zolotov et al.³⁷ The data (Figure 3 in ref 37) show that the initial spike increases with decreasing wavelength, while the amplitude of the slower component decreases. However, the pulse duration was not exactly the same for both measurements.

The wavelength dependence observed with IR140 indicates that the different positions within the absorption band of the probe molecule correspond to different solvent configurations with different dynamics. The solvent configurations for the red side involve more diffusional motion than the configurations corresponding to blue side absorption. Interestingly, the absorption band of IR140 is shifted to a shorter wavelength as the polarity of the solvent increases. For example, the absorption maximum goes from 811 nm in OcCN ($\epsilon = 13.9$) to 802 nm in ACN ($\epsilon = 37.5$). The same trend is observed in the alcohols. Coming back to the absorption band of IR140 in MeOH, these data imply that the molecule is better solvated when absorbing in the blue part of the band than when absorbing at longer wavelengths. Moreover, a compact and dense solvent shell will also result to shorter wavelength absorption than a looser and less dense shell. It is therefore quite reasonable to assume that inertial motion is much more important in the dense solvent shell than in the loose one. The latter configuration corresponds to instants where solvent molecules are diffusing and leave some free space around the solute. This could explain why solvation dynamics is dominated by diffusive motion at 830 nm and by inertial motion at 780 nm. A good proof of this model would be the observation of the opposite wavelength dependence with a probe molecule exhibiting a red shift of the absorption band with increasing solvent polarity. Such a probe molecule absorbing around 800 nm could not be found. All molecules with an absorption spectrum suitable to our laser also showed a blue shift with increasing solvent polarity. Moreover, TG measurements performed with two of them (1,1'-diethyl-2,2'-tricyanobenzene perchlorate and 1,1'-diethyl-2,2'-dicyanobenzene iodide) reveal qualitatively the same wavelength dependence as for IR140. However, the first absorption band of the dye R800, studied by Zolotov et al., shifts from 680 nm in acetone ($\epsilon =$

20.7) to 687 nm in dimethylformamide ($\epsilon = 36.7$).³⁷ As mentioned above, the wavelength dependence of the solvation dynamics of R800 seems to be the reverse of that observed with IR140, as would be expected by our hypothesis.

Conclusion

This investigation shows that the TG technique is well suited for investigating ultrafast solvation processes under the following conditions.

(i) Crossed grating geometry has to be used when working at high repetition rate to avoid interference effects with an accumulated thermal grating. Interference can also be avoided when working at a wavelength where the refractive index variation associated with the absorbance change is zero. This wavelength corresponds to the maximum of the absorption band of the probe molecule, as long as there is no transient absorption in this region.

(ii) The contribution of the coherent coupling must not be neglected. However, its relative contribution to the signal appeared to be basically independent of both the solvent and the wavelength.

(iii) In order to investigate the wavelength dependence of the solvation dynamics, the laser pulse duration should not be too short, to allow selective excitation within the broadened absorption band of the probe molecule.

The advantage of this technique over the fluorescence Stokes shift measurements is the possibility to perform measurements at different wavelengths within the absorption band of the probe molecule. The wavelength dependence of the solvation dynamics allows a new insight into the line broadening process to be gained. From the results obtained here, it appears that diffusional solvent motion is associated with a loose solvent shell around the solute molecule. When such motion dominates, the molecule is not well solvated and its transition energy is located on the red side of the absorption spectrum, in the case of IR140. On the other hand, inertial motion dominates in situations where the solvent shell is dense, i.e., when the molecule is well solvated. Thus, molecules such as IR140 absorb at shorter wavelength. For molecules with an absorption spectrum shifting to lower frequency with increasing solvent polarity, the opposite behavior is expected. This interpretation is supported by the solvent dependence of the solvation dynamics. Inertial motion is larger in solvents composed of small molecules, where the solute molecule is surrounded by a large number of polar heads, than in solvents composed of long molecules such as DeCN, where substantial reorientation of the polar head cannot occur without diffusive motion.

Such measurements might prove to be very fruitful for understanding more complex systems, such as chromophores embedded in a protein.

Acknowledgment. This work was supported by the Fonds national suisse de la recherche scientifique through Project 2000-055388.98. Financial support from the Fonds de la recherche and the Conseil de l'Université de Fribourg is also acknowledged.

References and Notes

- (1) Porter, G.; Suppan, P. *Pure Appl. Chem.* **1964**, *9*, 499.
- (2) Bagchi, B.; Oxtoby, D. W.; Fleming, G. R. *Chem. Phys.* **1984**, *86*, 257.
- (3) Simon, J. D. *Acc. Chem. Res.* **1988**, *21*, 128.
- (4) Barbara, P. F.; Jarzaba, W. *Adv. Photochem.* **1990**, *15*.
- (5) Kivelson, D.; Friedman, H. *J. Phys. Chem.* **1989**, *93*, 7026.
- (6) Maroncelli, M.; Fleming, G. R. *J. Chem. Phys.* **1988**, *89*, 5044.

- (7) Rosenthal, S. J.; Xie, X.; Du, M.; Fleming, G. R. *J. Chem. Phys.* **1991**, *95*, 4715.
- (8) Jimenez, R.; Fleming, G. R.; Kumar, P. V.; Maroncelli, M. *Nature* **1994**, *369*, 471.
- (9) Goldberg, S. Y.; Bart, E.; Meltsin, A.; Fainberg, B. D.; Huppert, D. *Chem. Phys.* **1994**, *183*, 217.
- (10) Fleming, G. R.; Cho, M. *Annu. Rev. Phys. Chem.* **1996**, *47*, 109.
- (11) Berg, M.; Bout, D. A. V. *Acc. Chem. Res.* **1997**, *30*, 65.
- (12) Tokmakoff, A.; Lang, M. J.; Larsen, D. S.; Fleming, G. R. *Chem. Phys. Lett.* **1997**, *272*, 48.
- (13) de Boeij, W. P.; Pshenichnikov, M. S.; Wiersma, D. A. *Annu. Rev. Phys. Chem.* **1998**, *49*, 99.
- (14) Lang, M. J.; Jordanides, X. J.; Song, X.; Fleming, G. R. *J. Chem. Phys.* **1999**, *110*, 5884.
- (15) Vauthey, E.; Voss, J.; Caro, C. D.; Renn, A.; Wild, U. P. *J. Lumin.* **1993**, *56*, 61.
- (16) Zollfrank, J.; Friedrich, J. *J. Phys. Chem.* **1992**, *86*, 7887.
- (17) Vauthey, E.; Holliday, K.; Wei, C.; Renn, A.; Wild, U. P. *Chem. Phys.* **1993**, *171*, 253.
- (18) Fleming, G. R. *Chemical Applications of Ultrafast Spectroscopy*; Oxford University Press: New York, 1986.
- (19) Simon, J. D. *Pure Appl. Chem.* **1990**, *62*, 2243.
- (20) Nishiyama, K.; Asano, Y.; Hashimoto, N.; Okada, T. *J. Mol. Liquids* **1995**, *65/66*, 41.
- (21) Horng, M. L.; Gardecki, J. A.; Papazyan, A.; Maroncelli, M. *J. Phys. Chem.* **1995**, *99*, 17311.
- (22) Joo, T.; Jia, Y.; Yu, J.-Y.; Lang, M. J.; Fleming, G. R. *J. Chem. Phys.* **1996**, *104*, 6089.
- (23) Passino, S. A.; Nagasawa, Y.; Fleming, G. R. *J. Phys. Chem.* **1997**, *101*, 725.
- (24) Gumy, J.-C.; Vauthey, E. *J. Phys. Chem.* **1996**, *100*, 8628.
- (25) Perrin, D. D.; Armarego, W. L. F.; Perrin, D. R. *Purification of Laboratory Chemicals*; Pergamon Press: Oxford, 1980.
- (26) Deeg, F. W.; Fayer, M. D. *J. Chem. Phys.* **1989**, *91*, 2269.
- (27) Myers, A. B.; Hochstrasser, R. M. *IEEE J. Quantum Electron.* **1986**, *QE-22*, 1482.
- (28) von Jena, A.; Lessing, H. E. *Appl. Phys.* **1979**, *19*, 131.
- (29) Eichler, H. J.; Langhans, D.; Massmann, F. *Opt. Comm.* **1984**, *50*, 117.
- (30) Etchepare, J.; Grillon, G.; Chambaret, J. P.; Hamoniaux, G.; Orzag, A. *Opt. Commun.* **1987**, *63*, 329.
- (31) Cong, P.; Deuel, H. P.; Simon, J. D. *Chem. Phys. Lett.* **1993**, *212*, 367.
- (32) Nelson, K. A.; Casalegno, R.; Miller, R. J. D.; Fayer, M. D. *J. Chem. Phys.* **1982**, *77*, 1144.
- (33) Vauthey, E.; Henseler, A. *J. Phys. Chem.* **1995**, *99*, 8652.
- (34) Högemann, C.; Vauthey, E. *Isr. J. Chem.* **1998**, *38*, 181.
- (35) Lee, S. H.; Lee, J. H.; Joo, T. *J. Chem. Phys.* **1999**, *110*, 10969.
- (36) Maroncelli, M.; Kumar, V. P.; Papazyan, A. *J. Phys. Chem.* **1993**, *97*, 13.
- (37) Zolotov, B.; Gan, A.; Fainberg, B. D.; Huppert, D. *Chem. Phys. Lett.* **1997**, *265*, 418.

4. Experiment with Amplified fs Pulses

4.1. Introduction

As shown in the previous chapter, fs pulses are necessary to study ultrafast phenomena. Nevertheless, working at 800 nm is a great limitation as only few molecules absorb at this wavelength. In order to study other systems, it is necessary to obtain fs pulses in the visible. Many nonlinear phenomena such as Second Harmonic Generation (SHG), SPM or stimulated Raman allow new wavelength to be produced. However, all these techniques need peak power in the GW/cm^2 range. The output pulses of the Tsunami have only twelve nJ and a maximum peak power of a quarter of a MW.

In order to allow efficient SHG and SPM, a fs amplification system is used, giving pulses of 2-3 GW peak power.

Such a system was used to study the excited-state lifetime the tetracene radical ion ($\text{TRC}^{\bullet+}$), and the rotational dynamics of perylene and perylene derivatives in low viscosity solvents.

4.2. Amplification of fs Pulses

In order to amplify fs pulses, one needs a gain medium that is pumped by an external source of radiation. The main difference with a laser cavity arises from the seed fs pulse that is injected in the system. It is no longer the

stimulated fluorescence which is amplified in the gain medium, but the seed pulse.

The first fs amplifiers were dye amplifiers. They consisted in series of four to five dye cells that were transversely pumped by a ns laser. They allowed a 10^6 amplification of the seed pulse, but had a major drawback: the spontaneous emission from the first cell is also often amplified by the following chain, leading to a ns background. This is called Amplification of Spontaneous Emission (ASE). Furthermore, the efficiency of dye amplifiers is usually very small, typically less than 0.3%⁹¹. For these reasons, solid state amplifiers are preferred.

However, solid state amplifiers have a small gain per pass, and regenerative amplification is necessary. The fs pulse is trapped in the amplifier cavity, amplified until all the energy is extracted and then dumped out of the cavity. In order to trap and dump the pulse, a Pockels cell and a broadband polarizer are used. Three steps can be distinguished (see Figure 4.1):

- 1) Injection of the pulse in the cavity. The Pockels cell is switched on, and it thus equivalent to a quarter-wave plate. The fs pulse passing twice through the cell undergoes a 90° rotation of its polarization. It is thus transmitted through the polarizer.
- 2) Amplification in the cavity. The Pockels cell is switched off and the pulse polarization is unchanged. The pulse is thus still transmitted by the polarizer. Note that the new incoming pulses are reflected out of the cavity.
- 3) Dumping out of the cavity. The Pockels cell is switched on again, leading to a 90° rotation of the polarization of the amplified fs pulse, which can be extracted.

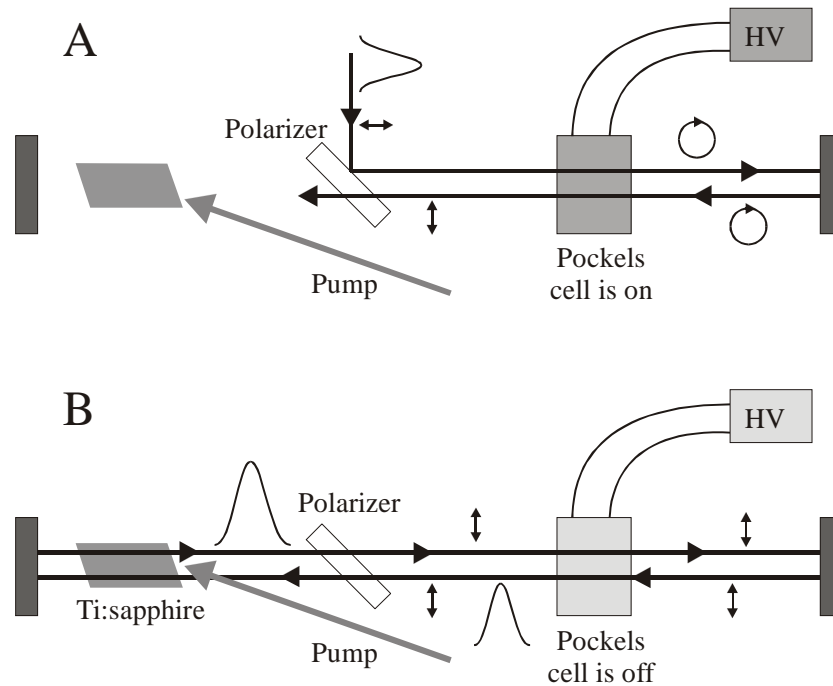


Figure 4.1: Solid state amplifier with regenerative amplification. A) Injection of the seed pulse in the cavity. The Pockels cell is on, and acts as a quarter-wave plate. B) Oscillation and amplification of the pulse in the cavity. The Pockels cell is off and does not change the polarization of the pulse. Note that the dumping of the amplified pulse is similar to the injection of the seed pulse (A).

With this technique, tens of passes can be performed in the gain medium, leading to mJ pulses without any ASE. The dumping out of the cavity is achieved by turning on the Pockels cell. The efficiency of solid state amplifiers can be as high as 10%.

There are nevertheless two drawbacks in working with solid gain medium.

- 1) The peak power of amplified fs pulses is very high (GW), and the damaging threshold of the crystal is reached. In order to avoid destruction of the gain medium, the fs pulse has first to be stretched by chirping to hundreds of ps. After amplification, the ps pulse is recompressed to a fs duration. These stretching-recompression are achieved by pairs of gratings⁹².

- 2) The amplified pulse is always longer than the Fourier transform limit of the seed pulse. This increase of the pulse duration is due to the loss of parts of the incoming spectrum. For instance, gratings used in the stretching are usually too small to diffract the whole spectrum of the fs pulse, and its duration is thus increased.

The gain narrowing also leads to an increase of the pulse duration. The gain medium amplifies more at the central frequency than at its wings, leading to a narrowing of the amplified pulse spectrum. The Fourier-transform-limited pulse has thus a longer duration.

4.2.1. Characteristics

In this thesis, we have worked with a 1 kHz regenerative Ti:sapphire amplifier (Spitfire™ from Spectra Physics™). It is pumped by a 4 W intracavity doubled Nd:YLF (Nd:LiYF₄) laser (Merlin™ from Spectra Physics™) giving 250 ns pulses at 527 nm at a 1 kHz frequency. The Merlin is pumped by a Kr arc lamp, which is water cooled.

The seeding is achieved by 0.4 W of the previously described Tsunami™ fs laser (see section 3.2.2).

The minimal amplified pulse duration is 100-120 fs with a 70 fs seed pulse.

The output power is 350 mW, and as the laser is working at 1 kHz, this corresponds to energy per pulse of 350 μJ.

The maximum peak power thus obtained is 3 GW.

The output beam diameter is 6 mm with a central wavelength at 800 nm. It can be tuned from 760 nm (0.25 W) to 840 nm (0.3 W), by changing the seed pulse wavelength and the stretcher-compressor gratings position.

4.3. Modifications of the Experiment

As the repetition rate of the amplifier is 1 kHz, the PM tube does no longer produce a continuous signal, but its response time is fast enough to produce 200 μs pulses at 1 kHz frequency. This implies a modification of the detection program, as it has now to be synchronized to the amplifier frequency. Furthermore, some drawbacks of the previous setup have been eliminated. For instance, the circulation cell has been replaced by a rotating one, and acquisitions at longer time delays are possible through a stepped delay line.

4.3.1. Stepped Delay Line

One major drawback of the fs setup described in chapter 3.4 is that the linearity of the translation stage is only accurate over 8 screw turns, limiting the acquisition time to 17 ps. In order to remove this limitation, an optical control of the delay line has been built.

A metallic disc of 5 cm diameter with 120 slits at its circumference, has been taken from an old HPLC pump and has been fixed at the end of the screw axis of the translation stage. A laser pointer (model FP-67/1AF from Laser ComponentTM) and a phototransistor (TIL78 n-p-n from Texas InstrumentsTM) are independently placed on each side of the disc (see Figure 4.2).

Each time a slit passes in front of the pointer beam, the diode produces a small voltage change, which is sent to a homemade discriminator that changes a TTL state. The acquisition is no longer "real time" controlled, but is made in a stepped way.

The resolution of this new controlled delay line is determined by the changes of TTL states per turn. With a 120 slits disc, TTL state changes 240 times per

turn, leading to a maximal resolution of 8.9 fs. As the amplified pulses are not shorter than 100 fs, this resolution is perfectly adapted. Furthermore, the maximal time delay is no longer limited by nonlinearity of the translation stage, but by its total length. One can thus achieve measurements over 130 ps with a 8.9 fs resolution.

Moreover, with this encoder, down motion of the translation stage is also linear, and acquisition can be performed in up and down directions. The S/N ratio is increased by a factor of $\sqrt{2}$ for the same acquisition time.

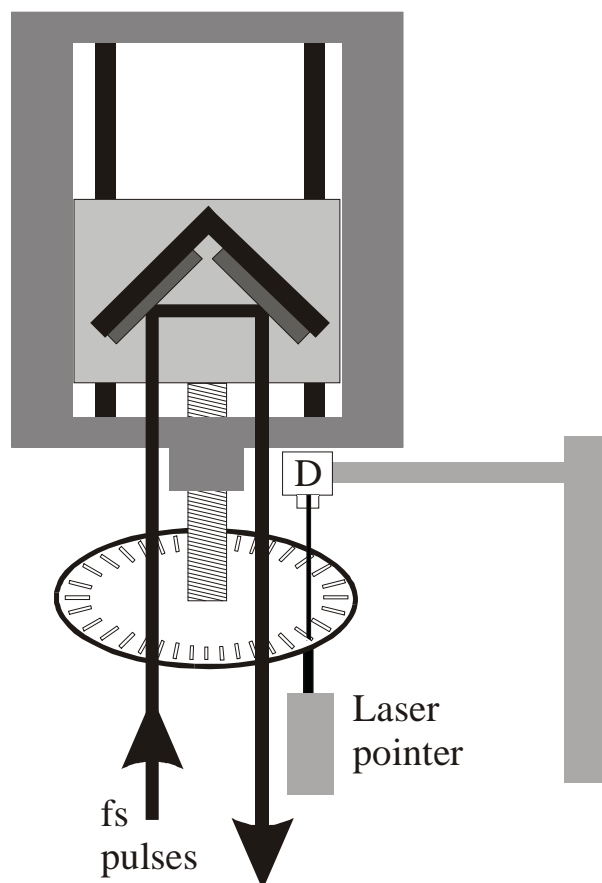


Figure 4.2: Front scheme of the vertical stepped delay line. A metallic disc with 120 slits at its circumference is placed at the end of the delay line screw. A pointer-transistor system is used to detect the screw rotation, allowing 9 fs resolution over 130 ps, without nonlinearity problems.


```

call upbit(2) ! impulsion sur op2           ! produce pulse for delay controller
call qwait(5) ! pulse length 1 ms
call dbit(2)

if (inbit(1).gt.pred) then                 ! the up loop ends when
    pred=inbit(1)                          ! slit-TTL state turns on
    goto 134
endif
pred=inbit(1)
call qwait(7)

135 continue
134 continue
    itheta=itheta+(isgn*istep)             ! calculate the new actual position
136 end

```

4.3.2. Acquisition Program

The modifications brought by the use of the 1 kHz amplifier are important. A new acquisition mode, called stepped mode, has to be developed, and the oscilloscope mode and the parameters need to be adapted.

Parameters

The acquisition frequency is no longer used, as the amplifier imposes a 1kHz working frequency. The parameter allowing the duration of the experiment to be chosen is simply an *acquisition time* parameter in seconds.

Furthermore, in order to allow both real time and stepped acquisition to be performed, conditional parameters have been used. By choosing a *acquisition time* (p_array[5]) of 0, one turns the computer in stepped mode, and a new parameter, *number of steps* (p_array[2]), is asked. To go back to the real time acquisition mode, the *number of steps* has to be set to 0.

The maximum number of allowed steps is 7500, leading to a 130 ps acquisition. Note that one step corresponds to two slit-TTL state changes.

```

if p_array[2]=0 then
  begin
    writeln('2) acquisition time [s]      : ',p_array[5]);
    writeln('  acquisition time in ps = ', p_array[5]/1000*p_array[10]:4:2);
  end
else
  begin
    writeln('2) number of steps          : ',p_array[2]);
    duration:=round(p_array[2]/120*18.3*2*p_array[3]);
    write('  acquisition time = ',duration div 60);
    writeln(' min ',duration mod 60,' sec');
    writeln('  acquisition time in ps = ', p_array[2]/1000*18.3:4:1);
  end;
end;

...

case rep2 of
  2:
    begin
      if p_array[2]=0 then
        begin
          writeln('type 0 to switch to slower acquisitions [step mode]');
          write('acquisition time in integer [1s = 116 fs, minimum 3 sec] : ');
          readln(p_array[5]);
          if p_array[5]=0 then
            begin
              writeln('type 0 to switch to ultrafast acquisitions in real time');
              write('number of steps [max:7500] : ');
              readln(p_array[2]);
            end;
          end
        else
          begin
            writeln('type 0 to switch to ultrafast acquisition in real time');
            write('number of steps [max:7500] : ');
            readln(p_array[2]);
            if p_array[2]=0 then
              begin
                writeln('type 0 to switch to slower acquisition [step mode]');
                write('acquisition time in integer [1s = 116 fs, minimum 3 sec]: ');
                readln(p_array[5]);
              end;
            end;
          end;
        end;
      end;
    end;
  end;
end;

```

{ displays the acquisition time or the number of steps }

{ turns the computer }
{ in stepped mode }

{ turns the computer }
{ in real time mode }

{ to change the acquisition time / step parameter }

Stepped acquisition mode

There are three main differences with the real time acquisition mode described in the chapter 3.4.3:

- 1) Triggering: in stepped mode, three trigger pulses are needed:

a) *trigger_acquisition*: it is produced by the delay computer to initiate the measurement. It is similar to that used in real time acquisition mode.

b) *trigger_pointer*: the acquisition computer has to know when a step is performed. This trigger is produced by the TZD, based on the pointer-transistor signal.

In order to adapt the time resolution to the length of the acquisition, a *double* and an *aerate* variable are defined.

Double: When the desired number of steps is smaller than 600 (= 10 ps), the time resolution is set to 8.9 fs by recording two values for each step. This is achieved by detection of each slit-TTL state change.

Aerate: For acquisition of more than 2000 steps (= 33 ps), the computer averages two consecutive steps in order to achieve a 36 fs resolution with a better S/N ratio. Similar treatment is performed for acquisition longer than 4000 steps (72 fs resolution over more than 53 ps) or 6000 steps (144 fs resolution over more than 106 ps).

c) *trigger_kHz*: the acquisition has to be synchronized to the 1 kHz amplifier frequency. This is achieved by the trigger pulse produced by the amplifier itself. Note that this trigger pulse is not A/D converted, but detected as a digital input. This detection is faster (0.3 μ s instead of 30 μ s for A/D conversion), and thus suitable to detect the 5 μ s trigger pulse from the amplifier.

2) Averaging: one screw turn is achieved in 18.3 seconds. This corresponds to 150 ms per slit. It is thus possible to average many pulses for each step, significantly increasing the S/N ratio. If no spikes are present in the signal, up to 30 pulses are averaged per step. Of

course, in the *double* case, this averaging is only performed over 15 pulses. Note that for each step, 10 spikes detections (based on two times three consecutive pulses) are achieved.

- 3) Down acquisition: the steps being physically defined, their position is also known during down motion of the translation stage. The acquisition program is modified in order to allow acquisition during up and down motion. The signal thus obtained after one scan is spike free and already averaged up to 60 times.

```

procedure conversion;                                     {stepped acquisition mode}
var                                                       {averaged up to 60 times per step}
  xx, yy, xx1, yy1, average, j, jj, sp, dat_moy, aeratetest: integer;
  dat_moy2000, kk, good, datmoyen: integer;
  time_ps :real;
  increm: string[2];
  increm1: string[1];
  ok2 :boolean;
  k1:text;

begin {n°1}
  axes;
  trigger_acquisition;                                 {wait for the trigger pulse
                                                       to initiate the acquisition}
  preced_pointer:=0;                                  {initiate the pointer trigger}
  for up_down:=1 to 2 do                               {loop for up(1) or down(2) acquisition}
    begin {n°2}
      spik:=0;
      aeratetest:=0;
      dat_moy2000:=0;
      fin:=0;
      if up_down=2 then axes else if double=1 then fin:=1;
      for k:=1 to (double*steps+fin) do                {acquisition}
        begin {n°3}
          aeratetest:=aeratetest+1;
          trigger_pointer;                             {wait for the slit-TZD trigger pulse}
          if keypressed then
            begin
              trash:=readkey;                          {manual emergency escape}
              sca:=scans;
              up_down:=2;
              k:=(double*steps)+fin;
            end;
          channel(start_ch);
          dat_moy:=0;
          for average:=1 to round(10/double) do        {average 10 (or five) times for each step}
            begin {n°4}
              sp:=3;
              good:=0;
              datmoyen:=0;

```

```

for i:=1 to 6 do                                     {eliminate a spike or average up to 3 times}
begin {n°5}
  trigger_khz;                                     {wait for the amplifier trigger}
  fun := nadc_ary;                                 {performe A/D conversion }
  dio[1] := 1;
  dio[2] := ofs(dat0);                             {destination of acquired data: dat0}
  dio[3] := timer_trg;
  flag := ax5210(fun,dio);
  if i=(sp-2) then dat1:=dat0;
  if i=(sp-1) then dat2:=dat0;
  if i = sp then
    begin                                           {spike detection test}
      dat3:=dat0;
      if (abs(dat2-dat1) > spike) or (abs(dat3-dat2)> spike) then
        begin
          sp:=i+3;
          spik:=spik+1;
          putpixel((80+3*spik),343,white);
          outtextxy (10,340,'spikes :');
        end
      else
        begin
          sp:=i+3;
          datmoyen:=datmoyen+dat1+dat2+dat3;         {average the data}
          good:=good+3;
        end;
      end;
    end; {n°5}
  if good=0 then
    begin                                           {if only spikes, then average last values}
      good:=3;
      datmoyen:=dat1+dat2+dat3;
    end;
    dat_moy:=dat_moy+round(datmoyen/good)           {average the data}
end; {n°4}
dat2:=round(dat_moy/10*double);
dat_moy2000:=dat_moy2000+dat2;                     {average if more than 2000 points}

if aeratetest>=aerate then                           {record and plot data}
begin {n°6}
  aeratetest:=0;
  dat2:=round(dat_moy2000/aerate);
  dat_moy2000:=0;
  if up_down=1 then                                  {up motion}
    begin
      kk:=round(k/aerate);
      xx:=80+round((500/(trunc(double*steps/aerate)-1))*(kk-1));
      xx1:=80+round((500/(trunc(double*steps/aerate)-1))*(kk-2));
      dat1:=2048+dat2;
      dat[kk]:=dat1+dat[kk];
      backup[kk]:=dat1;
      yy:=175-trunc(((dat[kk]/(2*sca-1))-2048)/16*zoom);
      yy1:=175-trunc(((dat[kk-1]/(2*sca-1))-2048)/16*zoom);
      if (kk>1) then line (xx1,yy1,xx,yy);
    end
  else                                              {down motion}
    begin
      kk:=round(double*steps/aerate)+1-round(k/aerate);
      xx:=80+round((500/(trunc(double*steps/aerate)-1))*(kk));

```

```

        xx1:=80+round((500/(trunc(double*steps/aerate)-1))*(kk-1));
        dat1:=2048+dat2;
        dat[kk]:=dat1+dat[kk];
        backup[kk]:=dat1+backup[kk];
        yy:=175-trunc(((dat[kk]/(2*sca))-2048)/16*zoom);
        yy1:=175-trunc(((dat[kk+1]/(2*sca))-2048)/16*zoom);
        if (kk<double*steps/aerate) then line(xx1,yy,xx,yy1);
    end;
end; {n°6}
end; {n°3}

if (up_down=2) then begin                                {save a scan-backup}
    str(sca, increm);
    nom3:='scan'+increm+{'_'+'increm1+'}.ctr';
    assign(k1,nom3);
    rewrite(k1);
    for jj:=1 to trunc(double*steps/aerate) do
        writeln(k1,backup[jj]:5);
    close(k1);
end;
end; {n°2}
end; {n°1}

```

As shown in the end of the program, a backup of each scan is also saved. If one has to stop an acquisition, all scans are saved separately in *.ctr files and can be restored. Furthermore, this allows to check that all scans were identical and that no acquisition problems (switching on a lamp in the lab, ...) happened.

4.3.3. Rotating Cell

The use of a circulation cell described previously (3.5.2) avoid heating and degradation of the solution, but is limited to samples of high absorption coefficient in non corrosive solvents. In order to overcome these limitations, the mechanical workshop of the Chemistry department built a new cell, which is rotating. The challenge is to place the glass windows perfectly parallel to each other to avoid displacement of the transmitted beams during rotation.

The two 2" diameter Suprasil windows, are fixed by 8 screws on a Teflon™ cylinder, forming a 1 mm thick cell. The cylinder can be inserted in a ball-bearing fixed in a plastic holder. A 12 V electrical motor (from Premetec™) is also fastened to this holder, and rotation is achieved through straps. To change the sample, two holes are made on the circumference of the cell, and a metallic syringe is used to change the solution.

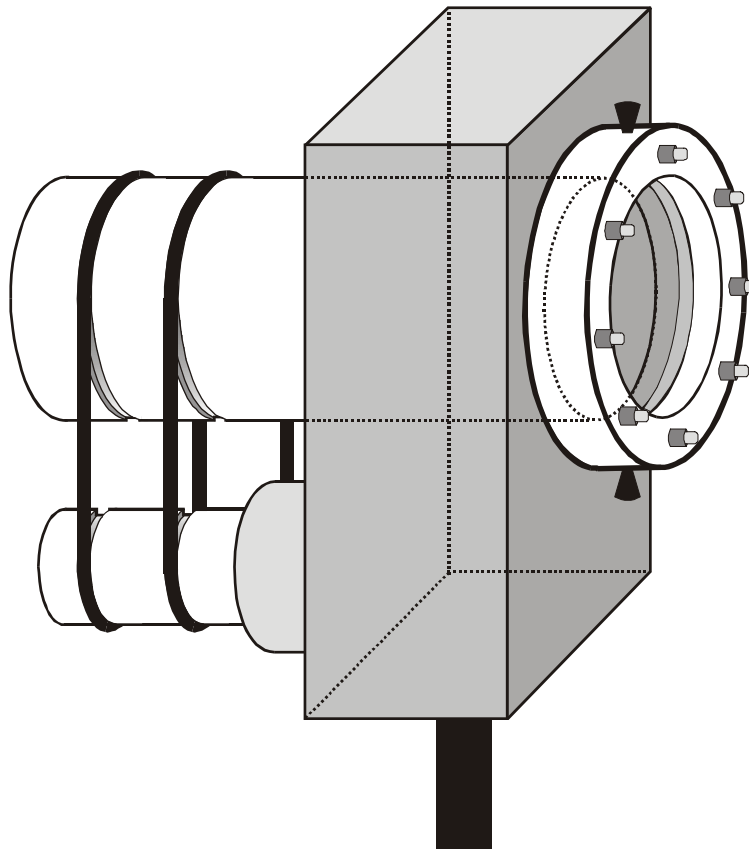


Figure 4.3: Schematic representation of the rotating cell. The Teflon™ cylinder containing the windows can be extracted to simplify the washing of the cell.

Rotation of the cell can be performed at a rate of 2 Hz. Placing the laser pulses near to the external border, the irradiated solution is renewed at a rate of 0.2 mm per ms. It is sometimes convenient to let a small bubble on the top of the cell to favor mixing of the solution during rotation.

4.3.4. Bi-directionally Adjustable Iris

Isolation of the signal after the sample is crucial to eliminate all parasitic light. In order to place the iris precisely, we asked the mechanical workshop to mount an iris on two small size Newport™ translation stages (MS-500), the all being fixed on an aluminum support. This system allows most of the signal spikes arising from the circulation cell to be eliminated, increasing significantly the S/N ratio.

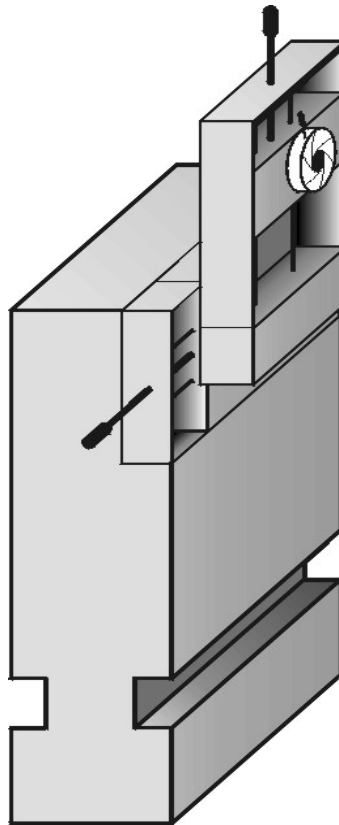


Figure 4.4: Scheme of the bi-directionally adjustable iris. The iris is mounted on two translation stages, in order to be adjusted precisely in both directions. Significant increase of the S/N ratio is achieved by use of this homemade device.

4.4. Femtosecond Investigation of Excited-State Dynamics of Radical Ions in the Condensed Phase

We showed in chapter 2.2 that the excited-state lifetime of $\text{PE}^{\bullet+}$, $\text{PE}^{\bullet-}$ and $\text{AQ}^{\bullet-}$ in solution are shorter than the time resolution of our ps experiment. In order to know these values precisely, we performed a similar experiment in the fs time scale. Working at 1 kHz, no thermal grating accumulation is possible, and intensity TG (with all parallel polarization) can be used.

As $\text{PE}^{\bullet+}$ gives only a weak signal at 765 nm, we turned on to tetracene radical cation ($\text{TRC}^{\bullet+}$) formed in H_2SO_4 and D_2SO_4 .

4.4.1. Perylene Radical Cation in H_2SO_4

Picosecond measurements indicated that the excited-state lifetime of $\text{PE}^{\bullet+*}$ formed in H_2SO_4 is shorter than 15 ps³⁴. The main absorption band of this species is centered at 540 nm, but a weak band is present around 740 nm⁹³.

In order to investigate the time evolution of this band, we tuned the laser to 765 nm and performed a TG experiment. Tuning the laser to even lower wavelength is difficult, as the output energy drops dramatically ($< 100 \mu\text{J}$) below 760 nm.

The experiment setup is depicted in Figure 4.5.

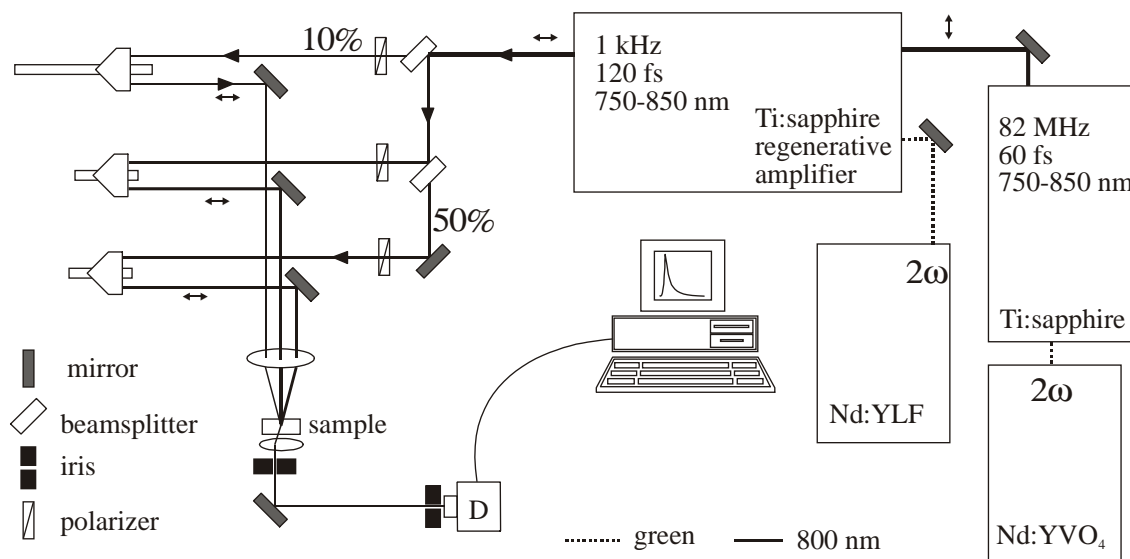


Figure 4.5: Setup of a TG experiment with amplified fs pulses.

The absorbance of the sample, formed in concentrated sulfuric acid (97%), is set to 0.5 on 1 mm at this wavelength.

Unfortunately, the very low absorption coefficient of $\text{PE}^{\bullet+}$ at 765 nm (around 4000) gives rise to two major problems:

- 1) High concentrations of PE have to be used ($\sim 10^{-4}$ M) in order to obtain a significant absorption. Increasing the $\text{PE}^{\bullet+}$ concentration also increases the formation of its cation dimer. Fortunately, the absorbance around 765 nm is mainly due to the monomer⁹³.
- 2) High power pulses are needed to create a significant transient absorption change in the sample. As a consequence, the high peak power needed, induces important nonresonant electronic Kerr effect in the solvent. To limit this problem, the pulse duration is increased to around 1 ps. The pulse power is kept constant, but the peak power drops significantly.

The observed dynamics have a very poor S/N ratio, and only an estimation of the excited-state lifetime can be obtained.

The data depicted below are fitted with a double exponential. The first contribution, of 660 fs, is due to the nonresonant response of the solvent during the pulse. This can be demonstrated by the presence at negative delay, of a broad wing of the pulse.

However, the 17 ± 3 ps time constant is due to repopulation of the ground-state of the cation, and thus corresponds to the excited-state lifetime.

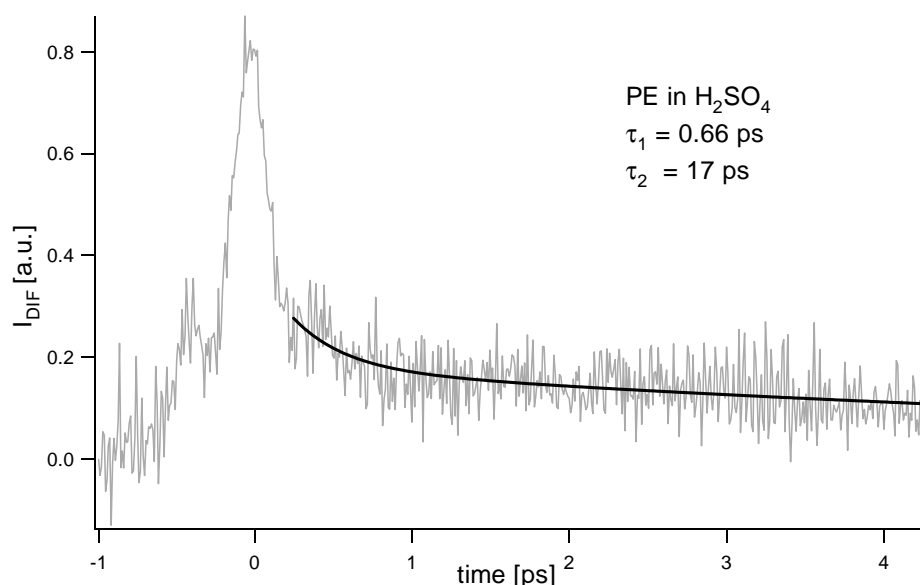


Figure 4.6: TG of the ground-state recovery dynamics of PE^{•+} formed in concentrated sulfuric acid and best biexponential fit. The pulse, centered at 765 nm, is stretched to 1 ps to limit the nonresonant electronic Kerr signal of the solvent. The 660 fs time constant accounts for the side of the excitation pulse, and the longer one (17 ± 3 ps) for the excited-state lifetime of PE^{•+}.

The noise present in this measurement does not allow to give a precise value of the lifetime, but confirms the results obtained with the ps TG experiment (around 15 ps or less).

In order to obtain accurate excited-state lifetimes of radical ions, we turned to TRC, whose cation possesses a strong absorption band centered at 865 nm⁵⁸ with an absorption coefficient of $15'000 \text{ l} \cdot \text{mol}^{-1} \cdot \text{cm}^{-1}$ ⁹⁴.

4.4.2. Tetracene Radical Cation in H_2SO_4 and D_2SO_4

The radical cation of TRC can be readily prepared by dissolution in concentrated H_2SO_4 ⁹⁴. The protonated form is dominant in the first hours following the dissolution, as shown by the 460 nm band. After a few hours, or 1 min UV irradiation, this band disappears, and only the $\text{TRC}^{\bullet+}$ remains⁹⁴.

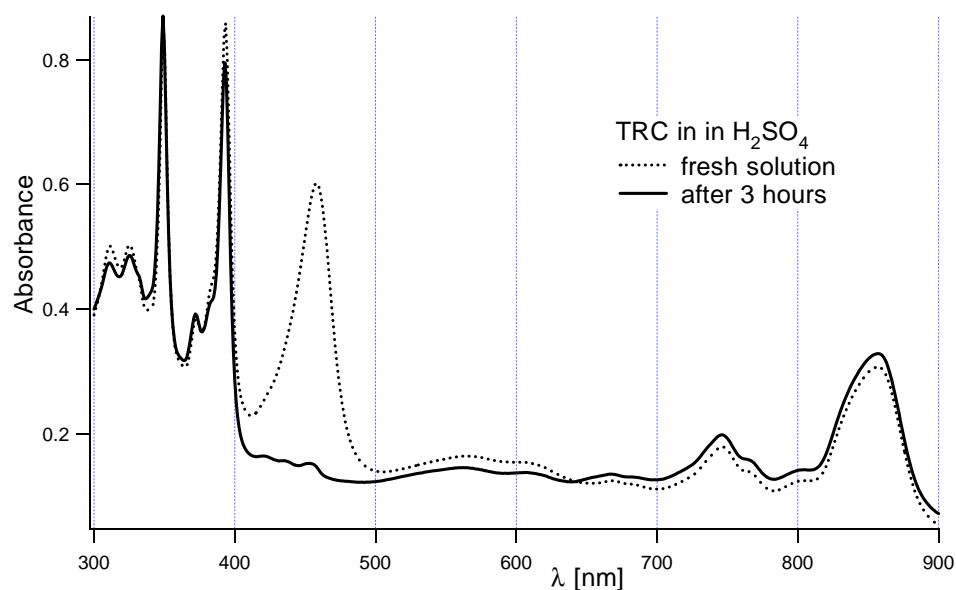


Figure 4.7: Absorption spectrum of fresh and 3 hours old solution of TRC in concentrated H_2SO_4 . The cation band at 850 nm increases as the band at 460 nm, from the protonated complex, vanishes.

Time Resolved TG Spectroscopy with TRC in H₂SO₄

In order to obtain the transient spectrum of the excited-state of TRC^{•+}, we performed white light TG spectroscopy with amplified fs pulses. This technique is similar to that described in chapter 2.3.2 with ps pulses. The fs version is described in details elsewhere⁹⁵.

The production of white light is easy with μJ pulses of 150 fs or less, as their peak power is more than a GW. Focalization of few μJ fs pulses in a 1 cm cell filled with water, gives a good quality white light from 400 nm to 750 nm. This can be used as probe beam in a TG experiment.

Chirping of the white light pulse is not a problem, as long as spectral resolution is achieved in the detection.

The two pump pulses at 400 nm are crossing with an angle of 2° in the sample. As the H₂SO₄ is viscous (25 cp at 20°C)⁹⁶, the 20 μJ pump pulses induce an important local heating. This problem is reduced by using the rotating cell described previously.

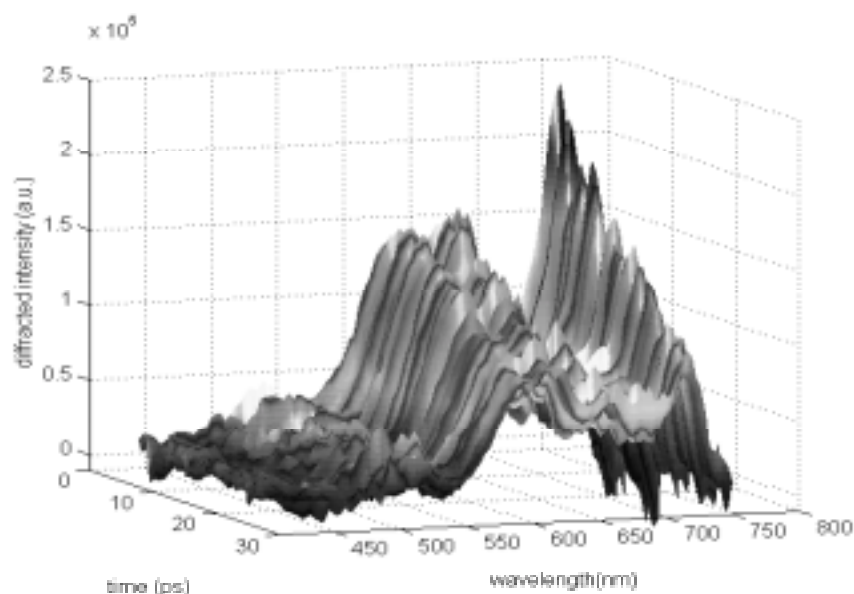


Figure 4.8: Time resolved TG spectrum of TRC^{•+} in concentrated sulfuric acid after excitation at 400 nm.

The depletion of $\text{TRC}^{\bullet+}$ by the 400 nm pulse is visible by the presence of a band at 740 nm in the TG spectra (Figure 4.8). This band decays in the ps time scale.

A new band, from 600 nm to 650 nm is also present. As it was not in the ground-state absorption spectrum, it can be either stimulated fluorescence or transient absorption of $\text{TRC}^{\bullet+*}$. It can be shown in Figure 4.9 that after 20 ps, a background signal is still present from 600 to 750 nm. It can thus be assumed that a fluorescence with a long lifetime is underlying the transient absorption in this spectral domain. According to the literature^{34,97}, most fluorescence from radical cation in concentrated sulfuric acid is in fact due to the protonated form. Furthermore, the decay of this background band being slower than the ground-state recovery time of $\text{TRC}^{\bullet+}$, it is reasonable to assign it to another species.

This fluorescence being still present under the 760 nm band, it affects the observation of the excited-state dynamics. This perturbation seems to be absent at longer wavelength.

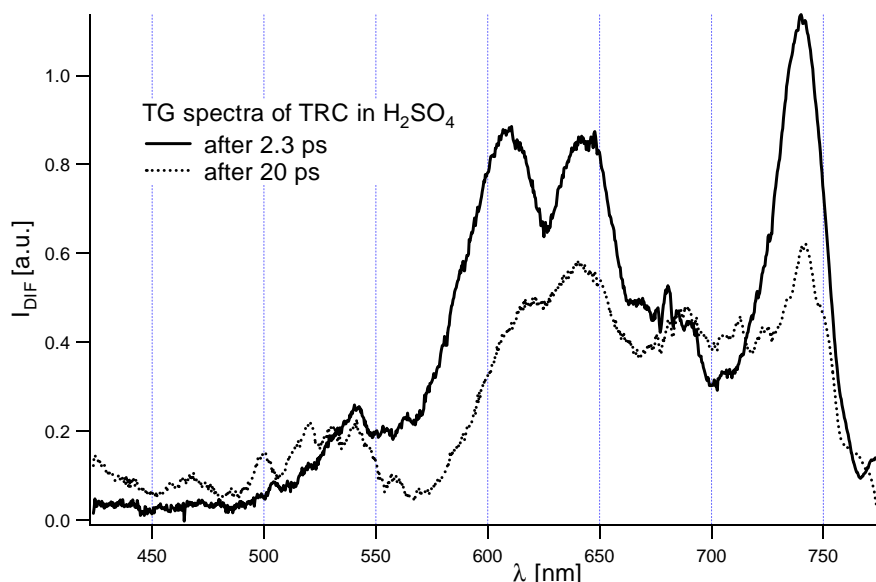


Figure 4.9: TG spectra of $\text{TRC}^{\bullet+}$ in H_2SO_4 at different time delays after excitation at 400 nm. Note that a constant background is visible around 700 nm, disturbing the decay dynamics of the 740 nm band.

In order to extract the lifetime of $\text{TRC}^{\bullet+}$, a single wavelength slice at 740 nm is made and shown in Figure 4.10. As the fluorescence is underlying the observed band, one has to assume a constant background (estimated here to about 0.25) while performing the exponential fit.

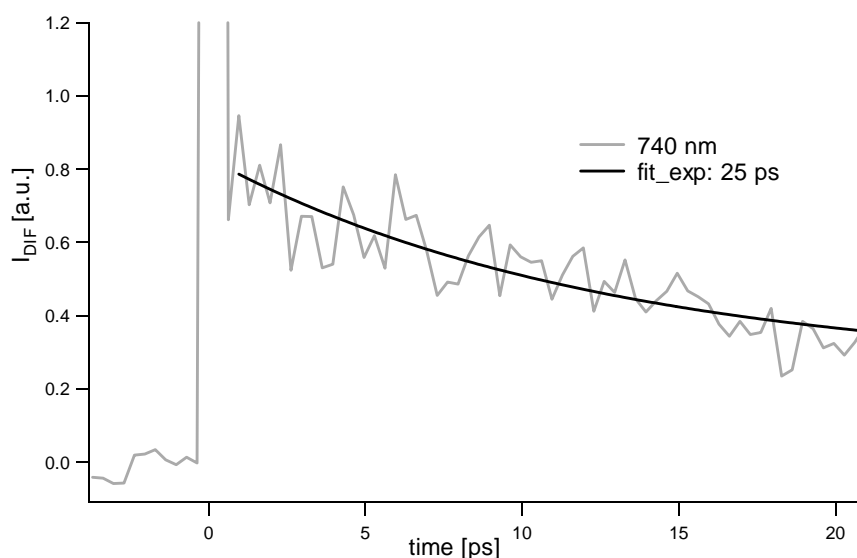


Figure 4.10: Kinetic at 740 nm, extracted from the white light time resolved TG spectra shown above. The best exponential fit gives a lifetime for $\text{TRC}^{\bullet+}$ around 25 ps, assuming a 0.25 constant background.

Even if the S/N ratio is pretty poor, the time delay too short and the background contribution only estimated, a reasonable value of 25 ± 5 ps can be extracted for the excited-state lifetime of $\text{TRC}^{\bullet+}$.

To confirm this preliminary result, single wavelength TG experiment is performed.

Time Resolved TG of TRC^{•+} in H₂SO₄ at 840 nm

As we can tune the amplified fs system up to 840 nm, we have performed fs time resolved TG at this wavelength, which is near to the absorption maximum of TRC^{•+}. Pumping and probing at this wavelength does not suffer from any fluorescence problem, and the obtained kinetics are background free. Nevertheless, it can be noticed from the below data, that the first 10 ps are not monoexponential. This complex behavior has not been further investigated, as it is assumed to be due to solvation processes.

The setup used is similar to that depicted in Figure 4.5.

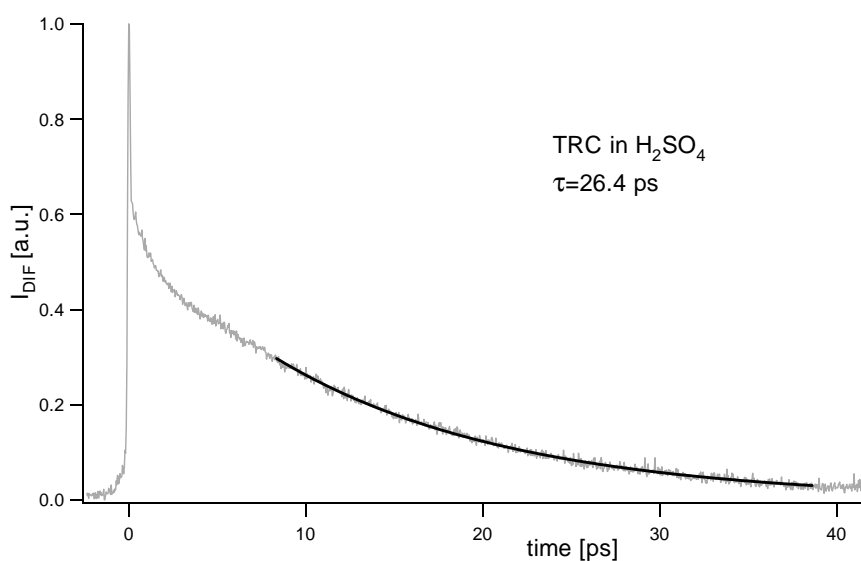


Figure 4.11: Ground-state recovery dynamics of TRC^{•+} in H₂SO₄, obtained by TG experiment with pump and probe pulses at 840 nm. Best exponential fit gives an excited-state lifetime of 26.4 ps. Note that the first 10 ps are possibly affected by solvation processes.

The dynamics obtained have a very good S/N ratio, even with a single acquisition scan. A time constant of 26.4 ps was obtained from

monoexponential fit (Figure 4.11). The logarithm of the data is fitted by a straight line, giving a lifetime for $\text{TRC}^{\bullet+}$ of 26.0 ps (Figure 4.12). In a logarithmic plot, the noise at the end of the kinetic is readily visible, and the fitting limits can be adjusted to avoid it, leading to a more precise value.

The value, 26 ± 0.5 ps thus obtained is in good agreement with the preliminary results from the white light TG.

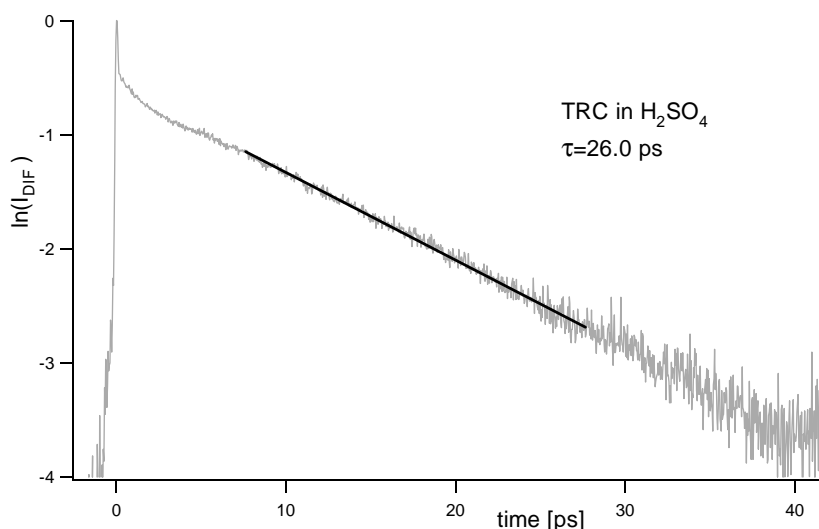


Figure 4.12: Log plot of the data shown in Figure 4.11. Fitting with a straight line gives a lifetime for $\text{TRC}^{\bullet+}$ of 26.0 ps.

To complete these measurements, we performed a similar experiment in deuterated sulfuric acid.

Time Resolved TG of $\text{TRC}^{\bullet+}$ in D_2SO_4

The formation of the cation is also achieved by dissolution in the deuterated acid (95-97% D_2SO_4 in D_2O , deuteration over 99% from Cambridge Isotope Laboratory). A new band at 460 nm accounts for the formation of TRC-D^+ . Waiting a few hours allows complete formation of the cation (band at 850 nm), and disappearance of the deuterated complex (see Figure 4.13).

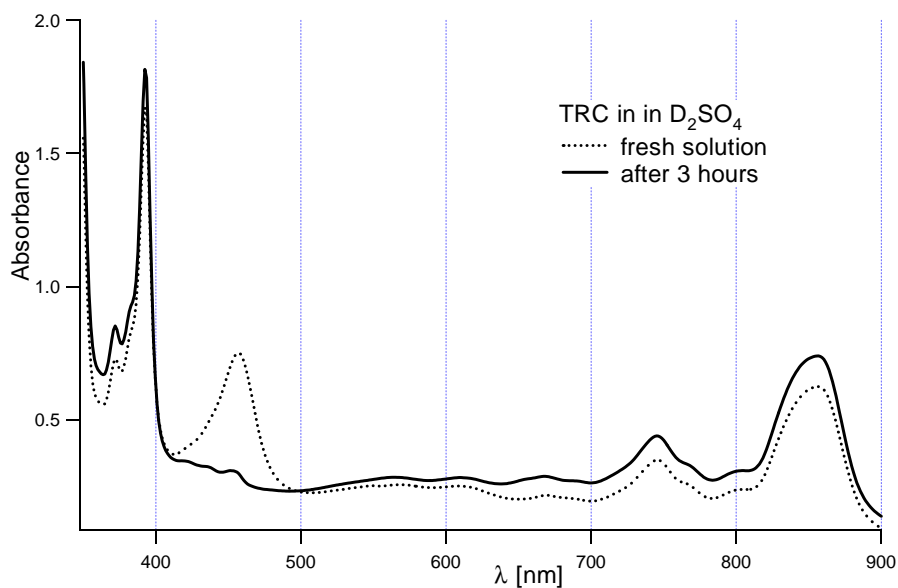


Figure 4.13: Absorption spectrum of fresh and 3 hours old solution of TRC^{•+} in concentrated D₂SO₄. After some time, the band from the deuterated complex, at 460 nm, vanishes, and the cation band at 850 nm increases.

Single wavelength TG experiment, achieved with 840 nm pulses, leads to the following kinetics.

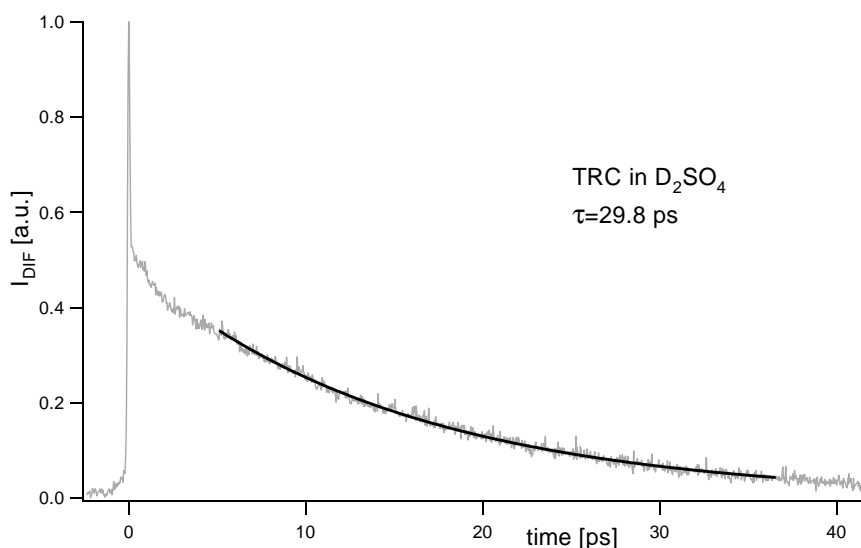


Figure 4.14: Ground-state recovery dynamics of TRC^{•+} in D₂SO₄. The pump and probe pulses for the TG experiment are centered at 840 nm. Best exponential fit gives an excited-state lifetime of 29.8 ps.

Again, the S/N ratio is excellent, already after one scan. The exponential fit gives 29.8 ps for the lifetime of $\text{TRC}^{\bullet+*}$. Logarithmic representation of the data is shown in Figure 4.15, where the straight line fit also gives 29.8 ps for the ground-state recovery time of $\text{TRC}^{\bullet+}$.

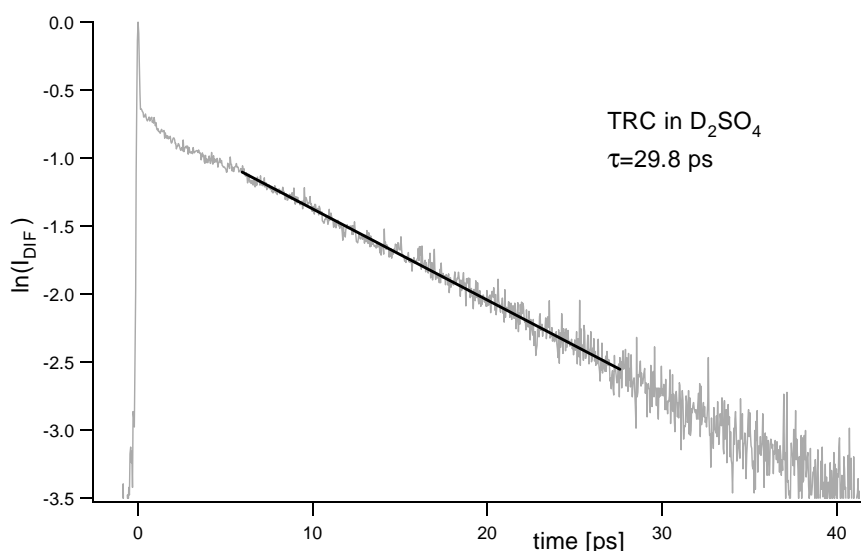


Figure 4.15: Log plot of the data shown in Figure 4.14. Fitting with a straight line gives a lifetime for $\text{TRC}^{\bullet+*}$ of 29.8 ps in D_2SO_4 .

Conclusions

All radical ions investigated so far with direct techniques ($\text{AQ}^{\bullet-}$, $\text{PE}^{\bullet+}$, $\text{PE}^{\bullet-}$ and $\text{TRC}^{\bullet+}$) show excited-state lifetime of less than 30 ps in condensed phase.

It is interesting to notice that in deuterated sulfuric acid, the excited-state lifetime of $\text{TRC}^{\bullet+}$ is almost 15% longer than in undeuterated solvent. The molecule being the same in both cases, one has to look at the heat dissipation by the solvent, in order to explain this behavior.

Once a molecule is excited, it can come back to its ground-state by radiative or nonradiative pathways. In the case of radical ions, genuine fluorescence is very weak³⁴, and the nonradiative deactivation dominates.

In order for the excited molecule to dissipate its excess energy, vibrational modes of the solvent are important. In other words, the excited molecule transmits its energy through collisions with solvent molecules, which become vibrationally excited. In the case of deuterated solvents, the O-D vibration is at lower frequencies than the O-H one. To absorb a given amount of energy, more vibrational quanta have to be excited for O-D than for O-H. This may explain the slower relaxation dynamics of TRC^{•+*} in D₂SO₄.

4.5. Investigation of the Rotational Dynamics of Perylene and Perylene Derivatives in Series of n-Alkanes and Nitriles using the Transient Dichroism Technique

The Stokes-Einstein-Debye (SED) relationship is widely used to explain rotational properties of molecules in liquids^{98,99}. It assumes that the solute rotational time is linearly proportional to the viscosity of the solvent.

A nonlinear relation between rotational time and viscosity is shown for PE in low viscosity solvents. Interactions with the solvent are also investigated through cyano and methyl substituted PE in polar and aliphatic solvents. As predicted, only interactions between the cyano substituted PE and polar solvents are observed.

4.5.1. Overview of Stokes-Einstein-Debye Theory

Einstein used the Stokes relationship to express the diffusion coefficient of spherical molecule as a function of the solvent viscosity¹⁰⁰:

$$D_s = \frac{k_B \cdot T}{6V \cdot \eta} \quad (4.1)$$

where V is the volume of the rotating body and η the solvent viscosity.

Most of the molecules do not possess a spherical shape, but are rather rod-like (prolate) or disc-like (oblate) ellipsoids. These shapes can be differentiated through their axial ratio ρ , that is larger than 1 for prolate, and smaller than 1 for oblate. To adapt eq.(4.1) to these shapes, two diffusion coefficients have to be defined, which corresponds to D_s multiplied by a shape factor $f_{\parallel,\perp}$ (for the two symmetry axis):

$$D_{\parallel} = f_{\parallel} \cdot D_s = \frac{3}{2} \cdot \frac{\rho \cdot (\rho - S)}{\rho^2 - 1} \cdot D_s \quad (4.2)$$

and

$$D_{\perp} = f_{\perp} \cdot D_s = \frac{3}{2} \cdot \frac{\rho \cdot [(2\rho^2 - 1) \cdot S - \rho]}{\rho^4 - 1} \cdot D_s \quad (4.3)$$

where

$$S_{oblate} = \frac{1}{\sqrt{1 - \rho^2}} \cdot \operatorname{atg} \left(\frac{\sqrt{1 - \rho^2}}{\rho} \right) \quad (4.4)$$

or

$$S_{prolate} = \frac{1}{\sqrt{\rho^2 - 1}} \cdot \ln \left(\rho + \sqrt{\rho^2 - 1} \right) \quad (4.5)$$

The diffusion coefficient is connected to the rate constant of rotational diffusion through³⁹:

$$k_{\parallel,\perp}^{rot} = 6 \cdot D_{\parallel,\perp} \quad (4.6)$$

When the transition dipole is parallel to the symmetry axis, the anisotropy decay is expressed as:

$$r(t) = r(0) \cdot e^{-k_{\perp}^{rot} \cdot t} \quad (4.7)$$

In other words, the anisotropy decays through rotational diffusion around the axes that are perpendicular to the symmetry axis.

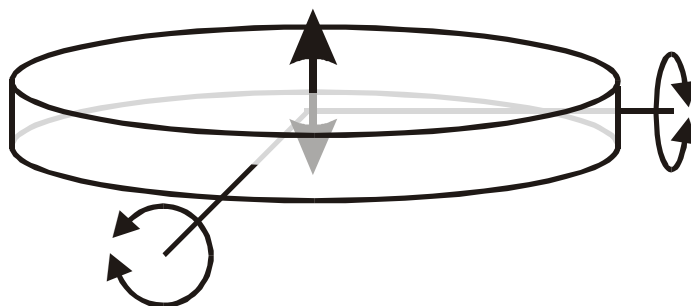


Figure 4.16: Rotational diffusion of an oblate molecule with transition dipole parallel to the symmetry axis. The both rotational motion are equivalent (tumbling).

The anisotropy at time zero depends on the relation between the pump and probe transition dipoles. When both dipoles are parallel, $r(0) = 0.4$, but when they are orthogonal, $r(0) = -0.2$ ³⁹.

When the transition dipole is perpendicular to the symmetry axis (see Figure 4.17), the analysis becomes more complex, as two distinct rotations lead to anisotropy decay, which is thus represented by a biexponential function.

$$r(t) = r(0) \cdot \left[\frac{1}{4} e^{-k_{\perp}^{rot} \cdot t} + \frac{3}{4} e^{-\left(\frac{1}{3}k_{\perp}^{rot} + \frac{2}{3}k_{\parallel}^{rot}\right) \cdot t} \right] \quad (4.8)$$

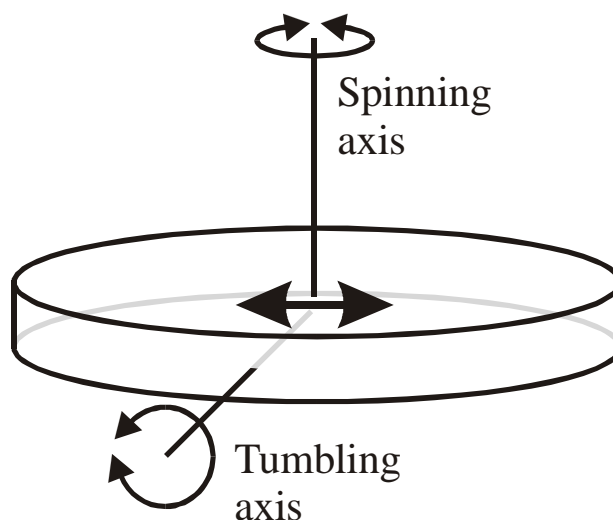


Figure 4.17: Rotational diffusion for an oblate molecule with transition dipole perpendicular to the symmetry axis. Two distinct rotations are involved in the anisotropy decay (tumbling and spinning).

Experimentally monoexponential decay of anisotropy is usually observed, and a modified SED equation has been derived³⁹:

$$\tau_{\text{rot}} = \frac{1}{k^{\text{rot}}} = f \frac{V \cdot C}{k_B \cdot T} \cdot \eta \quad (4.9)$$

where $f = \frac{2}{f_{\parallel} + f_{\perp}}$ is the shape factor for ellipsoids with dipole moment perpendicular to the symmetry axis.

The coefficient C in eq.(4.9) has been added to the initial equation, in order to take into account discrepancy between theory and experiment. In the Einstein model, the first solvation shell is supposed to rotate with the solute molecule. In this case, one speaks of *stick* boundary condition, and the coefficient C is equal to one. However, the observed anisotropy decay with small molecules is often faster than predicted^{101,102}. In such cases, good results are obtained with the coefficient C smaller than 1. One speaks of *slip* boundary condition, as the solvent is supposed to be slippery, and does not rotate with the solute molecule.

In other cases, the coefficient C has to be larger than one in order to correspond to experimental results¹⁰³⁻¹⁰⁵. To explain this behavior, dielectric friction has been invoked. Dipolar or ionic molecules polarizes the surrounding (polar solvent). This generates a reaction field that slows down the motion of the solute dipole, leading to a slower rotation than predicted. Many models have been proposed to calculate the dielectric friction. For instance, Nee and Zwanzig¹⁰⁶ consider the solute molecule as a point dipole moment, whereas Alavi and Waldeck¹⁰⁷ consider it as a distribution of point charges that reorient with the molecule.

It has to be noted that, according to the SED model, extrapolation to zero viscosity should give an infinite rotational time. Of course, this is never the case, and the lower limit for rotational time is given by the free rotor time defined as^{102, 108}:

$$\tau_0 = \frac{2\pi}{9} \sqrt{\frac{I}{k_B T}} \quad (4.10)$$

where I is the moment of inertia of the molecule. This corresponds to the rotation of the molecule in the gas phase. Nevertheless, extrapolation of the SED relation to viscosity zero, often leads to different rotational time, which are even sometimes negative^{109,110}.

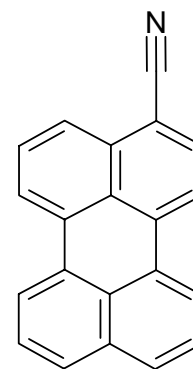
4.5.2. Experimental Conditions

Samples

The solute molecules studied are:

1) Perylene from Fluka™. It has been recrystallized twice in benzene.

2) 3-cyanoperylene. This compound was synthesized in our institute from 3-formylperylene oxime, according to the procedure of Buu-hoi and Long¹¹¹. It was then recrystallized twice in benzene, leading to yellow needles.



3) 3-methylperylene. This compound was produced in our institute from the formylperylene, according to the same literature¹¹¹, and recrystallized twice in benzene.

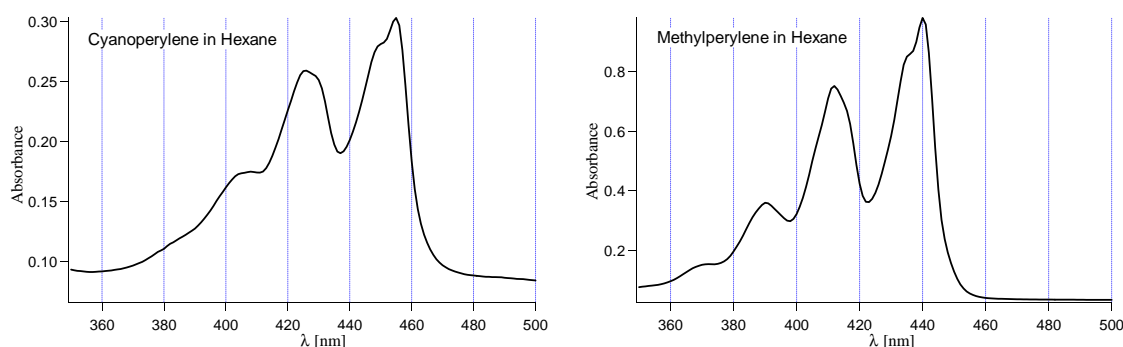
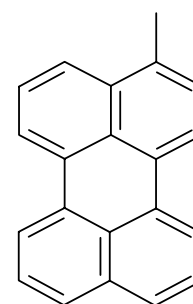


Figure 4.18: Absorption spectra of 3-cyano- and 3-methyl- PE in hexane.

After transmission through the sample, the probe pulse goes through a crossed polarizer. In absence of birefringence of the sample, only a small leak is detected by the PM tube (HamamatsuTM R928). When birefringence is induced by the pump pulse, interaction of the leak (the local oscillator) and the transmitted signal leads to heterodyne TD (see chapter 1.5 for details).

4.5.3. Rotational Dynamics of Perylene in Low Viscosity Solvents

The reorientation time, observed by extrapolation of the SED relation to zero viscosity, is often different from that predicted by the free rotor model. In order to confirm this observation, we first investigated the rotational dynamics of PE in a series of nitriles by heterodyne TD technique with fs pulses at 400 nm.

Rotational Dynamics of PE in a Series of Linear Nitriles

Due to the experimental improvement described in this chapter, three scans were sufficient to obtain good S/N ratio. Great care was taken when changing the solvent in the rotating cell, in order to avoid solvent mixing.

The heterodyne signal is obtained by subtraction of a constructive and destructive TD experiment, performed with 90° rotation of the pump pulse polarization.

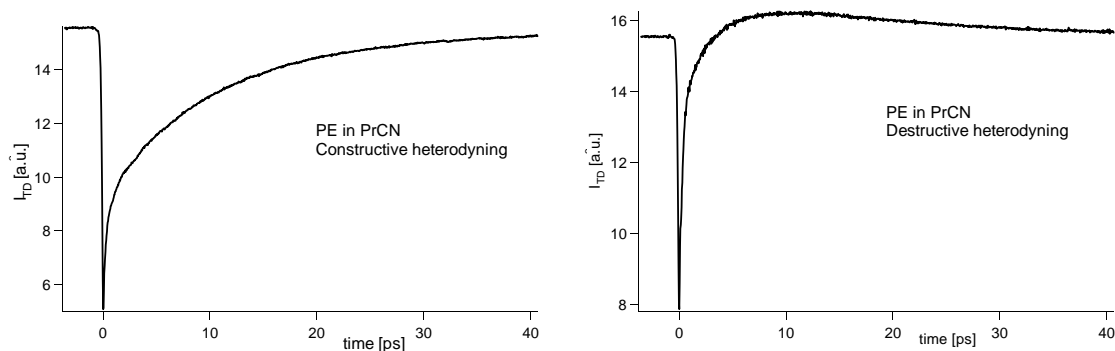


Figure 4.20: Constructive and destructive heterodyne TD of PE in PrCN. Note that the first 5 ps show a complex behavior, possibly due to solvation dynamics.

As it is often the case, the pure heterodyne anisotropy dynamics can be fitted with a single exponential. In order to confirm this behavior, the natural logarithm of the data is also shown, and a linear fit is performed.

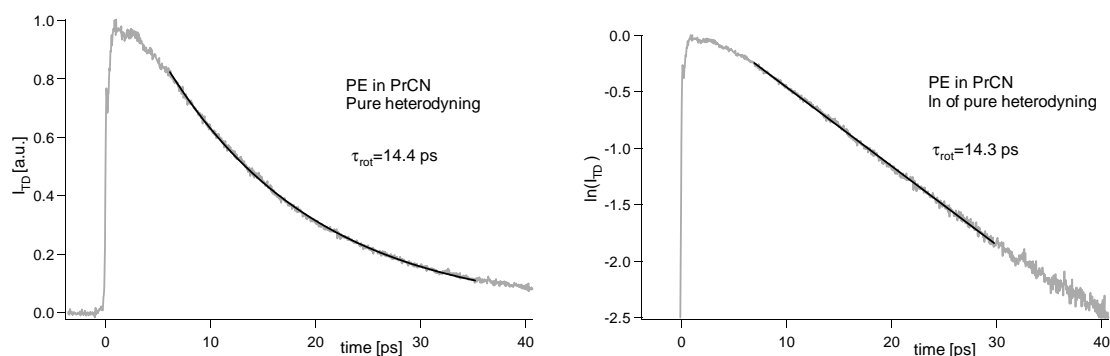


Figure 4.21: Pure heterodyne signal from PE in PrCN and its natural logarithm. The exponential, respectively linear, fits give rotational time of 14.3 ± 0.2 ps.

One has to remember that, in the case of pure heterodyne signal, the observed kinetic is directly proportional to the anisotropy time constant (and not two time faster as with TG experiments).

As already mentioned for $\text{TRC}^{\bullet+}$ (chapter 4.4.2), the first ps exhibit a complex behavior probably due to solvation processes.

In the following part, only the pure heterodyne signal (subtraction of constructive and destructive heterodyne TD) and its logarithm are shown for the other solvents.

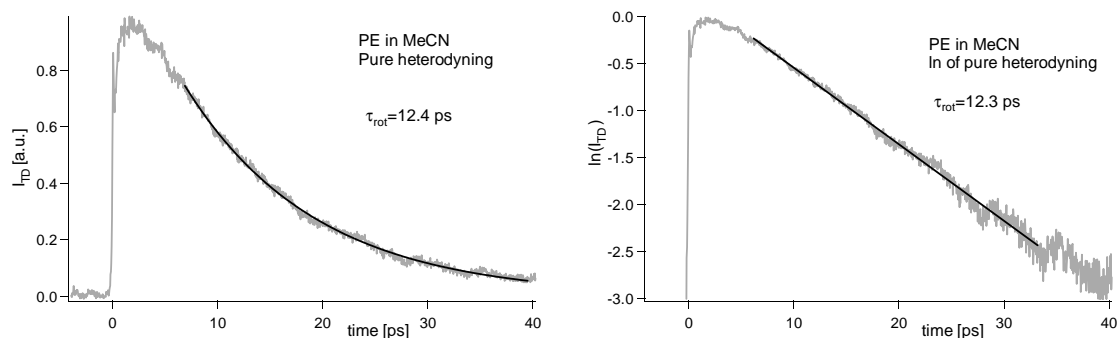


Figure 4.22: Pure heterodyne signal and natural logarithm of PE in MeCN. The rotational time is 12.4 ± 0.4 ps.

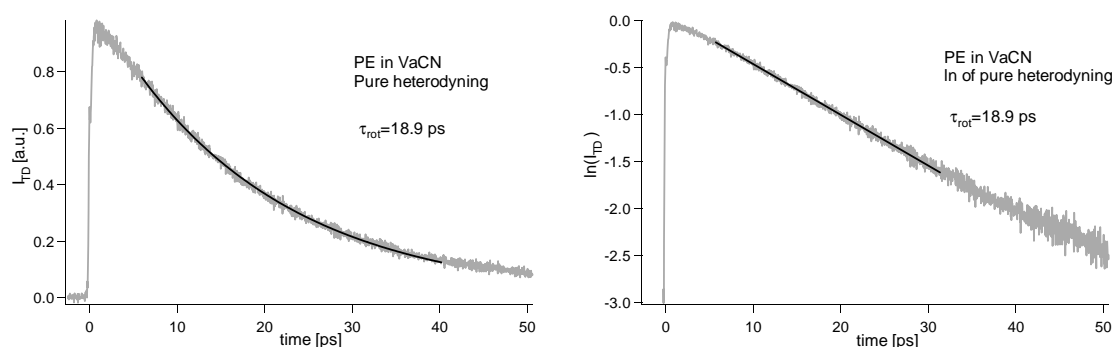


Figure 4.23: Heterodyne anisotropy decay of PE in VaCN has a time of 18.9 ± 0.5 ps.

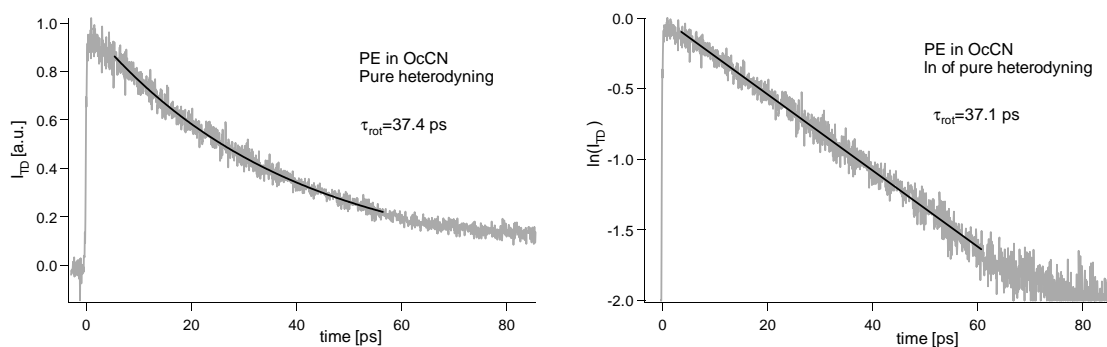


Figure 4.24: Rotational dynamics of PE in OcCN. The rotational time is 37 ± 2 ps. Note that increasing the viscosity also increases the noise from the rotating cell.

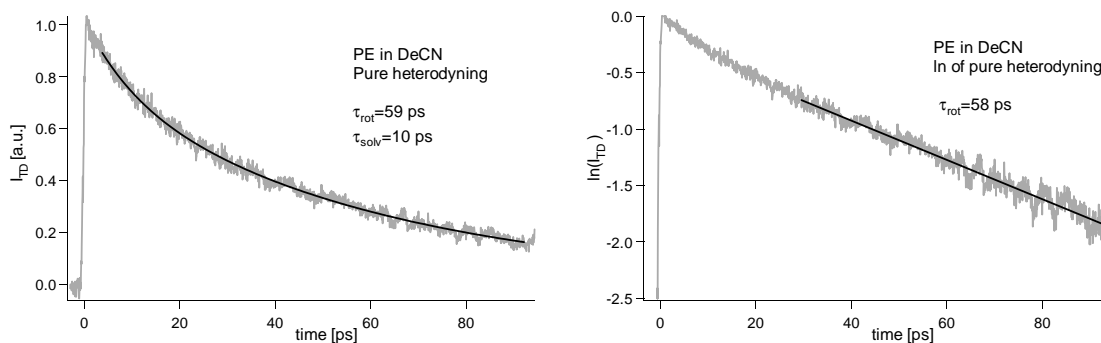


Figure 4.25: In DeCN, a double exponential fit is performed, leading to a rotational time of 59 ps and a fast contribution of 10 ps, probably due to solvation processes. A linear fit is possible on the end portion of the log plot, leading to a rotational time of PE is 58 ± 3 ps.

The data shown above can be summarized and represented as a function of the solvent viscosity.

	MeCN	PrCN	VaCN	OcCN	DeCN
η [cP] 20° 31,90	0.35	0.41	0.74	1.64	2.66
τ_{rot} [ps]	12.4 ± 0.4	14.3 ± 0.2	18.9 ± 0.5	37 ± 2	59 ± 3

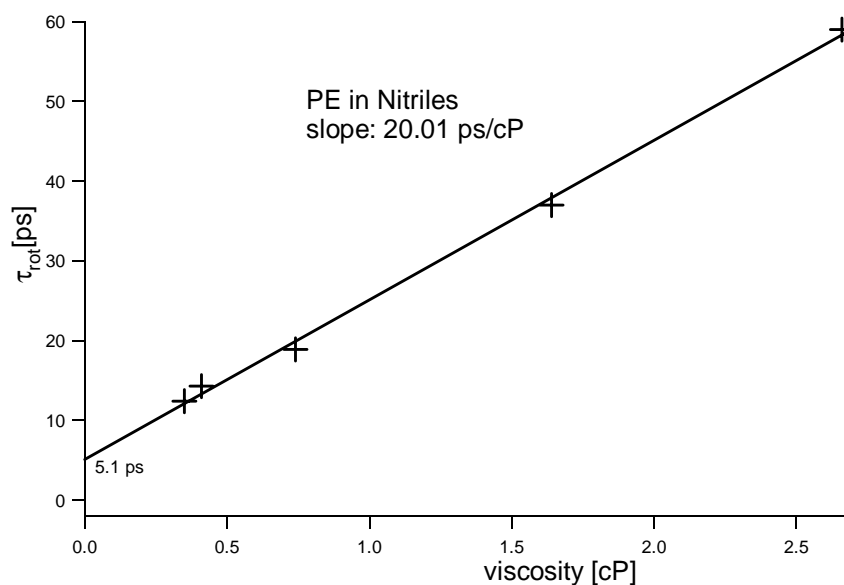


Figure 4.26: SED relation for PE in a series of linear nitriles from MeCN to DeCN. Extrapolation of the fitting line crosses the zero viscosity at 5.1 ps.

According to SED theory, one can estimate the stick boundary constant C . Assuming the benzene thickness to be 3.5 \AA and the medium diameter of the PE to be 7.5 \AA , the axis ratio is $\rho = 0.47$. As PE possesses an oblate shape, one finds that:

$$S_{oblate} = \frac{1}{\sqrt{1-\rho^2}} \cdot \text{atg}\left(\frac{\sqrt{1-\rho^2}}{\rho}\right) = 0.95$$

It can be easily shown that the S_0 - S_1 transition dipole of PE is along the long axis of the molecule, and thus perpendicular to the symmetry axis of the oblate ellipsoid. A double exponential should have been observed, but as shown above, single exponential gives good fits in all nitriles, except in DeCN. In this last case, only the longer time constant is attributed to rotation of the solute molecule.

The shape factor is expressed as $f = \frac{2}{f_{\parallel} + f_{\perp}} = \frac{2}{0.434 + 0.741} = 1.7$

The molecular volume of PE ($C_{20}H_{12}$), calculated by the Van der Waals increments¹¹², amounts to 226 \AA^3 .

According to these values, the slope of the rotational time as a function of viscosity is:

$$\begin{aligned} f \frac{V \cdot C}{k_B \cdot T} &= 1.7 \frac{226 \cdot 10^{-30}}{1.38 \cdot 10^{-23} \cdot 293} \cdot C \\ &= 9.51 \cdot 10^{-8} \cdot C \text{ [s/Pa]} = 95.1 \cdot C \text{ [ps/cP]} \end{aligned}$$

The observed slope being 20.01 ps/cP , one can calculate that

$$C = 0.21$$

The slip boundary condition is well suited to describe the rotation of PE in series of nitriles. This is consistent with other studies of small non polar molecules^{101,102}.

It can also be noted that the extrapolation of the SED relation to zero viscosity, gives a zero rotational time of

$$\tau_0 = 5.1 \text{ ps.}$$

To calculate the theoretical free rotor rotational time, one first need to calculate the moment of inertia of the PE for both the spinning and tumbling axes.

Assuming a C-C bond length of 1.4 Å (as in benzene), and a C-H bond length of 1.08 Å⁹⁶, one can calculate that the moment of inertia around the spinning axis is of $3.88 \cdot 10^{-44} \text{ kg} \cdot \text{m}^2$, and around the tumbling axis of $2.24 \cdot 10^{-44} \text{ kg} \cdot \text{m}^2$.

According to eq.(4.10), the free rotor rotational time is

2.2 ps for the spinning axis, and

1.6 ps for the tumbling one.

The observed value of 5.1 ps is more than 2 time larger than the mean theoretical value.

It must nevertheless be observed that the two points obtained at lowest viscosity (see Figure 4.26) tend to form a larger slope than the fit with all the data, and thus cross the zero viscosity at smaller rotational time.

In order to investigate in more details this low viscosity region, we performed a similar experiment in a series of linear alkanes. Viscosity as small as 0.235 cP can be reached with pentane at 20°C.

Rotational Dynamics of PE in a Series of Linear Alkanes

The same heterodyne TD experiment was performed in a series of linear alkanes from pentane (0.235 cP) to hexadecane (3.44 cP).

Linear fits are performed on the natural logarithm of the pure heterodyne TD, in order to determine the rotational time of PE in each solvent.

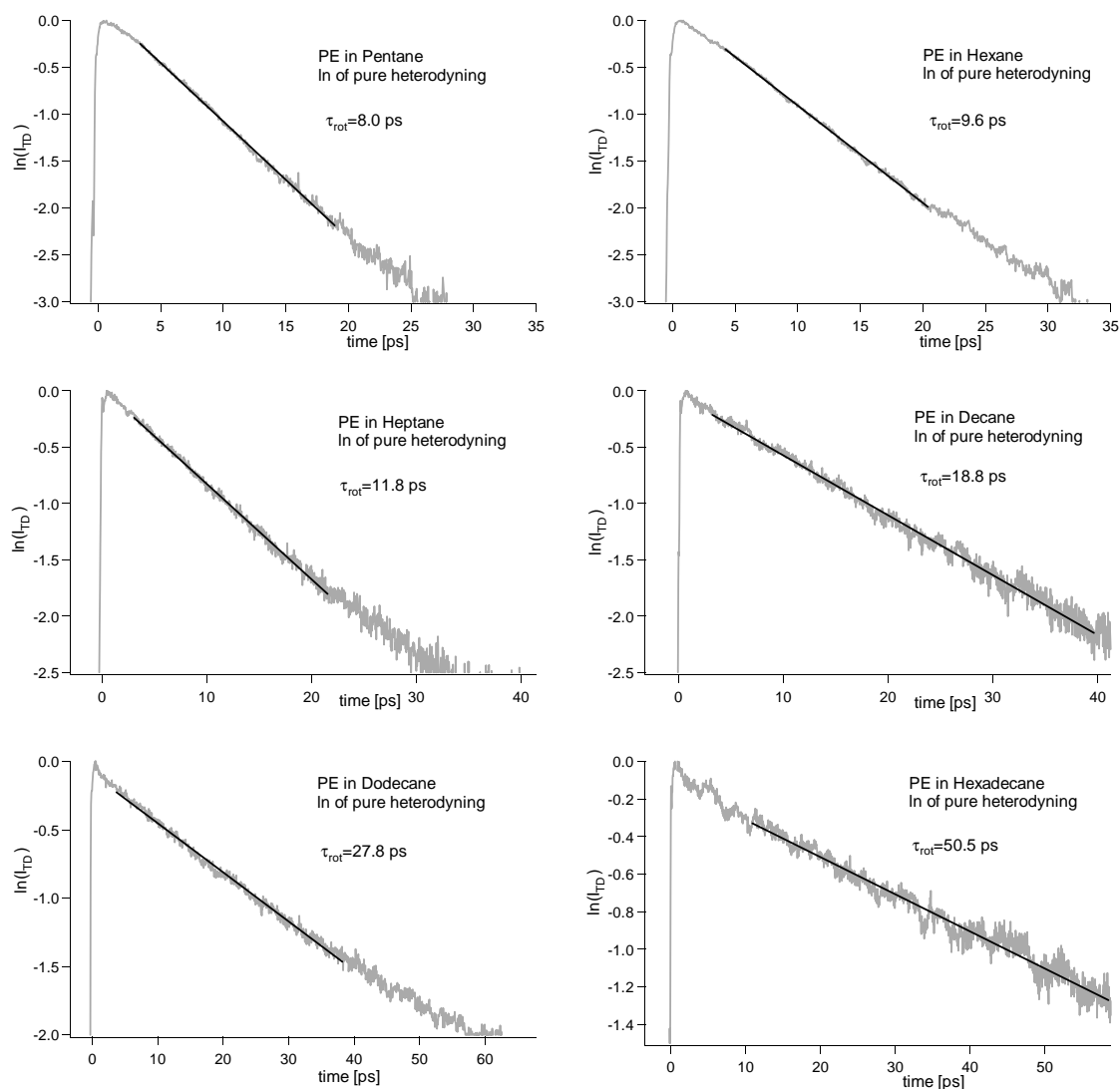


Figure 4.27: Natural logarithm of the pure heterodyne TD signal from PE, in a series of linear alkanes from pentane to hexadecane, and best linear fit.

The rotational time obtained are summarized in the following table and represented as a function of the solvent viscosity.

	C ₅ H ₁₂	C ₆ H ₁₄	C ₇ H ₁₆	C ₁₀ H ₂₂	C ₁₂ H ₂₆	C ₁₆ H ₃₄
η [cP] 20° 90	0.235	0.313	0.418	0.928	1.51	3.44
τ_{rot} [ps]	8.0 ± 0.2	9.6 ± 0.2	11.8 ± 0.3	18.8 ± 0.5	27.8 ± 1	50 ± 3

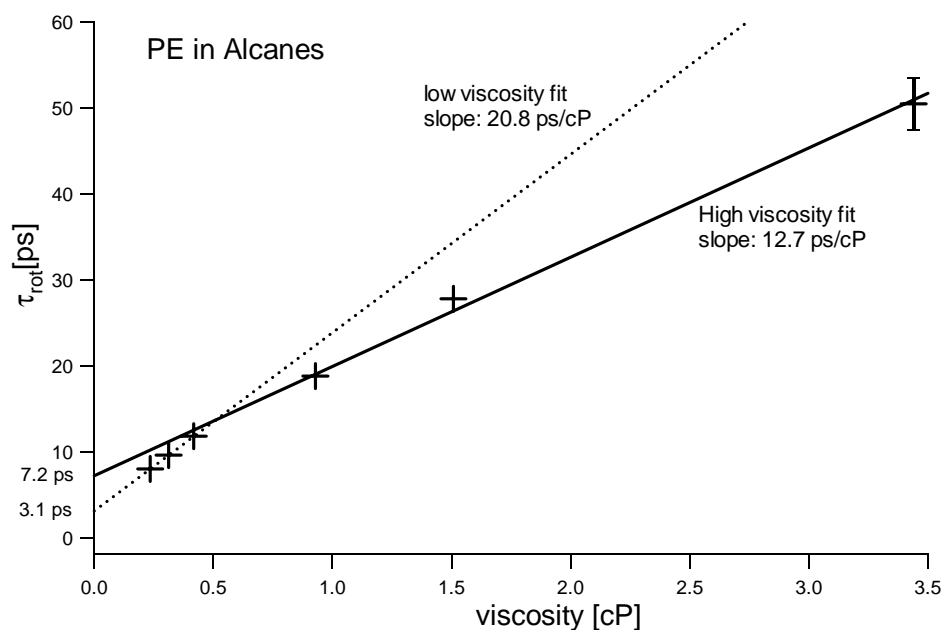


Figure 4.28: SED analysis of the rotational time of PE in a series of linear alkanes from pentane to hexadecane. Two linear fits are shown, one for low viscosity solvents (pentane to heptane), leading to a line crossing of the zero viscosity at 3.1 ps, and one for higher viscosity (from heptane to hexadecane) giving a 7.2 ps free rotor rotation constant.

Performing a linear fit on the rotational time obtained in higher viscosity solvents (above 0.4 cP) leads to a crossing with the zero viscosity at 7.2 ps. This result is even worse than that observed in the series of nitriles. However, analyzing only the low viscosity data (below 0.42 cP) gives a zero rotational time of 3.1 ps.

This value is still slightly above that calculated by the free rotor theory (1.6 ps or 2.2 ps). However, as the relation between the rotation and viscosity is no longer linear when approaching to zero viscosity, a curved behavior might be

more realistic to describe this viscosity domain. One can imagine that the boundary constant C , is no longer a constant, but depends on the size of the solvent molecule. This change of boundary conditions has already been reported for highly viscous solvents^{29,107}.

In order to confirm this curved behavior, investigations in even lower viscosity solvents should be done. This could be achieved, for instance, at higher temperatures. Unfortunately, the rotating cell used here is not suited to such an experiment.

4.5.4. Effect of Substitution on the Rotational Dynamics of PE in Series of Polar and Nonpolar Solvents

Adding a substituent on a PE molecule, should lead to a slowing down of the molecular rotation. This can be explained by two distinct factors:

- 1) Increase of the volume of the molecule
- 2) New interactions with the solvent (dipolar interactions)

In order to study the influence of the second contribution, we have investigated the rotational behavior of substituted PE in series of polar (nitriles) and nonpolar (linear alkanes) solvents.

The molecular volumes of 3-cyanoPE and 3-methylPE calculated with the Van der Waals increments are almost identical (240 \AA^3 for the 3-cyanoPE and 245 \AA^3 for the 3-methylPE). Solute-solvent interactions should also be almost identical in linear alkanes, as there is no dipole-dipole interactions. This is not the case in the series of nitriles, where the cyanoPE can interact strongly with the solvent, whereas the methylPE should not.

3-cyanoPE and 3-methylPE in a Series of Linear Alcanes

The pure heterodyne TD measurements were performed as described in the previous section. The S/N is good for the methyl substitution but much lower for cyanoPE as the signal intensity is smaller.

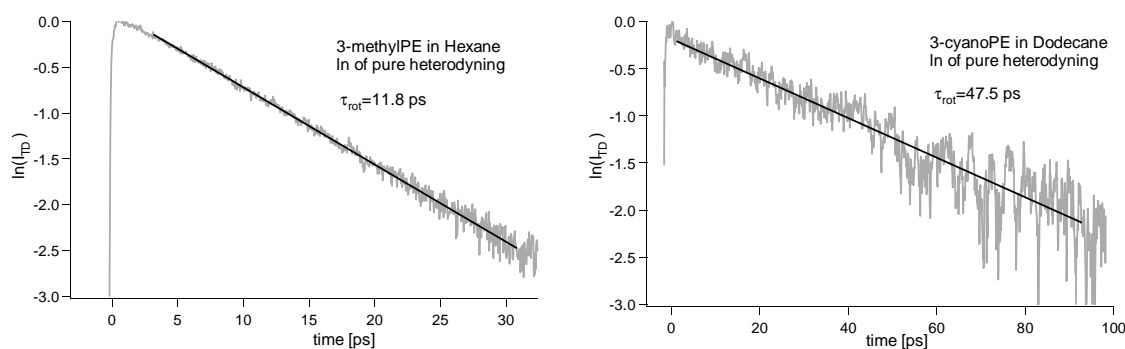


Figure 4.29: Typical natural logarithm of pure heterodyne TD measurement of 3-methylPE (here in hexane) and 3-cyanoPE (here in dodecane).

The data in four linear alkanes are summarized and graphically represented below.

	C_5H_{12}	C_6H_{14}	C_7H_{16}	$C_{12}H_{26}$
η [cP] 20° 90	0.235	0.313	0.418	1.51
τ_{rot} [ps] PE	8.0 ± 0.2	9.6 ± 0.2	11.8 ± 0.3	27.8 ± 1
τ_{rot} [ps] 3-methylPE	9.8 ± 0.3	11.8 ± 0.3	13.4 ± 0.5	37 ± 2
τ_{rot} [ps] 3-cyanoPE	11.0 ± 0.3	14.7 ± 0.4	17.3 ± 0.5	47 ± 5

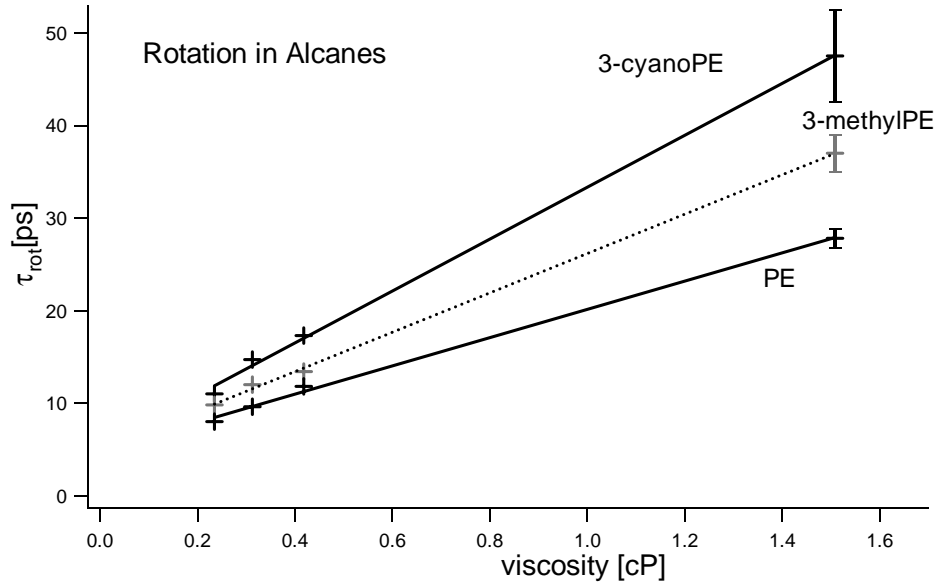


Figure 4.30: Rotational time of PE, 3-methylPE and 3-cyanoPE in a series of linear alkanes from pentane to dodecane, and SED linear fits. Note that no significant differences are present between the two substitution of PE.

From these experiments, one can determine that the crossing of the three interpolations with the zero viscosity is far from the free rotor prediction:

4.86 ps for PE

4.89 ps for 3-methylPE

5.27 ps for 3-cyanoPE

However, it can also be noted that in all cases, the low viscosity points show a nonlinear behavior as described in the previous section.

Assuming an axis ratio ρ of 0.42 for both substituted PE, the rotational time according to the SED model is:

$$\tau_{\text{rot}}(3\text{-methylPE}) = f \frac{V \cdot C}{k_B \cdot T} \cdot \eta = 1.395 \frac{245 \cdot 10^{-30}}{1.38 \cdot 10^{-23} \cdot 293} \cdot C \cdot \eta = 84.5 \cdot C \text{ [ps/cP]} \cdot \eta$$

$$\tau_{\text{rot}}(3\text{-cyanoPE}) = f \frac{V \cdot C}{k_B \cdot T} \cdot \eta = 1.395 \frac{240 \cdot 10^{-30}}{1.38 \cdot 10^{-23} \cdot 293} \cdot C \cdot \eta = 82.8 \cdot C \text{ [ps/cP]} \cdot \eta$$

From the slope of the fits, one can calculate the C parameter from the SED theory:

$$\text{3-methylPE: } C = \frac{21.3}{84.5} = 0.25$$

$$\text{3-cyanoPE: } C = \frac{28.1}{82.8} = 0.34$$

Compared to PE (0.14 to 0.20 depending on the low or high viscosity data), no significant leap between the 3-methyl and 3-cyano derivatives is present.

3-cyanoPE and 3-methylPE in a Series of Linear Nitriles

The experiment is repeated in a series of linear nitriles from MeCN to DeCN.

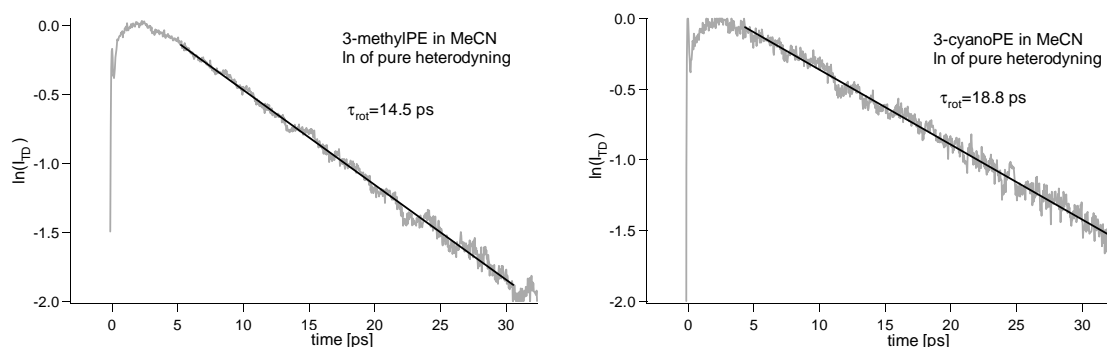


Figure 4.31: Natural logarithm of the rotational dynamics of 3-methylPE and 3-cyanoPE in MeCN, and best linear fits.

The rotational time obtained in all five nitriles are summarized in the following table, and graphically represented as a function of the solvent viscosity.

	MeCN	PrCN	VaCN	OcCN	DeCN
η [cP] 20° 90	0.35	0.41	0.74	1.64	2.66
τ_{rot} [ps] PE	12.4 \pm 0.4	14.3 \pm 0.2	18.9 \pm 0.5	37 \pm 2	59 \pm 3
τ_{rot} [ps] 3-methylPE	14.5 \pm 0.4	17.5 \pm 0.5	27 \pm 2	41 \pm 3	68 \pm 4
τ_{rot} [ps] 3-cyanoPE	18.8 \pm 0.5	22 \pm 1	39 \pm 2	81 \pm 3	131 \pm 6

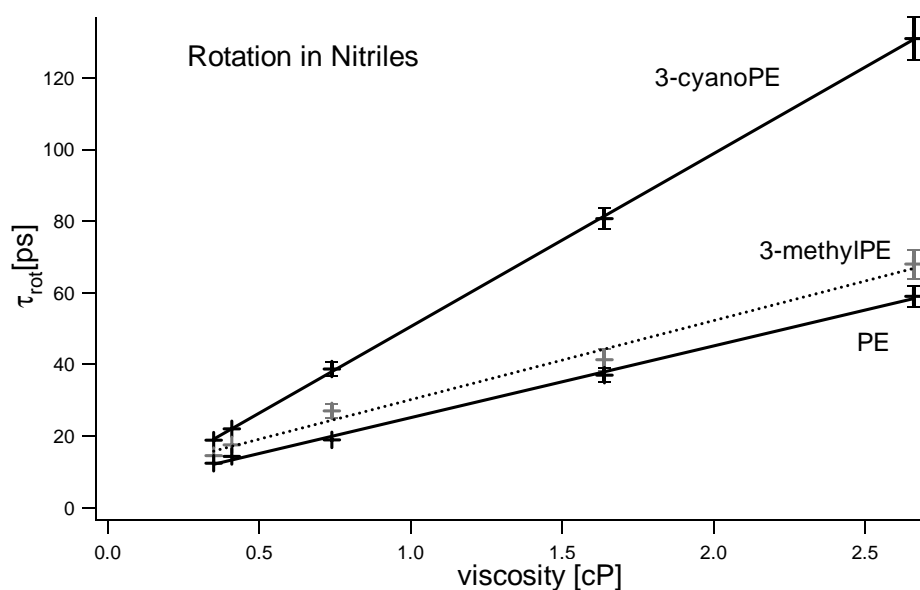


Figure 4.32: Rotational time of 3-cyanoPE, 3-methylPE and PE in a series of linear nitriles from MeCN to DeCN, and best linear fits. Note the different behavior of the cyano substituted PE.

The behavior of the PE and 3-methylPE is identical to that observed in the series of alkanes. However, the rotational time of the 3-cyanoPE is 70% slower in linear nitriles than in linear alkanes of identical viscosity.

This can be confirmed by the analysis of the parameter C .

According to the slope of the fits shown in Figure 4.32, the boundary constant C in the series of nitriles is calculated and compared to the values from the series of alkanes.

	Alcanes	Nitriles
3-methylPE	0.25	$22.1/84.5 = 0.26$
3-cyanoPE	0.34	$48.3/82.8 = 0.58$

One can conclude that a strong interaction between the 3-cyanoPE and the polar solvents is taking place. This increase of the rotational time being absent in the case of 3-methylPE and with nonpolar solvents, dipolar interaction is probably responsible for this behavior.

A complete analysis of this interaction is planned, as the dipole moment of the 3-cyanoPE is not reported in the literature yet.

It is also interesting to notice that for the PE and 3-methylPE the extrapolation to zero viscosity gives results far from the free rotor values (5.1 ps and 8 ps respectively). However, the steeper fit of the 3-cyanoPE crosses the zero viscosity at 2.2 ps, in complete agreement with free rotor rotation around the spinning axis (2.2 ps).

Additional Results

In order to complete the measurements, we have performed the same experiment in dioxane. This solvent has the particularity of being usually in a chair conformation and thus to be nonpolar. Nevertheless, it can isomerize to the boat conformation and become polar.



Figure 4.33: Chair and boat conformation of dioxane

3-methylPE being nonpolar, its rotational behavior should be identical to that observed in the linear alkane series. However, 3-cyanoPE has a permanent dipole moment and could thus favor locally the boat conformation. Its rotational behavior should then approach to that observed in the series of nitriles.

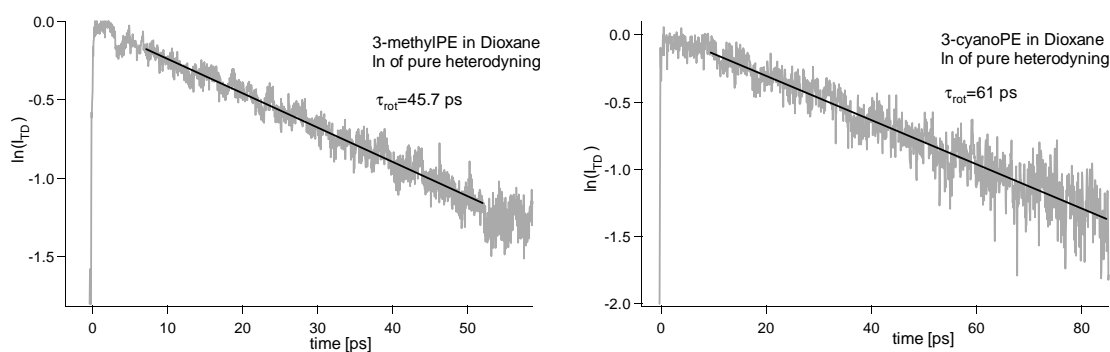


Figure 4.34: Natural logarithm of the pure heterodyne TD signal from 3-methylPE and 3-cyanoPE in dioxane, and best linear fit.

The viscosity of dioxane at 20° is 1.3 cP, and according to the SED fit previously shown (Figure 4.30 and Figure 4.32), one can extrapolate the rotational time for nonpolar and for polar solvents.

	Alkane type	Nitrile type	Dioxane
τ_{rot} [ps] 3-methylPE	32.6	36.7	46 ± 3
τ_{rot} [ps] 3-cyanoPE	41.7	65	61 ± 5

These results are consistent with the local boat conformation observed with 3-cyanoPE. However, neither the nonpolar, nor the polar predictions are suitable for the 3-methylPE.

In order to understand this behavior, one should first determine if the chair conformation of dioxane is slowing down the rotation of both 3-cyanoPE and 3-methylPE, or if a real local boat conformation is induced by the 3-cyanoPE. This could be achieved by a similar study in a series of cyclic alkanes for instance. The geometrical importance of the solute molecules could thus be determined.

5. Conclusion and Summary

In this thesis we have described several four wave mixing techniques and their corresponding experimental setup, and applied them to investigate ultrafast phenomena.

Special care was taken to describe the development of computer controlled experiments with fs pulses, which allow efficient and accurate acquisitions from 50 fs to more than 100 ps to be performed. Many technical aspects were also treated in detail in order to help research groups wanting to perform similar experiments.

We have also shown that four wave mixing techniques are powerful tools to investigate a wide range of photophysical and photochemical phenomena such as excited-state lifetimes, solvation dynamics, structural changes or orientational anisotropy.

The excited-state lifetime of PE, AQ and TRC radical ions were directly observed with TG technique to be shorter than 30 ps in condensed phase. A calorimetric detection was also developed, allowing low absorption coefficient species to be investigated.

Determination of solvent and solute vibrational frequencies was also achieved in a CARS experiment. TR²-CARS of intermolecular ET reaction was however hard to perform accurately, as the repetition rate of the ps laser used was too low. Hints on the direct formation of the LIP complex were nevertheless postulated.

Femtosecond time resolved polarization TG technique was used to characterize both inertial contributions of the solvation dynamics of an organic dye in series of alcohols and nitriles. Wavelength dependence was also investigated, showing that the diffusive motion can be associated with a loose

solvent shell, while inertial contribution dominates with highly solvated molecules.

The rotational dynamics of PE and PE derivatives in series of nitriles and alkanes was investigated with the TD technique. In low viscosity solvents, the linear relationship predicted by the SED model was not observed. Furthermore, a strong interaction between 3-cyanoPE and the polar solvents was determined, and attributed to dipolar interaction.

Four wave mixings techniques offer a wide range of possibilities only limited by imagination. Many parameters such as the wavelength, the incidence angle or the arrival time in the sample can be changed for each of the four pulses, leading to numerous combinations. Furthermore, additional pulses can also be used for instance to create transient species or, as described in chapter 2.2.4, to bleach a grating.

Only few of these pulses combinations have been used so far in chemical investigations, and it is probable that in the future, new four wave mixing (or even six wave mixing) techniques will be developed and allow new physical and chemical properties to be investigated.

Bibliography

- [1] M. Chergui, *Chimia*, **2000**, 83
- [2] P. Suppan, *Chemistry and Light*, The Royal Society of Chemistry, Cambridge, 1994
- [3] C. Baird, *Environmental Chemistry*, Freeman, New York, 1995
- [4] B. Coe, *The Birth of Photography : the Story of the Formative Years : 1800-1900*, Ash & Grant, London, 1976
- [5] R. G. W. Norrish and G. Porter, *Nature*, **1949**, 658
- [6] C. H. Townes, *O. L. E.*, **1999**, 20
- [7] T. Maiman, *Nature*, **1960**, 493
- [8] D. H. Sutter, G. Steinmeyer, L. Gallmann, N. Matuschek, F. Morier-Genoud, U. Keller, V. Scheuer, G. Angelow and T. Tschudi, *Opt. Lett.*, **1999**, 631
- [9] A. Zewail, *Femtochemistry, Ultrafast Dynamics of the Chemical Bond*, World Scientific Publishing, 1994
- [10] W. Demtröder, *Laser Spectroscopy*, Second Enlarged Edition, Springer Verlag, Berlin, 1996
- [11] D. Gabor, *Nature*, **1948**, 777
- [12] H. J. Eichler, G. Enterlein, J. Munschau and H. Stahl, *Z. Angew. Physik*, **1970**, 1
- [13] A. E. Siegman, *Lasers*, University Science Books, Mill Valley, 1986
- [14] H. J. Eichler, P. Günter and D. W. Pohl, *Laser-Induced Dynamic Gratings*, Springer Verlag, Berlin, 1986
- [15] N. A. Kurnit, I. D. Abella and S. R. Hartmann, *Phys. Rev. Lett.*, **1964**, 567

-
- [16] C. Kittel, *Introduction to Solid State Physics*, John Wiley & Sons, New York, 1986
- [17] A. Henseler and E. Vauthey, *J. Photochem. Photobiol. A: Chem*, **1995**, 7
- [18] L. Genberg, Q. Bao, S. Gracewski and R. J. D. Miller, *Chem. Phys.*, **1989**, 81
- [19] E. Vauthey and A. Henseler, *J. Phys. Chem.*, **1995**, 8652
- [20] A. A. Maznev, K. A. Nelson and J. A. Rogers, *Opt. Lett.*, **1998**, 1319
- [21] E. Vauthey and A. Henseler, *J. Phys. Chem.*, **1996**, 170
- [22] E. Vauthey and A. Henseler, *J. Photochem. Photobiol. A: Chem*, **1998**, 103
- [23] C. Högemann, M. Pauchard and E. Vauthey, *Rev. Sci. Instrum.*, **1996**, 3449
- [24] C. Högemann and E. Vauthey, *Isr. J. Chem.*, **1998**, 181
- [25] H. Kogelnik, *Bell. Sys. Tech. J.*, **1969**, 2909
- [26] R. W. Boyd, *Nonlinear Optics*, Academic Press, Boston, 1992
- [27] R. Magnusson and T. K. Gaylord, *J. Opt. Soc. Am.*, **1978**, 806
- [28] J. Michl and E. W. Thulstrup, *Spectroscopy with Polarized Light*, VCH Publisher, New York, 1986
- [29] R. S. Moog, M. D. Ediger, S. G. Boxer and M. D. Fayer, *J. Phys. Chem.*, **1982**, 4694
- [30] J. T. Fourkas and M. D. Fayer, *Acc. Chem. Res.*, **1992**, 227
- [31] J.-C. Gumy and E. Vauthey, *J. Phys. Chem.*, **1996**, 8628
- [32] P. Brodard, S. Matzinger, E. Vauthey, O. Mongin, C. Papamichael and A. Gossauer, *J. Phys. Chem. A*, **1999**, 5858
- [33] E. Vauthey, C. Högemann and X. Allonas, *J. Phys. Chem. A*, **1998**, 7362
- [34] J.-C. Gumy and E. Vauthey, *J. Phys. Chem. A*, **1997**, 8575

-
- [35] P. A. Franken, A. E. Hill, C. W. Peters and G. Weinreich, *Phys. Rev. Lett.*, **1961**, 118
- [36] F. W. Deeg and M. D. Fayer, *J. Chem. Phys.*, **1989**, 2269
- [37] A. B. Myers and R. M. Hochstrasser, *IEEE Quant. Electron.*, **1986**, 1482
- [38] J. Etchepare, G. Grillon, J. P. Chambaret, G. Hamoniaux and A. Orszag, *Opt. Commun.*, **1987**, 329
- [39] E. Vauthey, *Application of Real Time Holography for Investigating Ultrafast Photoinduced Processes*, Thèse d'agrégation, Université de Fribourg, Suisse, 1998
- [40] A. Materny, *Absorptions-, Resonanz-Raman- und Resonanz-CARS-Spektroskopie an Diacetylen-Einkristallen mit und ohne Farbzonen: Experiment und Theorie*, Dissertation, University of Würzburg, Germany, 1992
- [41] S. A. J. Druet and J.-P. E. Taran, *Prog. Quant. Electr.*, **1981**, 1
- [42] L. A. Carreira, L. P. Goss and T. B. J. Malloy, *Applications of CARS to Condensed Phase Systems*, Academic Press, 1981
- [43] H. Lotem and R. T. J. Lynch, *Phys. Rev.*, **1976**, 334
- [44] M. D. Levenson, *Nonlinear Laser Spectroscopy*, Academic Press, San Diego, 1987
- [45] D. Waldeck, A. J. Cross, Jr., D. B. McDonald and G. R. Fleming, *J. Chem. Phys.*, **1981**, 3381
- [46] C. Hoegemann and E. Vauthey, *J. Phys. Chem. A*, **1998**, 10051
- [47] A. Henseler and E. Vauthey, *Chem. Phys. Lett.*, **1994**, 66
- [48] R. A. Marcus, *J. Chem. Phys.*, **1956**, 966
- [49] G. L. Hug and B. Marciniak, *J. Phys. Chem.*, **1995**, 1478
- [50] S. Murata and M. Tachiya, *J. Phys. Chem.*, **1996**, 4064

-
- [51] K. Kikuchi, T. Katagiri, T. Niwa, Y. Takahashi, T. Suzuki, H. Ikeda and T. Miyashi, *Chem. Phys. Lett.*, **1992**, 155
- [52] N. Mataga, Y. Kanda, T. Asahi, H. Miyasaka, T. Okada and T. Kakitani, *Chem. Phys.*, **1988**, 239
- [53] M. Fujita, A. Ishida, T. Majima and S. Takamuka, *J. Phys. Chem.*, **1996**, 5382
- [54] C. Ruillère, T. Amand and X. Marie In *Femtosecond Laser Pulses*, C. Ruillère, Ed., Springer-Verlag, Berlin, 1998, 225
- [55] P.-A. Muller, C. Högemann, X. Allonas, P. Jacques and E. Vauthey, **submitted**,
- [56] C. Högemann, *Development and Application of Picosecond Transient Grating Spectroscopy*, Dissertation n°1259, Université de Fribourg, Suisse, 1999
- [57] N. Mataga, T. Asahi, Y. Kanda, T. Okada and T. Kakitani, *Chem. Phys.*, **1988**, 249
- [58] T. Shida, *Electronic Absorption Spectra of Radical Ions*, Elsevier Science Publishers B.V., Amsterdam, 1988
- [59] B. Schrader, *Raman: Infrared Atlas of Organic Compounds*, VCH Verlagsgesellschaft, Weinheim, 1989
- [60] S. Matsunuma, N. Akamatsu, T. Kamisuki, Y. Adachi, S. Maeda and C. Hirose, *J. Chem. Phys.*, **1987**, 2956
- [61] L. A. Carreira, T. C. Maguire and T. B. Malloy, *J. Chem. Phys.*, **1977**, 2621
- [62] A. Kummrov, A. Lau and H. G. Ludewig, *Opt. Commun.*, **1994**, 137
- [63] J. Oberlé, E. Abraham, A. Ivanov, G. Jonusauskas and C. Ruillère, *J. Phys. Chem.*, **1996**, 10179
- [64] S. A. Payne and R. M. Hochstrasser, *J. Phys. Chem.*, **1986**, 2068

-
- [65] A. P. Shkurinov, N. I. Koroteev, G. Jonusauskas and C. Ruillère, *Chem. Phys. Lett.*, **1994**, 573
- [66] L. Ujj, B. L. Volodin, A. Popp, J. K. Delaney and G. H. Atkinson, *Chem. Phys.*, **1994**, 291
- [67] G. H. Atkinson, A. Popp and L. Ujj In *Time-Resolved Vibrational Spectroscopy VI*, A. Lau, F. Siebert and W. Werncke, Eds., Springer-Verlag, Berlin, 1994, 153
- [68] L. A. Carreira, L. P. Goss and T. B. Malloy, *J. Chem. Phys.*, **1978**, 855
- [69] T. Tahara, B. N. Toleutaev and H. Hamaguchi, *J. Chem. Phys.*, **1994**, 786
- [70] E. Vauthey, A. W. Parker, B. Nohova and D. Phillips, *J. Am. Chem. Soc.*, **1994**, 9182
- [71] A. Sarbach, *Ions Radicalaires comme Produits du Transfert d'Electron Photoinduit: Emission à Basse Température et Photoconductivité*, Thèse n°1290, Université de Fribourg, Suisse, 2000
- [72] E. Vauthey, *Lasers and their applications. Part 1*, Lecture Notes, University of Fribourg, 1997
- [73] C. Ruillère (Ed.), *Femtosecond Laser Pulses*, Springer-Verlag, Berlin, 1998
- [74] C. Hirlimann In *Femtosecond Laser Pulses*, C. Ruillère, Ed., Springer-Verlag, Berlin, 1998, 31
- [75] D. T. Reid, M. Padgett, C. McGowan, W. E. Sleat and W. Sibbett, *Opt. Lett.*, **1997**, 233
- [76] J. K. Ranka, A. L. Gaeta, A. Baltuska, M. S. Pshenichnikov and D. A. Wiersma, *Opt. Lett.*, **1997**, 1344
- [77] D. N. Fittinghoff, J. L. Bowie, J. N. Sweetser, R. T. Jennings, M. A. Krumbugel, K. W. DeLong, R. Trebino and I. A. Walmsley, *Opt. Lett.*, **1996**, 884

-
- [78] C. Iaconis and I. A. Walmsley, *Opt. Lett.*, **1998**, 792
- [79] AXIOM, *AX5210 User's Manual*, 4th Edition, AXIOM Technology Co., Taiwan, 1994
- [80] J. D. Simon, *Acc. Chem. Res.*, **1988**, 128
- [81] P. F. Barbara and W. Jarzeka, *Adv. Photochem.*, **1990**, 1
- [82] Y. Nagasawa, A. P. Yartsev, K. Tominaga, A. E. Johnson and K. Yoshihara, *J. Chem. Phys.*, **1994**, 5717
- [83] H. Kandori, K. Kemnitz and K. Yoshihara, *J. Phys. Chem.*, **1992**, 8042
- [84] M. Maroncelli and G. R. Fleming, *J. Chem. Phys.*, **1988**, 5044
- [85] P. V. Kumar and M. Maroncelli, *J. Chem. Phys.*, **1995**, 3038
- [86] S. J. Rosenthal, X. Xie, M. Du and G. R. Fleming, *J. Chem. Phys.*, **1991**, 4715
- [87] K. Yoshihara, K. Tominaga and Y. Nagasawa, *Bull. Chem. Soc. Jpn.*, **1995**, 696
- [88] O. Nicolet, *Influence de la Viscosité du Solvant sur le Temps d'Isomérisation cis-trans du Perchlorate de 1,1'-diethyl 2,2'-tricarbo-cyanine (DTP)*, Travail de diplôme, Université de Fribourg, Suisse, 1999
- [89] P. Suppan and N. Ghoneim, *Solvatochromism*, The Royal Society of Chemistry, Cambridge, 1997
- [90] J. A. Riddick and W. Bunger, *Organic Solvents, third Edition*, Wiley Interscience, 1970
- [91] F. Salin In *Femtosecond Laser Pulses*, C. Ruillère, Ed., Springer-Verlag, Berlin, 1998, 164
- [92] Spectra-Physics Lasers, *Spitfire LCX User's Manual*, Spectra-Physics Lasers, Mountain View, CA, 1998
- [93] K. Kimura, T. Yamazaki and S. Katsumata, *J. Phys. Chem.*, **1971**, 1768

-
- [94] W. I. Aalbersberg, G. J. Hoijsink, E. L. Mackor and W. P. Weijland, *J. Chem. Soc.*, **1959**, 3049
- [95] E. Vauthey, **submitted**,
- [96] *Handbook of Chemistry and Physics*, 65th ed., CRC Press, Boca raton, 1984-85
- [97] D. T. Breslin and M. A. Fox, *J. Phys. Chem.*, **1994**, 408
- [98] K. G. Spears and L. E. Cramer, *Chem. Phys.*, **1978**, 1
- [99] A. v. Jena and H. E. Lessing, *Chem. Phys.*, **1979**, 245
- [100] G. R. Fleming, *Chemical Application of Ultrafast Spectroscopy*, Oxford University Press, New York, 1996
- [101] C. M. Hu and R. Zwanzig, *J. Chem. Phys.*, **1974**, 4354
- [102] G. R. Alms, D. R. Bauer, J. I. Brauman and R. Pecora, *J. Chem. Phys.*, **1973**, 5570
- [103] R. S. Hartman, W. M. Konitsky, D. H. Waldeck, Y. J. Chang and E. W. J. Castner, *J. Chem. Phys.*, **1997**, 7920
- [104] G. B. Dutt and S. Doraiswamy, *Inst. Phys. Conf. Ser.*, **1991**, 531
- [105] G. B. Dutt, S. Doraiswamy, N. Periasamy and B. Venkataraman, *J. Chem. Phys.*, **1990**, 8498
- [106] T. W. Nee and R. Zwanzig, *J. Chem. Phys.*, **1970**, 6353
- [107] D. S. Alavi and D. H. Waldeck, *J. Chem. Phys.*, **1991**, 6196
- [108] F. J. Bartoli and T. A. Litovitz, *J. Chem. Phys.*, **1972**, 413
- [109] J. L. Dote, D. Kivelson and R. N. Schwartz, *J. Phys. Chem.*, **1981**, 2169
- [110] J.-C. Gummy, *Influence d'un Excès d'Energie d'Excitation sur le Temps de Rotation de la Rhodamine 6 G à l'Etat Fondamental et Excité*, Travail de diplôme, Université de Fribourg, Suisse, 1995
- [111] N. P. Buu-hoï and C. T. Long, *Recl. Trav. Chim. Pays-Bas*, **1956**, 1221
- [112] J. T. Edward, *J. Chem. Educ.*, **1970**, 261

Remerciements

Je tiens à remercier chaleureusement toutes les personnes qui ont contribué à la réalisation de cette thèse, tant par leurs nombreuses et constructives discussions, que par l'atmosphère de travail toujours sympathique qu'ils ont maintenu:

- Emile Brosi et ses collaborateurs, pour la construction des cellules à circulation et à rotation ainsi que de nombreux autres appareils.
- Paul-Hervé Chassot et ses collaborateurs, pour le développement et la réalisation du TZD, de connecteurs d'interfaçage, et la résolution de tous les problèmes électroniques.
- Jean-Luc Roulin et ses collaborateurs, pour la synthèse des dérivés du perylène et la purification des substances chimiques utilisées dans ce travail.
- Verena Schwalm, pour s'être occupé de toute la partie administrative.
- Mes collègues de bureau durant ces années, à savoir Pierre Brodard, Dr. Claudia Högemann, Ana Morandeira, Pierre-Alain Muller, Dr. Markus von Raumer, Dr. Alexandre Sarbach.
- Les membres de l'institut de chimie physique, à savoir Prof. Dr. Michael Allan, Prof. Dr. Thomas Bally, Pawel Bednarek, Claudio Carra, Dr. Nagwa Ghoneim, Gilbert Handgartner, Prof. Dr. Werner Hug, Dr. Stephan Matzinger, Beat Müller, Anne-Christelle Sergenton, Prof. Dr. Paul Suppan[†] et Gerard Zuber.
- Le Fonds National Suisse de la Recherche Scientifique et le canton de Fribourg, pour leur financement.

Curriculum Vitae

Personal information

Name, first name GUMY Jean-Claude
Birth date 20th, March 1972
Citizenship Swiss
Marital status married



Education and research

1996 - 2000 Ph.D. in Physical Chemistry under the direction of Dr. E. Vauthey at the University of Fribourg.
1991 - 1996 Diploma in Chemistry at the Faculty of Science of the University of Fribourg. Physical Chemistry as main branch and Biochemistry as secondary branch.
1987 - 1991 "Maturité fédérale" at the College St-Michel of Fribourg

Languages

French : native tongue
German : good knowledge (partial language of study)
English : good knowledge (partial language of study and 4 weeks school in USA)

Publications

- *"Picosecond polarization grating study of the effect of excess excitation energy on the rotational dynamics of Rhodamine 6G in different electronic states."*

Gumy J.-C., Vauthey E., *J. Phys. Chem.*, **1996**, 100, 8628.

- *"Investigation of the excited-state dynamics of radical ions in the condensed phase using the picosecond transient grating technique."*

Gumy J.-C., Vauthey E., *J. Phys. Chem. A*, **1997**, 101, 8574.

- *"Investigation of the solvation dynamics of an organic dye in polar solvents using the femtosecond transient grating technique."*

Gumy J.-C., Nicolet O. and Vauthey E., *J. Phys. Chem. A*, **1999**, 103, 10737.

Oral Communication

- *"Solvation dynamics of a dye in alcohols and nitriles using fs 3rd order nonlinear spectroscopie."* Gumy J.-C., Nicolet O., Vauthey E.

◆ *Schweizerische Gesellschaft für Photochemie und Photophysik*, mars 1999, **Fribourg**.

Posters

- *"Picosecond polarization grating study of the rotational dynamics of Rhodamine 6G in different electronic states."* Gumy J.-C., Vauthey E.,
 - ◆ *Nouvelle Société Suisse de Chimie*, octobre 1996, **Berne**.
- *"Excited-state dynamics of radical ions in the condensed phase using picosecond transient grating technique."* Gumy J.-C., Vauthey E.
 - ◆ *European Photochemistry Association*, juin 1998, **Nordwijk** (Netherlands).
 - ◆ *Nouvelle Société Suisse de Chimie*, octobre 1998, **Zürich**.
- *"Solvation dynamics of a dye in alcohols and nitriles using fs Four-Wave-Mixing spectroscopies."*
Gumy J.-C., Nicolet O., Vauthey E.
 - ◆ *Workshop on bacteriorhodopsin*, mai 1999, **Lausanne**.
 - ◆ *Nouvelle Société Suisse de Chimie*, octobre 1999, **Zürich**.
 - ◆ *European Physical Society: Condensed Matter Division*, mars 2000, **Montreux**.